NUMERICAL MODELING OF NONLINEAR COUPLING BETWEEN LINES/BEAMS WITH MULTIPLE FLOATING BODIES

A Dissertation

by

CHAN KYU YANG

Submitted to the Office of Graduate Studies of
Texas A&M University
in partial fulfillment of the requirements for the degree of

DOCTOR OF PHILOSOPHY

May 2009

Major Subject: Ocean Engineering

NUMERICAL MODELING OF NONLINEAR COUPLING BETWEEN LINES/BEAMS WITH MULTIPLE FLOATING BODIES

A Dissertation

by

CHAN KYU YANG

Submitted to the Office of Graduate Studies of
Texas A&M University
in partial fulfillment of the requirements for the degree of

DOCTOR OF PHILOSOPHY

Approved by:

Chair of Committee,	Moo-Hyun Kim
Committee Members,	Jun Zhang
	Richard Mercier
	Alan B. Palazzolo
Head of Department,	David V. Rosowsky

May 2009

Major Subject: Ocean Engineering

ABSTRACT

Numerical Modeling of Nonlinear Coupling between Lines/Beams with Multiple Floating Bodies. (May 2009)

Chan Kyu Yang, B.S., Seoul National University;
M.S., Seoul National University
Chair of Advisory Committee: Dr. Moo-Hyun Kim

Nonlinear coupling problems between the multiple bodies or between the mooring/riser and the offshore platform are incorporated in the CHARM3D-MultiBody, a fully coupled time domain analysis program for multiple bodies with moorings and risers. The nonlinear spring connection module and the three dimensional beam module are added to appropriately solve the structural connection problem. The nonlinear spring connection module includes the hydro-pneumatic tensioner module with the friction & stick/slip implementation, the tendon/mooring disconnection (breakage/unlatch) module with the tendon down-stroke check, and the contact spring with the initial gap with the friction force implemented.

The nonlinear coupling may happen in many places for the offshore floating structures, such as hydro-pneumatic tensioner, tendon of TLP down stroke at the bottom joint, stick-slip phenomena at the tie down of the derrick and most of the fender-to-steel or steel-to-steel contact problem with initial gap during the installation. The

mooring/tendon broken and unlatch can be a nonlinear connection problem once the transient mode is taken into account.

Nonlinearity of the stiffness and friction characteristics of the tensioner combined with stick-slip behavior of riser keel joint is investigated. The relationship between tensions and strokes for hydro-pneumatic tensioner is based on the ideal gas equation where the isotropic gas constant can be varied to achieve an optimum stroke design based on tensioner stiffness.

A transient effect of tendon down-stroke and disconnection on global performance of ETLP for harsh environmental condition is also investigated by incorporating the nonlinear boundary condition of the FE tendon model in CHARM3D. The program is made to be capable of modeling the tendon disconnection both at the top and the bottom connection as well as the down stroke behavior for the pinned bottom joint.

The performance of the tie-down clamp of derrick is also investigated by using six degrees of freedom spring model and the three(3) dimensional FE beam model. The coupling of the TLP motion with the reaction force at the tie-down clamp is considered by using exact nonlinear dynamic equations of the motion with the reaction forces modeled with the spring or FE beam model. The method reduces too much conservatism when we design the tie-down system by the conventional method, in which all the environmental forces are combined without the phase lag effect between them.

The FE beam model is also applied to the connectors between the semisubmersible and the truss for the pre-service and in-place conditions to be verified with the model test results, which shows good agreements.

DEDICATION

I dedicate my dissertation work to my parents, who raised me to be the person I am today. I also dedicate this dissertation to my wife Jeonghyun and my children Kelly, Chloe and Andrew who continued to support and to encourage me to accomplish it.

ACKNOWLEDGEMENTS

I would like to thank my committee chair, Dr. Moo-Hyun Kim, and my committee members, Dr. Zhang, Dr. Mercier, and Dr. Palazzolo, for their guidance and support throughout the course work and the course of this research.

Thanks also go to my friends and colleagues and the department faculty and staff for making my time at Texas A&M University a great experience. I also want to extend my gratitude to Dr. Alex Ran, Dr. Arcandra Tahar and Dr. Bonjun Koo for sharing their knowledge and effort to discuss the problem.

I appreciate FloaTEC, LLC for sharing data to verify the program, and Mr. John Murray who shared the wide knowledge about the offshore engineering, which was very helpful to accomplish it.

Thanks to my mother and father for their encouragement and to my family for their patience and love. Finally, Most of all thanks to God the Divine who continues to make the impossible possible.

TABLE OF CONTENTS

Page

Page

LIST OF FIGURES

Page

Page

Page

Page

LIST OF TABLES

1. INTRODUCTION

1.1 Background

The development of the offshore petroleum industry is a remarkable story of inventiveness, entrepreneurship, hard work, and risk-taking. Many types of floating offshore platforms have been continually proposed and evaluated for better performance since the offshore oil and gas industry was started. Among them, Spar, semisubmersible, tension leg platform (TLP) and floating production, storage and offloading vessel (FPSO) are mostly selected to be installed for offshore developments worldwide due to their various advantages in global motion, transportation and installation.

The first transportable drilling rig installed in Gulf of Mexico in 1962 is a semi-submersible, called “Mr. Charlie”. The use of semi-submersible type floating offshore vessels in severe ocean environments has given rise to considerable design and research activities particularly with regard to wave induced motions as they affect the drilling operations. It thus becomes obvious that the natural periods of heave, roll and pitch should be as far removed from wave periods as possible to prevent the occurrence of large amplitude resonant motions. For this reason, the roll and pitch periods are generally in excess of 30 seconds where, hopefully wave energy is small and large resonant motions are unlikely. Therefore the semi-submersible is known to be more capable of operating in a much rougher sea environment than a conventional ship.

This dissertation follows the style of Journal of Ocean Engineering.

The heave period however generally lies much closer to wave periods and the probability of resonant heave motion is much higher. Thus, a fundamental principle of the response of a semisubmersible is that it is heave motion rather than roll or pitch that leads to the suspension of drilling. Furthermore if the swell wave period is equal to the natural heave period, then resonant motion will ensure leading to large amplitudes. What is worse, since the hulls are placed at a deep draft for drilling, the potential or wave generated damping which is the major source of damping for surface vessels, is so small as to be negligible (Paulling, 1977). The absence of linear potential damping makes it obvious that nonlinear quadratic drag force damping due to the vertical velocity of the submerged structure is the only source of damping which controls the resonant.

As mentioned previously, to reduce wave induced motion, the natural frequency of offshore structures are designed to be far away from the peak frequency of the force power spectra. Tension leg platforms (TLPs) and Spar platforms are two such attractive options proposed for deep water applications for the drilling, production, processing, storage and offloading of ocean deposits. Many investigations have been carried out to study the behavior and dynamic response of these platform concepts in order to optimize their designs. The favorable motion characteristics of TLPs have been well established by experiment and simulation.

The TLP is a kind of compliant type offshore platform which is generally used for deep water oil exploration. As reflected by its name, it is a buoyant structure anchored by pretensioned cables to the sea bed. They are designed to be more responsive to external loading than the fixed type offshore platforms. The cabling system of the platform may be vertical or spread which restrain vertical movements, but permits some horizontal displacement (Oran, et. al, 1983). The terminal of such a platform remains virtually horizontal. The tension cabling system consists of four or more tension legs, each leg being comprised of multiple parallel tension members terminated at the base of the structure.

In 1984, the world's first TLP in the U.K. North Sea Hutton field was installed. Since then, tens of TLPs have been installed around the world’s offshore including the first tension leg well platform (TLWP) installed in the Jolliet field in the Gulf of Mexico in 1989 and the first concrete TLP in the Heidrun field in the Norwegian sector of the North Sea in 1995.

The concept of the Spar proposed by Edward E. Horton is described as “a vessel with a circular cross-section that sits vertically in the water and is supported by hard tanks at the top and stabilized by a midsection hanging from the hard tanks”. If necessary, stability may be supplemented by solid ballast placed in compartments at the keel. The vessel is held in place by a catenary mooring system, providing the lateral station keeping. The first classic Spar(Neptune) was installed at the water depth of 588.2 m (1930 ft) in Gulf of Mexico in 1996, and more innovative hull shapes, such as Truss Spar, intended for use in a deeper region was invented. Now total twelve (13) Spar platforms are installed and operated in Gulf of Mexico.

The classic Spar has more entrapped mass and lower first order motions than the truss Spar. This reduces loads on a taut mooring when the water depth is relatively shallow and a high wave environment dominates the mooring system design. However, the truss Spar has much lower drag in currents and should result in a lower mooring system cost if currents control the mooring design. For a given payload, a truss spar has typically 20-30 % less total hull steel than a classic Spar. The additional hull weight for the classic Spar is in the midsections. Since the truss weight per foot is relatively less than the classic midsection, truss Spars can have longer midsections and less fixed ballast. An advantage of the Spar is that it can use buoyancy cans to decouple the relative platform and riser movement. Most of the efforts are made in Spar sizing to reduce the maximum heel angle and ensure it is acceptable to the risers, topsides equipment and operations, while of equal importance is the maximum heave motion. The Spar design has an extreme pitch angle, which includes both static heel and dynamic rotation of ten degrees. The dynamic rotation is on the order of four degrees in an extreme Gulf of Mexico environment, so the maximum heel angle should be six degrees or less.

Figure 1.1 shows the typical heave natural period ranges and the exemplified heave RAOs of TLP, FPSO, conventional semisubmersible, Spar and dry tree semisubmersible, with the typical power spectrum of wave in Gulf of Mexico.

Nowadays, fast development of offshore construction can be observed for a large variety of activities at sea. As offshore oil and gas exploration is pushed into deeper and deeper water with the heavier payload, many innovative floating offshore structures are being proposed for cost savings. Sometimes, little use can be made of the know-how obtained from the experience with earlier-built structures to design the advanced structures.

There is strong interest within the offshore industry in deep water explorations and development. Fields more than 8000ft water depth are being considered in such different areas as the Norwegian Sea, the Gulf of Mexico, Brazil and West Africa. Many of the field development requires a drilling rig as well as the production facility, which increases the payload above 30,000st, and it becomes very hard for the conventional platform to accommodate that heavy facilities in such deep water. To meet the new challenges, a variety of strategies and concepts for oil production have been developed which, although differing markedly in many aspects, share the common feature of being reliant on floater technology.

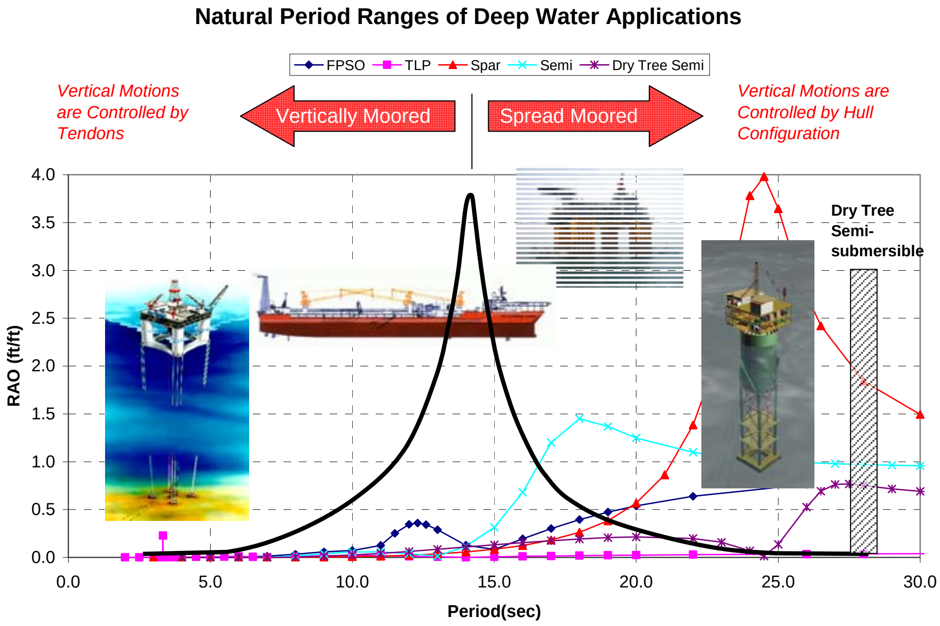

Figure 1.1 Typical Motion Characteristics of the Floating Platforms; TLP, FPSO, Semisubmersible and Spar

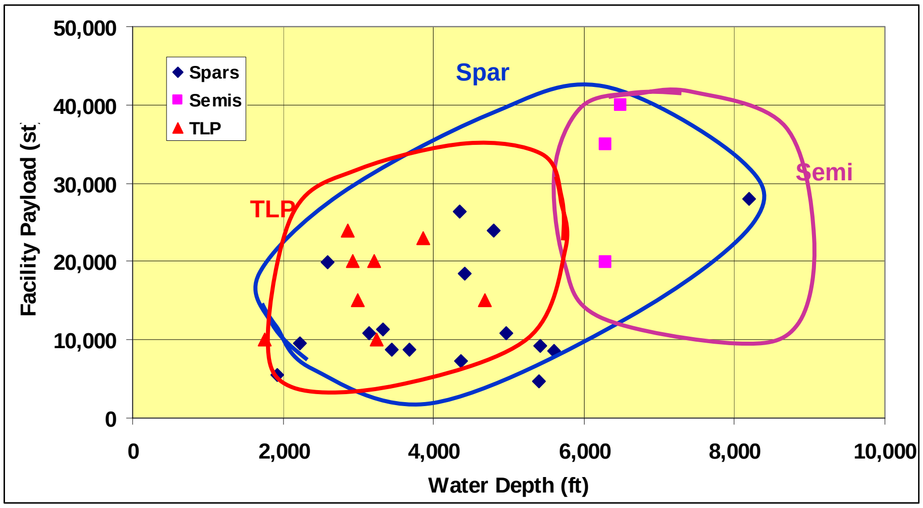

Figure 1.2 Summary of the Optimum Operation Ranges of the Platforms with Respect to the Payload and the Water Depth

Figure 1.2 shows the optimum operation ranges of the platforms with respect to the facitlity payloads and the water depth with the existing platforms exemplified. Spar has relatively larger ranges of water depth and payload for the optimum operation than TLP and semisubmersible. However, it is hard to accommodate the payload more than 35,000st at the water depth deeper than 8,000ft. The semisubmersible covers the deep water range, but it cannot support the dry tree units due to its large heave motion response (Kirk, 1985, Yang, et.al, 2007a and Murray et. al, 2006).

The more risky and expensive installation method, such as float-over is necessary with the heavy topside weight even though the conventional platform, either TLP or Spar is used. Figure 1.3 shows a snapshot of the float-over installation and the details of the sand jack system at the mating leg and at the temporary support bracing are exemplified in Figure 1.4. The elastometric material used for the shock absorber shows the nonlinear elastic behavior and the properties needs to be dealt with as a nonlinear connection with the initial gap contact problem, which is also challenging in design, and the other disadvantage of the float-over installation of Spar and TLP topside is that it is to be carried out on site where it is very hard to find the proper window to ensure the workability to keep the relative motion or the structural loads within the safe criteria.

The dry tree semisubmersible is one of the new concepts to make it possible to accommodate the heavy payloads in the ultra-deep water region. In addition, it makes the topside installation and the commissioning at the quay side possible. Therefore, the risk of float-over installation can be eliminated from its execution plan. There are many sorts of the dry tree semisubmersibles proposed, most of which are to increase the heave natural period to avoid the wave frequency range in the field of development. As the new concepts of the offshore platforms always do, the dry tree semisubmersibles usually result in their structural complexity to hire the advantages from the existing ones. Thus, the structural and the hydrodynamic interaction of the multiple floating bodies become the most concern. The innovative way of installation procedure also requires more complex analysis method. One example of the dry tree semisubmersible installation is dealt with by implementing the new feature of the elastic structure model in the Multi-body module of Charm3D.

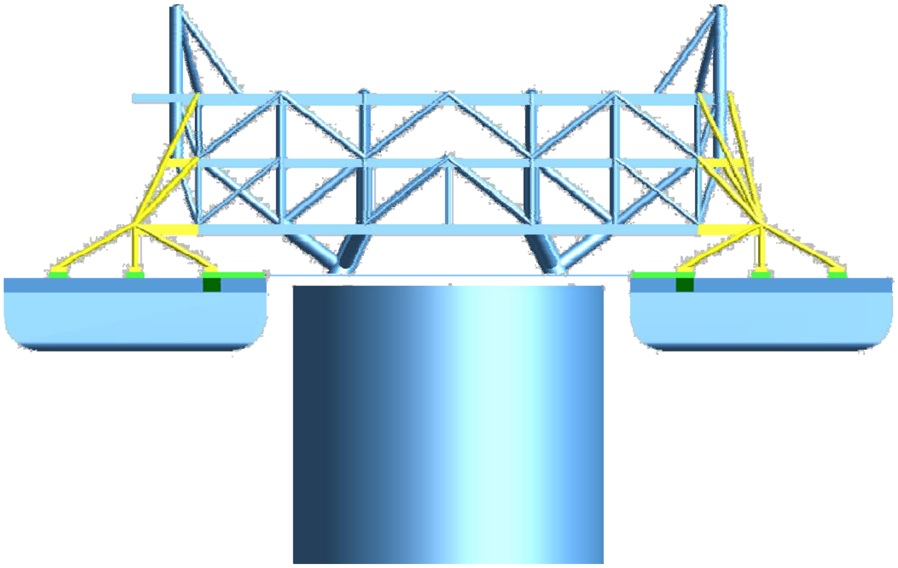

Figure 1.3 Float-over Installation of a Spar Topside

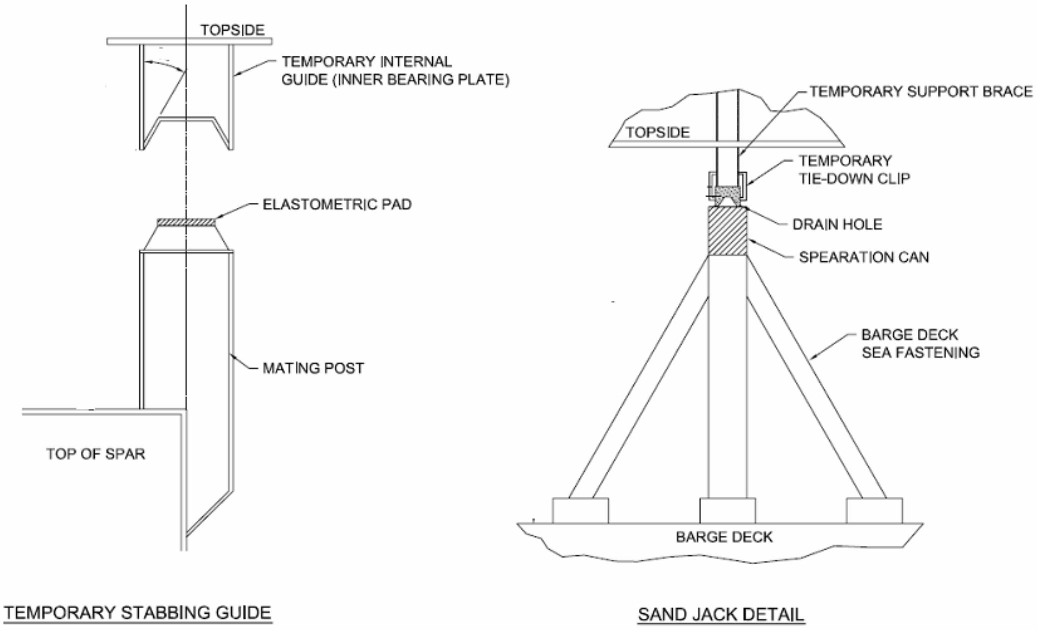

Figure 1.4 A Configuration of Sand Jack System for the Float-over Operation Causing the Nonlinear Contact Problem

On the other hand, the recent successive severe hurricanes such as Ivan, Katrina, and Rita gave rise to a strong motivation to update the criteria and procedures of designing the floating platforms in Gulf of Mexico(API, 2007). The harsher environmental criteria based on the hindcast of the hurricanes are also implemented by API, especially for central region of GoM(API, 2007b). Efforts are being made to reassess the global performance of the existing platforms under the Post-Katrina environment(Murray, et.al, 2008d), and the new designs of the platforms already follow the renewed criteria and procedures (Yang, et. al, 2009, Murray, et. al, 2008b and Murray, et.al, 2008b).

The harsh environment may affect the offshore platform in two different ways. At first, the system becomes the more nonlinear, if the more severe environmental loads are applied because of the larger motion response. Next, the severe hurricane events damaged tens of existing offshore platform on either the mooring system or the topside. As a result, more accurate modeling method between riser-to-body or body-to-body connections are required for the harsh design criteria.

The hydro-pneumatic tensioner is the most complicated one among the riser-to-body connection problems. The difficulty mostly comes from the nonlinearity of the stiffness and the friction force of it. The upper and down stroke limitation due to the definite length of accumulator also demands the sophisticated contact modeling.

The dry tree system involves a floating host platform to facilitate tieback of the sea bed wells, via top tensioned production risers, to a dry environment on the vessel to take advantage of the direct accessibility of the wells located below the production platform (Murray et al, 2006). This eliminates the need to mobilize special vessels for drilling and workover activities. In the dry tree unit, some risers are tensioned by buoyancy cans, or deck mounted tensioner systems, such as a hydro-pneumatic tensioner. The characteristics of the buoyancy can and the tensioner are compared in Table 1.1, which compares the buoyancy can and the tensioner in detail. It is more difficult and expensive to install the buoyancy can than the tensioner and the buoyancy can may have damage due to the material contact and is hard to repair, while the tensioner is installed on or below the deck easily and is relatively easy to maintain.

The buoyancy can is able to decouple the motion of the Spar and the riser which makes it able to accommodate unlimitedly large stroke, while the tensioner has variant nonlinear tension depending on the stroke and needs to be coupled with the floating platform to add the system stiffness. Buoyancy can model has been implemented in the coupled analysis program and the effect on the global motion of Spar has been investigated (Koo, et al, 2006), which showed the much different motion characteristics compared with the linearized model due to the contact and friction phenomena between the cans and the guiders.

Figure 1.5 and Figure 1.6 introduce the two types of the conventional tensioner systems, cassette type (pull-up type) and ram type (push-up type), respectively. The ram type is installed on the deck which makes the accessibility and maintenance relatively easy and can accommodate longer stroke than the cassette type, but the type needs to take more space on the deck and has to have enough deck height. In either cases the tensioner has nonlinearity and complicated friction mechanism. Accordingly, the global motion analysis for design purpose requires more and more complicated modeling of riser-body connection due to the complexity of the system itself and the harshness of the design criteria. The upper and down stroke limitation due to the definite length of accumulator also demands the correct contact modeling.

Especially, the tensioner for a Spar is known to be a more challenging design than a buoyancy can because the tensioner makes the heave motion stiffer and the heave natural period comes closer to the wave exciting period. On the other hand, the tensioner may decrease the heave motion RAO around the natural period by providing the Coulomb friction damping. The new FE model of the nonlinear tensioner coupling the riser and the hull motion is introduced herein. The model is implemented in the Charm3D(Ran et al, 1997 & 1999), a fully coupled time/frequency domain analysis program of floating bodies and mooring lines/risers.

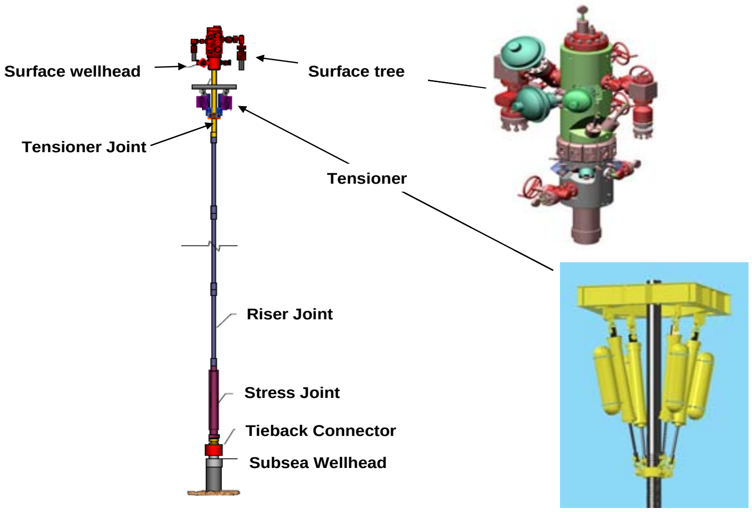

Figure 1.5 Cassette (Pull-up) Type Hydro-pneumatic Tensioner System

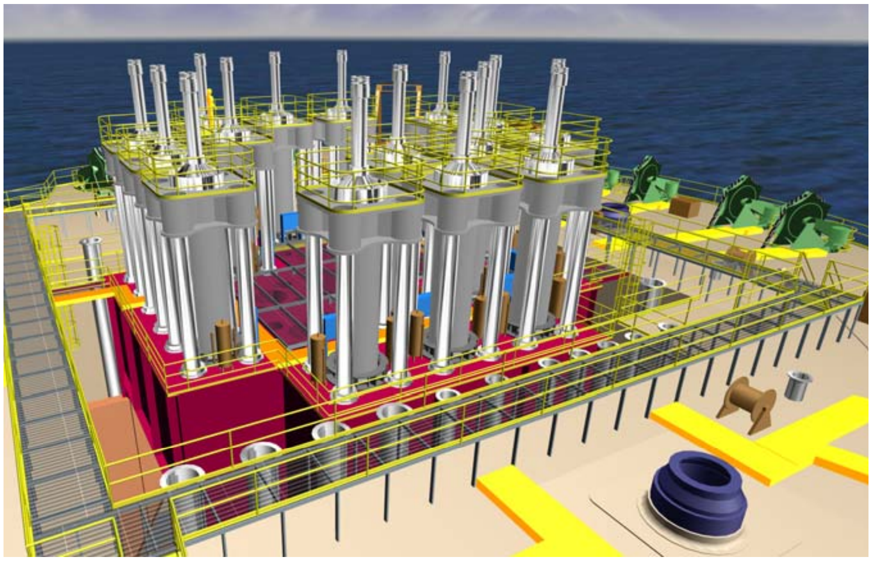

Figure 1.6 Ram (Push-up) Type Hydro-pneumatic Tensioner System

Table 1.1 Comparison of Buoyancy Can and Tensioner

	Buoyancy Can	**Tensioner**
Motion	- Decoupled motion - No effect by heave motion - More benefit for Spar/Semi	- Coupled motion - Reduce the heave period - More benefit for TLP
Size	Bigger	Smaller
Installation	Need barge	Easy
Maintenance	Hard to repair (due to damage, contact material failure)	Easy
Nominal tension limits	Size determines the tension	More cylinder can be put to get more tension, No limits Existing tensioner is 2300 kips
Stroke limits	- No limits - Stopper designed to prevent excess relative motion from jumper disconnection. - Keel guide should be designed to prevent ball joint out of keel.	- Less than 30 ft, - Otherwise cost expensive and need more deck space to install the tensioner
Accident	Stopper may breaks the deck stopper	Minimum
Tension variation	Constant	Nonlinear
Floater type	SPAR	TLP/SPAR/SEMI

TLP is one of the proven technologies to support the risers in the severe environment condition by providing negligible motions in the degrees of freedom such as heave, roll and pitch. The vertical motion characteristics of the TLP mainly are mainly determined by the tendon configuration, while the vertical motions of other floaters are mostly affected primarily by the hull geometry. Thus, damage to the tendon damage or a broken tendon may result in catastrophic impact on the TLP hull and risers. A significant damage to a TLP in the GoM during the hurricane Rita illustrates the importance of tendon design for the safety of TLP.

The break at the top connection and unlatch at the bottom connection are possible scenarios during the harsh environment. The break at the top may occur when the tension exceeds the breaking strength and the unlatch at the bottom may happen when the bottom tension becomes negative. An ETLP designed for GoM is selected to investigate the effect of the tendon disconnection during harsh environmental conditions.

However, after a recent failure which took place on a TLP where the Tendon Bottom Connector released prematurely, methods have been developed to prevent an uncontrolled release of a tendon from the tendon receptacle at the top of the foundation pile. The typical top and bottom connectors of the tendon are in shown in Figure 1.7.

Their bottom connector design was changed so that if a tendon goes slack and the bottom connector travels down a distance of 40” from the engaged position, it would make contact with a set of retaining pins, stopping the connector from releasing (see Figure 1.8). The connector can, therefore, only be released with manual removal of these pins. Three symmetrically located retaining pins have been incorporated in the design. These pins are installed into the receptacle once the tendons are fully installed, using a work-class remote operated vehicle (ROV) as in Figure 1.9.

The TLP tendons may break at the top or unlatch at the bottom during the harsh environment. The break at the top may occur when the tension exceeds the breaking strength. The unlatch at the bottom may happen when the bottom tension becomes negative and after it experience the down stroke. To the best of authors’ knowledge, the transient effects including both tendon break and unlatch have never been extensively reported in the open literature, which will be the main subject of the present study.

In this regard, an ETLP designed for GoM is selected to investigate the effects of sudden tendon disconnection during harsh wind-wave-current conditions. Kim et al (2001b) underscored the importance of using the hull-tendon-riser coupled dynamics program for this kind of study especially when analyzing deep-water TLPs because both tendons and risers contribute appreciably to the system stiffness, mass and damping (Ma et.al., 2000, Wichers and Devlin, 2004). The transient effect of the one tendon disconnections on the global motion has been investigated by implementing the new feature of the transient broken line simulation module to HARP/Charm3D program (Yang et. al., 2008), a coupled global motion analysis program in frequency and time domain.

Recently, the severe hurricane close to 1000 year return period events also caused the minor and major damages of the platforms on the deck, which raised the question whether the current design criteria is suitable or not, and more realistic modeling of the hull-superstructure. One of the most significant damage relating to floating systems involved the shifting or movement of the drilling or work-over rig packages as well as the mooring system damages (Yang et al., 2009).

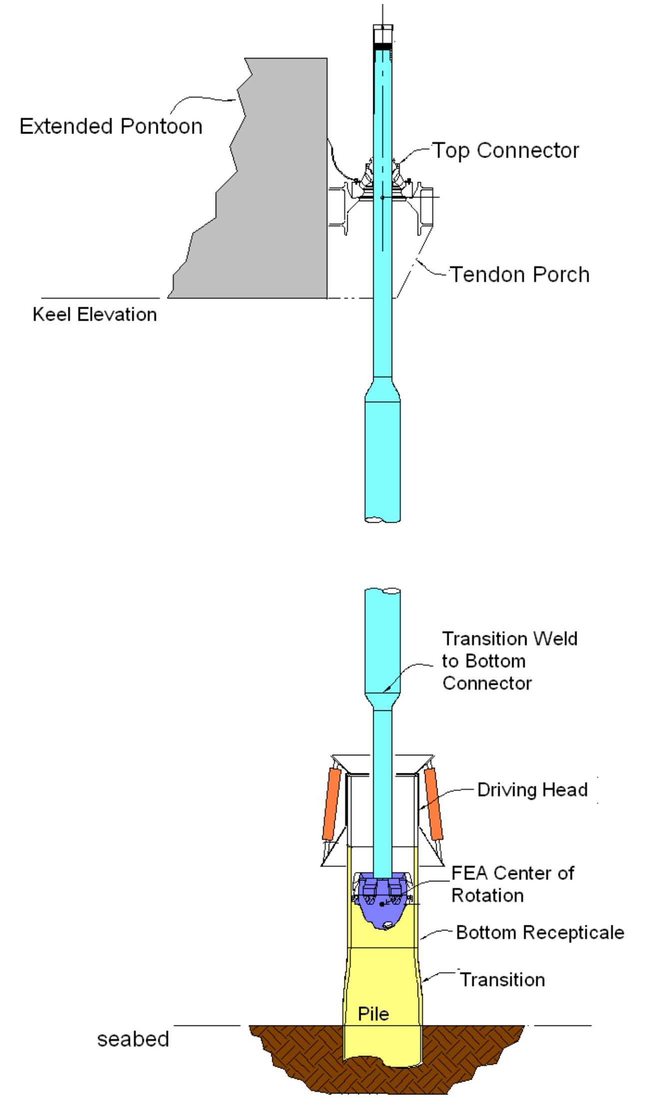

Figure 1.7 Configuration of Tendon Connections

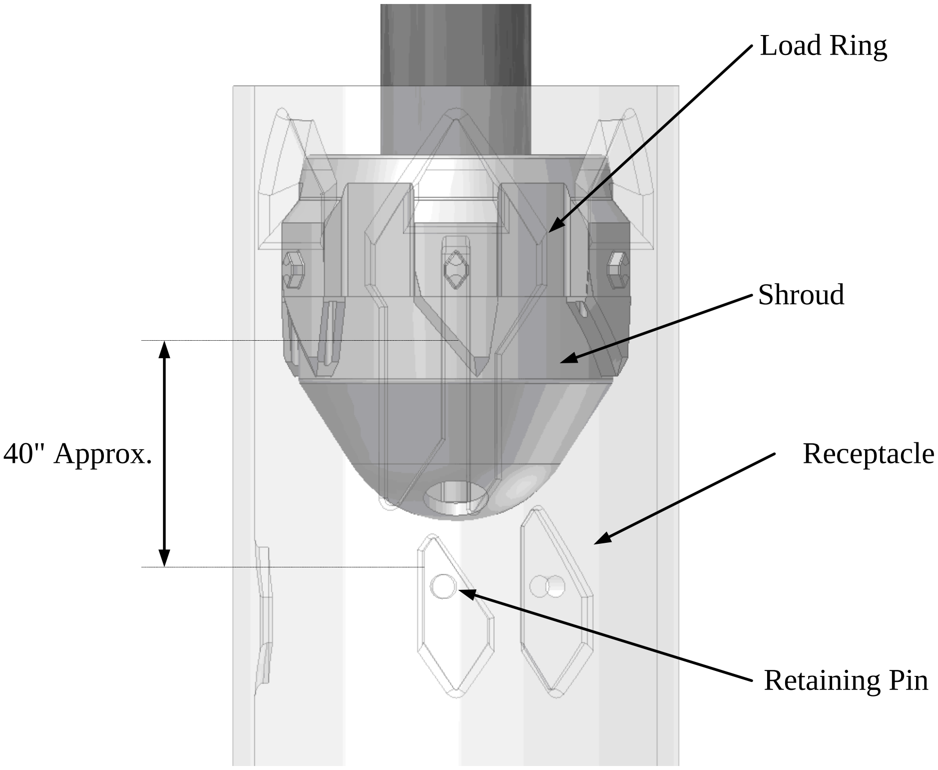

Figure 1.8 Layout of Bottom Connector

Figure 1.9 Pin Installation with ROV

Typically, the drilling and work-over rigs are tied down or fastened to the decks of offshore structures by storm sea fastenings, such as bolts, weldments, braces or the others. The failure of the storm sea fastenings observed after the hurricane events raised the question whether the current design philosophy or criteria for storm sea fastening are suitable or not. This study is based on such demands to ready the deepwater floating platforms for a hurricane and to avoid future damage (Ward et al., 2006, Yang, et.al, 2009).

Currently, the structural design of top-side equipment follows the governing design standards, e.g. API Spec 4F(API, 1995) and API RP 2A(API, 1993). The standard means to estimate the design load on the sea fastening device follows the recommendation by API-Spec 4F, in which the dynamic forces are obtained by linear motion assumption, and the phases of each force components, such as wind, inertia, gravity forces, are ignored. However, this method may lead to the over-estimation of the tie-down load, and more advanced method to accurately estimate the load is required.

A global motion analysis of a typical TLP in GoM, the Deep Star TLP, is performed in severe environmental condition using Charm3D. 10 year, 100 year and 1000 year return hurricanes are considered as environmental conditions. And the loads on the derrick and the substructure tie-down footings are calculated by using the local spring structural model.

As the oil and gas industry moves further offshore into ultra deepwater, the need for drilling and production platforms that can support dry trees and provide direct access to wells becomes more acute. An additional challenge of any deepwater floater design is the ability to install and commission topsides at a dockside location, which mitigates risks and significantly reduces the costs associated with mobilizing equipment to install the topsides and commission the system offshore. The dry tree semisubmersible is presently being considered as a viable option to meet this challenge. The design reduces the motions of a semisubmersible using heave plates attached to the lower hull similar to a Spar. This floater offers small in-place motions that allow the proven riser systems presently used on the Spar hull to be ported to this dry tree semisubmersible. The structural components can be built at numerous ship yards worldwide, further offering flexibility in resource capacity and delivery logistics.

The heave plates are installed beneath the semisubmersible hull during a near-shore marine operation by lifting a truss containing heave plates into position and securing the truss to the semisubmersible. The operation can be carried out in relatively low sea states with significant wave heights on the order of 6.0 ft. The large mass components and damping effects produce long natural periods well above the 6.0-sec peak period of the incident spectrum. The truss installation problem of a dry tree semisubmersible is simulated with the new feature of the elastic beam and the contact spring between the beam and the semisubmersible hull.

1.2 Literature Review

The second half of the last century has seen growing interest in and rapid development of the study of floating body motions due to waves. The pioneering work of Haskind (1946) introduced the concept of dividing the problem into components that could be considered individually. This decomposition separated the fluid flow into three distinct components: the steady flow due to translation, the flow caused by the body’s motions, and the flow due to the diffraction of the incident wave. Each component offered a simpler problem to address.

The earliest was the attempts at determining the force due to waves as the buoyant force due to still hydrostatics. The approximation of the force due to waves as the buoyant force due to still water taking the shape of a wave is still used by some to determine the bending moments on a vessel due to waves (Comstock, 1967).

The first significant improvement is credited to both William Froude (1961) and Krylov, a Russian naval officer (Krilloff 1896). Their approximation of the force due to a wave is simply a surface integration of the pressure due to a sinusoidal wave that is assumed not to be diffracted. The pressure is given by the linearization of Bernoullis equation. The force determined by this method is referred to as the Froude-Krylov force. In the range of wavelengths where the waves are much longer than the body dimensions, this approximation is accurate enough. The Froude-Krylov force represents the force due to the diffracted wave system. In general, the Froude-Krylov force is much the larger of the two.

Haskind first showed that the exciting force on a fixed body due to sinusoidal waves may be determined by the solution of the radiated wave problem, that is, the wave system due to the sinusoidal oscillation of the body about its mean position. These results have been extended by Newman (1965) to the case of a moving vessel. The relation between the radiated wave potential and the exciting force is referred to as the Haskind relation.

By using the Haskind relation, it is possible to determine the ship motions using only the solution to the radiation problems. Because of this fact, greater effort has been given to the solution of the forced oscillation radiation problem than the diffraction problem. The Haskind relation can only give forces on an entire body and cannot be used to determine sectional force. It also cannot be used for the determination of relative motion where the wave elevation for the diffracted wave is required. Thus, the solution of the diffraction problem has practical application as well as scientific interest.

Moving onto the multiple body hydrodynamics, one of the first research on it is by Ohkusu(1969). He extended the classical solution for a single heaving circular cylinder, first developed by Ursell(1949).

Many applications occur in the field of marine hydrodynamics where two or more vessels are in sufficiently close proximity to experience significant interactions. Catamarans and other multi-hull ships, offshore platforms supported by multiple columns, floating bridges, and arrays of wave-power devices are all examples where the proximity is a permanent feature of the design. In other cases, such as marine operations involving multiple vessels and platforms or replenishment operations of two ships, the proximity is temporary but nevertheless important. Hydrodynamic interactions related to wave effects are particularly significant, due to the oscillatory phase of the waves in relation to the spacing, and the large horizontal scale of the wave influence.

Multiple bodies can be studied with the same experimental and theoretical methods that are applied to wave effects on a single body. Typically, the analysis of two or three interacting bodies is a straightforward extension, but the analysis of very large configurations is fundamentally more difficult. On the experimental side, the physical size of the model may exceed the practical limits of the wave basin, and the sensitivity of the response to the wave period and direction may dictate an extensive series of tests. Thus there is a great need for reliable theories and associated computational tools suitable for analyzing these problems. Moreover, the variety of interesting interactions that occur for multiple bodies provides a rich source of stimulus for fundamental research.

In most cases of practical importance, the effects of ocean waves on floating and submerged bodies can be analyzed by the linear potential theory. This theory is well established for fixed structures, and for vessels which have no substantial forward velocity. Classical solutions exist for relatively simple body shapes such as circular cylinders. In some cases it is necessary to account for second-order effects, including mean drift forces and more complex time-varying nonlinearities.

The same fundamental theory can be extended to the analysis of wave effects on multiple bodies. In some of the examples cited above the different bodies are connected structurally, and in others they are dynamically independent. The distinction between structurally connected or independent bodies is not important from the hydrodynamic standpoint, except insofar as the total number of modes of body motion is reduced if the connections are rigid.

The necessity of the coupled analysis has long been recognized since Paulling and Webster (1986) indicated the significant difference between the uncoupled and the coupled method. Thereafter, a lot of coupled analysis results have been introduced by

Chakrabarti et al.(1996), Ormberg and Larsen(1998), Ma et al.(2000), Colby et al.(2000), Heurtier et al.(2001), Senra et al. (2002), Correa et al.(2002) and Garrett et al.(2002).

WINPOST(Ran et al, 1997 & 1999), a fully coupled time/frequency domain analysis program of floating bodies and mooring lines/risers, is also one of the results of the coupled analysis. The program utilizes WAMIT(Lee et al., 1999), a diffraction/radiation program, to calculate the frequency dependent hydrodynamic coefficients and the first-order wave excitation forces. The corresponding forces are converted to the time domain using two-term Volterra series expansion in Charm3D. The frequency-dependent radiation damping was included in the form of convolution integral in the time domain simulation. Viscous forces are included through the Morison drag elements.

1.3 Objective and Scope

The main objectives of the study is on developing the nonlinear coupling model of body-to-body, riser-to-body and mooring-to-body.

Nonlinearity of the stiffness and friction characteristics of the tensioner combined with stick-slip behavior of riser keel joint is investigated. The relationship between tensions and strokes for hydro-pneumatic tensioner is based on the ideal gas equation where the isotropic gas constant can be varied to achieve an optimum stroke design based on tensioner stiffness. Challenges of modeling the coupling effects in the finite element (FE) method between the tensioner and hull motion are also presented. The effect of nonlinearity of tensioner curve, tensioner friction and riser keel friction is intensively investigated. The resultant global motion, TTR stroke and tensions are systematically compared with those of a simple engineering approach in which the nonlinear coupling effect is captured by linearization.

A transient effect of tendon down-stroke and disconnection on global performance of ETLP for harsh environmental condition is also investigated by incorporating the nonlinear boundary condition of the FE tendon model in CHARM3D. The program is made to be capable of modeling the tendon disconnection at both top and bottom connection and the down stroke behavior for the pinned bottom joint. A sudden disconnection of one or more tendons causes the unbalance of force and moment of the total system, only to cause the transient motion and tension as well as the mean offset. The tendon down-stroke at the bottom also makes significant effect on the tendon tension. The transient responses and the mean offsets are compared and discussed in the viewpoint of the robustness of the system.

The connection loads between derrick and substructure and between the substructure and the deck are calculated to determine the safety of the connection during the harsh environmental condition. A structural elastic model is developed and incorporated for the study to calculate the reaction forces at the tie-down footings. The connection may fail if the forces acting on the connector exceed the capacity of slip, shear and tensile failure modes. The capacities are predetermined by the pretension of the bolts, friction coefficient and the number of bolts at each footing. The force components, such as wind, gravitational and inertia forces, acting on a derrick and the substructure are obtained through the global motion of the hull. The exact dynamic equation of derrick and the substructure is used to include the nonlinear force terms which are ignored in the API-4F[1]. Three directional spring model is positioned at the connection point to calculate the shear and axial reaction forces. The calculation is to evaluate the maximum load on the tie-down equipment in the extreme survival condition, and to determine if it is safe from the slip, shear and tensile failure.

The elastic FE frame model with the gap-contact model between the FE model and the body to calculate the reaction force between the truss and the fender during the truss installation of a dry tree semisubmersible. The model can be used to solve the more complicated installation problem such as float-over of topside.

WAMIT, a second order diffraction/radiation program, was utilized to calculate the frequency dependent hydrodynamic coefficients and the first-order and the second-order sum and difference frequency wave excitation forces. The modules developed herein are all implemented in Charm3D, coupled analysis program of floating platform and mooring/risers.

2. NUMERICAL MODEL

Marine structures are exposed to large dynamic forces, i.e. wave, wind and current, generated by the environment. In the case the structures are fixed to the sea bottom, they are to withstand these forces, where as, when they are floating, they are required to behave acceptably in that their motions must remain limited both for survival and for operation.

In order to determine the motions of a structure as a function of excitation forces, use is made of Newton’s second law, through which it will be possible to determine the position and velocity of the structures at each moment if the initial position and velocity of the structure are known at some time together with the excitation force at each moment. Additionally, the body is kept its position by constraining forces from the external support, such as mooring lines, tension legs, and so on, when the body is a kind of floating marine structure. The connection forces between the bodies, such as hawser, yoke, beam, truss and so on, are other types of constraining forces for each body, while they are the internal forces in the view of total system. In this section, the motion of n bodies subject to general forces in a space is described.

2.1 Fully Coupled Analysis Modeling

Marine structures are exposed to large dynamic forces, i.e. wave, wind and current, generated by the environment. In the case the structures are fixed to the sea bottom, they are to withstand these forces, where as, when they are floating, they are required to behave acceptably in that their motions must remain limited both for survival and for operation.

In order to determine the motions of a structure as a function of excitation forces, use is made of Newton’s second law, through which it will be possible to determine the position and velocity of the structures at each moment if the initial position and velocity of the structure are known at some time together with the excitation force at each moment. Additionally, the body is kept its position by constraining forces from the external support, such as mooring lines, tension legs, and so on, when the body is a kind of floating marine structure. The connection forces between the bodies, such as hawser , beam, truss and so on, are other types of constraining forces for each body, while they are the internal forces in the view of total system.

In this section, the motion of multiple bodies subject to general forces in a space is described. The platform, derrick and the substructure are treated as separate multiple bodies, each of which has six DOF (degree of freedom). Generally speaking, the n body system can be 6×n DOF system. The dynamics of n body system is derived herein, assuming each body is rigid, though only one body system is used herein.

The body fixed frame ($B^{(i)}$) for i-th body as well as inertia frame (*N*) is to be defined in Figure 2.1 to describe the motion of an arbitrarily moving body. At first, flexible body whose reference point is not at the center of the rotation is chosen to start from the few assumptions. The displacement of the rotational center of the i-th body in inertia coordinate is defined as $\underline{r}_C^{(i)}$. The rotational center of the body and the body reference point need not be the same for generality.

If one chooses a unit mass, its motion can be described by the following equation.

$$\underline{r}^{(i)} = \underline{r}_C^{(i)} + \underline{b}^{(i)} \tag{2.1}$$

Assuming the rigid body motion, the inertial acceleration is calculated by taking the inertial derivative of velocity as:

$$\frac{{}^{N}d^2 \underline{r}^{(i)}}{dt^2} = \underline{\ddot{r}}_C^{(i)} + \underline{\ddot{\theta}}_{B/N} \times \underline{b}^{(i)} + \underline{\dot{\theta}}_{B/N} \times \underline{\dot{\theta}}_{B/N} \times \underline{b}^{(i)} \tag{2.2}$$

where $\underline{\dot{\theta}}_{B/N}$ = rotational velocity of the body with respect to the inertia frame.

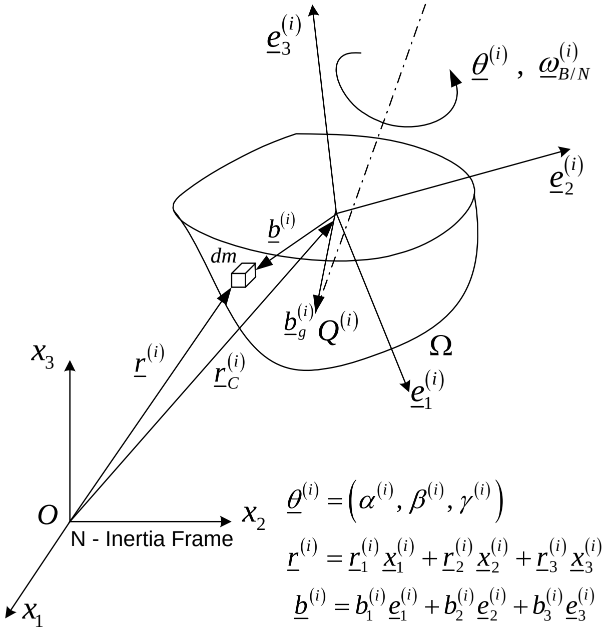

Figure 2.1 Inertia and Body Coordinate System of i-th Body among the n Body Dynamics

Integrating the infinitesimal linear inertial force contributions over the entire body, the total linear inertia force is given by:

$$\int_{\Omega^{(i)}}^{N} \frac{d^2 \underline{r}^{(i)}}{dt^2} dm = \left[M^{(i)}\right]\left\{\ddot{\underline{r}}_C^{(i)}\right\} - \left[m\underline{b}_G^{(i)\times}\right]\left\{\ddot{\underline{\theta}}_{B/N}\right\} - \left[\dot{\underline{\theta}}_{B/N}{}^{\times}\right]\left(\left[m\underline{b}_G^{(i)\times}\right]\left\{\dot{\underline{\theta}}_{B/N}\right\}\right) \tag{2.3}$$

where

$$\left[M^{(i)}\right] = \begin{bmatrix} m^{(i)} & 0 & 0 \\ 0 & m^{(i)} & 0 \\ 0 & 0 & m^{(i)} \end{bmatrix},$$

$$\left[m\underline{b}_G^{(i)\times}\right] = \int_{\Omega} \left[\underline{b}_g^{(i)\times}\right] dm ,$$

and the cross matrix $\left[\underline{b}_g^{(i)\times}\right]$ is a skew matrix defined with the components of the vector $\underline{b}_G^{(i)}$ as:

$$\left[\underline{b}_G^{(i)\times}\right] = \begin{bmatrix} 0 & -b_{g3}^{(i)} & b_{g2}^{(i)} \\ b_{g3}^{(i)} & 0 & -b_{g1}^{(i)} \\ -b_{g2}^{(i)} & b_{g1}^{(i)} & 0 \end{bmatrix}.$$

Also, the cross matrix $\left[\dot{\underline{\theta}}_{B/N}{}^{\times}\right]$ is a skew matrix defined with the components of the vector $\dot{\underline{\theta}}_{B/N}$ as :

$$\left[\dot{\underline{\theta}}_{B/N}{}^{\times}\right] = \begin{bmatrix} 0 & -\dot{\theta}_3^{(i)} & \dot{\theta}_2^{(i)} \\ \dot{\theta}_3^{(i)} & 0 & -\dot{\theta}_1^{(i)} \\ -\dot{\theta}_2^{(i)} & \dot{\theta}_1^{(i)} & 0 \end{bmatrix}$$

The angular momentum is obtained by integrating the infinitesimal angular momentum contributions over the entire body.

$$\underline{H} = \int_{\Omega} \underline{b}^{(i)} \times {}^{N}\frac{d\,\underline{r}^{(i)}}{dt}\,dm = \int_{\Omega} \underline{b}^{(i)} dm \times \dot{\underline{r}}_{C}^{(i)} + \int_{\Omega} -\left[\underline{b}^{(i)\times}\right]\left[\underline{b}^{(i)\times}\right] dm \left\{\dot{\underline{\theta}}_{B/N}\right\} \tag{2.4}$$

Taking the time derivative of angular momentum and assuming the moment of inertia, $\left[I^{(i)}\right]$ with respect to the body fixed frame does not change in time gives

$$\frac{d\,\underline{L}}{dt} = \left[m\underline{b}_{g}^{(i)\times}\right]\left\{\ddot{\underline{r}}_{C}^{(i)}\right\} + \left[I^{(i)}\right]\left\{\ddot{\underline{\theta}}_{B/N}\right\} + \left[\dot{\underline{\theta}}_{B/N}^{\;\times}\right]\left[I^{(i)}\right]\left\{\dot{\underline{\theta}}_{B/N}\right\} \tag{2.5}$$

where $\left[I^{(i)}\right] = \int_{\Omega} -\left[\underline{b}^{(i)\times}\right]\left[\underline{b}^{(i)\times}\right] dm$

The i-th body is exposed to the body force ($\underline{f}_{G}^{(i)}$) and external force ($\underline{f}_{E}^{(i)}$). The body force is the gravitational and the external forces consist of environmental forces (wave/wind/current), viscous drag force and the contact reaction forces. In the most cases the force vectors $\underline{f}_{G}^{(i)}$ and $\underline{f}_{E}^{(i)}$ are expressed in the inertia frame, and the coordinate transformation is necessary to express them in the body fixed coordinate. The Euler angle representation of the transformation is used to derive the transformed forces. The standard yaw-pitch-roll angles are selected as a sequence of rotational angles. Then, resultant transform matrix is obtained in Equation (2.6).

$$\left\{\underline{e}\right\} = \begin{Bmatrix} \underline{e}_{1} \\ \underline{e}_{2} \\ \underline{e}_{3} \end{Bmatrix} = \begin{bmatrix} \cos\theta_{3}^{(i)} & \sin\theta_{3}^{(i)} & 0 \\ -\sin\theta_{3}^{(i)} & \cos\theta_{3}^{(i)} & 0 \\ 0 & 0 & 1 \end{bmatrix} \begin{Bmatrix} \underline{x}_{1} \\ \underline{x}_{2} \\ \underline{x}_{3} \end{Bmatrix} = \left[E\left(\theta_{3}\right)\right]\left\{\underline{x}\right\} \tag{2.6}$$

$$\{\underline{e}\} = \begin{Bmatrix} \underline{e}_1 \\ \underline{e}_2 \\ \underline{e}_3 \end{Bmatrix} = \begin{bmatrix} \cos\theta_2^{(i)} & 0 & -\sin\theta_2^{(i)} \\ 0 & 1 & 0 \\ \sin\theta_2^{(i)} & 0 & \cos\theta_2^{(i)} \end{bmatrix} \begin{Bmatrix} \underline{x}_1 \\ \underline{x}_2 \\ \underline{x}_3 \end{Bmatrix} = \left[E(\theta_2)\right]\{\underline{x}\} \tag{2.7}$$

$$\{\underline{e}\} = \begin{Bmatrix} \underline{e}_1 \\ \underline{e}_2 \\ \underline{e}_3 \end{Bmatrix} = \begin{bmatrix} 1 & 0 & 0 \\ 0 & \cos\theta_1^{(i)} & \sin\theta_1^{(i)} \\ 0 & -\sin\theta_1^{(i)} & \cos\theta_1^{(i)} \end{bmatrix} \begin{Bmatrix} \underline{x}_1 \\ \underline{x}_2 \\ \underline{x}_3 \end{Bmatrix} = \left[E(\theta_1)\right]\{\underline{x}\} \tag{2.8}$$

$$\{\underline{e}\} = \left[E(\theta_1)\right]\left[E(\theta_2)\right]\left[E(\theta_3)\right]\{\underline{x}\} = \left[E(\underline{\theta})\right]\{\underline{x}\} \tag{2.9}$$

The body forces and the external forces acting on the body in the body fixed coordinate system can be calculated as:

$$\left\{\underline{f}_g\right\} = \left[E(\underline{\theta})\right]\left\{\underline{f}_G^{(i)}\right\}, \quad \left\{\underline{f}_e^{(i)}\right\} = \left[E(\underline{\theta})\right]\left\{\underline{f}_E^{(i)}\right\} \tag{2.10}$$

The corresponding moment due to the body and the external forces are as follows.

$$\underline{b}_g^{(i)} \times \left\{\underline{f}_g\right\} = \left[\underline{b}_g^{(i)\times}\right]\left[E(\underline{\theta})\right]\left\{\underline{f}_G^{(i)}\right\}, \qquad \underline{b}_e^{(i)} \times \left\{\underline{f}_e^{(i)}\right\} = \left[\underline{b}_e^{(i)\times}\right]\left[E(\underline{\theta})\right]\left\{\underline{f}_E^{(i)}\right\} \tag{2.11}$$

where

$\underline{b}_g^{(i)}$ = center of the body force,

$\underline{b}_e^{(i)}$ = the equivalent point where the external forces are applied.

Thus, the force and the moment equilibrium give the equations of the motion for the i-th body. The set of equations can be combined to give simpler form as:

$$\left[\mu^{(i)}\right]\left\{\ddot{\underline{y}}^{(i)}\right\} + \{\underline{N}v\} = \left\{\underline{F}_g^{(i)}\right\} + \left\{\underline{F}_e^{(i)}\right\} \tag{2.12}$$

where

$$\left[\mu^{(i)}\right]=\begin{bmatrix}\left[M^{(i)}\right] & -\left[m\underline{b}_g^{(i)\times}\right]\\ \left[m\underline{b}_g^{(i)\times}\right] & \left[I^{(i)}\right]\end{bmatrix},$$

$$\left\{\underline{\ddot{y}}^{(i)}\right\}=\begin{Bmatrix}\underline{\ddot{r}}_C^{(i)}\\ \underline{\ddot{\theta}}_{B/N}\end{Bmatrix},$$

$$\left\{\underline{Nv}\right\}=\begin{bmatrix}\left[\underline{\dot{\theta}}_{B/N}{}^{\times}\right] & [0]\\ [0] & \left[\underline{\dot{\theta}}_{B/N}{}^{\times}\right]\end{bmatrix}\begin{bmatrix}\left[-m\underline{b}_g^{(i)\times}\right] & [0]\\ [0] & \left[I^{(i)}\right]\end{bmatrix}\begin{Bmatrix}\underline{\dot{\theta}}_{B/N}\\ \underline{\dot{\theta}}_{B/N}\end{Bmatrix},$$

$$\left\{\underline{F}_g^{(i)}\right\}=\begin{bmatrix}\left[E\left(\underline{\theta}\right)\right] & [0]\\ [0] & \left[\underline{b}_g^{(i)\times}\right]\left[E\left(\underline{\theta}\right)\right]\end{bmatrix}\begin{Bmatrix}\underline{f}_G^{(i)}\\ \underline{f}_G^{(i)}\end{Bmatrix},$$

$$\left\{\underline{F}_e^{(i)}\right\}=\begin{bmatrix}\left[E\left(\underline{\theta}\right)\right] & [0]\\ [0] & \left[\underline{b}_e^{(i)\times}\right]\left[E\left(\underline{\theta}\right)\right]\end{bmatrix}\begin{Bmatrix}\underline{f}_E^{(i)}\\ \underline{f}_E^{(i)}\end{Bmatrix}.$$

The nonlinear inertia term $\left\{\underline{N_v}\right\}$ becomes negligible when the small rotational motion is assumed. However, when the large rotational motion is considered, the effect is too large to be ignored.

When the number of the body is n, the set of 6xn equations are formulated as follows

$$[\mu]\left\{\underline{\ddot{Y}}\right\}+\left\{\underline{Nv}\right\}=\left\{\underline{F}_g\right\}+\left\{\underline{F}_e\right\} \tag{2.13}$$

$$\left\{\underline{\ddot{Y}}\right\}=\begin{bmatrix}\underline{\ddot{r}}_C^{(1)} & \underline{\ddot{\theta}}_{B/N}^{(1)} & \cdots & \underline{\ddot{r}}_C^{(i)} & \underline{\ddot{\theta}}_{B/N}^{(i)} & \cdots & \underline{\ddot{r}}_C^{(n)} & \underline{\ddot{\theta}}_{B/N}^{(n)}\end{bmatrix}^T$$

and the other vectors and the matrices are arranged in the same order of the acceleration. The external forces which are possible for the offshore platforms are environmental loads, such as wave, wind and current forces and the structural contact loads.

$$\begin{aligned}\left\{\underline{F}_e\right\} = -\left[M^a(\infty)\right]\ddot{\underline{Y}} + \left\{\underline{F}_R\left(\dot{\underline{Y}},t\right)\right\} - \left[K + K_C\left(\underline{Y},t\right)\right]\left\{\underline{Y}\right\} \\ + \left\{\underline{F}_{We}(t) + \underline{F}_{Mor}\left(\underline{Y},t\right) + \underline{F}_{Wind}(t)\right\} + \underline{F}_C(\underline{Y},\dot{\underline{Y}},t)\end{aligned} \tag{2.14}$$

where

$\left[M^a(\infty)\right]$: added mass,

$\underline{F}_R\left(\dot{\underline{Y}},t\right) = -\int R(t-\tau)\dot{\underline{Y}}d\tau$: wave radiation damping force,

$R(t) = \frac{2}{\pi}\int_0^\infty C(\omega)\frac{\sin\omega t}{\omega}d\omega$: Retardation function from damping coefficient($C(\omega)$),

K : system stiffness matrix (hydrostatic),

K_C : nonlinear implicit time and motion dependent stiffness matrix,

$\underline{F}_C\left(\underline{Y},\dot{\underline{Y}},t\right)$: motion and time dependent force coupling tendon dynamics with TLP motion,

$\underline{F}_{We}(t) = \underline{F}_{We}^{(1)}(t) + \underline{F}_{We}^{(2)}(t)$: Wave exciting force of the first and the second order,

$F_{Wind}(t)$: wind force,

$\underline{F}_{Mor}\left(\underline{Y},\dot{\underline{Y}},t\right)$: Force on the Morison Members,

The case when the body is not exposed to the wave and the current, such as derrick and the substructure, the added mass, radiation damping, wave excitation force and the Morison force terms disappear and gives;

$$\{\underline{F}_e\} = -\left[K_C\left(\underline{Y},t\right)\right] + F_{Wind}\left(t\right) + F_C\left(\underline{Y},\dot{\underline{Y}},t\right) \tag{2.15}$$

The nonlinear stiffness K_C and the force $F_C\left(\underline{Y},\dot{\underline{Y}},t\right)$ due to the nonlinear structural coupling between bodies or on the body are mostly from the nonlinear FE model of mooring/tendon and risers for the offshore platforms or the nonlinear/linear spring between the bodies.

2.2 Hydrodynamic Modeling

2.2.1 Introduction

The problem considered herein is the determination of the forces and fluid motions due to waves coming in contact with a body that is either fixed or freely floating on a sea. A subject of great interest to ocean engineers and naval architects is the effect suffered by a floating or submerged vessel in the presence of ocean waves. The types of bodies of importance here include fixed structures and freely floating vessels, as well as the intermediate category of moored vessels.

2.2.2 Gravity Wave Theory

The subject of this section is to mathematically study waves on an ideal fluid, namely a fluid which is incompressible and in which wave motion takes place without loss of mechanical energy. For all of the water-wave problems discussed herein, a Cartesian coordinate system (x, y, z) is adopted with the z-axis directed vertically upwards and with $z = 0$ in the plane of the undisturbed free surface. For purely tow-dimensional motion the dependence on y will be omitted and time is denoted by t (Zhang, 2005).

The fluid is assumed to be inviscid and incompressible and its motion to be irrotational. For irrotational motion the fluid velocity $\underline{u}$ may be expressed as the gradient of a scalar velocity potential $\Phi(x, y, z, t)$, that is

$$\underline{u}(x, y, z, t) = \nabla\Phi(x, y, z, t) \tag{2.16}$$

where gradient $\nabla = \hat{i}\partial/\partial x + \hat{j}\partial/\partial y + \hat{k}\partial/\partial z$ and $\hat{i}$, $\hat{j}$ and $\hat{k}$ are the unit vector in x, y and z direction, respectively.

Conservation of mass requires that the divergence of the velocity is zero so that $\Phi(x, y, z, t)$ satisfies Laplace's equation throughout the fluid.

$$\nabla^2\Phi(x, y, z, t) = 0 \tag{2.17}$$

The vertical elevation of a point on the free surface is written

$$z = \eta(x, y, t) \tag{2.18}$$

The kinematic condition that fluid particles cannot cross the free surface, i.e. air-water interface is obtained by

$$\frac{\partial\eta}{\partial t} + \frac{\partial\Phi}{\partial x}\frac{\partial\eta}{\partial x} + \frac{\partial\Phi}{\partial y}\frac{\partial\eta}{\partial y} = \frac{\partial\Phi}{\partial z} \quad \text{on } z = \eta(x, y, t) \tag{2.19}$$

If surface tension is neglected, which is valid for waves longer than a few centimeters, the pressure must be continuous across the interface, and at any point in the fluid Bernoulli's equation holds, i.e.

$$\frac{\partial \Phi}{\partial t}+\frac{1}{2}\left|\nabla \Phi\right|^{2}+\frac{p}{\rho}+gz=0 \tag{2.20}$$

where ρ is the fluid density, g is the gravitational acceleration, and p is the pressure in the fluid. Because of the comparatively small density of the air, its motion may be neglected and the pressure along the interface can be taken to be constant in space. Bernoulli's equation evaluated at the interface, where $p/\rho \equiv -C$, then gives the dynamic condition

$$\frac{\partial \Phi}{\partial t}+\frac{1}{2}\left|\nabla \Phi\right|^{2}+g\eta=C \text{ on } z=\eta(x,y,t) \tag{2.21}$$

where $C(t)$ is properly determined to ensure $z=0$ located at the still water level. Equation (2.21) is a non-stationary version of the Bernoulli equation.

When there is an impermeable sea bed so that the local fluid depth is $h(x,y)$, then there must be no flow normal to the bed and hence

$$\frac{\partial \Phi}{\partial n}=0 \text{ on } z=-h(x,y) \tag{2.22}$$

where $\hat{n}$ is a coordinate measured normal to the bed.

Eliminating the unknown η in equation (2.21) by applying the operator $\left(\frac{\partial}{\partial t}+\nabla\phi\cdot\nabla\right)$ on it and using equation (2.19) gives the free-surface boundary condition only involving the potential.

$$\frac{\partial^{2}\Phi}{\partial t^{2}}+g\frac{\partial \Phi}{\partial z}+\frac{\partial\left|\nabla\Phi\right|^{2}}{\partial t}+\frac{1}{2}\nabla\Phi\cdot\nabla\left(\left|\nabla\Phi\right|^{2}\right)=0 \text{ on } z=\eta(x,y,t) \tag{2.23}$$

Mode coupling method, also known as Stokes Expansion, are applied to a wave field in deep or intermediate water depth with respect to its typical wavelength. First, the wave potential and elevation are perturbed in a series decaying rapidly with the increase in the superscript, j.

$$\Phi = \Phi^{(1)} + \Phi^{(2)} + \Phi^{(3)} + \cdots + \Phi^{(j)} \cdots \tag{2.24}$$

$$\eta = \eta^{(1)} + \eta^{(2)} + \eta^{(3)} + \cdots + \eta^{(j)} \cdots \tag{2.25}$$

$$C = C^{(1)} + C^{(2)} + C^{(3)} + \cdots C^{(j)} + \cdots \tag{2.26}$$

where $\Phi^{(j)} = O(\varepsilon)\Phi^{(j-1)} = \cdots = O\left(\varepsilon^{j-1}\right)\Phi^{(1)}$, $\eta^{(j)} = O(\varepsilon)\eta^{(j-1)} = \cdots = O\left(\varepsilon^{j-1}\right)\eta^{(1)}$ for j = 2, 3, …. , $\varepsilon = ak$ is smallness parameter for the perturbation, and a and k is wave amplitude and wave number, respectively.

The free surface boundary conditions (2.23) and (2.21) are expanded at the still water level, i.e. $z = 0$. The perturbed potential, elevation and the Bernoulli constant given in (2.24) through (2.26) are substituted into the expanded free-surface boundary conditions, the Laplace equation and bottom boundary condition. The equations are sorted and grouped according to the order in wave steepnesses. The governing equation and boundary conditions for j^{th} order solutions are given by

$$\nabla^2 \Phi^{(j)}(x, y, z, t) = 0, \qquad -h \le z \le 0 \tag{2.27}$$

$$\frac{\partial \Phi^{(j)}}{\partial z} = 0 \quad \text{at} \quad z = -h \tag{2.28}$$

$$\frac{\partial^2 \Phi^{(j)}}{\partial t^2} + g\frac{\partial \Phi^{(j)}}{\partial z} = P^{(j)}\left[\Phi^{(j-1)}, \eta^{(j-1)}\right] \quad \text{at} \quad z = 0 \tag{2.29}$$

$$\eta^{(j)} = -\frac{1}{g}\frac{\partial \Phi^{(j)}}{\partial t} + \frac{1}{g}Q^{(j)}\left[\Phi^{(j-1)}, \eta^{(j-1)}\right] + C^{(j)} \quad \text{at } z = 0 \qquad (2.40)$$

where the j-th order source term of $P^{(j)}$ and $Q^{(j)}$ can be derived in terms of the solutions for the potential and elevation of order j-1 or lower. Therefore, the above equations should be solved

The linear solution is given as

$$\text{Velocity Potential}: \phi^{(1)} = \sum_{j=1}^{N} \frac{a_j g}{\sigma_j} \frac{\cosh\left[k_j\left(z+h\right)\right]}{\cosh k_j h} \sin\theta_j \qquad (2.41)$$

$$\text{Surface Elevation}: \eta^{(1)} = \sum_{j=1}^{N} a_j \cos\theta_j \qquad (2.42)$$

where

$\sigma_j^2 = gk_j \tanh k_j h,$ for j =1 and 3,

$\theta_j = k_{xj}x + k_{yj}y - \sigma_j t + \varphi_j$,

$k_{xj} = k\cos\chi_j$, $k_{yj} = k\sin\chi_j$, $k_{xj}^2 + k_{yj}^2 = k_j^2$,

2.2.3 Wave-Body Interaction (Morison Formula)

The prediction of wave forces on an offshore structure is one of the primary tasks in studying the dynamics of the floating platform. For a large-displacement floating structures, the diffraction theory is the most appropriate method to predict the wave load on the platform. On the other hand, for the structures with slender members (e.g., some semi-submersibles, truss spars), the Morison's formula approach is also widely used. Furthermore, the viscous force may become important in extreme environmental conditions and must be included in the analysis. In such cases, a hybrid diffraction with Morison's drag formula is required, where the drag force calculation is usually based on the undisturbed flow. In this section, both the diffraction theory and Morison's formula are discussed

This is the ratio of the wave motion to the size of a Morison member and is a measure of the importance of the drag force. It is given by:

KC = $U_o T / D$, (2.43)

where, U_0 = wave particle velocity amplitude,

T = wave period and

D = Morison member diameter.

Using Particle kinematic relationship, this is also expressed as

KC = $2\pi\zeta_o / D$, (2.44)

where, ζ_o =wave particle motion amplitude.

This is the ratio of inertia force to viscous force and is given as

Re = VD / ν, (2.45)

where, V = characteristic velocity (relative current, particle or a combination)

ν = kinematic viscousity = 1.134×10^{-5} ft^2/sec for sea water at 68^o F

This gives a measure of the diffraction effect. It is given as $\pi D / \lambda$, where λ is wave length. The use of Morison equation to calculate wave loads on cylinders is considered to be valid when this parameter is less that 0.5, as shown in Chakrabarti (1994). For the current Spar, all truss members will easily fall within this category. However, for the 120 ft hard tank, the diffraction effects will start to become important for wave length less than $\lambda = 2\pi D$ = 753.6 feet, or wave periods less than 12.13 ($T = \sqrt{2\pi\lambda/g}$) seconds.

As may be seen from the above, the coefficients vary with environment. For design purpose, this is generally divided in three main frequency ranges corresponding to “storm”, “loop current” and “fatigue” sea states. The “storm” case refers to high wave cases such as hurricane and winter storm environments, with peak wave period in the 10-16 second range. The “loop” case refers to the high current cases that are somewhat unique to the Gulf of Mexico. These are associated with smaller waves with peak period in the 8-12 second range. These usually occur as a result of run-off after a severe storm. The “fatigue” case refers to sea states with low wave period in the 6-9 second range (typically less than 8 seconds). It may be noted that in the fatigue analysis, the “storm” model is used for higher period waves and the “fatigue” model for smaller waves.

2.2.4 Wave-Body Interaction (Diffraction & Radiation Theory)

On the surface of a structure, the normal component of the structural velocity must equal the velocity component in the same direction of an adjacent fluid particle if slip is admitted on the body wall. In terms of the velocity potential $\Phi(x, y, z, t)$ introduced in the previous section, the condition can be expressed as:

$$\frac{\partial \Phi}{\partial n} = \hat{n} \cdot \nabla \Phi = V_n \tag{2.46}$$

where V_n is the component of the structural velocity in the direction of the normal coordinate $\hat{n}$ directed into the fluid (out of the body). In the linearized theory this condition is applied on the equilibrium surface of the structure which will be denoted by S_B.

A wave train incident upon a floating structure will be diffracted to produce a scattered wave field and also set the structure in motion to produce a radiated field. By linear superposition, the velocity potential may be decomposed into two parts as

$$\Phi(x,y,z,t)=\Phi_S(x,y,z,t)+\Phi_R(x,y,z,t). \tag{2.47}$$

where Φ_S is the solution of the scattering problem in which the structure is held fixed in the waves. The scattering wave potential may be further decomposed as

$$\Phi_S(x,y,z,t)=\Phi_I(x,y,z,t)+\Phi_D(x,y,z,t) \tag{2.48}$$

where Φ_I represents the incident wave train and Φ_D the diffracted waves.

Because the structure is held fixed for the scattered wave field problem, the appropriate boundary condition is

$$\frac{\partial\Phi_S}{\partial n}=\frac{\partial\Phi_I}{\partial n}+\frac{\partial\Phi_D}{\partial n}=0 \quad \text{on } S_B \tag{2.49}$$

The potential Φ_R is the solution of the radiation problem, in which the structure is forced to oscillate in the absence of an incident wave, and satisfies

$$\frac{\partial\Phi_R}{\partial n}=V_n \text{ on } S_B. \tag{2.50}$$

In general, the normal velocity V_n is found from the equation of motion of the structure(Mei 1983). And will depend, in particular on the forces that result from any incident waves.

Assuming the time-harmonic motions with radian frequency ω, the time variation in the scattering potential is separated out by writing

$$\Phi_S(x,y,z,t) = \mathrm{Re}\left\{\left(\phi_I(x,y,z) + \phi_D(x,y,z)\right)e^{-i\omega t}\right\} \tag{2.51}$$

where, for the constant finite depth, the incident wave ϕ_I has the form of equation (2.41). Similarly, for the radiation potential the time variation is separated out by writing

$$\Phi_R(x,y,z,t) = \mathrm{Re}\left\{\phi_R(x,y,z)e^{-i\omega t}\right\}. \tag{2.52}$$

Both $\phi_D(x,y,z)$ and $\phi_R(x,y,z)$ are complex-valued functions of position only.

To obtain a unique solution, the diffracted field $\phi_D(x,y,z)$ and the radiated field $\phi_R(x,y,z)$, defined in equations (2.50) and (2.52), respectively, must each satisfy a radiation condition specifying that the waves corresponding to these potentials propagate away from the structure. For any ϕ equal to either $\phi_D(x,y,z)$ or $\phi_R(x,y,z)$, the radiation condition in two dimension can be written

$$\lim_{kx \to \pm\infty}\left(\frac{\partial \phi}{\partial x} \mp ik\phi\right) = 0 \tag{2.53}$$

where k is the wave number.

In three dimensional problems, the condition can be written

$$\lim_{kr \to \pm\infty} r^{1/2}\left(\frac{\partial \phi}{\partial r} - ik\phi\right) = 0 \tag{2.54}$$

where r is the horizontal polar coordinate. In three dimensions a radially spreading cylindrical wave of decreasing amplitude is obtained and energy conservation arguments require the factor of $r^{1/2}$ in formulating integral equations is demonstrated in the previous sections.

Similar to the method used for the wave theory, by assuming weak nonlinearity, i.e. small amplitude waves, the total velocity potential can be written by a perturbation series with respect to the wave slope parameter ε.

Let a body oscillate in a single mode j with complex velocity amplitude $\hat{u}_j$. The radiated wave is associated with a velocity potential $\hat{\phi}_r$ given by

$$\hat{\phi}_r = \varphi_j \hat{u}_j \tag{2.55}$$

where $\varphi_j = \varphi_j(x, y, z)$ is a coefficient of proportionality, as introduced in equation (2.55). The radiated wave reacts with a force on the body. The component i of the force is the integration of the pressure overall the wetted surface of the body.

$$F_{r,i} = i\omega\rho \iint_s \varphi_j \hat{u}_j n_i dS \tag{2.56}$$

Whether j denotes a translational mode ($j = 1, 2, 3$) or a rotational mode ($j = 4, 5, 6$), $\hat{u}_j$ is constant under the integration. This reflects the fact that the body is rigid. Hence, we may write

$$F_{r,i} = -Z_{ij} \hat{u}_j \tag{2.57}$$

where

$$Z_{ij} = -i\omega\rho \iint_s \varphi_j n_i dS$$

is an element of the so-called radiation impedance matrix. The unit of the radiation impedances are (force)/(velocity) for $i, j = 1, 2, 3$ and (moment)/(angular velocity) for $i, j = 4, 5, 6$, where angular velocities are in rad/sec. Using the boundary condition on the body surface equation gives

$$Z_{ij} = -i\omega\rho \iint_{s} \varphi_j \frac{\partial \varphi_i}{\partial n} dS \tag{2.58}$$

Whereas φ_j is complex, $\partial\varphi_i / \partial n$ is real on S, because n_j is real. Hence, we may in the integrand replace $\partial\varphi_i / \partial n$ with $\partial\varphi_i^* / \partial n$, if we wish to. Thus, we have the alternative formula

$$Z_{ij} = -i\omega\rho \iint_{s} \varphi_j \frac{\partial \varphi_i^*}{\partial n} dS \tag{2.59}$$

Note that φ_j must satisfy the sea bed and the free surface boundary condition, which means, for instance, that the radiation-impedance matrix of a body does not have the same value if it is placed in a wave channel as if it is placed in open sea.

We may interpret $-Z_{ij}$ as the i component of the reaction force which is due to wave radiation from mode j oscillating with unit amplitude ($\hat{u}_j = 1$). This follows from the "reciprocity" relation

$$Z_{ij} = Z_{ji} \tag{2.60}$$

Thus, the 6×6 radiation-impedance matrix is symmetric. The following derivation proves the reciprocity relation. Using equation (2.60), we obtain

$$Z_{ij} - Z_{ji} = -i\omega\rho \iint_{s} \left(\varphi_j \frac{\partial \varphi_i}{\partial n} - \varphi_i \frac{\partial \varphi_j}{\partial n} \right) dS = 0 \tag{2.61}$$

When we utilize the fact that φ_j and φ_i satisfy the same radiation condition. For certain body geometries some of the elements of the radiation impedance matrix vanish. If $y = 0$ is a plane of symmetry (which is typical for a ship hull), then n_2, n_4 and n_6 in equation (2.56) are the odd functions of *y*, whereas φ_1, φ_3 and φ_5 are even functions. Hence, $\mathrm{Z}_{21} = \mathrm{Z}_{23} = \mathrm{Z}_{25} = \mathrm{Z}_{41} = \mathrm{Z}_{43} = \mathrm{Z}_{45} = \mathrm{Z}_{61} = \mathrm{Z}_{63} = \mathrm{Z}_{65} = 0$. Moreover, if *x=0* is a plane of symmetry, then n_1, n_5 and n_6 in equation (2.56) are the odd functions of *x*, whereas φ_2, φ_3 and φ_4 are even functions. Hence $\mathrm{Z}_{12} = \mathrm{Z}_{13} = \mathrm{Z}_{14} = \mathrm{Z}_{52} = \mathrm{Z}_{53} = \mathrm{Z}_{54} = \mathrm{Z}_{62} =$ $\mathrm{Z}_{63} = \mathrm{Z}_{64}$ =0. From this observation, while noting equation (2.60), it follows that if both *y=0* and *x=0* are planes of symmetry, then the only non-vanishing off-diagonal elements of the radiation impedance matrix are $\mathrm{Z}_{15} = \mathrm{Z}_{51}$ and $\mathrm{Z}_{24} = \mathrm{Z}_{42}$.

Because ω is real, it is convenient to split Z_{ij} into real and imaginary parts

$$\mathrm{Z}_{ij} = R_{ij} + iX_{ij} = R_{ij} + i\omega m_{ij}^{a} \tag{2.62}$$

where we term R_{ij} the radiation resistance matrix, X_{ij} the radiation reactance matrix and m_{ij}^{a} the added-mass matrix. Note that R_{ij} is also called the “added damping coefficient matrix”.

We can express equation (2.56) in the alternative way as:

$$\hat{F}_r = -\mathrm{Z}\hat{u} = -\mathrm{Z}(\omega)\hat{u} \tag{2.63}$$

We may interpret $-\mathrm{Z}(\omega)$ as the transfer function of a linear system, where $\hat{u}$ is input and $\hat{F}_r$ is the output. Similarly to this definition of a linear system for the radiation problem, we may define the following linear system for the excitation problem:

$$\hat{F}_e = f(\omega)A \tag{2.64}$$

where the system's input is $A = \hat{\eta}(0,0)$, which is the complex elevation amplitude of the undisturbed incident wave at the origin, $(x, y) = (0,0)$. Further, the transfer function is the six-dimensional column vector f, which we shall call the excitation-force coefficient vector.

In the following, let us generalize the situation in which the oscillation need not be sinusoidal. Then, we have the Fourier transforms of the reaction force $F_{r,\,t}(t)$ caused by radiation, and the excitation force $F_{e,\,t}(t)$.

$$F_r(\omega) = -\mathrm{Z}(\omega)\hat{u}(\omega) \tag{2.65}$$

$$F_e(\omega) = f(\omega)A(\omega) \tag{2.66}$$

Here $u(\omega)$ is the Fourier transform of $u_t(t)$, and $A(\omega)$ is the Fourier transform of $a(t) \equiv \eta_0(0,0,t)$, the wave elevation of the undisturbed incident wave at the origin $(x, y) = (0,0)$. (A subscript *t* is used to denote the inverse Fourier transforms, which are functions of time.)

The inverse Fourier transforms of transfer functions $f(\omega)$ and $Z(\omega)$ correspond to time-domain impulse response functions, introduced into ship hydrodynamics by W.E. Cummins(1962).

The retardation function or the impulse response function, $R_{ij}(t)$ is calculated by the following definition.

$$R_{ij}(t) = \frac{2}{\pi}\int_0^\infty b_{ij}(\omega)\frac{\sin\omega t}{\omega}d\omega \tag{2.67}$$

where

$b_{ij}(\omega)$ = frequency dependent radiation damping coefficient.

Then the radiation damping forces and moments, $F_{Di}(t)$ are obtained by the convolution integration of retardation function and the motion velocity of the platform CG as:

$$F_{Di}(t) = \int_{-\infty}^{t} R_{ij}(t-\tau)\dot{x}_j(\tau)d\tau \qquad (2.68)$$

where

$\dot{x}_j(\tau)$ = j-th mode motion velocity of the platform CG.

2.3 Spring Model of Connectors

The i-th and the j-th body are to be assumed to be connected with the linear spring with translational and rotational stiffness $[k]$ and $[k_\theta]$ in inertia frame. In general, the springs may not coincide with the axes of a coordinate system and the principal axes of the springs may have some rotational angle with respect to them. If the stiffness matrices with respect to the principal axis are $[k']$ and $[k'_\theta]$ and the translational matrix is $[\underline{T}_s]$ then the stiffness matrices in the coordinate system can be obtained as (Refer to Figure 2.2):

$$[k] = [\underline{T}_s]^T [k'][\underline{T}_s]$$

$$[k_\theta] = [\underline{T}_s]^T [k'_\theta][\underline{T}_s]$$

The motion of the point where the spring is attached on the i-th body can be calculated in the inertia frame as follows.

$$\left\{\underline{r}^{(i)}\right\}=\left\{\underline{r}_C^{(i)}\right\}+\left[\underline{p}^{(i)\times}\right]\left\{\underline{\theta}_{N/B}^{(i)}\right\} \tag{2.69}$$

where

$\left\{\underline{r}_C^{(i)}\right\}$ =column vector of a point at the body at the inertia frame,

$\left[\underline{p}^{\times}\right]$ =cross product matrix of the local coordinate of the spring attachement point on the i-th body,

$\left\{\underline{\theta}_{B/N}^{(i)}\right\}$ =rotational motion of the i-th body in the inertia frame.

Also, the motion of the point on the j-th body can be illustrated in the similar way:

$$\left\{\underline{r}^{(j)}\right\}=\left\{\underline{r}_C^{(j)}\right\}-\left[\underline{p}^{(j)\times}\right]\left\{\underline{\theta}_{N/B}^{(j)}\right\} \tag{2.70}$$

Then, the reaction force on the i-th body by the spring is

$$\left\{\underline{r}^{(j)}\right\}=\left\{\underline{r}_C^{(j)}\right\}-\left[\underline{p}^{(j)\times}\right]\left\{\underline{\theta}_{N/B}^{(j)}\right\} \tag{2.71}$$

The moment acting on the i-th body due to the linear spring and the rotational spring can be calculated as:

$$\left\{\underline{L}^{(i)}\right\}=\left[\underline{p}^{(i)\times}\right]\left\{\underline{N}^{(i)}\right\}+\left[k_\theta\right]\left\langle\left\{\underline{\theta}_{B/N}^{(j)}\right\}-\left\{\underline{\theta}_{B/N}^{(i)}\right\}\right\rangle \tag{2.72}$$

The reaction force and the moment on the j-th body is in the opposite direction to those on the i-th body.

$$\left\{\underline{N}^{(j)}\right\}=-\left\{\underline{N}^{(i)}\right\} \tag{2.73}$$

$$\left\{\underline{L}^{(j)}\right\}=\left[\underline{p}^{(j)\times}\right]\left\{\underline{N}^{(j)}\right\}-\left[k_{\theta}\right]\left\langle\left\{\underline{\theta}_{B/N}^{(j)}\right\}-\left\{\underline{\theta}_{B/N}^{(i)}\right\}\right\rangle \tag{2.74}$$

In the iteration and the time marching schemes, the reaction forces are derived from the reaction forces of the previous step and the variation of the relative motions. The displacement due to the force is obtained by the derivative of equation (2.69)

$$\{\Delta\underline{x}\}=\{\Delta\underline{X}\}-\left[\underline{p}^{\times}\right]\{\Delta\underline{\theta}\} \tag{2.75}$$

The reaction force at the spring is calculated by the spring constant

$$\{Fs\}=-[k]\{\Delta\underline{x}\}=-[k]\{\Delta\underline{X}\}+[k]\left[\underline{p}^{\times}\right]\{\Delta\underline{\theta}\} \tag{2.76}$$

The moment due to the spring reaction force is derived by:

$$\{Ns\}=\left[\underline{p}^{\times}\right]\{Fs\}=-\left[\underline{p}^{\times}\right][k]\{\Delta\underline{X}\}+\left[\underline{p}^{\times}\right][k]\left[\underline{p}^{\times}\right]\{\Delta\underline{\theta}\} \tag{2.77}$$

Resultantly, the global stiffness matrix due to the spring is as follows, and the stiffness matrix is to be added to $\left[K_C\right]$

$$[K]=\begin{bmatrix}[k] & -[k]\left[\underline{p}^{\times}\right]\\ \left[\underline{p}^{\times}\right][k] & -\left[\underline{p}^{\times}\right][k]\left[\underline{p}^{\times}\right]\end{bmatrix} \tag{2.78}$$

The body motion can be obtained through the static equilibrium between the body forces and the spring force as:

$$\begin{Bmatrix}\Delta\underline{X}\\ \Delta\underline{\theta}\end{Bmatrix}=-[K]^{-1}\begin{Bmatrix}\underline{F}\\ \underline{M}\end{Bmatrix} \tag{2.79}$$

where, $\underline{F}$ and $\underline{M}$ are the total forces and moments obtained. After then, the spring reaction forces are calculated by equation (2.76).

2.4 FE Beam Model of Connectors

With the assumption of small deformation, the three dimensional frame element has its independent 6 deformation modes such as longitudinal, torsional The 2 node beam element of three dimensional frame motion has 12 degrees of freedom(6 DOF per node). Figure 2.3 illustrates the twelve displacement degrees of freedom of a generic beam element. These quantities are shown in both the element (local) and system (global) coordinate directions, respectively.

All non-nodal displacements along the beam may be obtained by utilizing known interpolation functions. Thus the twelve nodal degrees of freedom with the known interpolation functions provide a complete kinematic description of the beam's deformation. The slope and displacement degrees of freedom in local coordinates are shown as projections onto $x_1 - x_3$ and $x_1 - x_2$ planes in Figure 2.4 and Figure 2.5, respectively. The remaining twist degrees of freedom are shown in Figure 2.6.

The element displacement vector is expressed in local and global coordinates.

$$\left\{ \underset{\sim}{q} \right\} = \left\{ q_1 \quad q_2 \quad q_3 \quad q_4 \quad q_5 \quad q_6 \quad q_7 \quad q_8 \quad q_9 \quad q_{10} \quad q_{11} \quad q_{12} \right\}^T \tag{2.80}$$

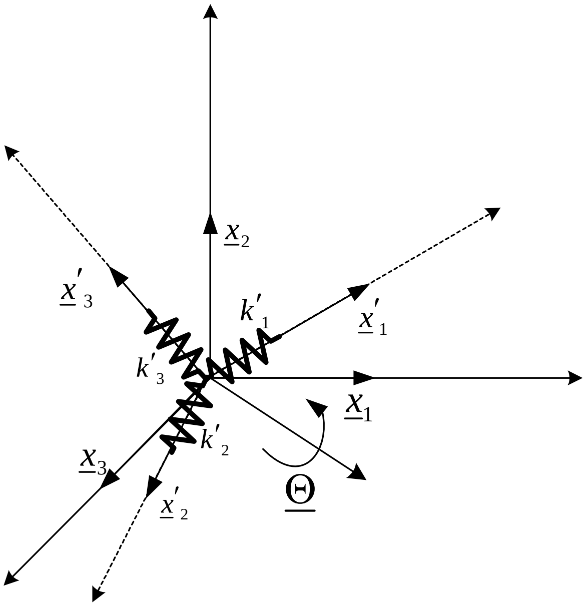

Figure 2.2 Spring with the Principal Axis

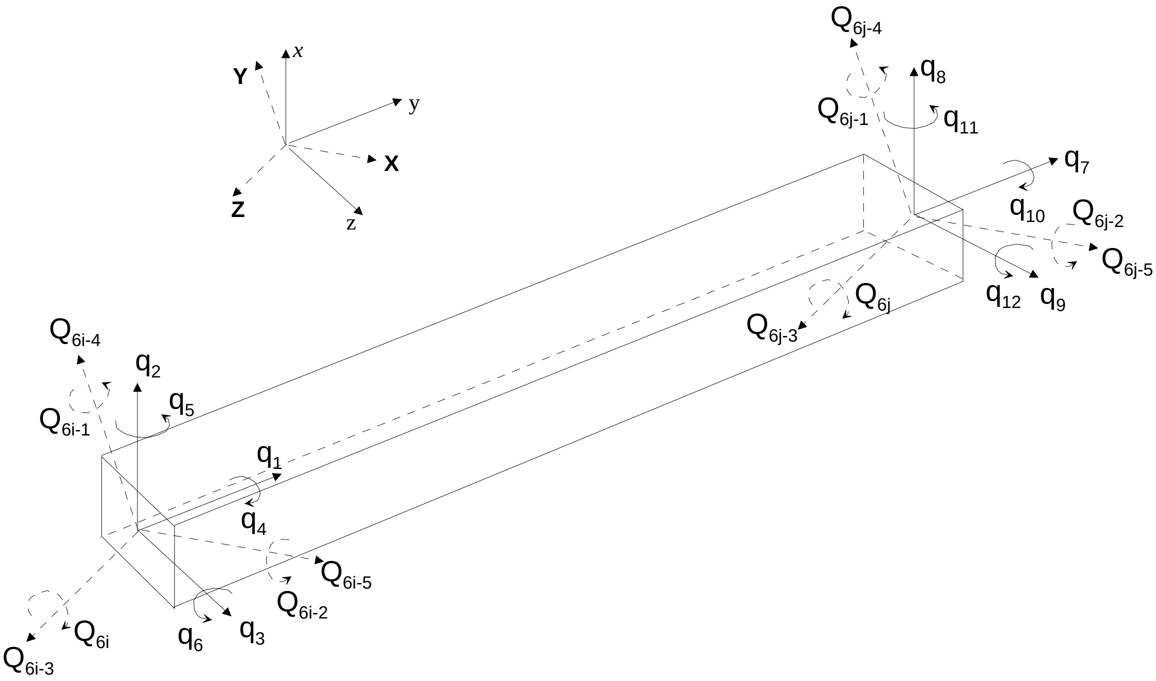

Figure 2.3 Displacements of Element e in Global and Local Coordinates.

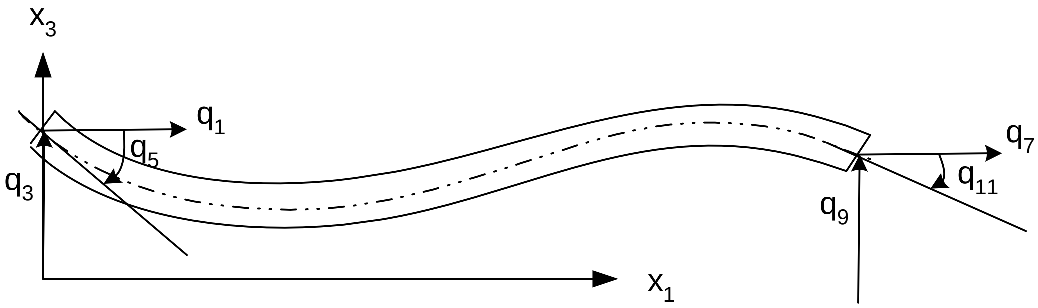

Figure 2.4 Projections of Local Coordinate System Displacements and Slopes onto the $x_1 - x_3$ Plane

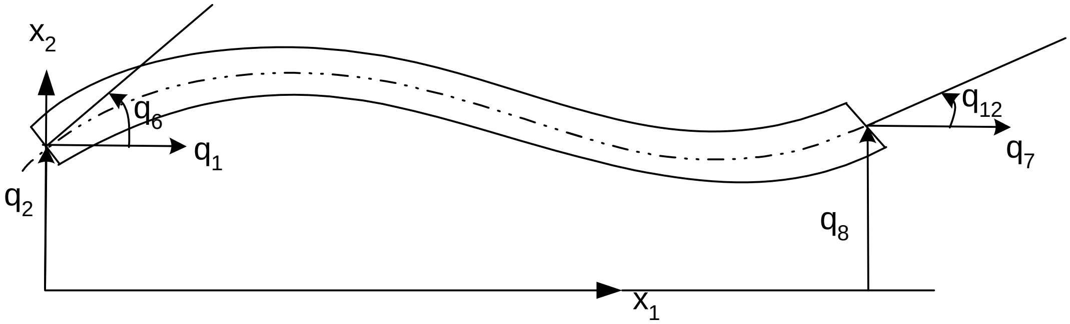

Figure 2.5 Projections of Local Coordinate System Displacements and Slopes onto the $x_1 - x_2$ Plane

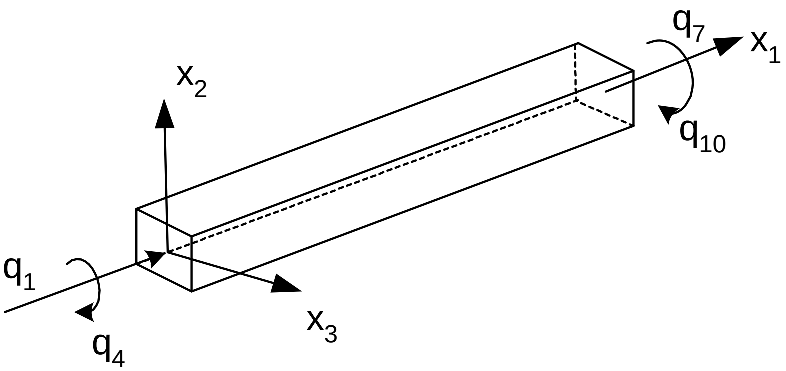

Figure 2.6 The Twist Degrees of Freedom in the Local Coordinate System

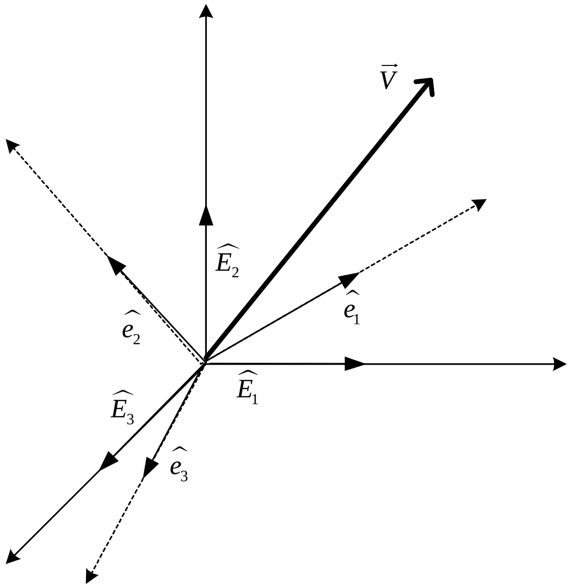

Figure 2.7 Unit Vectors of the Global and Local Coordinates

$$\left\{ \underset{\sim}{Q} \right\} = \left\{ Q_1 \quad Q_2 \quad Q_3 \quad Q_4 \quad Q_5 \quad Q_6 \quad Q_7 \quad Q_8 \quad Q_9 \quad Q_{10} \quad Q_{11} \quad Q_{12} \right\}^T \tag{2.81}$$

Both types of displacements are used in a frame analysis, i.e. local coordinate displacements are used in reaction force and stress calculations whereas the global coordinate displacements are printed and plotted for aid in determining the deformation of the structure. The system matrices are formulated in the local coordinate for each element and transformed to the global to form the total equation of the motion. After the system matrices are solved and the global displacements and reaction forces are obtained, the vectors are transformed to the local to get the stress at each element.

Any vector may have its components transformed between two distinct coordinate systems illustrated in Figure 2.7 and expressed by:

$$\underline{V} = \underline{X} + \underline{v} \tag{2.82}$$

where

$\underline{V} = \{V\}^T\{\underline{x}\} = [V_1 \quad V_2 \quad V_3]\{\underline{x}\}$,
$\underline{X} = \{X\}^T\{\underline{x}\} = [X_1 \quad X_2 \quad X_3]\{\underline{x}\}$,
$\underline{v} = \{v\}^T\{\underline{e}\} = [v_1 \quad v_2 \quad v_3]\{\underline{e}\}$,
$\{\underline{x}\} = \{\underline{x}_1 \quad \underline{x}_2 \quad \underline{x}_3\}$ = unit vector in global coordinate,
$\{\underline{e}\} = \{\underline{e}_1 \quad \underline{e}_2 \quad \underline{e}_3\}$ = unit vector in local coordinate.

Then, the local and the inertia coordinate components are related by the coordinate transformation as.

$$\{\underline{e}\} = \left[C^e\right]\{\underline{x}\} \tag{2.83}$$

where $\left[C^e\right]$ is the transformation matrix of the element.

Consequently, the local coordinates can be transformed to the global coordinate system by using the transformation matrix.

$$\{\underline{q}\} = \left[T^e\right]\{\underline{Q}\} \tag{2.84}$$

where

$$\left[T^e\right] = \begin{bmatrix} C^e & \underline{0} & \underline{0} & \underline{0} \\ \underline{0} & C^e & \underline{0} & \underline{0} \\ \underline{0} & \underline{0} & C^e & \underline{0} \\ \underline{0} & \underline{0} & \underline{0} & C^e \end{bmatrix},$$

$$\underline{0} = \begin{bmatrix} 0 & 0 & 0 \\ 0 & 0 & 0 \\ 0 & 0 & 0 \end{bmatrix}.$$

Adopting the shape function for the element gives the following equation of motion of the frame element

$$\left[m^e\right]\left\{\underline{\ddot{q}}^e\right\}+\left[k^e\right]\left\{\underline{q}^e\right\}=\left\{\underline{f}^e\right\}+\left\{\underline{n}^e\right\}$$

where

$m_{ij}^e=\int m\Psi_i\Psi_j dx$,

$k_{ij}^e=\int k\Psi_i'\Psi_j' dx$,

$f_j^e=\int f\Psi_j dx$

$\underline{n}^e$: nodal force,

$\underline{f}^e$: distributed load on the element,

and Ψ_j is the shape function.

In the global coordinate system, the equation can be presented in the global coordinate of the nodal displacement, $\underline{Q}$ as:

$$\left[M^e\right]\left\{\underline{\ddot{Q}}^e\right\}+\left[K^e\right]\left\{\underline{Q}^e\right\}=\left\{\underline{F}^e\right\}+\left\{\underline{N}^e\right\}$$

where

$\left[M^e\right]=\left[T^e\right]^T\left[m^e\right]\left[T^e\right]$,

$\left[K^e\right]=\left[T^e\right]^T\left[k^e\right]\left[T^e\right]$,

$\left\{\underline{F}^e\right\}=[T^e]^T\left\{\underline{f}^e\right\}$, and

$$\left\{\underline{N}^e\right\} = [T^e]^T \left\{\underline{n}^e\right\}.$$

Therefore, if we know the elements matrices of an element “e” in the local coordinate system, then the element matrices of the element in the global coordinate system through the transformation matrix.

2.5 FE Model of Slender Rod Theory

2.5.1 Introduction

The theory and the numerical method for the dynamic and static analysis of the mooring line and riser are introduced in this section. The line dynamics presented here is based on the formulation of the dynamics of inextensible slender rods (Garrett, 1982). The formulation is further expanded by Webster (Paulling and Webster, 1986) to include stretch and various loads appropriate to the line dynamic problem. These include the effect of gravity forces due to the mass of the line, the buoyancy and the hydrodynamic forces due to the line and wave motion, and the ocean bottom boundary conditions.

2.5.2 Slender Rod Theory

The behavior of a slender rod can be expressed in terms of the variation of the position of the rod centerline. The coordinate system and A position vector $\underline{r}(s,t)$ is the function of the arc length s of the rod and time t.

$$\sum \underline{F} = \underline{F} + d\underline{F} - \underline{F} + \underline{q}ds = mds\underline{\ddot{r}} \tag{2.85}$$

$$\frac{d\underline{F}}{ds}+\underline{q}=m\ddot{\underline{r}} \tag{2.86}$$

$$\sum_{@\underline{r}}\underline{M}=\underline{M}+d\underline{M}-\underline{M}+\left(\underline{r}'+d\underline{r}'\right)\times\left(\underline{F}+d\underline{F}\right)ds+\underline{\mu}ds=ds^{3}\ddot{\underline{\theta}} \tag{2.87}$$

as $ds\rightarrow 0$,

$$\frac{d\underline{M}}{ds}+\underline{r}'\times\underline{F}+\underline{\mu}=ds^{2}\ddot{\underline{\theta}}\rightarrow 0 \tag{2.88}$$

Furthermore, the bending moment and the curvature has the relationship of

$$\underline{M}=\underline{r}'\times EI\underline{r}''+H\underline{r}' \tag{2.89}$$

where E is the Young's modulus of the rod, I is the cross sectional moment of inertia, and H is the torque. Equation (2.88) and (2.89) can be combined and give the

$$\left(\underline{r}'\times EI\underline{r}''+H\underline{r}'\right)'+\underline{r}'\times\underline{F}+\underline{\mu}=0$$

or

$$\underline{r}'\times\left[\left(EI\underline{r}''\right)'+\underline{F}\right]+H'\underline{r}'+H\underline{r}''+\underline{\mu}=0 \tag{2.90}$$

The scalar product with $\underline{r}'$ for the equation (2.90) yields

$$\underline{H}'+\underline{\mu}\cdot\underline{r}'=0 \tag{2.91}$$

where $\underline{\mu}\cdot\underline{r}'$ is the distributed torsion. If there is no distributed torsion, $\underline{\mu}\cdot\underline{r}'=0$ and $\underline{H}'=0$. This means that the torque is independent on the arc length s. Furthermore, the torque in the line is usually small enough to be neglected, i.e. $H=0$. Thus, equation (2.90) can be rewritten in the following form.

$$\underline{r}'\times\left[\left(EI\underline{r}''\right)'+\underline{F}\right]=0 \tag{2.92}$$

If a scalar function, $\lambda(s,t)$, which is also called Lagrangian multiplier, is introduced to the equation (2.92) and the product with $\underline{r}'$ is taken, then the following formula is obtained.

$$\underline{F} = -\left(EI\underline{r}''\right)' + \lambda\underline{r}' \tag{2.93}$$

where λ is the Lagrangian multiplier. $\underline{r}'$ should satisfy the stretch constrained equation and it can be approximated as follows with the assumption that the stretch of the rod is linear and small;

$$\underline{r}' \cdot \underline{r}' = \left(1 + \frac{T}{EA_I}\right)^2 \approx 1 + 2\frac{T}{EA_I} \approx 1 + 2\frac{\lambda}{EA_I} \tag{2.94}$$

where A_I is the cross section area of the rod. If the inextensibility condition is applied, equation (2.94) can be reduced as:

$$\underline{r}' \cdot \underline{r}' = 1 \tag{2.95}$$

Applying dot product of $\underline{r}'$ to equation (2.93) and using the relation of equation (2.95) give to

$$\lambda = \underline{F} \cdot \underline{r}' + \left(EI\underline{r}''\right)' \cdot \underline{r}' = T - EI\kappa^2 \tag{2.96}$$

Substituting equation (2.93) into equation (2.86) gives the following equation of motion.

$$-\left(EI\underline{r}''\right)'' + \left(\lambda\underline{r}'\right)' + \underline{q} = \rho\ddot{\underline{r}} \tag{2.97}$$

2.5.3 Force Acting on the Rod

In the case dealing with the floating platforms, the applied forces on the rod are mostly from hydrostatic and hydrodynamic ones. Therefore, the distributed load, $\underline{q}$ may be divided as follows.

$$\underline{q} = \underline{w} + \underline{F}^s + \underline{F}^d \tag{2.98}$$

where $\underline{w}$ is the weight of the rod per unit length, $\underline{F}^s$ is the hydrostatic force on the rod per unit length, and $\underline{F}^d$ is the hydrodynamic force per unit length. The hydrostatic forces acting on a rod element is depicted in Figure 2.8 and can be formulated as

$$\delta s \underline{F}^s = \underline{B}\delta s + PA\underline{r}' - \frac{1}{2}\delta\left(PA\underline{r}'\right) - PA\underline{r}' - \frac{1}{2}\delta\left(PA\underline{r}'\right) \tag{2.99}$$

where $\underline{B}$ is the buoyancy force on the rod per unit length, and P is the hydrostatic pressure at the point $\underline{r}$ on the rod. Simplifying equation (2.99) gives

$$\underline{F}^s = \underline{B} - \left(PA\,\underline{r}'\right)' \tag{2.100}$$

The procedure for calculating hydrodynamic forces on offshore structures when wave is applied can be split up into fundamentally different approaches depending on the ratio of structural member diameter to wave length (D/λ) and wave height to structural member diameter (H/D).

For relatively small structural members with D/λ<0.2, the members does not alter the incident wave characteristics to any significant extent and is subjected to so-called Morison wave loading. On the other hand, for larger structural members with D/λ>0.2, the members may disturb the wave field significantly and more exact diffraction theory is required. However, the potential diffraction theory cannot account for viscous drag forces.

The second parameter of interest is the ratio H / D whose importance is based on the fact that drag forces on structures in an oscillatory wave flow are dominated by the separation of flow behind the cylinder and the formation of large vorticies. A non-dimensional parameter called the Keulegan-Carpenter number is a more rational measure of the ratio of water particle motion double amplitude to cylinder diameter than H / D which is only valid close to the water surface. The Keulegan-Carpenter number is defined as

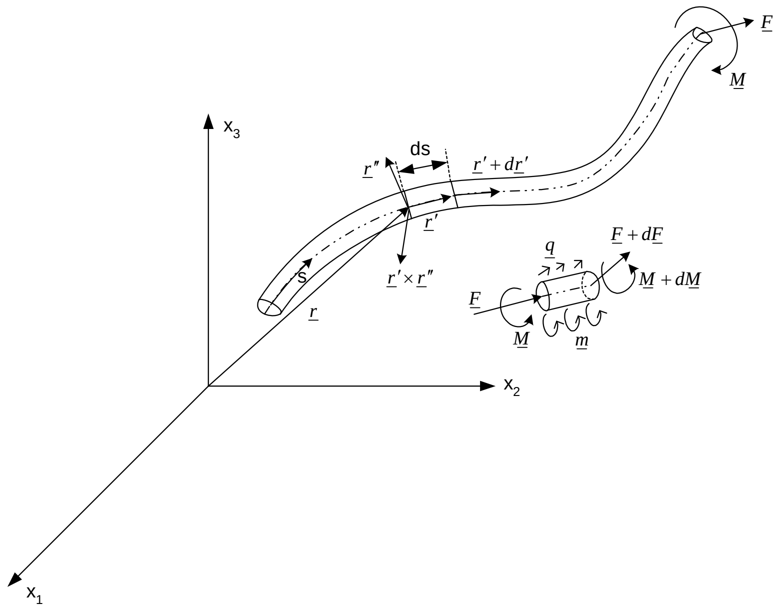

Figure 2.8 Configuration of Slender Rod Model and Free Body Diagram of Forces and Moments

$$K_C = \frac{U_m T}{D} \tag{2.101}$$

where U_m is the maximum normal velocity in the oscillatory flow of period T about the cylinder of diameter D.

For a small K_C (<5.0), the orbital diameter of fluid particle motions does not remain unidirectional long enough for the flow to initiate separation and develop or shed vortices, in which drag forces are relatively small compared with the acceleration-dependent inertia forces. At the other extreme, for approximately K_C>25.0, the wave flow will have been unidirectional long enough for a substantial vortex flow to develop. Drag forces will then be large and a Morison formulation, which accounts for these, must be used. An intermediate region, where 5.0< K_C <25.0 also exists where the flow regime is highly complicated and wave forces are difficult to compute.

The Keulegan-Carpenter number in wave-current field is often defined as

$$K_C = \frac{(U_m + u_C)T}{D} \tag{2.102}$$

where u_c is the constant current velocity.

Slender tubular subsea pipe lines or mooring lines are such structures whose D/λ is less than 0.2 and are subjected to Morison hydrodynamic force. When a line structure member is free to move in wave and current, the independent flow field model is obtained by linear superposition of two independent flow fields, a far field due to the wave motion and relatively unaffected by the structure motion and a near field resulting from the structure motion.

$$\underline{F}^{d} = -C_{A}\rho A_{I}\underline{\ddot{r}}^{n} + C_{M}\rho A_{I}\underline{\dot{V}}^{n} - C_{D}'\rho A_{D}\left|\underline{\dot{r}}^{n}\right|\underline{\dot{r}}^{n} + C_{D}\rho A_{D}\left|\underline{V}^{n}\right|\underline{V}^{n} \tag{2.103}$$

where ρ is the water density, and C_M and C_D is the inertia and the drag coefficients, respectively, for the line member fixed in wave and current, while C_A and C_D' are the added mass and the drag coefficients, respectively, obtained from the experiments of oscillating cylinder in calm water. A_I is the cross sectional area of the rod member and A_D is the area of the unit-length rod projected to the plane which is normal to the rod centerline. $\underline{\dot{r}}^{n}$ is the component of the rod member velocity normal to rod centerline and $\underline{\dot{r}}^{n}$ is the component of the rod member acceleration normal to rod centerline, which are derived by substituting the tangential velocity and acceleration component from the total velocity and acceleration, respectively, of the member.

$$\underline{\dot{r}}^{n} = \underline{\dot{r}} - \left(\underline{\dot{r}} \cdot \underline{r}'\right)\underline{r}' \tag{2.104}$$

$$\underline{\ddot{r}}^{n} = \underline{\ddot{r}} - \left(\underline{\ddot{r}} \cdot \underline{r}'\right)\underline{r}' \tag{2.105}$$

$\underline{V}^{n}$ and $\underline{\dot{V}}^{n}$ are respectively the velocity and the acceleration of the water particle normal to the rod centerline due to the incident wave and the current, which can be derive with the same way as that of equation (2.104) and (2.105)

$$\underline{V}^{n} = V - \left(\underline{V} \cdot \underline{r}'\right)\underline{r}' \tag{2.106}$$

$$\underline{\dot{V}}^{n} = \underline{\dot{V}} - \left(\underline{\dot{V}} \cdot \underline{r}'\right)\underline{r}' \tag{2.107}$$

When the dynamic force is written in the terms of relative motion, single coefficients are assumed to apply. Thus

$$\underline{F}^{d} = C_M \rho A_I \left(\underline{\dot{V}}^{n} - \underline{\ddot{r}}^{n} \right) + \rho A_I \underline{\dot{V}}^{n} + C_D \rho A_D \left| \underline{V}^{n} - \underline{\dot{r}}^{n} \right| \left(\underline{V}^{n} - \underline{\dot{r}}^{n} \right) \tag{2.108}$$

It is more convenient to separate the inertia coefficient from the added mass coefficient with the relation, i.e. $C_M = C_A + 1$.

$$\underline{F}^{d} = -C_A \rho A_I \underline{\ddot{r}}^{n} + C_M \rho A_I \underline{\dot{V}}^{n} + C_D \rho A_D \left| \underline{V}^{n} - \underline{\dot{r}}^{n} \right| \left(\underline{V}^{n} - \underline{\dot{r}}^{n} \right) \tag{2.109}$$

Using equation (2.99), (2.100) and (2.109) leads the governing equation to

$$m\underline{\ddot{r}} + C_A \rho A_I \underline{\ddot{r}}^{n} + \left(EI \underline{r}'' \right)'' - \left(\tilde{\lambda} \underline{r}' \right)' = \underline{\tilde{w}} + \underline{\tilde{F}}^{d} \tag{2.110}$$

where

$\tilde{\lambda} = \tilde{T} - EI\kappa^2$,

$\underline{\tilde{w}} = \underline{w} + \underline{B}$: wet weight of the rod,

$\tilde{T} = T + P$: effective tension in the rod,

$\underline{\tilde{F}}^{d} = C_M \rho A_I \underline{\dot{V}}^{n} + C_D \rho A_D \left| \underline{V}^{n} - \underline{\dot{r}}^{n} \right| \left(\underline{V}^{n} - \underline{\dot{r}}^{n} \right)$.

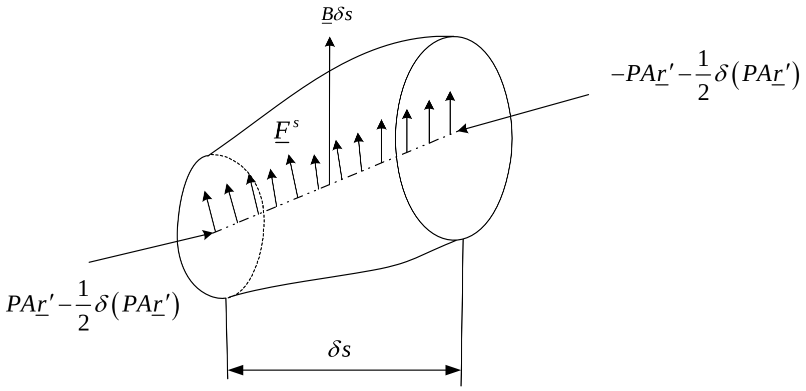

Figure 2.9 Surface Forces on the Rod Element

2.5.4 Finite Element Formulation

The equation (2.110) with the equation (2.94) is the governing equation of the motion for the elastic rod to be applied to the finite element model. For the convenience, the equations are described with Einstein index notation as:

$$-m\ddot{r}_i - C_A\rho A_I\ddot{r}_i^{\,n} - \left(EIr_i''\right)'' + \left(\tilde{\lambda} r_i'\right)' + \tilde{w}_i + \tilde{F}_i^{d} = 0 \tag{2.111}$$

$$\frac{1}{2}\left(r_i' r_i' - 1\right) - \frac{\lambda}{AE} = 0 \tag{2.112}$$

Here the unknown variable r_i and λ can be approximated by shape functions.

$$r_i(s,t) = C_l(s)U_{il}(t) \tag{2.113}$$

$$\lambda(s,t) = Q_m(s)\lambda_m(t) \tag{2.114}$$

where $0 \le s \le L$ and L is the length of one element member.

Multiplying equation (2.111) and (2.112) with a weighting functions, i.e. $\delta r_i = C_l(s)\delta U_{il}(t)$ and $\delta\lambda = Q_m(s)\delta\lambda_m(t)$ and integrating over all the element gives

$$\int_0^L C_l(s)\left[-m\ddot{r}_i - C_A\rho A_I\ddot{r}_i^{\,n} - \left(EIr_i''\right)'' + \left(\tilde{\lambda} r_i'\right)' + \tilde{w}_i + \tilde{F}_i^{d}\right]\delta U_{il}(t)\,ds = 0 \tag{2.115}$$

$$\int_0^L Q_m(s)\left[\frac{1}{2}\left(r_i' r_i' - 1\right) - \frac{\lambda}{AE}\right]\delta\lambda_m(t)\,ds = 0 \tag{2.116}$$

Integrating the resulting expression by parts yields the weak form of the equations.

$$\begin{aligned}\int_0^L &\left[C_l(s)\left(m\ddot{r}_i + C_A\rho A_I\ddot{r}_i^{\,n}\right) + C_l''(s)EIr_i'' + C_l'(s)\tilde{\lambda}r_i' - C_l(s)\left(\tilde{w}_i + \tilde{F}_i^{d}\right)\right]ds \\ &= C_l(s)\left[\left(EIr_i''\right)' - \tilde{\lambda}r_i'\right]\Big|_0^L - C_l'(s)EIr_i''\Big|_0^L\end{aligned} \tag{2.117}$$

$$\int_0^L Q_m(s)\left[\frac{1}{2}\left(r_i' r_i' - 1\right) - \frac{\lambda}{AE}\right] ds = 0 \tag{2.118}$$

The specific shape functions for and element of the rod are to be selected. From the equation (2.117) it is found that $C_l(s)$ is at least $C^{(2)}$ continuous on the element, i.e. not only its first but also the second derivatives are continuous. The first boundary term of equation (2.117) is the forces and the second boundary term is the moments at the ends of the rod. It is also seen that the admissible function of $Q_m(s)$ is $C^{(1)}$ continuous on the element. The cubic and the quadratic functions are chosen for $C_l(\xi)$ and $Q_m(\xi)$, respectively, to keep the requirement of the shape function. The functions are defined using the normalized coordinate $\xi(= s/L)$ as follows and are plotted in Figure 2.10 and Figure 2.11, respectively.

$$C_1(\xi) = 1 - 3\xi^2 + 2\xi^3, \quad C_2(\xi) = l\left(\xi - 2\xi^2 + \xi^3\right) \tag{2.119}$$

$$C_3(\xi) = 3\xi^2 - 2\xi^3, \; C_4(\xi) = l\left(-\xi^2 + \xi^3\right)$$

$$Q_1(\xi) = 1 - 3\xi + 2\xi^2, \; Q_2(\varsigma) = 4\xi(1 - \xi), \; Q_3(\xi) = \xi(2\xi - 1) \tag{2.120}$$

$U_{il}(t)$ and $\lambda_m(t)$ in equation (2.113) and (2.114) are time-dependent system unknowns representing the displacement and slope of the element at each node and tensions which are to be solved in the end. With the special selection of shape functions the unknowns in the summations in equation (2.113) and (2.114) become

$$U_{i1}(t) = r_i(0,t), \quad U_{i2}(t) = r_i'(0,t) \tag{2.121}$$

$$U_{i3}(t)=r_i(l,t), \quad U_{i4}(t)=r_i'(l,t)$$

$$\lambda_1(t)=\lambda(0,t), \;\; \lambda_2(t)=\lambda\left(\frac{l}{2},t\right), \;\; \lambda_3(t)=\lambda(l,t) \tag{2.122}$$

Inserting the expansions in equation (2.113) and (2.114) with the shape functions in equation (2.119) and (2.120) into equation (2.118) gives

$$\int_0^L mC_l(s)\ddot{r}_i ds = \int_0^L mC_l(s)C_k(s)\delta_{ij} ds\ddot{U}_{jk}(t) \tag{2.123}$$

$$\begin{aligned}\int_0^L C_A\rho A_I C_l(s)\ddot{r}_i^n ds &= \int_0^L C_A\rho A_I C_l(s)\left[\ddot{r}_i-\left(\ddot{r}_i\cdot r_i'\right)r_j'\right]ds \\ &= \int_0^L C_A\rho A_I C_l(s)C_k(s)\left[\delta_{ij}-C_t'(s)C_s'(s)U_{jt}(t)U_{is}(t)\right]ds\ddot{U}_{jk}(t)\end{aligned} \tag{2.124}$$

$$\int_0^L C_l''(s)EIr_i''ds = \int_0^L EIC_l''(s)C_k''(s)\delta_{ij}dsU_{jk}(t) \tag{2.125}$$

$$\int_0^L C_l'(s)\tilde{\lambda}r_i'ds = \lambda_n(t)\int_0^L Q_n(s)C_l'(s)C_k'(s)\delta_{ij}dsU_{jk}(t) \tag{2.126}$$

$$\int_0^L Q_m(s)\frac{1}{2}r_i'r_i'ds = \frac{1}{2}\int_0^L Q_m(s)C_l'(s)C_k'(s)dsU_{jl}U_{jk} \tag{2.127}$$

$$\int_0^L Q_m(s)\frac{\lambda}{AE}ds = \int_0^L Q_m(s)Q_n(s)\frac{1}{AE}ds\lambda_n(t) \tag{2.128}$$

Substituting equation (2.123) through (2.128) gives the equation of the rod element motion.

$$\left(M_{ijlk}+M_{ijlk}^a\right)\ddot{U}_{jk}+\left(K_{ijlk}^1+\lambda_n K_{nijlk}^2\right)U_{jk}-F_{il}=0 \tag{2.129}$$

$$G_m = A_{mlk} U_{jl} U_{jk} - B_m - C_{mn} \lambda_n = 0 \tag{2.130}$$

where

$$M_{ijlk} = \int_0^L m C_l(s) C_k(s) \delta_{ij} ds \tag{2.131}$$

$$M^a_{ijlk} = \int_0^L C_A \rho A_I C_l(s) C_k(s) \left[\delta_{ij} - C_t'(s) C_s'(s) U_{jt}(t) U_{is}(t) \right] ds \tag{2.132}$$

$$K^1_{ijlk} = \int_0^L EI C_l''(s) C_k''(s) \delta_{ij} ds \tag{2.133}$$

$$K^2_{nijlk} = \int_0^L Q_n(s) C_l'(s) C_k'(s) \delta_{ij} ds \tag{2.134}$$

$$K^2_{nijlk} = \int_0^L Q_n(s) C_l'(s) C_k'(s) \delta_{ij} ds \tag{2.135}$$

$$A_{mlk} = \frac{1}{2} \int_0^L Q_m(s) C_l'(s) C_k'(s) ds \tag{2.136}$$

$$B_m = \frac{1}{2} \int_0^L Q_m(s) ds \tag{2.137}$$

$$C_{mn} = \frac{1}{AE} \int_0^L Q_m(s) Q_n(s) ds \tag{2.138}$$

and δ_{ij} is the Kronecker Delta function. The equation (2.129) and (2.130) are used for solving the rod dynamics. The program is implemented for calculating the equations (2.131) through (2.138) by using the system parameters and the integration of the shape functions. Since the force vector, F_{il} contains nonlinear terms, the total equations are nonlinear. So, in addition to the above manipulation, some numerical approaches for solving the nonlinear time-domain solution technique is required, which will be introduced and explained in the following sections.

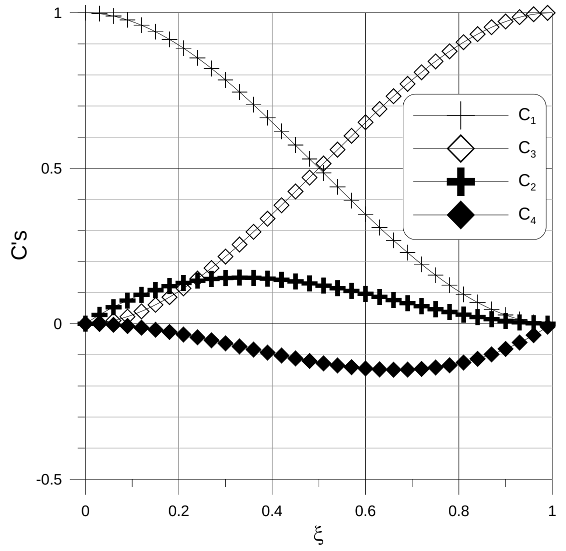

Figure 2.10 The Cubic Shape Functions for Displacement and Tangential Vectors

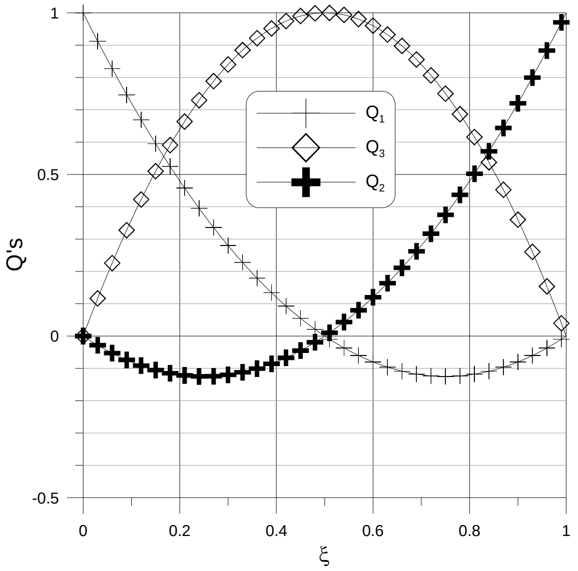

Figure 2.11 The Quadratic Shape Functions for the Tension

2.5.5 Static Problem

For the static problem, the first (inertia) term in equation (2.129) is removed, and the governing equations of rod become a nonlinear algebraic equations:

$$R_{il} = \left(K^{1}_{ijlk} + \lambda_n K^{2}_{nijlk}\right) U_{jk} - F_{il} = 0 \tag{2.139}$$

$$G_m = A_{mlk} U_{jl} U_{jk} - B_m - C_{mn} \lambda_n = 0 \tag{2.140}$$

and F_{il} is a static forcing term from the gravity force, drag force from the steady current and other applied static force on the line.

The Newton's method, an iterative method, is used to solve the nonlinear equations. The iterative method, i.e. Newton's method is used to solve the nonlinear equations. Using Taylor series to expand the above two equations about the guessed solution or solution from previous iteration, $U^{(n)}$ and $\lambda^{(n)}$ (n is the iteration number), and neglecting the higher order terms leads to

$$R^{(n+1)}_{il} = R^{(n)}_{il} + \frac{\partial R_{il}}{\partial U_{jk}} \Delta U_{jk} + \frac{\partial R_{il}}{\partial \lambda_n} \Delta \lambda_n = 0 \tag{2.141}$$

$$G^{(n+1)}_{m} = G^{(n)}_{m} + \frac{\partial G_{m}}{\partial U_{jk}} \Delta U_{jk} + \frac{\partial G_{m}}{\partial \lambda_n} \Delta \lambda_n = 0 \tag{2.142}$$

Rearranging the terms gives

$$\begin{bmatrix} K^{t0(n)}_{ijlk} & K^{t1(n)}_{iln} \\ D^{t0(n)}_{mjk} & D^{t1(n)}_{mn} \end{bmatrix} \begin{Bmatrix} \Delta U_{jk} \\ \Delta \lambda_n \end{Bmatrix} = \begin{Bmatrix} -R^{(n)}_{il} \\ -G^{(n)}_{m} \end{Bmatrix} \tag{2.143}$$

where

$$K^{t0(n)}_{ijlk} = K^{1}_{ijlk} + \lambda^{(n)}_{n} K^{2}_{nijlk}$$

$$K_{iln}^{t1(n)} = K_{nijlk}^{2} U_{jk}^{(n)} = \int_0^L Q_n(s) C_l'(s) C_k'(s) \delta_{ij} ds\, U_{jk}^{(n)} = \int_0^L Q_n(s) C_l'(s) C_k'(s) ds\, U_{ik}^{(n)}$$

$$D_{mjk}^{t0(n)} = \frac{\partial}{\partial U_{jk}} \left\{ \int_0^L Q_m(s) \left[\frac{1}{2}\left(C_p'(s) U_{rp}^{(n)} C_q'(s) U_{rq}^{(n)} - 1 \right) - \frac{1}{AE} Q_p(s) \lambda_p^{(n)} \right] ds \right\}$$
$$= \int_0^L Q_m(s) C_k'(s) C_q'(s) ds\, U_{jq}^{(n)}$$

$$D_{mn}^{t1(n)} = -C_{mn} = -\frac{1}{AE} \int_0^L Q_m(s) Q_n(s) ds$$

$$R_{il}^{(n)} = \left(K_{ijlk}^{1} + \lambda_n K_{nijlk}^{2} \right) U_{jk}^{(n)} - F_{il}$$

$$G_m^{(n)} = \int_0^L Q_m(s) \left[\frac{1}{2}\left(C_p'(s) U_{rp}^{(n)} C_q'(s) U_{rq}^{(n)} - 1 \right) - \frac{1}{AE} Q_p(s) \lambda_p^{(n)} \right] ds$$

It is seen that the matrix in equation (2.143) is symmetric. At each iteration, there is fifteen (or eleven for two dimensional problem) linear algebraic equations for each element. The subscript arrangement in the above equation is inconvenient for algebraic solution. Thus, in the programming, a renumbered system is employed as follows: the global degree of freedom number associated with the parameter U_{jk} and λ_n for two dimensions is

DOF of $U_{il} = \begin{bmatrix} 1 & 2 & 7 & 8 \\ 3 & 4 & 9 & 10 \end{bmatrix} \quad for\ i = 1, 2 \quad l = 1, 2, 3, 4$

DOF of $\lambda_m = \begin{bmatrix} 5 & 6 & 11 \end{bmatrix} \quad for\ m = 1, 2, 3$ (2.144)

For three dimensions,

$$\text{DOF of } U_{il} = \begin{bmatrix} 1 & 2 & 9 & 10 \\ 3 & 4 & 11 & 12 \\ 5 & 6 & 13 & 14 \end{bmatrix} \quad \textit{for } i = 1, 2, 3 \qquad l = 1, 2, 3, 4$$

$$\text{DOF of } \lambda_m = \begin{bmatrix} 7 & 8 & 15 \end{bmatrix} \qquad \textit{for } m = 1, 2, 3 \tag{2.145}$$

After the renumbering, the equation (2.143) is to be written as:

$$\left[K^{(n)}\right]\{\Delta y\} = \left\{F^{(n)}\right\} \tag{2.146}$$

where

$$\{y\}^T = \{U_{11}, U_{12}, U_{21}, U_{22}, U_{31}, U_{32}, \lambda_1, \lambda_2, U_{13}, U_{14}, U_{23}, U_{24}, U_{33}, U_{34}, \lambda_3\} \tag{2.147}$$

and $\left[K^{(n)}\right]$ is the 15×15 stiffness matrix. The renumbering system which is mentioned above is used to determine the locations of each stiffness coefficient in the matrix $\left[K^{(n)}\right]$. For example, in three dimensional problems, the term K^{t0}_{3214} in equation (2.143) is located at row 5 and column 12 in the stiffness matrix $\left[K^{(n)}\right]$, and K^{t}_{312} is located at row 5 and column 8. $\left\{F^{(n)}\right\}$ is the force vector and has the following 15 components:

$$\{F\}^T = \{R_{11}, R_{12}, R_{21}, R_{22}, R_{31}, R_{32}, -G_1, -G_2, R_{13}, R_{14}, R_{23}, R_{24}, R_{33}, R_{34}, -G_3\} \tag{2.148}$$

In order to obtain the nodal variable U and λ along the line, the element equations (2.146) are assembled to constrain U's i.e., the U's of the constrain nodes are specified, and $\Delta U = 0$. Numbering the nodes in a ascending order from one end of the line to the other, the assembled global stiffness matrix is symmetric and narrow banded. For a line with N elements, the total number of equation is (N+1)×8-1 for three dimensional problem and the band width is 15, which can be solved efficiently using the symmetric and banded equations. An iterative procedure is applied with initially guessed values of y, i.e. U and λ. The variables are updated by $y^{(n+1)} = y^{(n)} + \Delta y$, where Δy is obtained by the assembled equation (2.146). The stiffness matrix $\left[K^{(n)}\right]$ and the forcing term $\left\{F^{(n)}\right\}$ in equation (2.146) are re-evaluated to solve Δy again. This iterative procedure continues until Δy becomes smaller than the pre-defined tolerance.

The resultant forces and moments at the end nodes of a element is not included in the derivation because they are canceled out during the element assembly. However, after the nodal variables are computed, the internal forces are usually desired for the structural design of the mooring lines and risers. From the right hand side of equation (2.117),

$$\left\{F^r\right\} = \left\{-N_1^{[1]} - L_1^{[1]} - N_2^{[1]} - L_2^{[1]} - N_3^{[1]} - L_3^{[1]}\ 0\ 0\ N_1^{[2]}\ L_1^{[2]}\ N_2^{[2]}\ L_2^{[2]}\ N_3^{[2]}\ L_3^{[2]}\ 0\right\}^T \tag{2.149}$$

where

$$N_i^{[1]} = \tilde{\lambda} r_i' - \left(EIr_i''\right)'\Big|_{s=0},$$

$$N_i^{[2]} = \tilde{\lambda} r_i' - \left(EIr_i''\right)'\Big|_{s=L},$$

$$L_i^{[1]} = EIr_i''\Big|_{s=0},$$

$$L_i^{[2]} = EIr_i''\Big|_{s=L},$$

and the superscript [1] denotes the first end of the element ($s = 0$) and [2] denotes the second end ($s = L$). From the definition of the resultant force and moment in equation

(2.89) and (2.93), $\underline{N} = \{N_1, N_2, N_3\}$ is the nodal resultant force and $\underline{L} = \{L_1, L_2, L_3\}^T$ is related with the nodal resultant moment $\underline{M}\left(\underline{M} = \underline{L} \times \underline{r}'\right)$. Therefore, after solving the model variables U and λ at (n+1)th iteration, the resultant force at the end nodes of an element can be obtained from force vector $\underline{F}^r$ and

$$\underline{F}^r = -\underline{F}^{(n+1)} \tag{2.150}$$

2.5.6 Dynamic Problem – Time Domain Integration

Recalling the motion equation of line (equation (2.129)) and the stretch condition (equation (2.130)) gives

$$\widehat{M}_{ijlk}\ddot{U}_{jk} = -\left(K^1_{ijlk} + \lambda_n K^2_{nijlk}\right)U_{jk} + F_{il} = -F^1_{il} - F^2_{il} + F_{il} = \widehat{F}_{il} \tag{2.151}$$

$$G_m = A_{mlk}U_{jl}U_{jk} - B_m - C_{mn}\lambda_n = 0 \tag{2.152}$$

where

$\widehat{M}_{ijlk} = M_{ijlk} + M^a_{ijlk}$,

$F^1_{il} = K^1_{ijlk}U_{jk}$,

$F^2_{il} = \lambda_n K^2_{nijlk}U_{jk}$.

Equation (2.151) is a second order differential equation and equation (2.152) is an algebraic equation with no time derivatives of the variables. In order to derive the integration scheme, equation (2.151) is split into two first order differential equations using the state variables:

$$\widehat{M}_{ijlk}\dot{V}_{jk} = \widehat{F}_{il} \tag{2.153}$$

$$\dot{U}_{jk} = V_{jk} \tag{2.154}$$

Integrating the above two equations from the (n)th time step to the (n+1)th time step gives

$$\int_{t^{(n)}}^{t^{(n+1)}} \widehat{M}_{ijlk} \dot{V}_{jk} dt = \int_{t^{(n)}}^{t^{(n+1)}} \widehat{F}_{il} dt \tag{2.155}$$

$$\int_{t^{(n)}}^{t^{(n+1)}} \dot{U}_{jk} dt = \int_{t^{(n)}}^{t^{(n+1)}} V_{jk} dt \tag{2.156}$$

Note that in equation (2.153), $\widehat{M}_{ijlk}$ is not a constant since it contains the added mass term M^{a}_{ijlk} which is a function of the line position, which can be convinced by looking at equation (2.130). The time varying $\widehat{M}_{ijlk}$ can be approximated to be a constant $\widehat{M}^{(n+1/2)}_{ijlk}$ for the time interval $\Delta t\left(t^{(n+1)} - t^{(n)}\right)$. $\widehat{M}^{(n+1/2)}_{ijlk}$ is the mass at time $t^{(n)} + \dfrac{\Delta t}{2}$. The left hand side of equation (2.155) can be simplified as follows while achieving second order accuracy such that the numerical error is $O\left(\Delta t^{2}\right)$:

$$\widehat{M}^{(n+1/2)}_{ijlk} V^{(n+1)}_{jk} - \widehat{M}^{(n+1/2)}_{ijlk} V^{(n)}_{jk} = \int_{t^{(n)}}^{t^{(n+1)}} \widehat{F}_{il} dt \tag{2.157}$$

Using the trapezoidal method, which is also called the first-order Adam-Moulton integration and of second-order accuracy, leads equation (2.156) to

$$U^{(n+1)}_{jk} = U^{(n)}_{jk} + \frac{\Delta t}{2}\left[V^{(n+1)}_{jk} + V^{(n)}_{jk}\right] \tag{2.158}$$

Re-arranging the above two equations (2.157) and (2.158) gives

$$\frac{4}{\Delta t^2}\widehat{M}_{ijlk}^{(n+1/2)}\Delta U_{jk} = \frac{4}{\Delta t}\widehat{M}_{ijlk}^{(n+1/2)}V_{jk}^{(n)} + \frac{2}{\Delta t}\int_{t^{(n)}}^{t^{(n+1)}}\widehat{F}_{il}\,dt \tag{2.159}$$

$$V_{jk}^{(n+1)} = \frac{2}{\Delta t}\Delta U_{jk} - V_{jk}^{(n)} \tag{2.160}$$

where $\Delta U_{jk} = U_{jk}^{(n+1)} - U_{jk}^{(n)}$, and the integral term in (2.159) is

$$\int_{t^{(n)}}^{t^{(n+1)}}\widehat{F}_{il}\,dt = -\int_{t^{(n)}}^{t^{(n+1)}}F_{il}^{1}dt - \int_{t^{(n)}}^{t^{(n+1)}}F_{il}^{2}dt + \int_{t^{(n)}}^{t^{(n+1)}}F_{il}\,dt \tag{2.161}$$

Applying the trapezoidal rules for the first and second terms at the right hand side leads to

$$\int_{t^{(n)}}^{t^{(n+1)}}F_{il}^{1}dt = \frac{\Delta t}{2}\left(F_{il}^{1(n+1)} + F_{il}^{1(n)}\right) = \frac{\Delta t}{2}\left[K_{ijlk}^{1}\left(\Delta U_{jk}\right) + 2K_{ijlk}^{1}U_{jk}^{(n)}\right] \tag{2.162}$$

$$\begin{aligned}
\int_{t^{(n)}}^{t^{(n+1)}}F_{il}^{2}dt &= \frac{\Delta t}{2}\left(F_{il}^{2(n+1)} + F_{il}^{2(n)}\right)\\
&= \frac{\Delta t}{2}\left(\lambda_n^{(n+1)}K_{nijlk}^{2}U_{jk}^{(n+1)} + \lambda_n^{(n)}K_{nijlk}^{2}U_{jk}^{(n)}\right)\\
&\approx \frac{\Delta t}{2}\left(\lambda_n^{\left(n+\frac{1}{2}\right)}K_{nijlk}^{2}U_{jk}^{(n+1)} + \lambda_n^{\left(n+\frac{1}{2}\right)}K_{nijlk}^{2}U_{jk}^{(n)}\right)\\
&= \frac{\Delta t}{2}\left(\lambda_n^{\left(n+\frac{1}{2}\right)}K_{nijlk}^{2}\Delta U_{jk} + 2\Delta\lambda_n K_{nijlk}^{2}U_{jk}^{(n)} + 2\lambda_n^{\left(n-\frac{1}{2}\right)}K_{nijlk}^{2}U_{jk}^{(n)}\right)
\end{aligned} \tag{2.163}$$

where $\Delta\lambda_n = \lambda_n^{n+\frac{1}{2}} - \lambda_n^{n-\frac{1}{2}}$. The third term in equation (2.161) contains the applied force F_{il} which is from gravity force and hydrodynamic forces. The gravity force is independent of time, but the hydrodynamic force, which is calculated using Morison's formula, is not known at time step (n+1) since the force is a function of the unknown rod position and velocity. Therefore, we use the Adams-Bashforth explicit scheme for the integral:

$$\begin{aligned}\int_{t^{(n)}}^{t^{(n+1)}} F_{il}\,dt &= \frac{\Delta t}{2}\left(3F_{il}^{(n)} - F_{il}^{(n-1)}\right) \qquad , \ n>1 \\ &= \frac{\Delta t}{2}F_{il}^{(0)} \qquad , \ n=1\end{aligned} \tag{2.164}$$

Combining equations (2.160), (2.161), (2.162), (2.163), and (2.164), we can obtain the integration scheme for the motion equation (2.151)

$$\begin{aligned}&\left[\frac{4}{\Delta t^2}\widehat{M}_{ijlk}^{(n+1/2)} + K_{ijlk}^{1} + \lambda_n^{\left(n+\frac{1}{2}\right)} K_{nijlk}^{2}\right]\Delta U_{jk} + 2K_{nijlk}^{2}U_{jk}^{(n)}\Delta\lambda_n \\ &\quad = \frac{4}{\Delta t}\widehat{M}_{ijlk}^{(n+1/2)}V_{jk}^{(n)} - 2K_{ijlk}^{1}U_{jk}^{(n)} - 2\lambda_n^{\left(n-\frac{1}{2}\right)}K_{nijlk}^{2}U_{jk}^{(n)} + \left(3F_{il}^{(n)} - F_{il}^{(n-1)}\right)\end{aligned} \tag{2.165}$$

and the mass term $\widehat{M}_{ijlk}^{(n+1/2)}$ is approximated using Adams-Bashforth method:

$$\widehat{M}_{ijlk}^{(n+1/2)} = \frac{1}{2}\left(3\widehat{M}_{ijlk}^{(n)} - \widehat{M}_{ijlk}^{(n-1)}\right) \tag{2.166}$$

The $G_m^{(n+1)}$ at time step $(n+1)$ from $G_m^{(n)}$ at time step (n) for the stretch condition equation (2.152) can be approximated using Taylor expansion as:

$$\begin{aligned}2G_m^{(n+1)} &\approx 2G_m^{(n)} + 2\frac{\partial G_m^{(n)}}{\partial U_{jk}}\Delta U_{jk} + 2\frac{\partial G_m^{(n)}}{\partial \lambda_n}\Delta\lambda_n \\ &= 2G_m^{(n)} + 2K_{miljk}^{2}U_{il}^{(n)}\left(\Delta U_{jk}\right) + 2D_{mn}^{t1(n)}\left(\Delta\lambda_n\right) = 0\end{aligned} \tag{2.167}$$

Note that the equation is multiplied by 2 for the numerical convergence (to make the element stiffness matrix symmetric). Equations (2.165) and (2.167) are re-written in a form similar to the static problem:

$$\begin{bmatrix} \hat{K}_{ijlk}^{t0(n)} & \hat{K}_{iln}^{t1(n)} \\ \hat{D}_{mjk}^{t0(n)} & \hat{D}_{mn}^{t1(n)} \end{bmatrix} \begin{Bmatrix} \Delta U_{jk} \\ \Delta \lambda_n \end{Bmatrix} = \begin{Bmatrix} \hat{R}_{il}^{(n)} \\ -\hat{G}_m^{(n)} \end{Bmatrix} \tag{2.168}$$

where

$$\hat{K}_{ijlk}^{t0(n)} = \frac{2}{\Delta t^2}\left(3\widehat{M}_{ijlk}^{(n)} - \widehat{M}_{ijlk}^{(n-1)}\right) + K_{ijlk}^1 + \lambda_n^{(n+1/2)} K_{nijlk}^2$$

$$\hat{K}_{iln}^{t1(n)} = 2K_{nijlk}^2 U_{jk}^{(n)}$$

$$R_{il}^{(n)} = \frac{4}{\Delta t}\widehat{M}_{ijlk}^{(n+1/2)} V_{jk}^{(n)} - 2K_{ijlk}^1 U_{jk}^{(n)} - 2\lambda_n^{(n-1/2)} K_{nijlk}^2 U_{jk}^{(n)} + \left(3F_{il}^{(n)} - F_{il}^{(n-1)}\right)$$

$$\hat{D}_{mjk}^{t0(n)} = 2K_{miljk}^2 U_{il}^{(n)}$$

$$\hat{D}_{mn}^{t1(n)} = 2D_{mn}^{t1(n)}$$

$$\hat{G}_m^{(n)} = 2G_m^{(n)}$$

The formulation of these coefficients, such as K_{ijlk}^1, K_{nijlk}^2 and $G_m^{(n)}$ are the same as that in the static analysis, with the superscript n indicating the n-th time step instead of n-th iteration. Like the static problem, the final equation for a rod element can be written as:

$$\left[\hat{K}^{(n)}\right]\{\Delta y\} = \left\{\hat{F}^{(n)}\right\} \text{ at the time step n+1} \tag{2.169}$$

where $\{y\}$ is defined in equation (2.147) and the arrangement of $\left[\hat{K}^{(n)}\right]$ and $\left\{\hat{F}^{(n)}\right\}$ is similar to that in the static problem. After the element equations are assembled and solved for time step (n+1), the nodal resultant force can be obtained by evaluating the resultant force vector

$$\underline{F}^{r} = -\hat{\underline{F}}^{(n+1)} \tag{2.170}$$

The above time-domain integration scheme has second order accuracy. Although the Adam-Moulton scheme, an implicit scheme, which is unconditionally stable, is used at the first in our formulation, the nonlinearity in the mass term $\hat{M}_{ijlk}$ (especially in the added mass term) and forcing term F_{il} (wave force from Morison's formula) was treated using explicit scheme. Thus the integration we developed is a mixture of implicit and explicit scheme. An alternative way to deal with the nonlinear terms without using implicit scheme is to use iterative procedure in each time step. This improves the stability of the scheme but not the accuracy (still second order). In addition, it requires more computing time. Experience indicates that it is more efficient to use the single calculation per time step than to continue the interactive process event though a smaller time step may be required.

The advantage of the time domain integration is the accuracy in predicting the dynamics of the nonlinear system. The drawback of the method is that it usually requires very long duration of the simulation to ensure accurate statistical information of the dynamics, which results in a very long computing time. In some of the applications of a floating structure dynamics, such as the vertical tethers of a TLP and vertical risers, where the nonlinearity of the system is weak, or in the structural fatigue life estimation, where the dynamics are needed for hundreds of environmental conditions, a linear analysis in frequency domain may give decent results with much less computing effort. Therefore, in our study, the frequency domain formulation of the rod model is also developed and is discussed in the following section.

2.5.7 Spring Coupling of the FE Line Members with the Body

The numerical modeling of the connection between the mooring lines (risers) and the platform is developed in this section. The connection is modeled as a combination of linear spring, which defines the relation of the translational motion between the platform (at the connecting point) and the top of the line and rotational spring which defines the relation between the rotation of the platform and the tangential direction of the line. The reason to use the springs to model the connection is two fold: first, this modeling is numerically convenient to couple the motion equations

Under the assumption that the platform undergoes small angular motions, which is consistent with the platform motion analysis described in the Section 3 leads to

$$\underline{N} = \left[\underline{K}^L\right]\left(\underline{X} + \underline{p} + \theta \times \underline{p} - \underline{r}\right) \qquad (2.171)$$

where $\left[\underline{K}^L\right]$ is 3×3 diagonal stiffness matrix of the linear spring with the nontrivial diagonal terms, K_1^L, K_2^L and K_3^L which are the spring stiffness in x, y and z direction, respectively. $\underline{X}$ is the translational motion of the rigid body (ς_1, ς_2 and ς_3 in vector $\underline{\varsigma}$ of from the equation motion) at its origin of the body coordinate system, and $\underline{\theta}$ is the angular motion (ς_4, ς_5 and ς_6 in vector $\underline{\varsigma}$ of equation of motion) of the rigid body, $\underline{p}$ is the position vector (in body coordinate system) of the point of the line which is attached to the rigid body by springs. In our program, the node attached to the platform is numbered as the second node ($s = L$) of the last element.

Obviously, the force and moment on the platform from the linear spring connector are;

$$\underline{F}^L = -\underline{N} \tag{2.172}$$

$$\underline{M}^L = \underline{p} \times \left(-\underline{N}\right) \tag{2.173}$$

For the rotational spring connector, the moment applied on the end node is proportional to the angle between the direction vector of the spring and the tangent of the line at the connection. Assuming the angular motion is small gives

$$\underline{L} = K^\theta \left(\underline{E} - \frac{\underline{r}'}{\left|\underline{r}'\right|} \right) = K^\theta \left(\underline{e} + \underline{\theta} \times \underline{e} - \frac{\underline{r}'}{\left|\underline{r}'\right|} \right) \tag{2.174}$$

where $\underline{r}'$ is the tangent to the riser centerline. Since, in some applications, the line is considered stretchable as in equation (2.174), $\underline{r}' / \left|\underline{r}'\right|$ is used instead of $\underline{r}'$ to ensure the unity of the tangent. $\underline{E}$ (a unit vector) is the direction of the spring reference, $\underline{e}$ is $\underline{E}$ in the rigid body coordinates, K^θ is the rotational spring constant.

The force and moment on the rigid body from the rotational spring are

$$\underline{F}^\theta = 0 \tag{2.175}$$

$$\underline{M}^\theta = \underline{L} \times \underline{r}' \approx \underline{L} \times \underline{e} \tag{2.176}$$

The connector force and the moment on the end node of the line can be re-written by using the subscript notations;

$$N_i = K_i^L \left(X_i + p_i + \theta_j C_{ji} - r_i \right) \tag{2.177}$$

$$L_i = K^{\theta}\left(e_i + \theta_j D_{ji} - \frac{r_i'}{\left(r_k' r_k'\right)^{1/2}} \right) \tag{2.178}$$

and the connector force on the rigid body as:

$$F_i = -N_i \tag{2.179}$$

$$M_i = N_k C_{ki} + L_k D_{ki} \tag{2.180}$$

where

$$[C] = \begin{bmatrix} 0 & -p_3 & p_2 \\ p_3 & 0 & -p_1 \\ -p_2 & p_1 & 0 \end{bmatrix}$$

and

$$[D] = \begin{bmatrix} 0 & -e_3 & e_2 \\ e_3 & 0 & -e_1 \\ -e_2 & e_1 & 0 \end{bmatrix}$$

for the 3 dimensional problem.

The above connector forces will be included in the relative motion equations of the mooring line and the platform as external forces. In the following static and dynamic analysis, we will derive the formula which defines coupling between the line and the platform.

In the static analysis of the mooring line where the Newtons method is used, we can approximate the connector force at the end node connected to the springs in the $(n+1)^{th}$ iteration from $(n)^{th}$ iteration:

Equation for r_i : $N_i^{(n+1)} = N_i^{(n)} + \frac{\partial N_i}{\partial r_j}\Delta r_j + \frac{\partial N_i}{\partial X_j}\Delta X_j + \frac{\partial N_i}{\partial \theta_j}\Delta\theta_j + \cdots$ (2.181)

Equation for r_i' : $L_i^{(n+1)} = L_i^{(n)} + \frac{\partial L_i}{\partial r_j'}\Delta r_j' + \frac{\partial L_i}{\partial \theta_j}\Delta\theta_j + \cdots$ (2.182)

We can see that the equation of the line at the connected node (r and r') is coupled with the unknown motion of the platform. Using symbol K_{ij}^{AB} to indicate the tangential stiffness coefficient for degree of freedom B_j in equation A_i, we have:

$$K_{ij}^{rr} = -\frac{\partial N_i}{\partial r_j} = K_i^L \delta_{ij} \tag{2.183}$$

$$K_{ij}^{rX} = -\frac{\partial N_i}{\partial X_j} = -K_i^L \delta_{ij} \tag{2.184}$$

$$K_{ij}^{r\theta} = -\frac{\partial N_i}{\partial \theta_j} = K_i^L C_{ij} \tag{2.185}$$

$$K_{ij}^{r'r'} = -\frac{\partial L_i}{\partial r_j'} = K_\theta \left[\frac{\delta_{ij}}{\sqrt{r_m' r_m'}} - \frac{r_i' r_j'}{\sqrt[3]{r_m' r_m'}} \right] \tag{2.186}$$

$$K_{ij}^{r'\theta} = -\frac{\partial L_i}{\partial \theta_j} = K_\theta D_{ij} \tag{2.187}$$

Note that the coefficient $K_{ij}^{r'r'}$ is nonlinear an dependent on the tangent (which is unknown) of the line at the node. In order to combine the equation of the platform with that of line, Newton's method also used for the equation of the platform. Similarly, the connector force on the rigid body at iteration (n+1) can be approximated by:

Equations for X_i : $F_i^{(n+1)} = F_i^{(n)} + \frac{\partial F_i}{\partial r_j}\Delta r_j + \frac{\partial F_i}{\partial X_j}\Delta X_j + \frac{\partial F_i}{\partial \theta_j}\Delta\theta_j + \cdots$ (2.188)

Equations for θ_i : $M_i^{(n+1)} = M_i^{(n)} + \frac{\partial M_i}{\partial r_j}\Delta r_j + \frac{\partial M_i}{\partial X_j}\Delta r_j' + \frac{\partial M_i}{\partial \theta_j}\Delta\theta_j + \cdots$ (2.189)

And we have

$$K_{ij}^{Xr} = -\frac{\partial F_i}{\partial r_j} = K_i^L \delta_{ij} \tag{2.190}$$

$$K_{ij}^{XX} = -\frac{\partial F_i}{\partial X_j} = K_i^L \delta_{ij} \tag{2.191}$$

$$K_{ij}^{X\theta} = -\frac{\partial F_i}{\partial \theta_j} = K_i^L C_{ij} \tag{2.192}$$

$$K_{ij}^{\theta r} = -\frac{\partial M_i}{\partial r_j} = K_\theta C_{ij} \tag{2.193}$$

$$K_{ij}^{\theta r'} = -\frac{\partial M_i}{\partial r_j'} = K_\theta D_{ji} \tag{2.194}$$

$$K_{ij}^{\theta\theta} = -\frac{\partial M_i}{\partial \theta_j} = K_i^L C_{ki} C_{kj} + K_\theta D_{ki} D_{kj} \tag{2.195}$$

In the iterative process, the stiffness coefficients K_{ij}^{rr} and $K_{ij}^{r'r'}$ will be included in the equation of the element which is connected to the platform and the coefficients

2.6 Nonlinear Hydro-Pneumatic Tensioner Model

Figure 2.12 shows a typical TTR system with hydro-pneumatic tensioner at the top and with the contact guide at the keel. The tension due to the pneumatic tensioner is related with stroke z of the piston, and satisfies the following nonlinear equation based on the gas law. As there is a surface tree above the tensioner, the nominal tension is to include the weight.

$$T = \frac{T_0}{\left(1 + z / z_0\right)^n} \tag{2.196}$$

where

T_0 = nominal top pretension of the riser(initial tension+tree weight),

z_0 = nominal length of the accumulator,

n = gas constant.

Figure 2.12 shows the free body diagram of the tensioner and riser with the surface tree weight, in which also the definitions of the up-stroke and the down-stroke are depicted. The surface tree is located above the tensioner and it does not affect the riser nominal tension, but it does affect the tensioner tension. Total tensison is uniformly distributed to the N tensioners.

Figure 2.13 shows the tension-stroke relationship of a typical tensioner(z_0 = 7.62 m = 25ft, T_0 =5248.9kN = 1180 kips and n =1.1).

The coulomb friction force (F_f) on the tensioner piston by the cylinder is assumed to be related to the tension and is written as follows (Andrighetto et al., 2005).

$$F_f = \mu T sign\left(-\dot{z}\right) \tag{2.197}$$

where

μ = dynamic friction factor,

$\dot{z}$ = time derivative of the stroke.

The time varying friction force changes its direction due to the relative velocity sign. The dynamic friction factor μ is set in the range of 0.02-0.05.

There are stoppers up and down the cylinder to restrict the piston motion in a certain range, and the corresponding upstroke and down-stroke limitations, z_{up}, z_{down} are to be defined. When the stroke limit is exceeded, a spring is attached between the piston and the stopper which is infinitely stiff to represent a rigid connection. The tensioner stroke curve becomes theoretically constant at this stopper as shown in Figure 2.13.

The sudden change of the stiffness can cause a numerical instability problem. One way to solve the problem is to use the nonlinear spring, such as cubic spring, instead of the normal linear spring to make the stiffness change smoother. The other way is to reduce the spring constant k. However, if k is too small, the spring stiffness itself becomes dominate the system stiffness and this may be changed. Figure 2.14 shows the sensitivity of the TTR stretch, spring stretch and their ratio to the spring constant when cubic spring is implemented. If the spring stretches too much(more than 5% of TTR stretch), then the spring cannot represent the rigid connection. When $k = 1.46\times10^{11}$N/m (=10^{10} lbs/ft) is given, the spring stretch is around 5% of the TTR stretch, in which case almost all the strain energies are stored in the riser, not in the spring. Spring represents the rigid connection between the stopper and piston. With the results herein, $k = 1.46\times10^{11}$N/m (=10^{10} lbs/ft) is stiff enough to be considered as a rigid connection.

The conventional way to model the tensioner in the global motion analysis is linear spring-dashpot, in which case a natural boundary condition in vertical direction is applied to model the pretension at the top node.

$$k_L z + C_L \dot{z} + T_0 \tag{2.198}$$

where

k_L = linear spring constant at the top node,

C_L =linear damping coefficient at the top node,

T_0 = pretension at the top node.

The linear spring constant k_L is obtained by taking the slope at the initial stroke from the tension-stroke curve in Figure 2.13. The linear damping coefficient can be obtained by carrying out the free decay test. The stroke limits are not applied to the spring-dashpot model of tensioner.

As shown in Figure 2.12, the TTR has the surface tree, whose weight is assumed to be 18.14 tonnes (40 kips), at the top of tensioner. It is above the connection point to the pneumatic tensioner, and it is not transferred to the riser, while the tensioner is affected by it. Therefore, the riser tension T_{riser} can be obtained by subtracting the tree weight W_{Tree} from the nominal tensioner tension as:

$$T_{riser} = T - W_{Tree} \tag{2.199}$$

The riser keel joint also has the nonlinear stick-slip behavior due to Coulumb friction forces in vertical direction (Murray et al., 2002). In horizontal direction, a gap contacting behavior is implemented through gap spring model (Koo et al., 2004) with stick-slip feature added. The horizontal springs are put at the contact point of riser and keel joint to keep it in the position and to calculate the reaction force as in Fig.6. The friction force acting on the riser node at the keel joint is calculated by the following equation.

$$F_{dyn} = \mu_d N_h \times sign\left(V_r\right) \tag{2.200}$$

where

F_{kf} =Coulumb friction force at the keel guide,

μ_d =dynamic friction factor between riser and joint,

N_h =reaction force of horizontal spring,

V_r =relative velocity between joint and riser.

Equation (2.200) causes sudden changes of the dynamic force due to the direction of relative velocity (Zardecki et al., 2002). An alternative function to avoid the stepwise change of the function can be adopted (Breedveld, 2000), but the equation (2.200) without any alternation is used herein. If the relative velocity V_r becomes zero, the riser get stuck to the joint, and rigid connection is applied to calculate the static spring force, F_{stat}. The riser begins to slip when the vertical reaction force is greater than the static friction force as:

$$N_v > \mu_s N_h \tag{2.201}$$

where μ_s is the static friction factor between riser and joint.

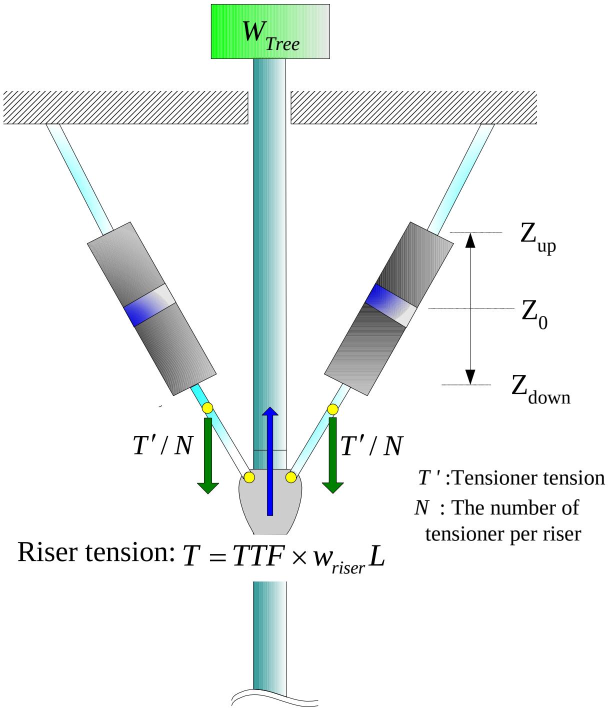

Figure 2.12 Free Body Diagram of the Tensioner

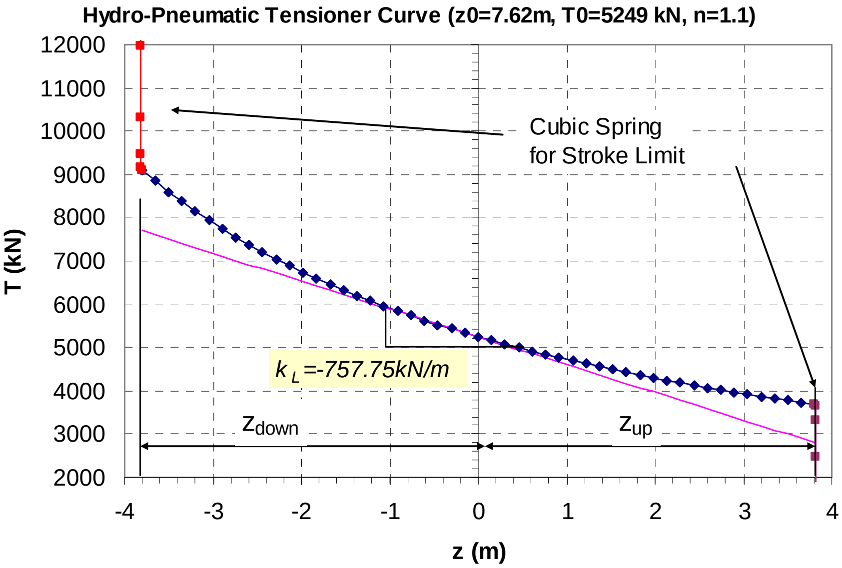

Figure 2.13 Tensioner Curve for z_0=7.62 m, T_0=5249kN, n=1.1, z_{down}=-3.81ft, and z_{up}=3.81ft

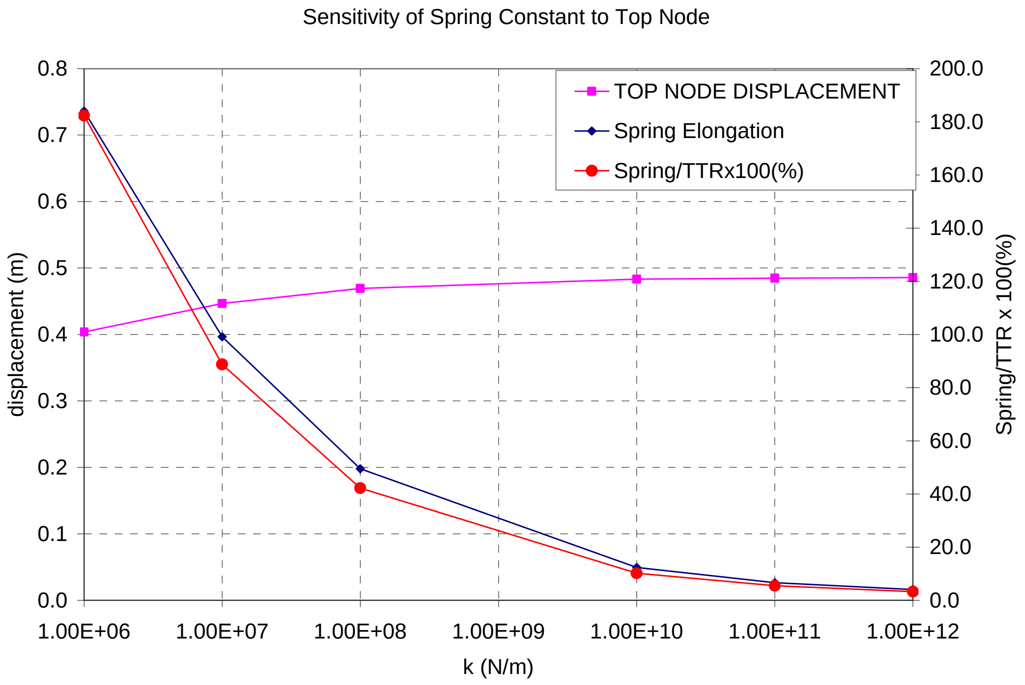

Figure 2.14 Sensitivity of the Spring and TTR Stretch to Cubic Spring Stiffness Modeled for the Upper and Lower Stroke Limit

3. ENVIRONMENT

3.1 Wave Generation

The realistic waves are random and multi-directional. Sometimes, they are the combination of local wind-generated (or sea) waves and swell. A fully developed wave condition is usually modeled in terms of energy spectra which can describe ensembles of regular wave trains combining in random phases. Typically a wind generated random waves have a narrow-banded energy spectra where the statistics of individual wave height can be approximated by Rayleigh distribution.

$$S(\omega,\theta)=S(\omega)G(\theta) \tag{3.1}$$

where

$S(\omega)$ = frequency energy spectrum,

$G(\theta)$ = Spreading function,

ω = incident wave frequency,

θ = incident wave direction.

Traditionally, ocean waves are simulated by superposing many periodic wave trains (also known as free or linear waves) of different frequencies and amplitudes, advancing in different directions. In the context of linear wave theory, the interactions among these free waves are neglected. If the free-wave components or free waves of an irregular wave field are known, then the corresponding linear solution for the resultant wave elevation and potential can be obtained simply by the superposition of the corresponding solutions for these free waves. The resultant elevation and potential of an irregular wave field, $\eta(x, y, t)$ and $\phi(x, y, z, t)$, is given by

$$\eta = \sum_{n=1}^{N} \sum_{m=1}^{M} a_{nm} \cos \theta_{nm} \tag{3.2}$$

$$\phi = \sum_{n=1}^{N} \sum_{m=1}^{M} \frac{a_{nm} g}{\sigma_n} \frac{\cosh[k_n(z+h)]}{\cosh k_n h} \sin \theta_{nm} \tag{3.3}$$

$$\theta_{nm} = k_n(\cos \chi_{nm} x + \sin \chi_{nm} y) - \sigma_n t + \beta_{nm} \tag{3.4}$$

It is noticed that wave frequency, σ_n, and wavenumber, k_n, are related through the dispersion relation. Without the loss of generality, we define that $\sigma_1 < \sigma_2 < \sigma_3 < ....$, that is, a larger subscript corresponds to a higher frequency. The outer summation in Equation (3.2 & 3.3) is with respect to wave frequency. It is practically truncated at a high frequency, σ_N, known as the cutoff frequency. The choice of a cutoff wave frequency depends on several factors. First, the energy distribution of the represented irregular wave field is insignificant beyond the cutoff frequency, σ_N. Secondly, if the wave elevation is computed based on the measurements of other wave properties, then the measured wave energy up to the cutoff frequency must be reliable. That is, below the cutoff frequency, the ratio of signal to noises in the measurements must be significant enough. Finally, it is also limited by the Nyquist frequency or sampling rate of the measurements to avoid 'aliasing' (Oppenheim and Schafer 1975). The inner summation in Equation (3.2 & 3.3) is with respect to wave direction. The choice of *M* depends on the resolution of wave direction, which is equal to $\Delta\theta = 2\pi / M$. The inner summation indicates there exist several wave trains of the same frequency but in different directions. These wave trains may form a partial standing wave pattern and consequently the related resultant wave amplitude at this frequency is no longer uniform in the *x*-*y* plane. To avoid non-uniformity, it was suggested that the inner summation be eliminated and the representation of irregular wave elevation reduces to,

$$\eta = \sum_{n=1}^{N} a_n \cos\theta_n \tag{3.5}$$

where $\theta_n = k_n(\cos\chi_n x + \sin\chi_n y) - \sigma_n t - \beta_n$

In Equation (3.5), we assume that at each discrete frequency there is only one wave train advancing at certain direction angle χ_n. However, wave trains of different frequencies likely advance in different directions. That is, $\chi_m \neq \chi_n$, if $m \neq n$. Increment of frequency should be much smaller in a single summation simulation model than that in a double summation model, say $m\Delta f_s = \Delta f_d$, where *m* is an integer number and larger than one. Hence, in a single summation model there are several (*m)* free waves with slightly different frequencies near by each discrete frequency in the corresponding double summation model. These free waves of slightly different frequencies may advances in different directions so that the directional spreading can be approximately represented as in a double summation simulation. In the absence of significant wave reflection, a single summation model seems to be able to represent the directional spreading of ocean waves adequately.

When all free waves constituting an irregular wave field advance in the same direction, say in the *x*-direction, it is known as uni-directional or long-crested irregular wave train. Its elevation is expressed by,

$$\eta = \sum_{n=1}^{N} a_n \cos\theta_n \tag{3.6}$$

where

$\theta_n = k_n x - \sigma_n t - \beta_n$,

The resultant wave potential and consequently resultant wave properties, such as wave pressure, velocities and accelerations, can be obtained by the superposition of those of free waves.

The information of free waves constituting an irregular wave field can be obtained in two different ways. The free waves can be retrieved by decomposing an irregular wave field based on its measurements, which will be described in the next section. They also can be determined by frequency spectra, such as Pierson-Moskowitz (PM) spectrum (Pierson and Moskowitz, 1964) and JONSWAP spectrum (Hasselmann et al., 1973). A frequency spectrum describes wave energy density as a function of wave frequency. In a PM spectrum,

$$S_{pm}(f) = \frac{\alpha g^2}{(2\pi)^4 f^5} \exp\left[-\frac{5}{4}\left(\frac{f}{f_p}\right)^{-4} \right] \tag{3.7}$$

where α is a constant depending on wind velocity, g the gravitational acceleration, f is wave frequency in terms of *Hz* and f_p the frequency where the spectral peak is located. In a JONSAPW spectrum,

$$S_{JONSWAP}(f) = \frac{\alpha g^2}{(2\pi)^4 f^5} \exp\left[-\frac{5}{4}\left(\frac{f}{f_p}\right)^{-4} \right] \gamma^d \tag{3.8}$$

$$d = \exp\left[-\frac{(f - f_p)^2}{2\sigma^2 f_p^2} \right]$$

$$\sigma = \begin{cases} 0.07 & \text{for } f \le f_p \\ 0.09 & \text{for } f > f_p \end{cases}$$

where γ is known as the peak-shape parameter, representing the ratio of the maximum spectral energy density to the maximum of the corresponding PM spectrum. The term, γ^d, is known as the peak enhancement factor. In essence, Equation (3.8) shows a JONSWAP spectrum is the product of the corresponding PM spectrum and the peak enhancement factor. Based on ocean wave measurements, γ is assumed to be a random variable of a normal distribution with a mean 3.30 and the variance 0.62 (Ochi 1979). In addition to these two well-known frequency spectra, there are many other frequency spectra proposed for various ocean waves. A summary of these spectra can be found in Goda (1990) and Ochi (1998).

To simulate irregular waves, a frequency spectrum in an analytic form is first discretized using a uniform frequency increment Δf . The non-repeatable duration of the simulated wave elevation is hence equal to $1/\Delta f$. Thus for longer time simulation, a smaller Δf or non-uniform frequency increments should be adopted. Energy density at a discrete frequency $f_n = n\Delta f$ is related to a frequency spectrum through,

$$S_n = S(f_n)\Delta f \tag{3.9}$$

In the case of uni-directional irregular waves or directional irregular waves simulated by a single summation model, the amplitude at frequency f_n is equal to,

$$A_n = \sqrt{2S(f_n)\Delta f} \tag{3.10}$$

The initial phases of free waves are randomly selected between 0 to 2π . For a uni-directional wave train, the resultant elevation and potential can be obtained by superposing the corresponding values of all free waves. For a directional irregular wave field simulated by a single summation model, the directions of free waves at discrete frequency must be specified. The selection of the directions of free waves is similar to that described below.

Wave spreading about the main direction at a discrete frequency has been proposed by many different spreading models. Among them, the spreading function of $\cos^{2s}\chi$ type, also known as Mitsuyasu-type, is widely adopted in wave simulation, which is briefly described below.

$$G(f,\chi) = G_0 \cos^{2s}\left(\frac{\chi - \chi_0}{2}\right) \tag{3.11}$$

where χ is the wave direction and χ_0 the main wave direction at frequency *f*; *s* a parameter for adjusting direction spreading; G_0 a constant which ensures the integration of the spreading function with respect to the wave direction is equal to unit.

$$\int_{-\pi}^{\pi} G(f,\chi)d\chi = 1 \tag{3.12}$$

The parameter, *s*, varies with respect to the frequency. Mitsuyasu at al. (1975) suggested the following formula for wind waves.

$$s = \begin{cases} s_0(f/f_p)^5 & f \le f_p \\ s_0(f/f_p)^{-2.5} & f > f_p \end{cases} \tag{3.13}$$

$$s_0 = 11.5(2\pi f_p U/g)^{-2.5}$$

where *U* is the wind velocity. In order to apply the spreading function other than wind waves, Goda (1985) proposed $s_0 = 10$ for wind waves, $s_0 = 25$ for swell of short decay distance and $s_0 = 75$ for swell of long decay distance. Using Equations (3.9) and (3.11), the energy density and amplitude of a wave component of discrete frequency f_n and direction angle χ_{nm} can be determined by,

$$S_{n,m} = S_n G(f_n, \chi_{nm})\Delta\chi \tag{3.14}$$

$$\Delta\chi = 2\pi/M, \qquad \text{and} \qquad \chi_{nm} = m\Delta\chi$$

$$A_{n,m} = \sqrt{2S_{n,m}} \tag{3.15}$$

3.2 Wind Generation

AIP or NPD wind velocity spectrum is used to generate the time varying wind speed, and the wind force and the moment acting on the topside and the hulls above MWL are calculated based on the wind speed. API spectrum is introduced herein, and difference of the method to generate the wind speed is compared.

$$S(f)=\frac{\sigma^2}{f_p\left(1+\frac{1.5}{f_p}f\right)^{5/3}} \tag{3.16}$$

Assuming the spectrum is discretized into N intervals with equal area, and the minimum frequency and the maximum cut-off frequencies are f_0 and f_N, respectively.

Overall area can be calculated as follows.

$$\begin{aligned} A_{ALL} &= \int_{f_0}^{f_N} S(f)\,df = \int_{f_0}^{f_N} \frac{\sigma^2}{f_p\left(1+\frac{1.5}{f_p}f\right)^{5/3}}\,df \\ &= -\sigma^2\left(1+\frac{1.5}{f_p}f\right)^{-2/3}\Bigg|_{f_0}^{f_N} = \sigma^2\left(1+\frac{1.5}{f_p}f_0\right)^{-2/3} - \sigma^2\left(1+\frac{1.5}{f_p}f_N\right)^{-2/3} \end{aligned} \tag{3.17}$$

The area up to n-th frequency f_n is:

$$A_n = -\sigma^2\left(1+\frac{1.5}{f_p}f\right)^{-2/3}\Bigg|_{f_0}^{f_n} = \sigma^2\left(1+\frac{1.5}{f_p}f_0\right)^{-2/3} - \sigma^2\left(1+\frac{1.5}{f_p}f_n\right)^{-2/3} \tag{3.18}$$

The area up to n-th frequency f_n is n/N times the total area, i.e.

$$A_n = n / N \cdot A_{ALL} \tag{3.19}$$

Substituting equation (3.17) and (3.18) into equation (3.19) gives f_n as:

$$f_n = \frac{f_p}{1.5}\left(A^{-3/2} - 1\right) \tag{3.20}$$

where

$$A = \left(1 - \frac{n}{N}\right)\left(1 + \frac{1.5}{f_p} f_0\right)^{-2/3} + \frac{n}{N}\left(1 + \frac{1.5}{f_p} f_N\right)^{-2/3} .$$

The frequency interval is calculated by:

$$df_n = f_n - f_{n-1} \tag{3.21}$$

The frequency representing each interval is taken at the middle of the interval.

$$\bar{f}_n = \frac{1}{2}\left(f_{n-1} + f_n\right) \tag{3.22}$$

The amplitude of the wind velocity component at the n-th frequency is

$$a_n = \sqrt{2S\left(f_n\right) df_n} \tag{3.23}$$

Thus, the amplitude of each velocity component becomes uniform if the equal area method is used, which improves the wind force generation scheme currently using the uniform period interval method.

Figure 3.1 shows the amplitude distribution by the uniform period interval method. Figure 3.2 shows the amplitude distribution by the equal area method, which shows the uniform amplitude. Figure 3.3 through Figure 3.4 show the time signal of the wind velocity and the spectrum regenerated. The spectrum measured matches well in the low frequency region, but some errors in the high frequency region. Figure 3.5 through

Figure 3.7 show the improved results by the equal area method. It is shown that the equal area method shows better agreement in the high frequency region.

Conclusively, the equal area method improved the statistics of the wind velocity by giving more frequencies to the high frequency region and by keeping the frequencies clustered in the low frequency region.

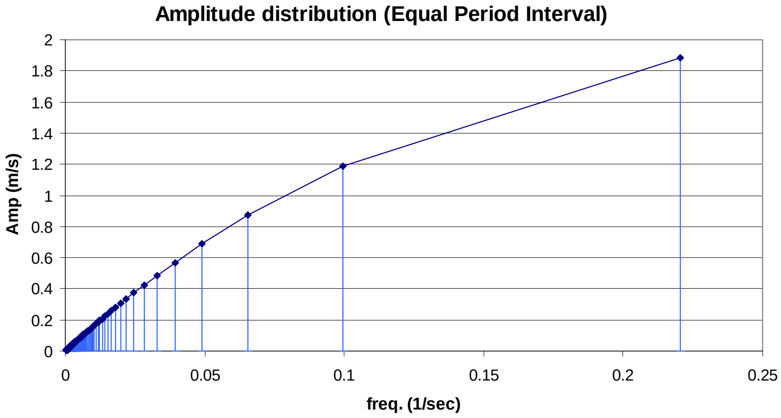

Figure 3.1 Amplitude Distribution for Uniform Period Interval Method

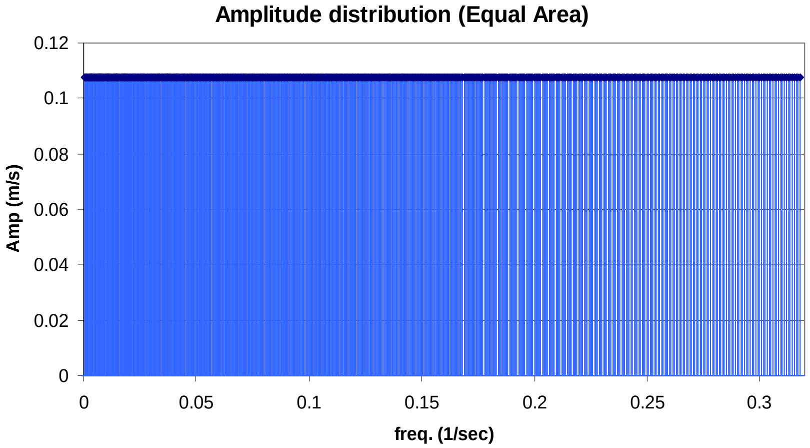

Figure 3.2 Amplitude Distribution for Equal Area Method

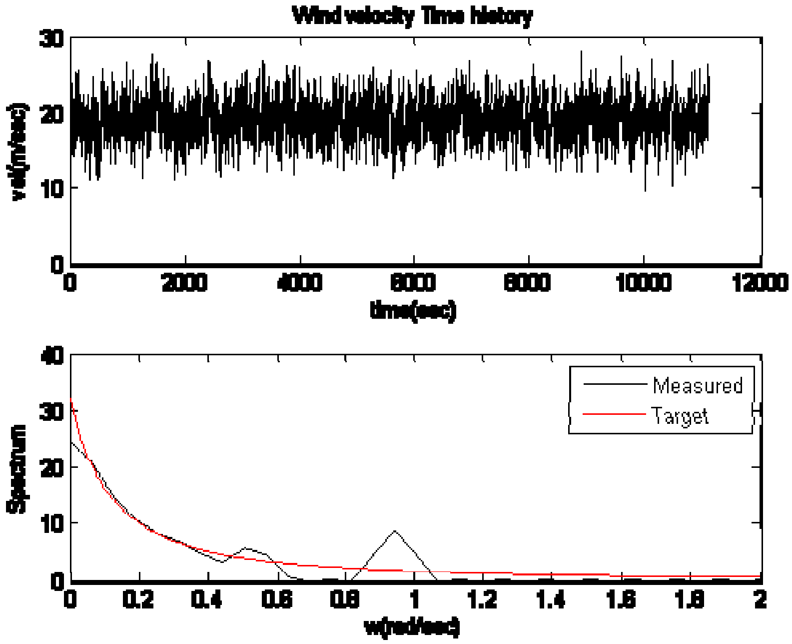

Figure 3.3 Wind Spectrum Regeneration by the Uniform Period Interval (V10=19m/sec, Wind Speed at z=24.782m above MWL, alpha=0.025)

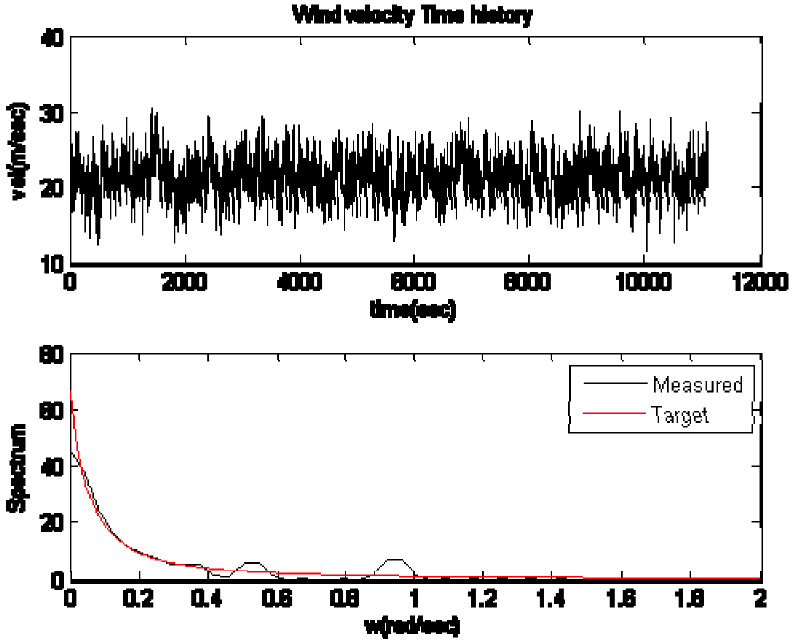

Figure 3.4 Wind Spectrum Regeneration by the Uniform Period Interval (V10=19m/sec, Wind Speed at z=10.m above MWL, alpha=0.025)

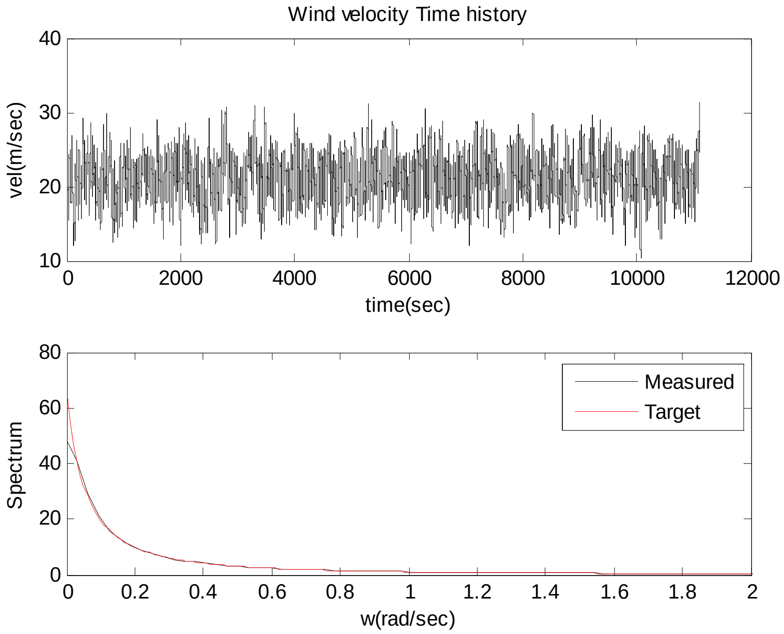

Figure 3.5 Wind Spectrum Regeneration by the Equal Area Method (V10=19m/sec, Wind Speed at z=23 m above MWL and alpha=0.025)

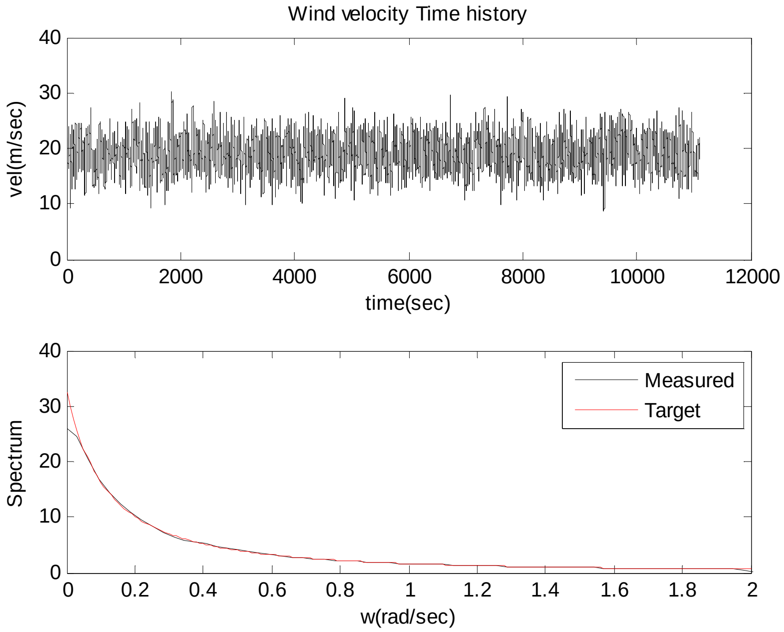

Figure 3.6 Wind Spectrum Regeneration by the Equal Area Method (V10=19m/sec, Wind Speed at z=10 m above MWL and alpha=0.025)

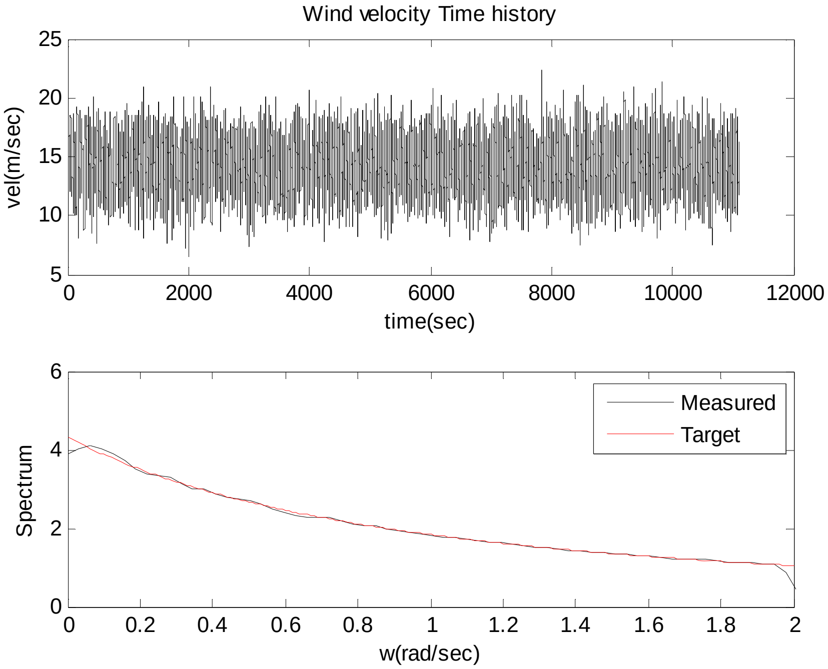

Figure 3.7 V=19m/sec, Wind Speed at z=1 m above MWL and alpha=0.025

4. CASE STUDY 1: HYDRO-PNEUMATIC TENSIONER MODEL FOR SPAR GLOBAL PERFORMANCE ANALYSIS

4.1 Introduction

The new FE model of the nonlinear tensioner coupling the riser and the hull motion is introduced herein. The model is implemented in the Charm3D(Ran et al, 1997 & 1999), a fully coupled time/frequency domain analysis program of floating bodies and mooring lines/risers.

WAMIT(Lee et al., 1999), a diffraction/radiation program, was utilized to calculate the frequency dependent hydrodynamic coefficients and the first-order wave excitation forces. The corresponding forces are converted to the time domain using two-term Volterra series expansion in Charm3D. The frequency-dependent radiation damping was included in the form of convolution integral in the time domain simulation. Viscous forces are included through the Morison drag elements.

A typical Spar in GoM with 9 mooring lines and 8 TTRs(top tension risers) is selected for the analysis. The results are compared with the conventional linear spring-dashpot model to show the significant difference in motion and the riser tension.

4.2 Principal Dimensions of Spar System

The principal dimensions of the Spar hull are shown in Table 4.1. The hard tank diameter is 94ft and the draft at the intact condition is 163.4 m (536 ft). It has 12.8 m (42 ft) by 12.8 m (42 ft) rectangular center wells at the hard tank and soft tank.

The chain-wire-chain mooring system is used, the properties of which are shown in Table 4.2. W_{wet} is the weight per unit length in the water, W_{dry} the weight per unit length in the air, and EA and EI are axial and bending stiffness, respectively. D is the nominal outer diameter, and C_i and C_d are, respectively, inertia and drag coefficients. The riser properties are in Table 4.3. The outer diameter of the riser is 0.34 m (1.1146 ft), and the top tension is 535.2 tonnes (1180 kips). A total of 8 risers are attached to the Spar hull at the top of the hull.

Table 4.1 Principals of Spar Hull

Topsides	
Topsides Payload (MT) (100-yr Hurricane)	8,243
Topsides VCG (m above MWL)	35.9
Topsides Wind Area (m^2)	2,921
Topsides CP (m above MWL)	36.5
Hull Dimensions	
Draft (m)	163.4
Hard Tank Diameter (m)	28.6
Hard Tank Length (m)	68.9
Center Well Size (m × m)	12.8 × 12.8
Keel Tank Side Length (m)	28.6
Keel Tank Height (m)	12.2
Keel Tank Center Well Size (m × m)	12.8 × 12.8
Weight	
Normal Total Weight (MT)	41772.7
Vertical CG (m, below MWL)	68.9
TTR/Mooring Vertical Force (MT)	5,986
Nominal Total Buoyancy (MT)	47,759
Vertical CB (m below MWL)	57.9

Table 4.2 Principals of Mooring Line System

	Fairlead Cain	Wire Rope	Anchor Chain
Length (m)	209.1	1377.6	106.7
W_{wet}(kg/m)	385.3	80.1	385.3
W_{dry}(kg/m)	445.8	88.6	445.8
EA(kN)	8.05E+05	1.64E+06	8.05E+05
EI (kN-m)	0	0	0
D (m)	0.146	0.133	0.146
C_i	2.1	2	2.1
C_d	2.4	1.3	2.4

Table 4.3 Principals of Riser

Top Pretension (kN)	5248.9
W_{wet} (kg/m)	320.0
W_{dry} (kg/m)	547.7
EA (kN)	5.52E+06
EI (kN-m^2)	5.91E+04
D (m)	0.340
C_i	2.1
C_d	2.4

4.3 Numerical Model

The added mass and radiation damping coefficients, first-order wave excitation forces are calculated by the diffraction/ radiation program, WAMIT. All the hydrodynamic coefficients are calculated in the frequency domain, and the corresponding forces are converted to the time domain using two-term Volterra series expansion. The frequency-dependent radiation damping is included in the form of a convolution integral in the time domain simulation.

Figure 4.1 shows the panel configuration for the WAMIT. The body fixed coordinate reference is on the free surface at the centroid of water plane area of the hard tank. The x-axis is parallel to the platform north, and the z-axis is upward positive. The Spar hull is discretized by 691 panels.

Figure 4.2 shows the global configuration of the platform and mooring/riser coupled system. The water depth is 914 m (3000 ft), and the 9 mooring lines are attached to the hull and anchored to the sea bed. The 8 TTRs are coupled with hull by a numerical pneumatic tensioner model.

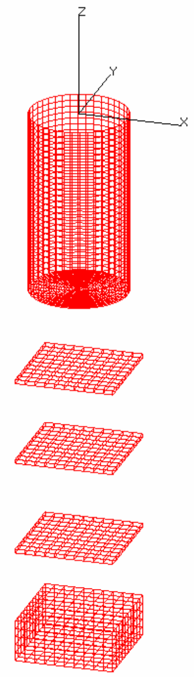

Figure 4.1 Panel for Hydrodynamic Calculation – Total 691 Panels Used

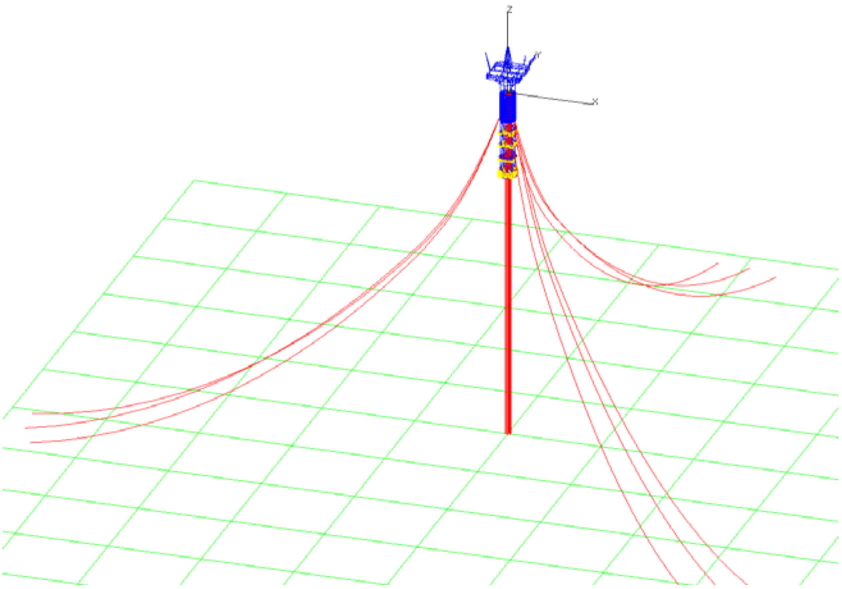

Figure 4.2 Fully Coupled Spar and Mooring/Riser Model

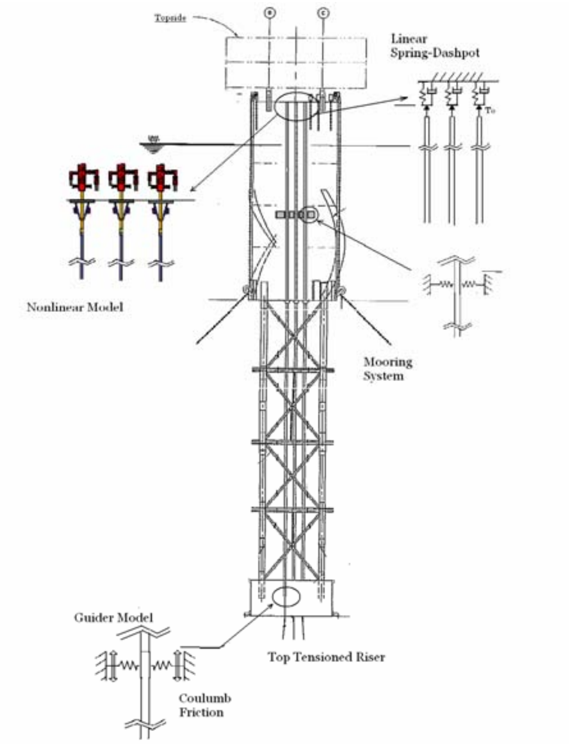

Figure 4.3 Configuration of Pneumatic Tensioner and Keel Guide Model

4.4 Validation of the Model

The numerical model is validated by carrying out preliminary static and dynamic test. Static heave tests for linear and nonlinear model are used to check the spring effects. A static force is applied in the range between -44,482.2 kN and 44,482.2 kN (10,000 Kips). The corresponding heave, stroke and riser tension are measured, which are plotted in Figure 4.4 and Figure 4.5. In Figure 4.4, the heave and vertical force curve of the nonlinear model shows the nonlinearity affected by the tensioner, while the linear model has linear relation between them. In Figure 4.5, the stroke and the riser tension curves for both linear and nonlinear models are recovered and are identical to the original curves.

In Figure 4.6, the free decay test with only one TTR and without radiation and the viscous damping shows the difference between the stick-slip and slip-only cases. The stick-slip occurs at the keel joint and the guide of the TTR. The dynamic friction factor is assumed to be 0.3 for both models, and the static friction factor is set 0.5 for stick-slip model. The preload of 177.93 kN (40 kips) between the riser and guide is applied to give the normal reaction force. The stick-slip model shows the oscillation with constant amplitude after the riser sticks to the keel joint because the friction damping disappears after it sticks and there is no other damping mechanism assumed. However, in the slip-only model, the heave decays off by the friction damping without sticking. The heave natural period decreases slightly because the TTR stiffness is also added to the system stiffness.

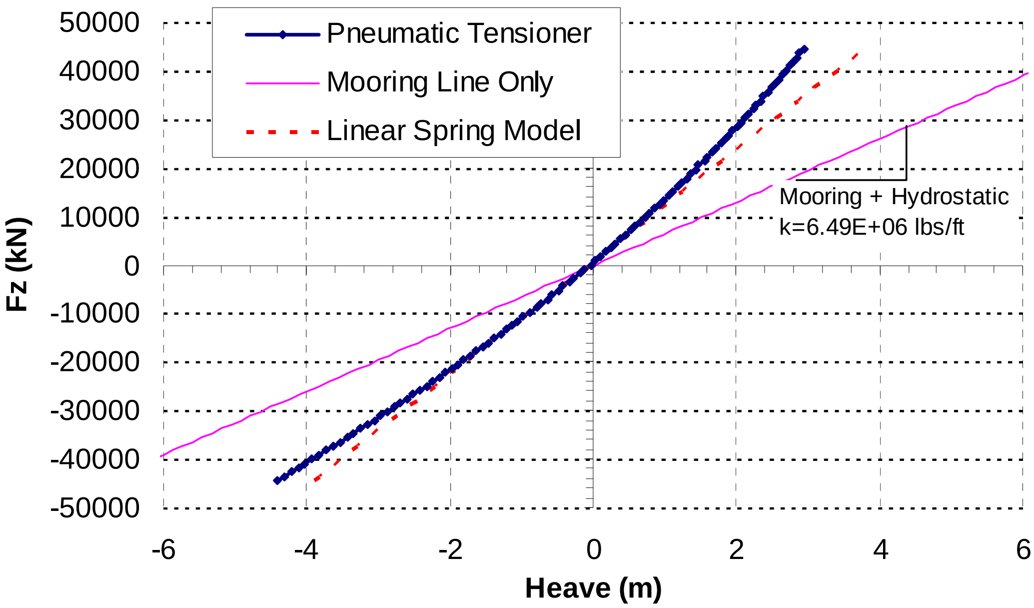

Figure 4.4 Static Vertical Force and Heave Relation for Linear and Nonlinear Model Obtained from the Static Heave Test

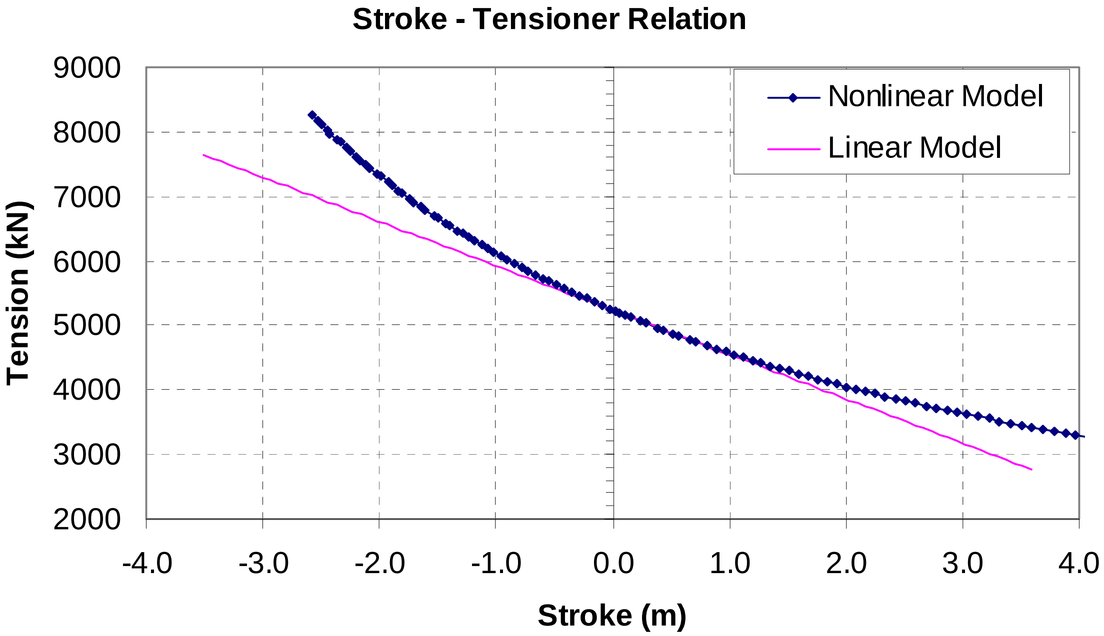

Figure 4.5 Static Tension and the Stroke Relation Obtained from the Static Heave Test

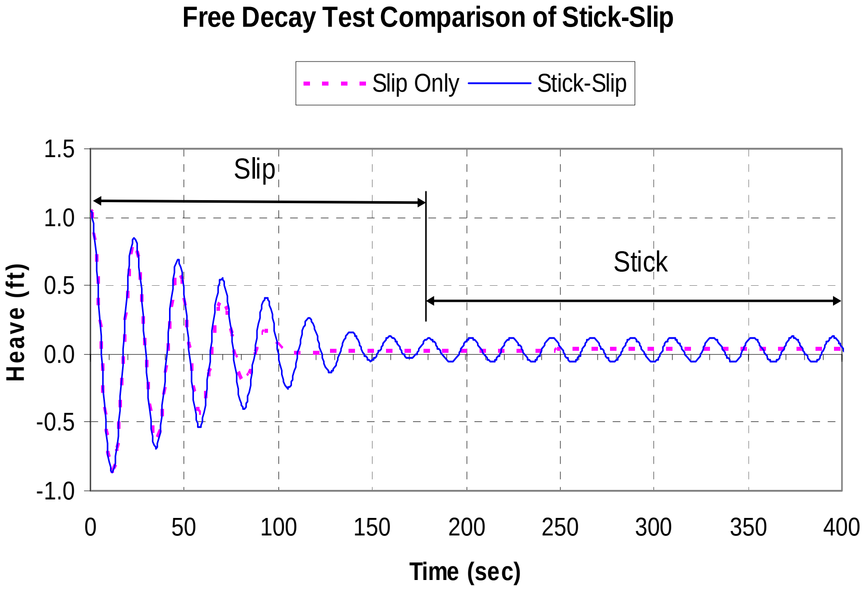

Figure 4.6 Stick-Slip Effect of the Keel Joint Compared with the Slip-Only Case

4.5 Results and Discussion

Prior to time simulation for the hurricane events, heave and pitch free decay tests are carried out to examine the system characteristics and to determine the linear damping ratio. The friction at the keel joint is discarded, but the friction at the tensioner is modeled. Figure 4.7 shows the results of heave free decay. The dotted red line indicates the nonlinear model (μ=0.025, z_0=7.62m=25ft and T_0=5249kN=1180kips), the solid dark blue line is for linear spring model (k_L=757.75kN/m=51.92kips/ft) without a dashpot and the solid light blue line is for a linear spring with a dashpot (C_L=518.1 kN·sec/m=35.5 kips·sec/ft). As the tensioner damping makes a little effect on the pitch motion, only the linear spring without damping is plotted in Figure 4.8. Table 4.4 shows the natural period and the damping ratio for linear model without a dashpot and the nonlinear model for the six degree of freedom. In this case, the linear model without a dashpot does not have the linear damping. Thus, the difference of the damping between the linear model without a dashpot and the nonlinear model is due to the friction at the tensioner and it will be included in the linear model by the dashpot. By adding the linear damping to the linear model with a dashpot, the decay behavior is similar to the nonlinear model. Figure 4.9 shows the damping ratio dependency on the motion amplitude. The linear spring model shows little dependency on the motion amplitude which comes from the radiation damping. However, the nonlinear model shows that it highly depends on the motion amplitude due to the nonlinear damping effects. At some ranges the linear damping and the nonlinear damping match well, but they do not at the other ranges.

Three hour time simulations are carried out in three extreme environmental conditions, such as 10 year, 100 year and 1000 year hurricane events (Refer to Table 4.5). JONSWAP spectrum is used for the irregular wave generation with the given overshooting parameter(γ). The wind speed is the one-hour-averaged value at 10m above MWL, and the API wind spectrum is used for the time varying wind speed generation. Wave, wind and current are collinear and have 0 degree of incident angle. All the properties for the hydro-pneumatic tensioner which is obtained from the free decay test are adopted herein. At the keel joint, the dynamic friction factor of 0.3 and the static friction factor of 0.5 are applied with no preload.

Figure 4.10, Figure 4.11 and Figure 4.12 provide the incident wave time history and their power spectrum for 10 year, 100 year and 1000 year hurricane condition, respectively. The target and the simulated matches very well.

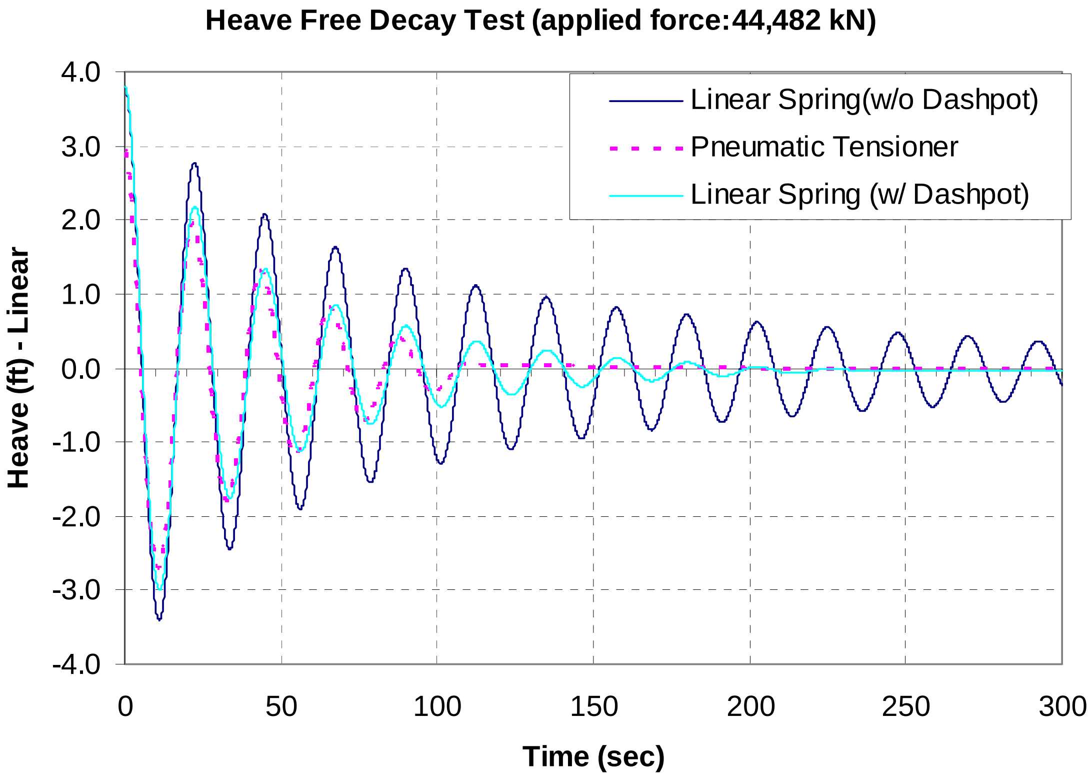

Figure 4.7 Heave Free Decay Time History – Comparison between the Linear Spring Model and the Nonlinear Tensioner Model

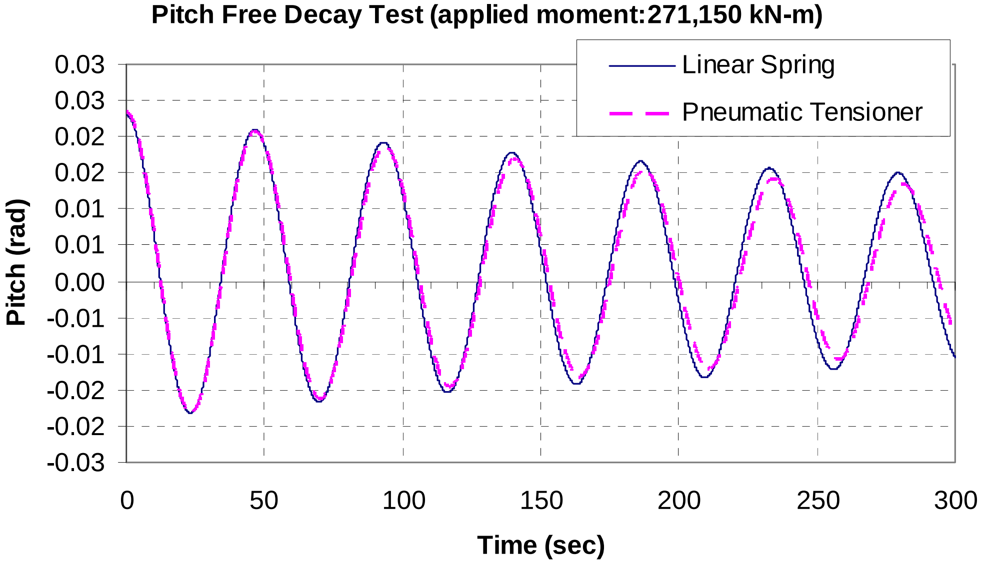

Figure 4.8 Pitch Free Decay Time History – Comparison between the Linear Spring Model and the Nonlinear Tensioner Model

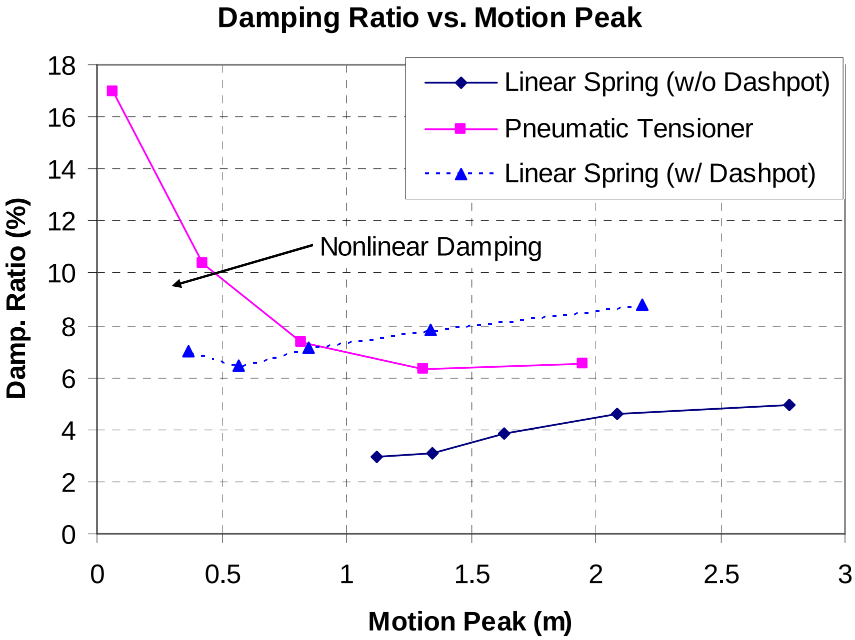

Figure 4.9 Comparison of the Damping Ratio – Linear and Nonlinear Model of the Tensioner

Table 4.4 Natural Period and Damping Ratio (in % Critical Damping)

	Nonlinear		Linear	
	Tn (sec)	Damping	Tn (sec)	Damping
Surge	375.90	11.94%	371.28	11.21%
Sway	377.14	13.33%	382.05	10.80%
Heave	21.79	12.00%	22.42	4.10%
Roll	46.74	3.30%	46.34	3.62%
Pitch	46.45	3.30%	46.34	3.45%
Yaw	140.25	8.25%	136.30	6.11%

Table 4.5 100 Year and 1000 Year Hurricane Events

Return Period	10 year		100 year		1000 year	
Hs (m)	7.59		12.19		15.57	
Tp (sec)	11.9		14		15.6	
Peakedness Parameter	2.4		2.4		3	
Wind Speed (m/sec)	26.18		41.82		45.22	
Current Profile	Depth(m)	V(m/s)	Depth(m)	V(m/s)	Depth(m)	V(m/s)
	0.00	0.79	0.00	1.50	0.00	2.50
	29.99	0.60	29.99	1.15	5.00	2.50
	60.01	0.29	60.01	0.56	24.99	1.19
	90.00	0.10	90.00	0.10	50.02	1.12
	914.36	0.10	914.36	0.10	80.49	0.74
					100.00	0.31
					150.02	0.29
					300.00	0.27
					914.36	0.00

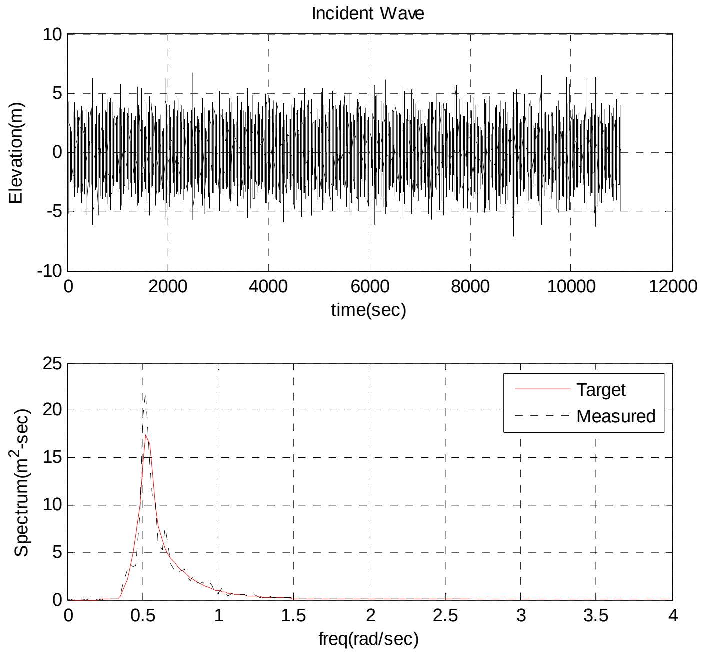

Figure 4.10 Wave Time History and Power Spectrum (10 Year Hurricane)

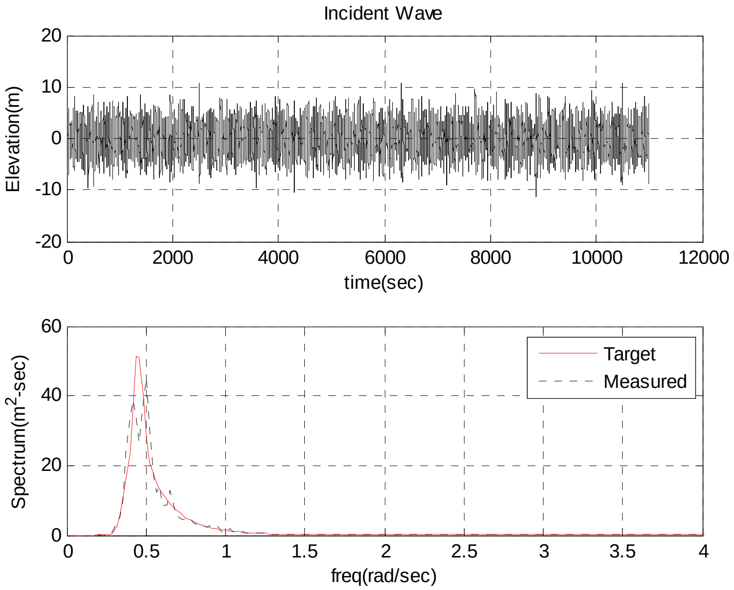

Figure 4.11 Wave Time History and Power Spectrum (100 Year Hurricane)

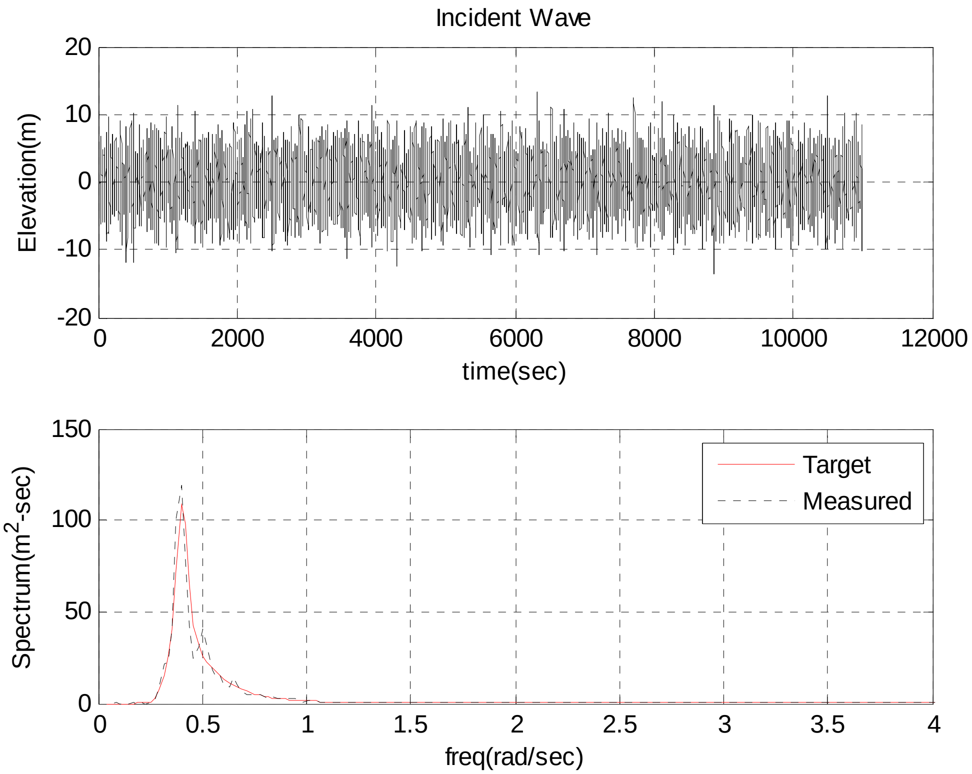

Figure 4.12 Wave Time History and Power Spectrum (1000 Year Hurricane)

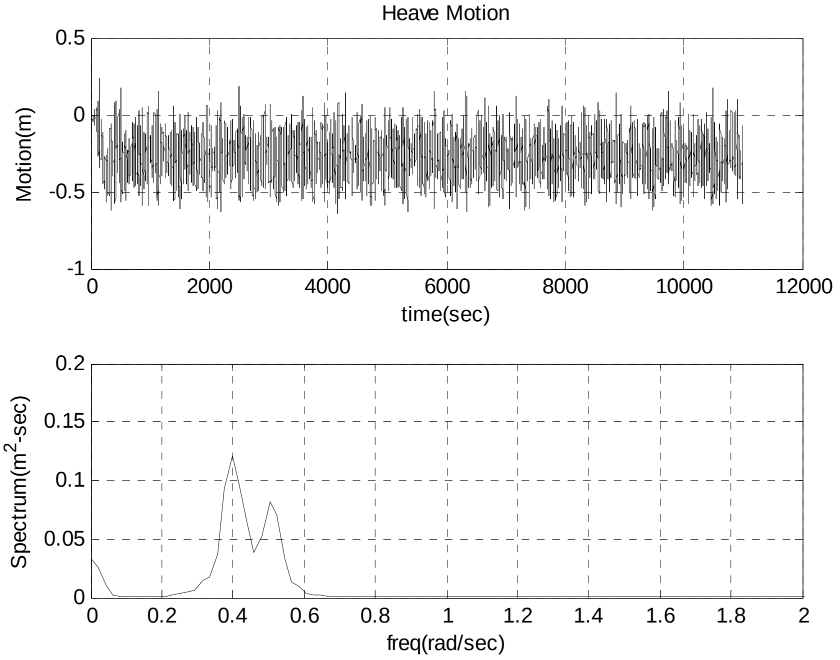

(a) Linear Spring Model

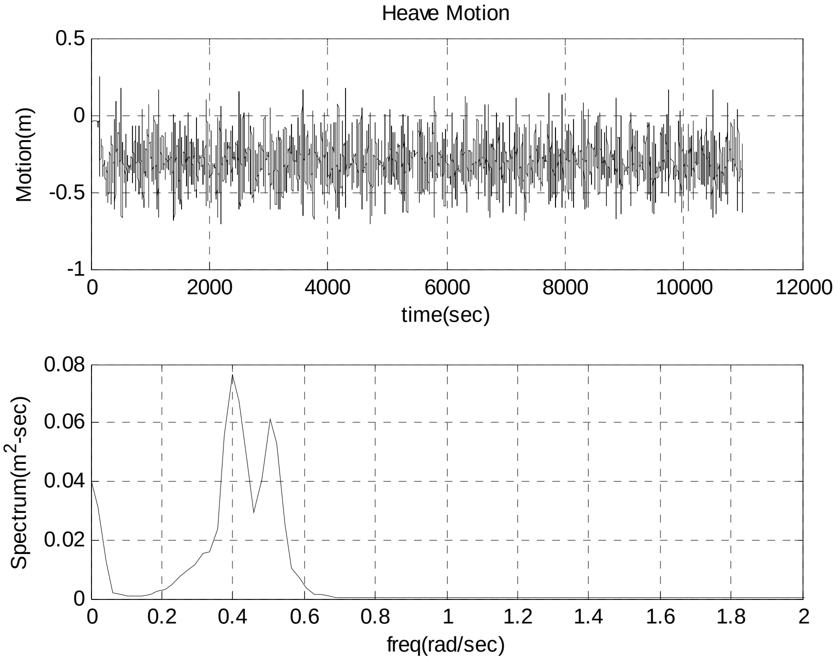

(b) Nonlinear Pneumatic Tensioner Model

Figure 4.13 Heave Motion for 10 Year Hurricane

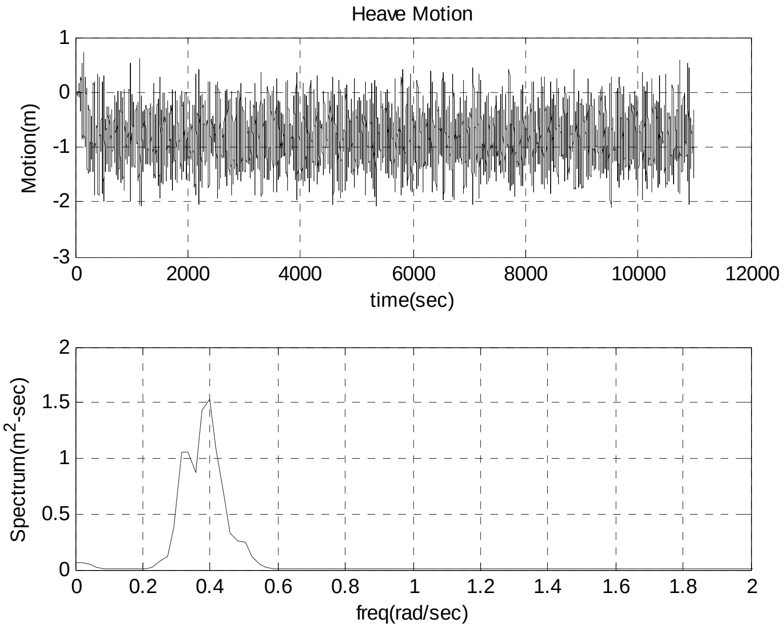

(a) Linear Spring Model

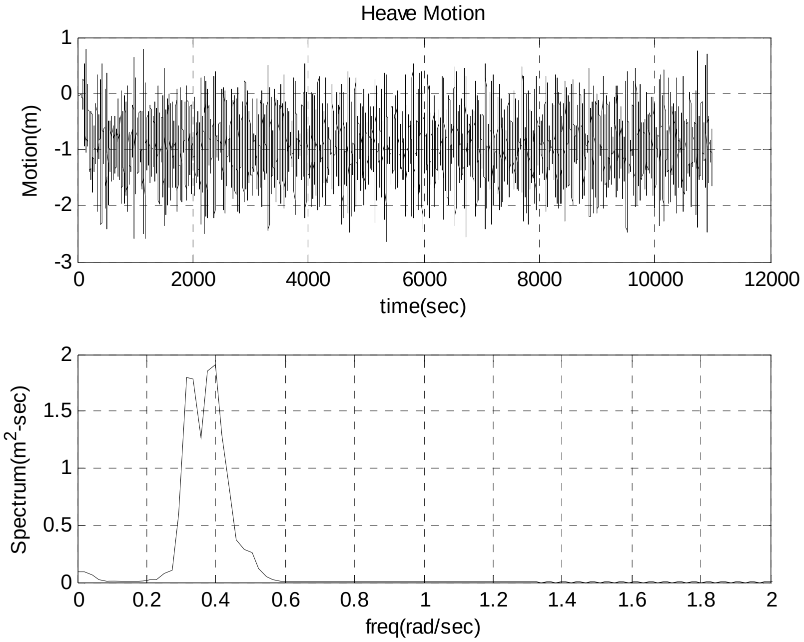

(b) Nonlinear Pneumatic Tensioner Model

Figure 4.14 Heave Motion for 100 Year Hurricane

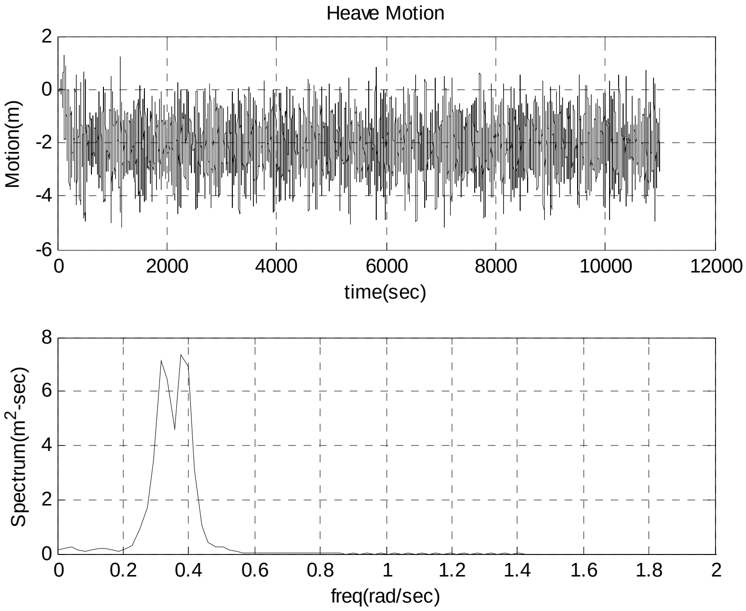

(a)Linear Spring Model

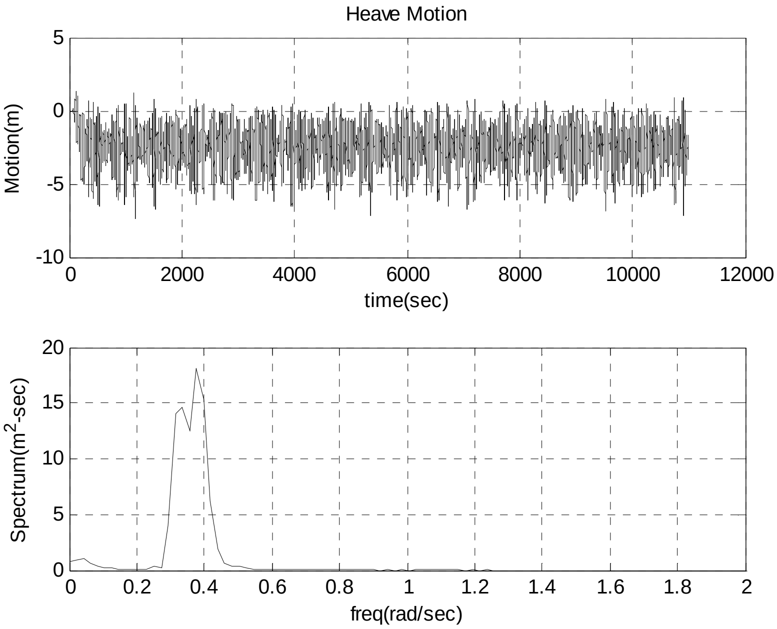

(b) Nonlinear Pneumatic Tensioner

Figure 4.15 Heave Motion for 1000 Year Hurricane

Figure 4.13, Figure 4.14 and Figure 4.15 show the heave motion time history and its spectrum for 10 year, 100 year and 1000 year hurricane conditions. The spectrums show peaks at the range of wave period, and some energy at the low frequency region due to the wind and the slowly varying wave force. The magnitude of the spectrum of linear spring model is larger than the nonlinear model for 10 year condition, but for the other conditions, the nonlinear model has larger energy than the linear model.

The statistics of the surge, heave and pitch motion for the environmental conditions are depicted in Figure 4.16 through Figure 4.18. The surge motions are not affected by the nonlinearity of the tensioner stiffness and the damping, and the offset of linear and nonlinear model for all the environmental condition show almost identical numbers. The heave standard deviation and mean with nonlinear tensioner model are larger than that with linear spring model because the nonlinear spring becomes stiffer as due to the pull down of riser by horizontal offset, and the heave natural period become closer to the wave period. However, such mild environment as 10 year hurricane condition would not be affected by the nonlinearity of the spring, and even the rms of heave of nonlinear model is smaller than the linear model.

The heave rms of the linear model is 14 % and 30 % lower than nonlinear model, respectively, for 100 year and 1000 year hurricane. The mean values are also different by 10.5%, 12 % and 18 % between the nonlinear and the linear model for the 10 year, 100 year and the 1000 year hurricane conditions, respectively. The nonlinearity of the tensioner stiffness has a significant effect on the heave motion and mean set-down, especially for the harsh environmental condition, which the linear model cannot predict.

The pitch motion statistics also shows some differences within 10 % due to the coupled effect of heave and the pitch stiffness change caused by the tensioner stiffness change in nonlinear model. The pitch motion is less dependent on the tensioner model. The maximum pitch angles for 100 year hurricane are 6.74 degrees and 7.04 degrees, respectively, for the linear and nonlinear model both of which are within the range of 10 degrees.

In Figure 4.19, the sensitivity of the heave motion difference to the environmental harshness is investigated. The rms of heave increases as the environment become severe and the maximum heave range also show the same trend, and it becomes 25% difference between the linear and nonlinear model for 1000 year condition.

The linear and nonlinear tensioner stroke time histories for 1000 year hurricane event are plotted in Figure 4.20. The stroke is defined as (riser top node motion)-(body motion), and it has similar magnitude and opposite sign to the heave. However, the exception is when it exceeds the stroke limit. The nonlinear stroke has its limits in down (z_{down}) and up (z_{up}), and they are, respectively, set -12.5 ft and 12.5 ft. Thus, the nonlinear stroke does not exceed the limit (Figure 4.20-(b)), but the linear stroke becomes about -16.54 ft (Figure 4.20-(a)) for 1000 year hurricane event.

Figure 4.21, Figure 4.22 and Figure 4.23 compare the heave motion spectrum and the stroke spectrum of linear and the nonlinear model for 10 year, 100 year and 1000 year condition. The solid lines without the symbol present the incident wave spectrum for each environment. The heave motion spectrum and the stroke spectrum within the wave frequency region show similar shape, but the stroke spectrum is smaller than the heave motion spectrum because the riser itself absorbs the strain energy and the friction force at the keel joint may reduce the relative motion between riser and the hull, which results in the reduction of the stroke compared with the hull heave motion. There is captured a low frequency region stroke around 23-25 seconds which seems to be due to the difference frequency wave force effect. At larger than 30 seconds, the energy at the stroke spectrum is seen for 10 year hurricane condition which is due to the wind induced horizontal and heeling motion. However, for 100 year and 1000 year, the wave induced stroke is dominant and the wind driven stroke at the low frequency is very small. Thus, the wind and current driven stroke is mostly applied to the mean stroke for this case.

The stroke statistics for 10 year, 100 year hurricane as well as for 1000 year hurricane are shown in Figure 4.24. It is also shown that the linear model has the stroke of lower standard deviation than the nonlinear model by 9 % for 100 year hurricane and 24 % for 1000 year hurricane event.

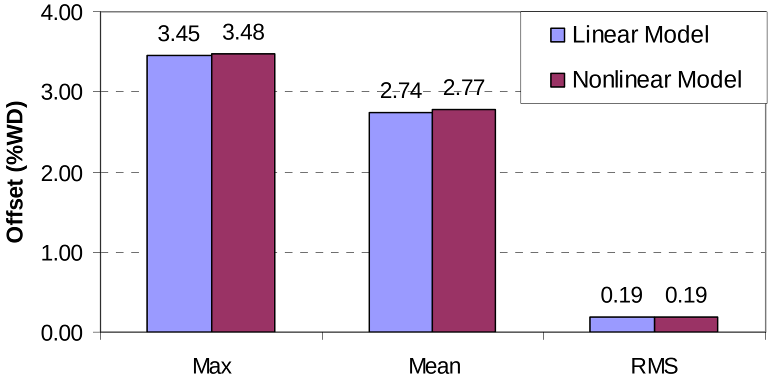

(a) Offset (%WD)

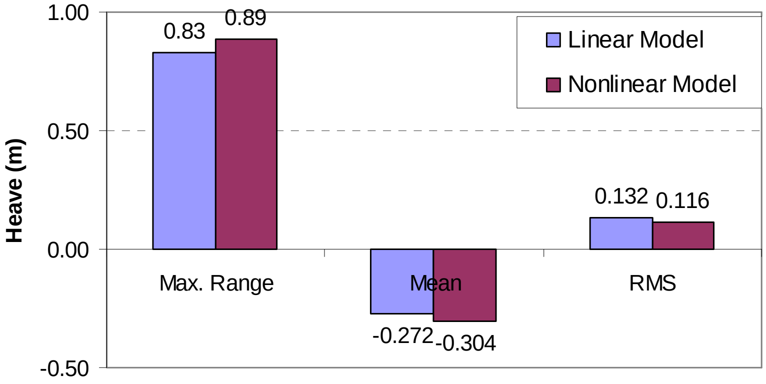

(b) Heave (in m)

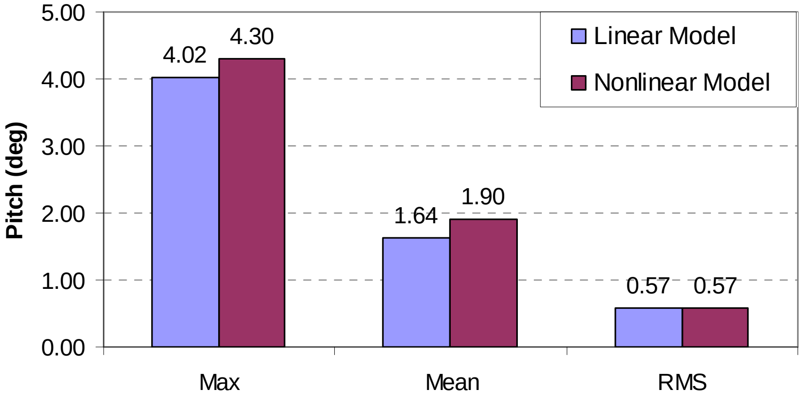

(c) Pitch (in degree)

Figure 4.16 Motion Statistics for 10 Year Hurricane

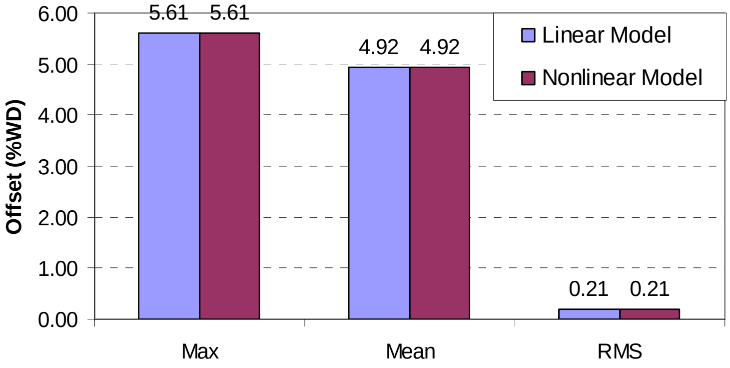

(a) Offset (%WD)

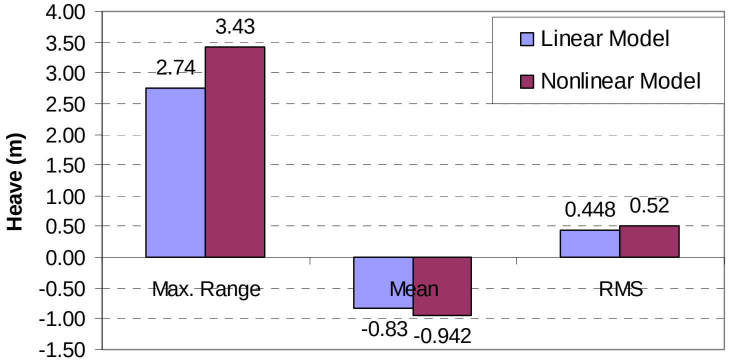

(b) Heave (m)

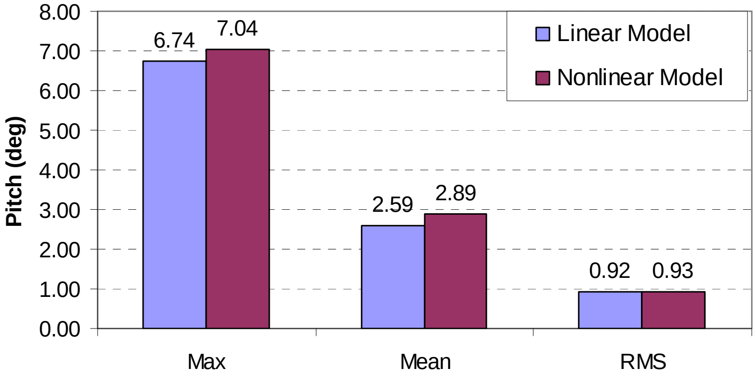

(c) Pitch (in degree)

Figure 4.17 Motion Statistics for 100 Year Hurricane

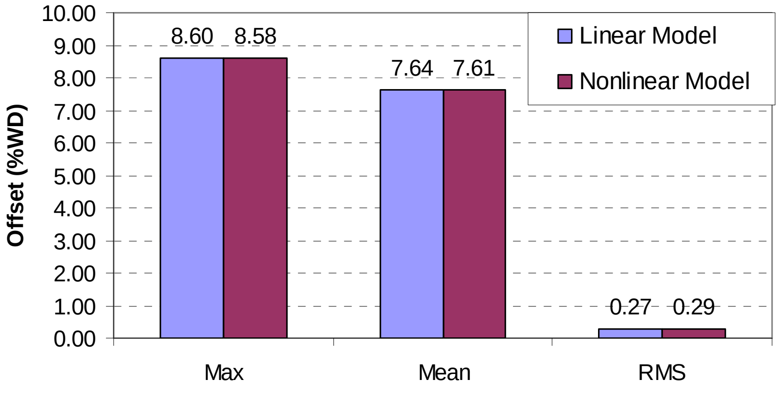

(a) Offset (%WD)

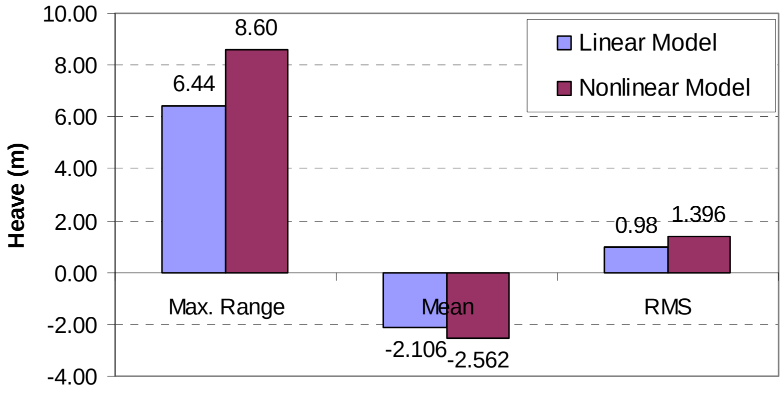

(b) Heave (m)

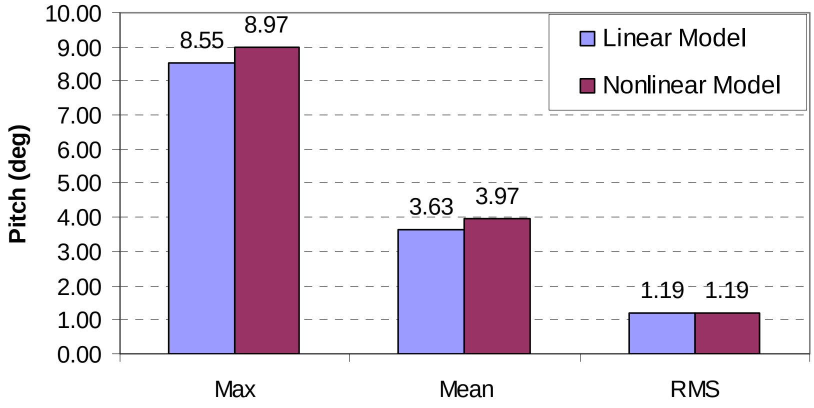

(c) Pitch (in Degree)

Figure 4.18 Motion Statistics for 1000 Year Hurricane

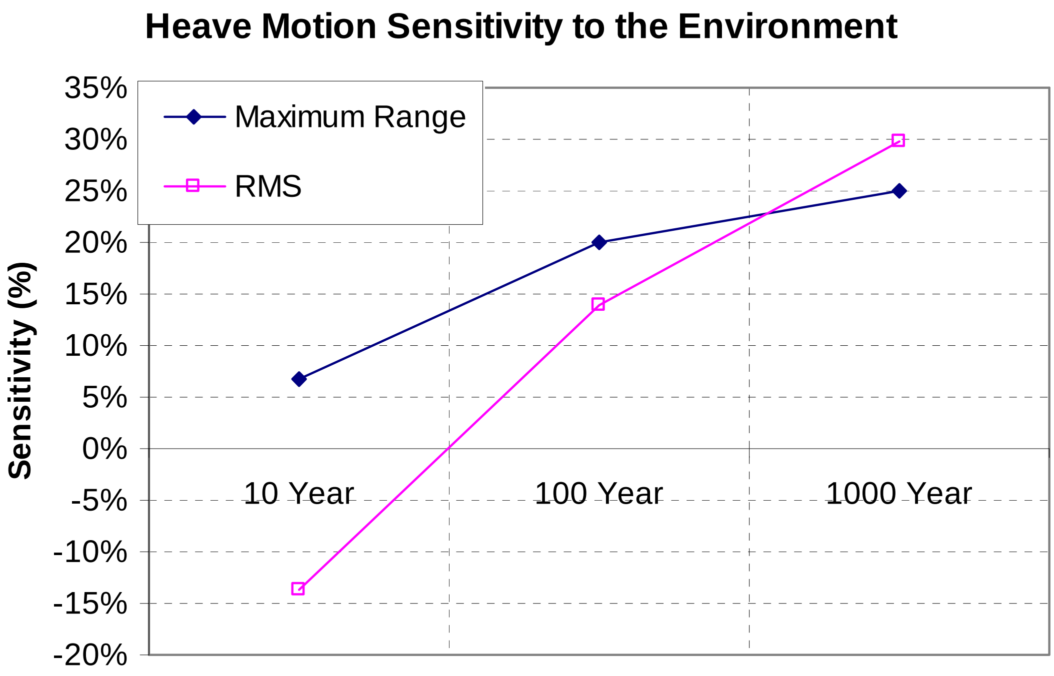

Figure 4.19 Sensitivity of the Heave Motion to the Environment Dependent on the Tensioner Model

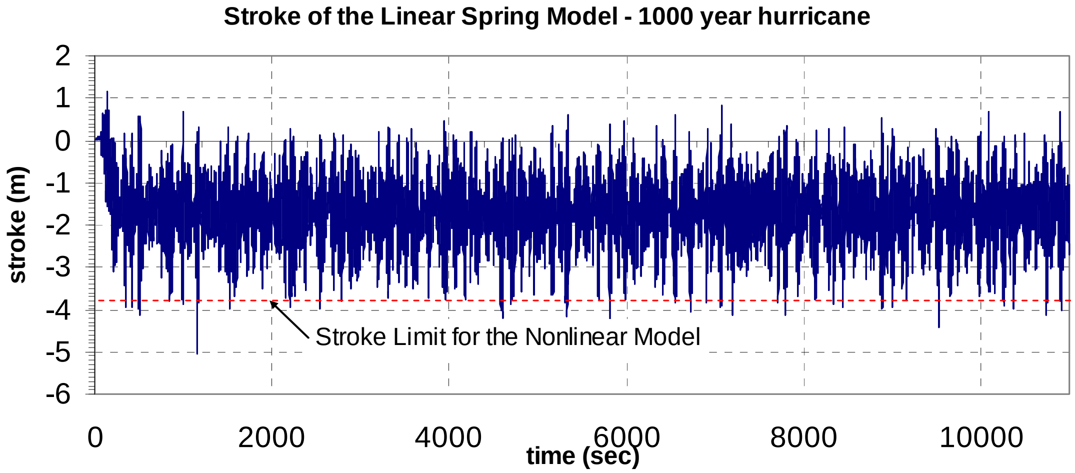

(a) Linear Spring-Dashpot Model

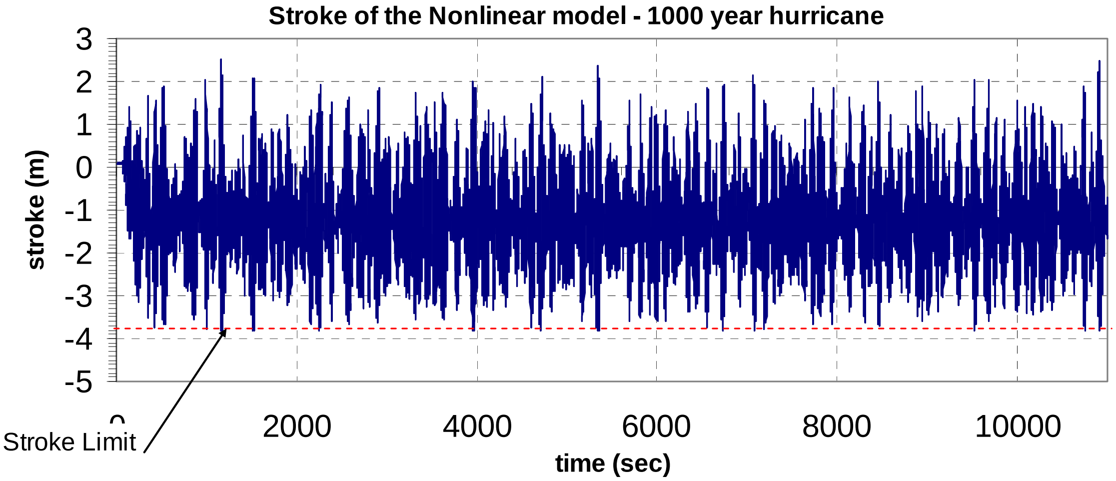

(b) Nonlinear Model

Figure 4.20 Time History of Stroke of the Piston – Upstroke Positive

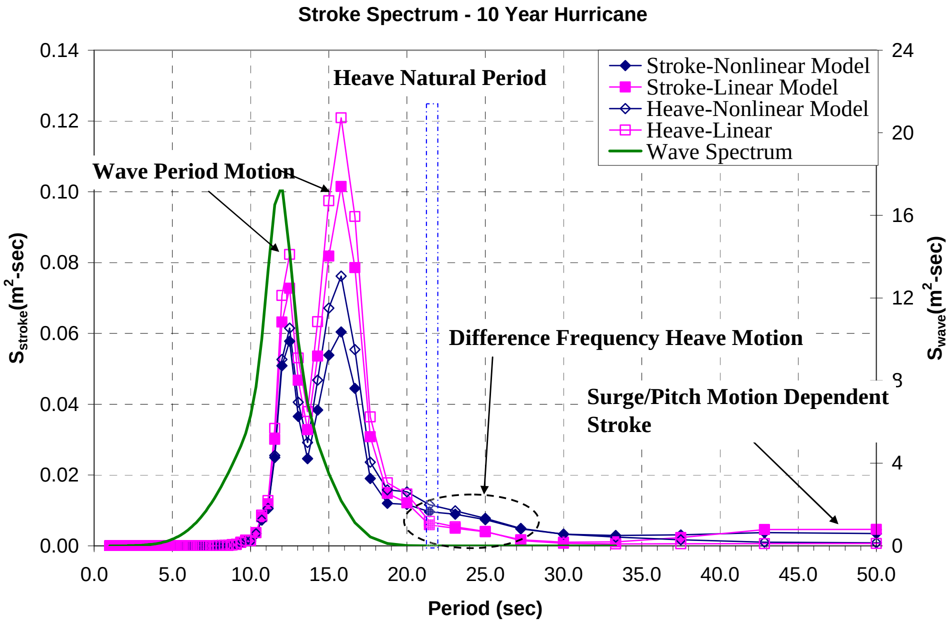

Figure 4.21 Heave Motion and Stroke Spectrum with the Wave Power Spectrum – 10 Year Hurricane

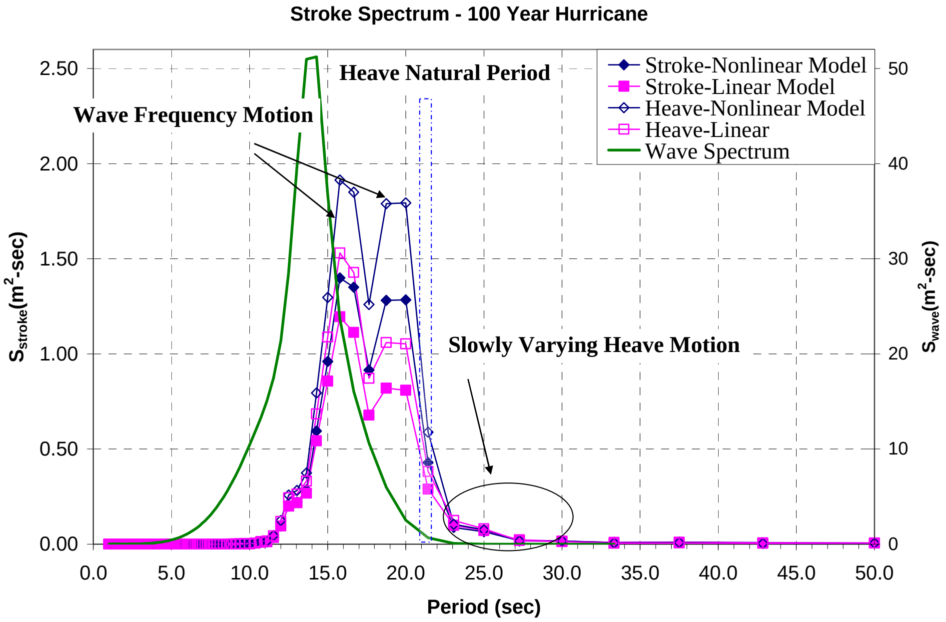

Figure 4.22 Heave Motion and Stroke Spectrum with the Wave Power Spectrum – 100 Year

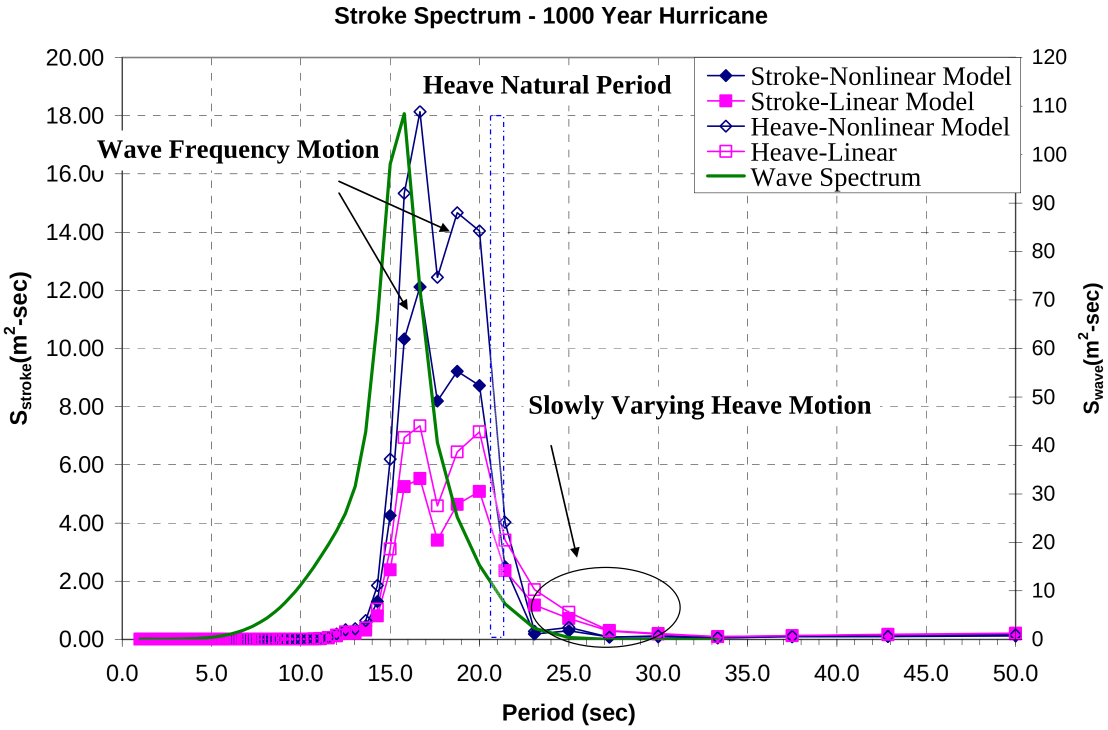

Figure 4.23 Heave Motion and Stroke Spectrum with the Wave Power Spectrum – 1000 Year

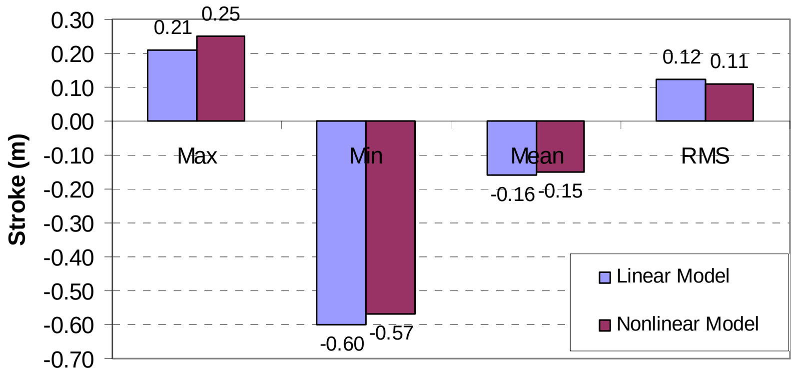

(a) 10 Year Hurricane

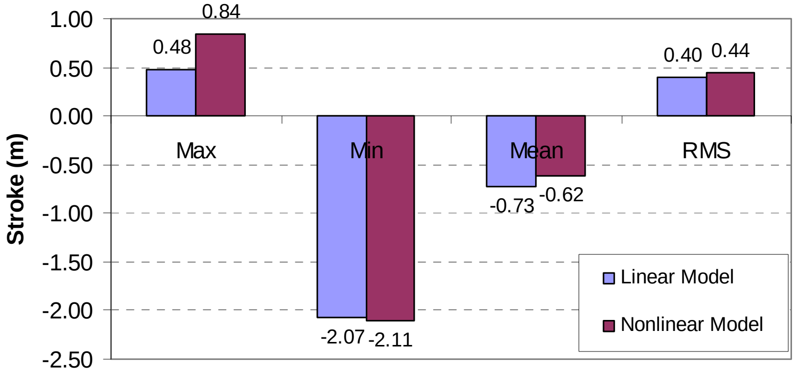

(b) 100 Year Hurricane

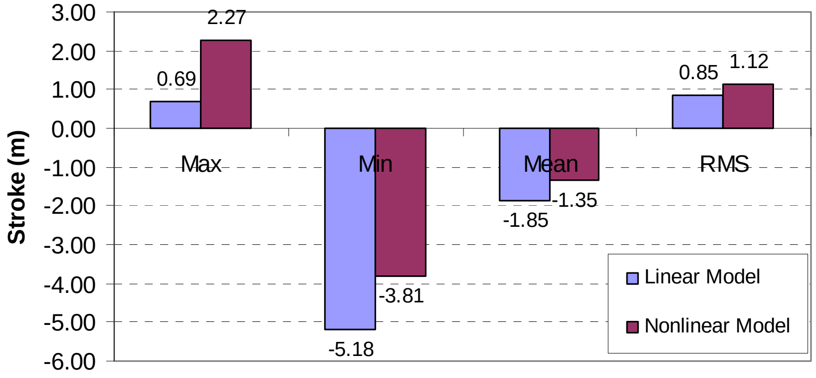

(c) 1000 Year Hurricane

Figure 4.24 Statistics of Stroke – Comparison of linear and nonlinear model

Figure 4.25 summarize the sensitivity of the stroke range and rms difference to the environment. The more severe environment gives more difference in the dynamic strokes as well as the maximum.

In Figure 4.26, the time signal of tensioner friction force relevant to stroke and tension of nonlinear model for 1000 year hurricane condition is exemplified for a time interval. The interval includes the time when the stroke meets the down-stroke limit. The tension is multiplied by 0.025 to make the magnitude same as that of friction force. It is shown that the riser tension is highly related with the stroke, and that the friction force is related with both the stroke and the tension by Equation (2). A sudden sign change of the friction force is observed when the stroke passes its hollows and humps, and the magnitude of the friction force changes with that of tension.

In Figure 4.27, the top tension of a riser is statistically described for the environmental conditions. The tension also shows much discrepancy between the linear and the nonlinear model, especially for the more severe environmental condition. The tensioner piston gets stopped at the down-stroke limitation for the 1000 year hurricane condition, and the impact load in that instant increases the maximum tension. Therefore, for the 1000 year hurricane condition, the maximum tension is different by 42%, while the difference is only 10% for 100 year hurricane condition. The standard deviation is also affected by the stroke behavior, and they are different by 28% for the 100 year hurricane and by 53% for the 1000 year hurricane condition.

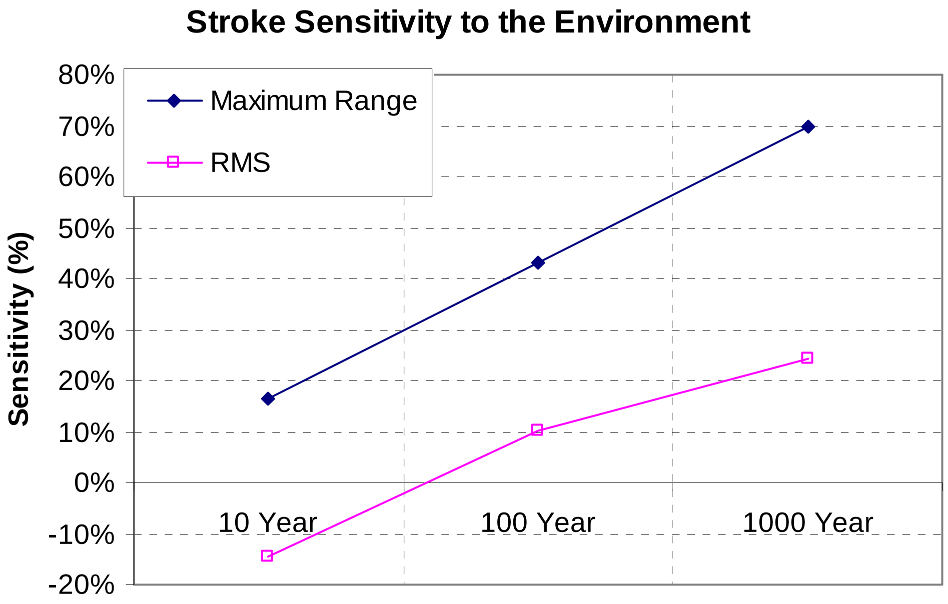

Figure 4.25 Sensitivity of the Stroke to the Environment Dependent on the Tensioner Modeling

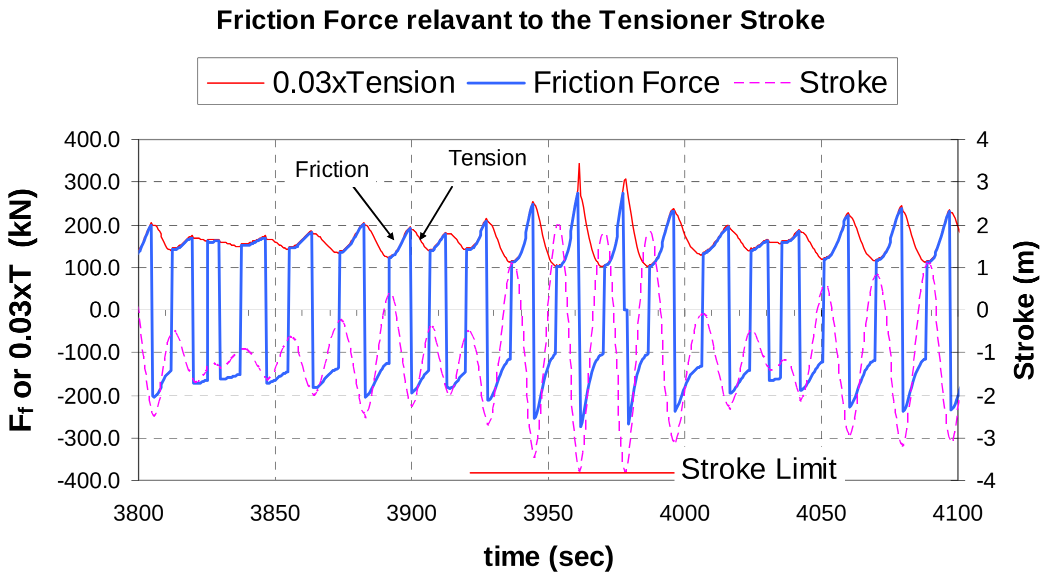

Figure 4.26 Time History of Stroke and Friction Force Relationship – Exemplified around the time interval where stroke exceeds its limit

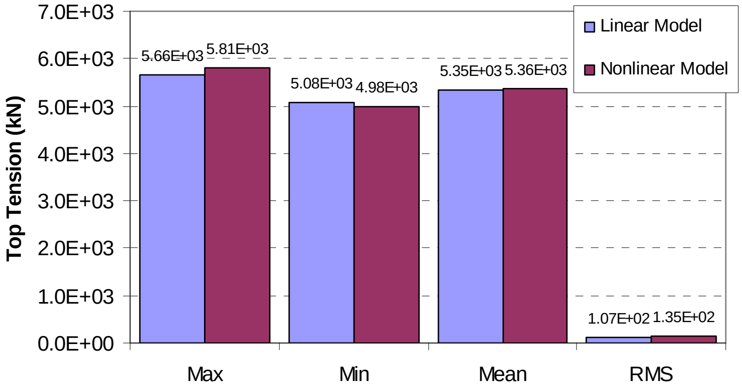

(a) 10 Year Hurricane

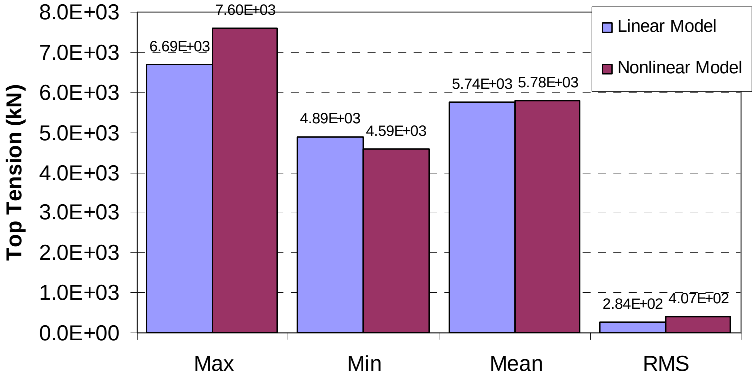

(b) 100 Year Hurricane

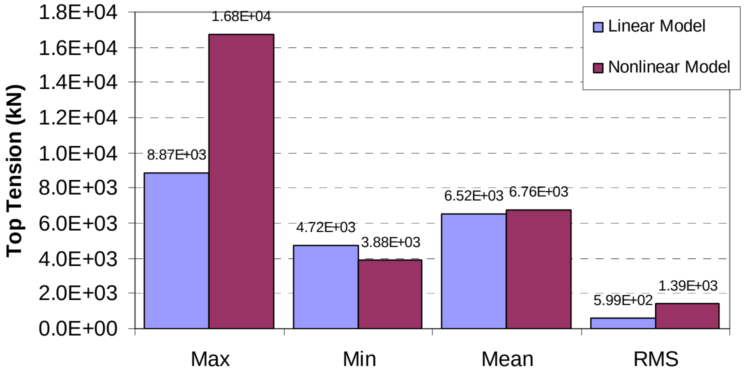

(c) 1000 Year Hurricane

Figure 4.27 Statistics of the Top Tension of a Riser

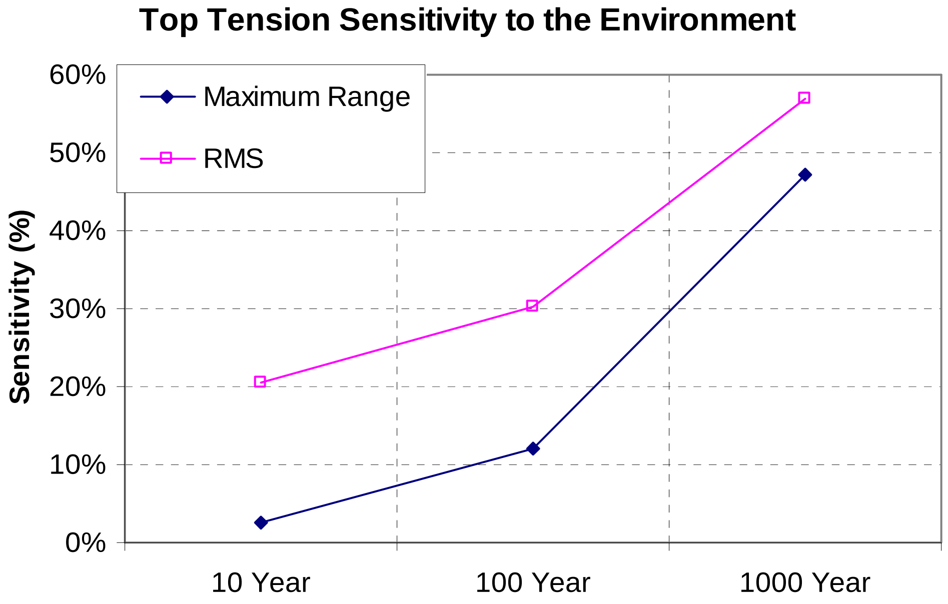

Figure 4.28 Sensitivity of the Top Tension to Environment dependent on the Tensioner Modeling

5. CASE STUDY 2: TRANSIENT EFFECT OF TENDON DISCONNECTION FOR THE ROBUSTNESS CHECK OF TLP

5.1 Introduction

A numerical study of the transient effect of tendon disconnection on global performance of ETLP for harsh environmental condition in GoM (Gulf of Mexico) has been carried out. Twelve tendons support the platform with twelve production TTRs and one drilling riser attached by hydro-pneumatic tensioner.

Charm3D, a program for global motion analysis of multiple floating hulls coupled with risers/mooring lines, is made to be capable of modeling the tendon disconnection at both top and bottom connection.

The study includes the break due to high tension at the top and the unlatch due to negative tension at the bottom. A sudden disconnection of one or more tendons causes the unbalance of force and moment of the total system, only to cause the transient motion and tension as well as the mean offset. The breakage and the unlatch also make the different effects. The breakage and unlatch also make the different effects. The transient responses and the mean offsets are compared and discussed in the viewpoint of the robustness of the system.

The effects of significant effect of the transient on the tendon tension as well as the pitch motion for the more critical environmental heading are addressed herein.

The Charm3D is based on the hybrid model of Morison members to a panelized body (Ran et al., 1997). The Morison members are used to incorporate the viscous drag forces and the added mass of the slender body.

A 3D second-order diffraction-radiation panel program WAMIT (Lee et al., 1991) is used to calculate the frequency-domain hydrodynamic coefficients of the hull, such as added mass and radiation damping as well as the first- and second-order wave excitation forces. The importance of the inclusion of the second-order wave-force QTFs (quadratic transfer function) for TLP vertical-plane dynamics has been demonstrated by Kim and Yue (1988). The external stiffness due to tendon and riser is included in the WAMIT computations in addition to the hydrostatic stiffness so that more accurate motion-dependent wave-force QTFs are obtained. In the ensuing time-domain simulation, the tendon and riser restoring forces are automatically coupled with hull motions. The time-domain simulation is carried out by using the hybrid model of Morison members and panelized bodies. The diffraction-radiation forces on the hull are obtained from WAMIT, which uses potential flow approach, while the viscous forces on the hull, tendons, and risers are considered through the Morison equation. The extremely nonlinear impact-like loading by highly skewed nonlinear waves is beyond the scope of the present study, and thus not considered.

5.2 ETLP Concept

The ETLP is an efficient hull design that delivers a proven, stable drilling and wellhead facility maximizing uptime and drilling efficiency for minimum capital expenditure. The four-column configuration is extremely stable during wet tow, enabling a fully integrated facility to be completed quayside, with no temporary or additional devices required to meet safe and acceptable stability requirements. The four-column ETLP with three tendons at each corner is shown in Figure 5.1. The pontoon extensions move the tendon connection point outboard of the columns, which provides two benefits. First, the columns are moved inward towards the TLP center, to minimize the deck span and increase the efficiency of the deck structure. Second, the tendons are maintained further apart to minimize platform motions and maximize drilling uptime. TLPs are well known for having negligible roll, pitch and heave, and ETLP maximizes the characteristics.

The columns are circular for structural efficiency and to minimize environmental loading. The mooring configuration provides twelve stepped tendons, three per corner. The stepped tendon design incorporates a change in thickness along the length of the tendon to minimize steel material as well as underwater weight, which results in increasing platform payload.

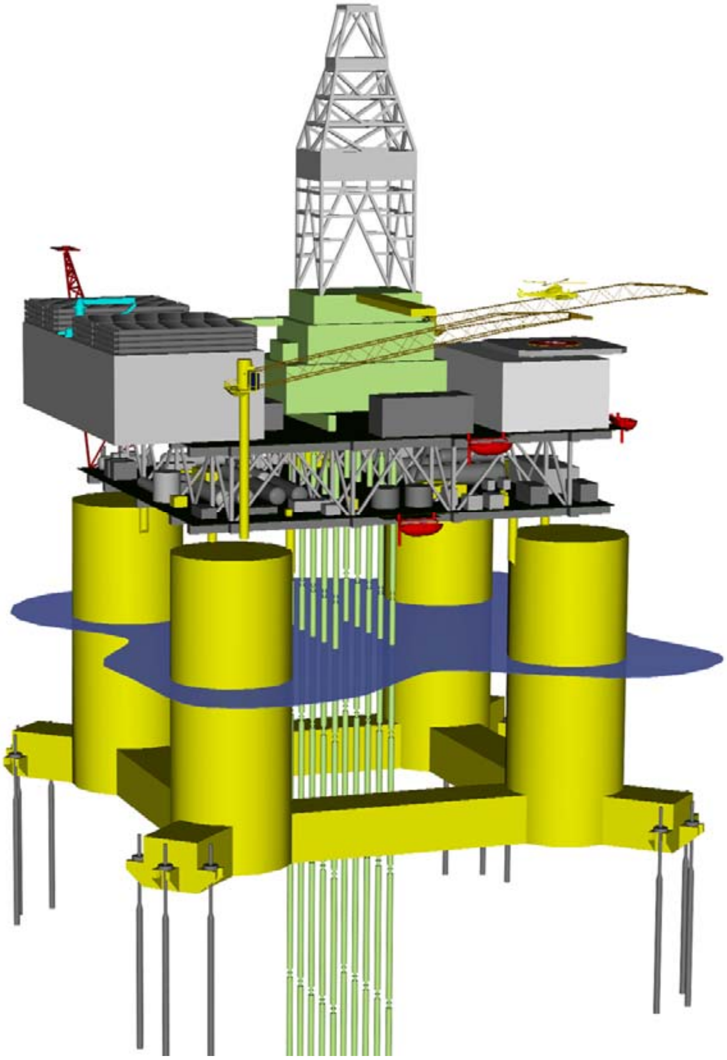

Figure 5.1 Configuration of ETLP with Circular Column Section

5.3 ETLP and Riser Configuration

The payloads and the principal dimensions of ETLP are shown in Table 5.1. The operating payload is 34,464 st (total weight=63,659 st) and the total tendon top tension is 21,525 st. The corresponding displacement to support the payload and the tendon vertical load is 90,017 st. The tendon consists of bottom, mid and top section with the same outside diameters and the different wall thickness. The lengths of the sections are 198.1m (650ft), 541.9m (1778ft) and 350.5m (1150ft), respectively. There are additional transition parts at both top and bottom for the connection to the porch and to the foundation, respectively. The equivalent properties of the tendons are summarized in Table 5.2. Twelve production TTRs are attached to dry trees at the production deck and the drilling riser at the drilling deck is supported by hydro-pneumatic tensioner, whose properties are shown in Table 5.3.

The layout of the tendons and TTRs at the deck plane is depicted in Figure 5.2. The TLP is originally designed for the pre-Katrina condition, but is used for this study for the severer environment to reassess the impact of the environmental changes on the robustness of the system.

The drag coefficients used for the tendon and risers are 1.0 and for the hull, 1.0 for circular columns and 0.77 for rounded rectangular pontoons are used (API, 2005).

Figure 5.3 shows a typical discretization of the TLP when obtaining the hydrodynamic forces from WAMIT. The total of 1402 quadrilateral panels are used to dscretize the hull surface. The free-surface discretization with 544 panels is necessary only for the second-order sum-frequency QTF calculation, for which the truncation radius of 196.5m (645 ft) is used. Outside the truncation radius analytic integration is done. Figure 5.4 shows the coupled model with the tendons and TTRs included. The tension due to the pneumatic tensioner is related to the stroke z of the piston, and satisfies a nonlinear equation based on the gas law. The relationship between the nominal tension, nominal length, and stroke of the pistion is shown in Equation 4 (Yang et al., 2007). As there is a surface tree above the tensioner, the nominal tension includes the tree weight.

Table 5.1 Principals of ETLP

Water Depth (m)	1,127.7
Dry Payload (st)	25,306
Operating Payload (st)	34,464
Draft (m)	32.6
Displacement (st)	90,017
KB (m)	18.2
Tendon @ Top (st)	21,528
TTR @ Top (st)	4,830
Total Weight (st)	63,659
KG (m)	48.1

Table 5.2 Tendon Configuration

Length (m)	1,103.6
Wet Weight (kg/m)	340.5
Dry Weight (kg/m)	3,330.7
Equivalent EA (kN)	6,329.8

Table 5.3 Production Top Tensioned Riser Properties

Casing/Tube	OD (m)	Thickness (mm)
Outer Casing	0.346	13.05
Inner Casing	0.273	12.57
Tubing	0.140	9.17
GL Tube	0.060	4.83

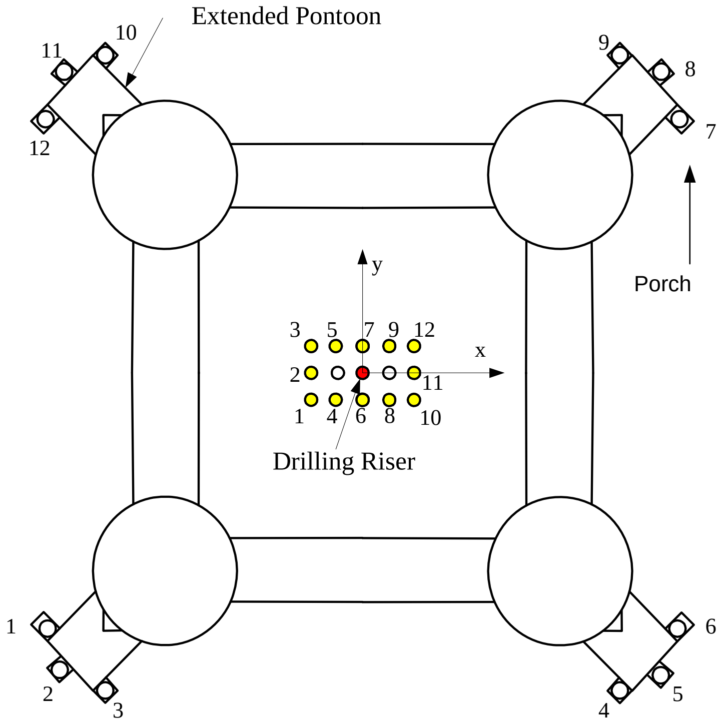

Figure 5.2 Layout of Tendon and the TTRs

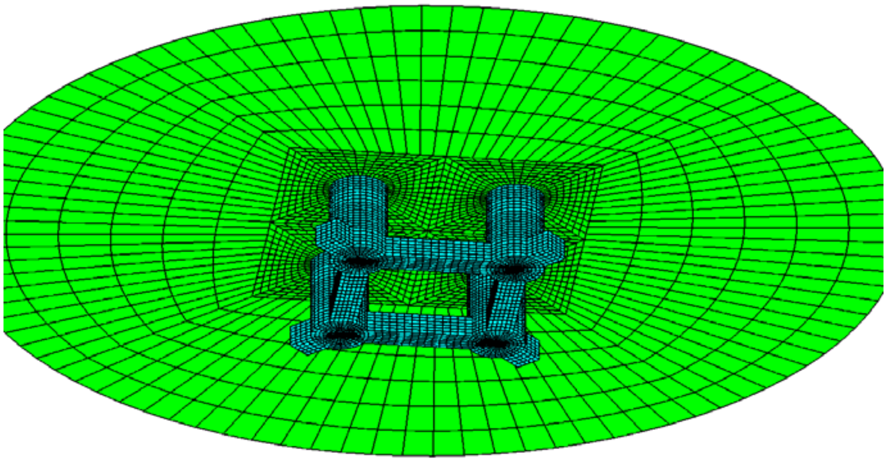

Figure 5.3 Body Surface Panel for Hydrodynamics

Table 5.4 Drilling Riser Properties

Casing/Buoy	OD (m)	Thickness (mm)
Outer Casing	0.473	29.2
Buoyancy Modules	0.945	236.0

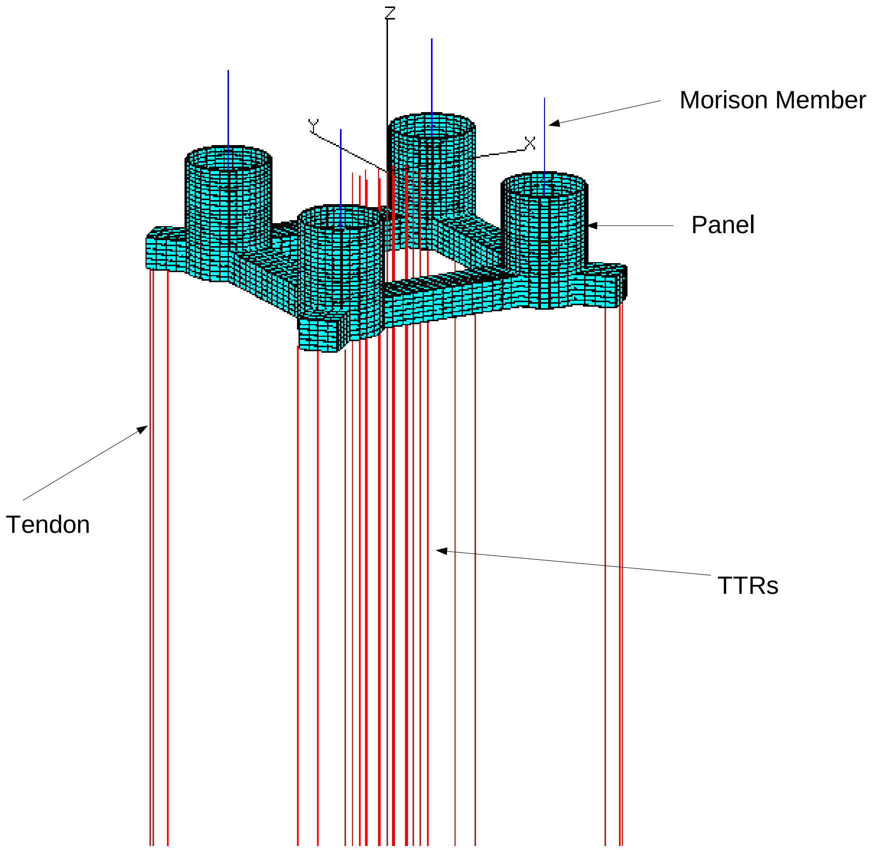

Figure 5.4 Fully Coupled Model with Morison Member

5.4 Environmental Criteria

10-year, 100-year, and 1000-year Hurricane Post-Katrina environmental criteria representing the central region of GoM are applied (API, 2007b). The detailed wave-wind-current data are shown in Table 5.5. The new criteria for long-crested waves recommend 15.1 seconds peak period for 100 year hurricane at the central region. The new criteria impose higher wave heights, wind speed, and current speed compared to older criteria. The wind, wave, and current are assumed to be co-linear. The shear currents are assumed to decay linearly between the given values. The dynamic wind loads are generated from the given NPD spectrum with the force coefficients 7282.9 m^2 (7.83E+04 ft^2) with center of pressure 44.2 m (145 ft) from MWL.

Table 5.5 Environmental Criteria

Description	10 yr Hurricane		100 yr Hurriccane		1000 yr Hurricane	
Wave	**JONSWAP**		**JONSWAP**		**JONSWAP**	
Hs (m)	10.0		15.01		18.81	
Tp (sec)	13		15.1		16.95	
γ	2.2		2.2		2.2	
Wind (NPD)						
V (1hr'@10 m, m/sec)	33.00		48.00		60.00	
Current	**Depth (m)**	**Vel (m/s)**	**Depth (m)**	**Vel (m/s)**	**Depth (m)**	**Vel (m/s)**
	0.00	1.32	0.00	1.80	0.00	2.25
	-34.99	0.99	-49.98	1.35	-63.00	1.69
	-69.31	0.00	-100.79	0.00	-126.00	0.00
	-1127.70	0.00	-1127.70	0.00	-1127.70	0.00

5.5 Results and Discussion

The intact, up-wave tendon breakage at the top followed by one more up-wave tendon breakage at the top, and the down-wave tendon unlatch at the bottom due to the down stroke at the bottom connector are simulated and compared. For each breakage and unlatch, the transient and non-transient simulations are carried out to examine the significance of the transient effect. Three different storms (10-yr, 100-yr, and 1000-yr) are applied for comparison. The non-transient simulations assume that the tendon breakage or unlatch occur before the start of the simulation, and thus the transient effects are ignored. Whereas, the transient case imposes the tendon disconnect or unlatch during the simulation when the tension reaches the maximum for the breakage or minimum for the unlatched. It is assumed that the tendons break or unlatch for each storm case by different reasons. Thus, in this study, the tendons are assumed to be broken and unlatched regardless the tensions reach the breaking strength at the top or the negative tension at the bottom.

The incident angle is 45 degrees i.e. wave heading is 45 degrees counterclockwise from the positive x-direction. The z-axis is positive upwards and is located at the still-water surface. It is assumed that the tendon #2(see Figure 5.2), the up-wave tendon, is broken first at the top in the breakage case and the down-wave tendon, tendon #8 is unlatched at the bottom in the unlatch case. The respective neighboring tendons are tendon #1 and tendon #7. The #3 and the #9 tendon are additionally broken and unlatched for the two tendon broken and unlatched cases, respectively.

The horizontal offset and the vertical set-down curves are shown in Figure 5.5. About 400-ft horizontal offset corresponds to 20-ft set down. The natural periods and the damping factors for intact condition are shown in Table 5.6. The heave natural period is 4.01 seconds and the roll/pitch natural periods are 4.34 /4.32, respectively. Also given is the change of natural periods in case of the loss of one or two tendons. The missing of the tendons decreases the vertical stiffness of the system which is significantly governed by the tendon system and the natural periods of the heave and roll/pitch increase. The natural period of the horizontal motions such as surge, sway and yaw does not change due to the tendon missing because those are governed by the top tension and the tensions are over-taken by the other tendons even though one or two tendons are missing. Figure 5.6-Figure 5.7 show the free decay of the heave and the pitch for intact, one tendon broken/unlatch and two tendon broken/unlatch, where the change of the natural period and the initial heave and pitch motion due to the tendon missing or unlatch. The unlatched tendon still has the wet weight of it and slightly less change of the initial heave and pitch is seen.

Table 5.6 Natural Periods and Damping Factor-Intact Condition and Tendon Damaged Case

	Intact		1 Tendon Missing	2 Tendon Missing
Mode	T (sec)	Damping	T (sec)	T (sec)
Surge	182.05	13.10%	182.3	182.6
Sway	180.00	12.00%	181.0	181.5
Heave	4.01	5.20%	4.2	4.4
Roll	4.34	3.70%	4.4	4.8
Pitch	4.32	3.60%	4.4	4.8
Yaw	115.3	6.80%	115.1	115.2

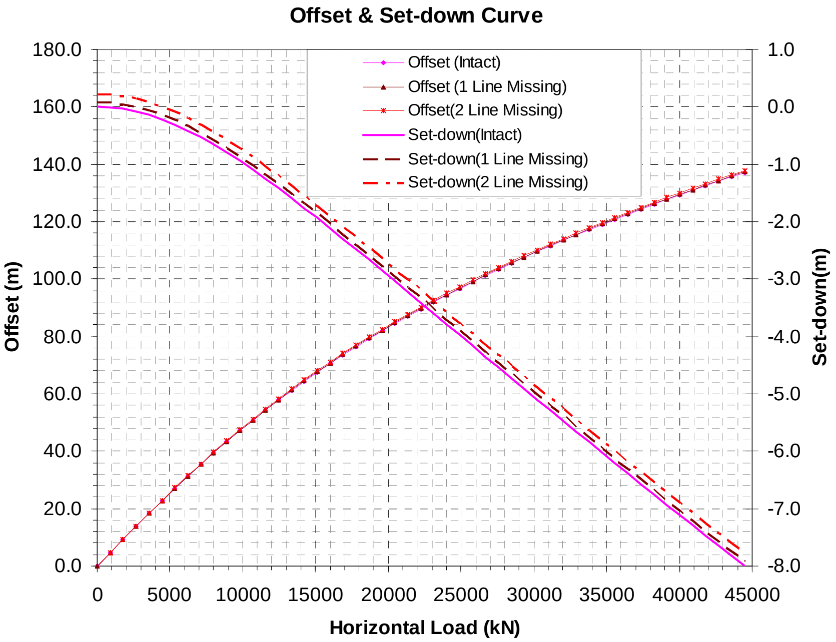

Figure 5.5 Horizontal Offset and Vertical Set-down Curve in 45 Degree Direction – Intact, One and Two Tendon Missing Cases

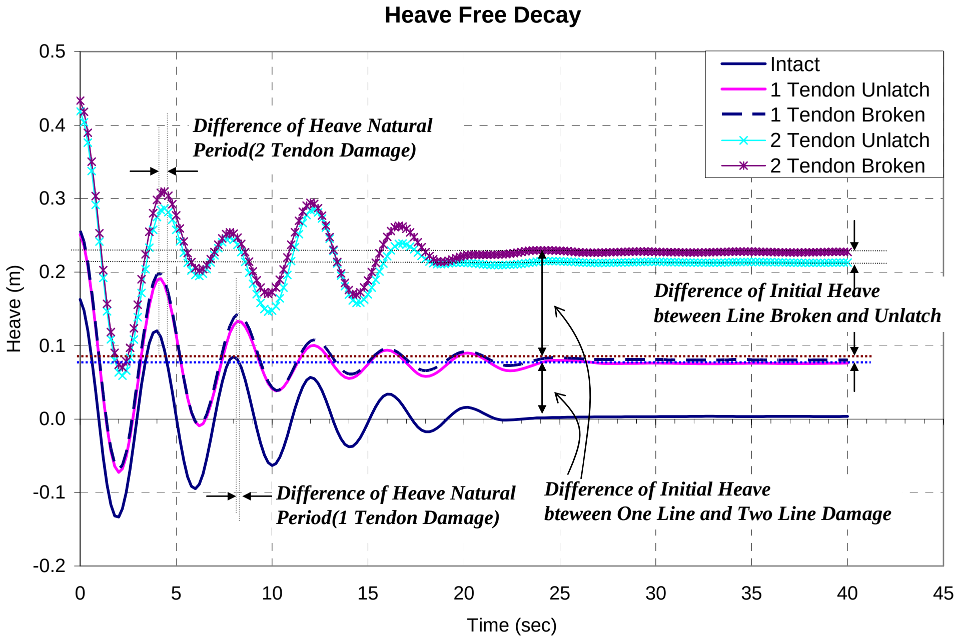

Figure 5.6 Heave Free Decay of Intact and the Tendon Damage Cases

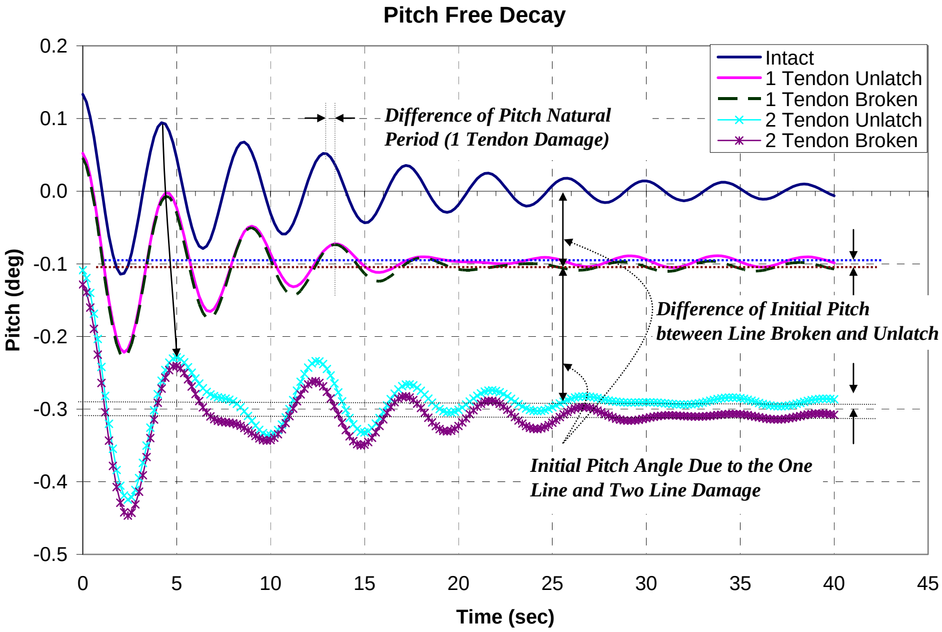

Figure 5.7 Pitch Free Decay of Intact and the Tendon Damage Cases

Figure 5.8 and Figure 5.9 show, respectively, the heave wave-force and pitch wave-moment spectra for three different environments. The graphs compare the time domain wave forces and the moments with the frequency domain wave frequency wave forces and moments. The differences are from the second order QTF effect which is included only in the spectra from the time domain. Since the second-order wave-force QTF is included, the springing-force components are shown in the high frequency region. It is interesting to note that 10-yr-storm case has appreciable springing-force components near the natural periods (4-4.3 seconds) of vertical-plane motions. The difference frequency wave forces and moments are also captured at the low frequency region.

The resultant heave and pitch motion RAOs due to the 1st order wave force are shown in Figure 5.10 and Figure 5.11, respectively. The resonance modes are shown at around 4 seconds for heave and 4.3 seconds for pitch, which is correspondent to the free decay test results. The first humps right after the resonance peak period is due to the existence of the extended pontoon, and the next hump is due to the interaction between the column and the pontoon. The RAOs are plotted with the wave spectra of 10 year, 100 year and 1000 year hurricane, and it can expected that the 10 year environment may affect more on the high frequency region than the other conditions.

In Figure 5.12, the tendon tension RAOs of up-wave, diagonal and down-wave tendons are plotted with the wave spectra. The down-wave tendon tension RAO has largest hump around 10 seconds which is due to the phase coincide of the heave and pitch motion at the down-wave side. The diagonal tendon has relatively very small wave induced tensions than the other two positions. It is expected that the down-wave tendon has the largest dynamic tension in wave frequency.

Figure 5.13 and Figure 5.14 show the time histories of the pitch motions when up-wave tendon breaks at the top and down-wave tendon unlatches at the bottom. In the former case, the mean pitch angle is shifted to the positive value. The opposite is true for the latter because the unlatched down-wave tendon affects the balance of the heel in the opposite way. The damaged cases show more fluctuation than the intact case, and the tendon unlatched case has larger pitch motion amplitude than the breakage at the top because the hanging tendon add the mass of the system and the fluctuation free hanging tendon also excites the platform.

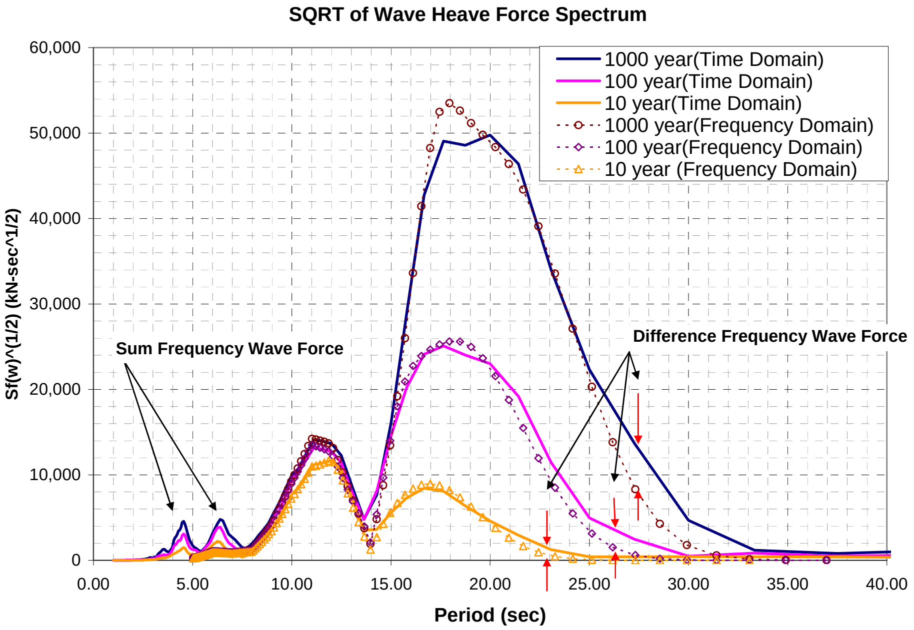

Figure 5.8 Square Root of Heave Wave-Force Spectra as a Function of Wave Period

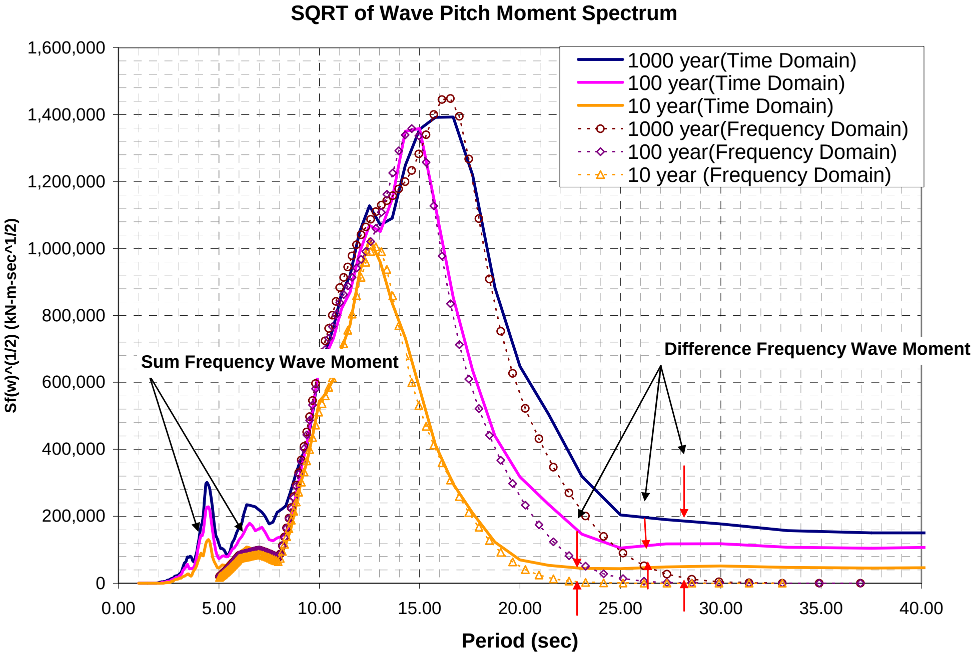

Figure 5.9 Square Root of Pitch Wave-Moment Spectra as a Function of Wave Period

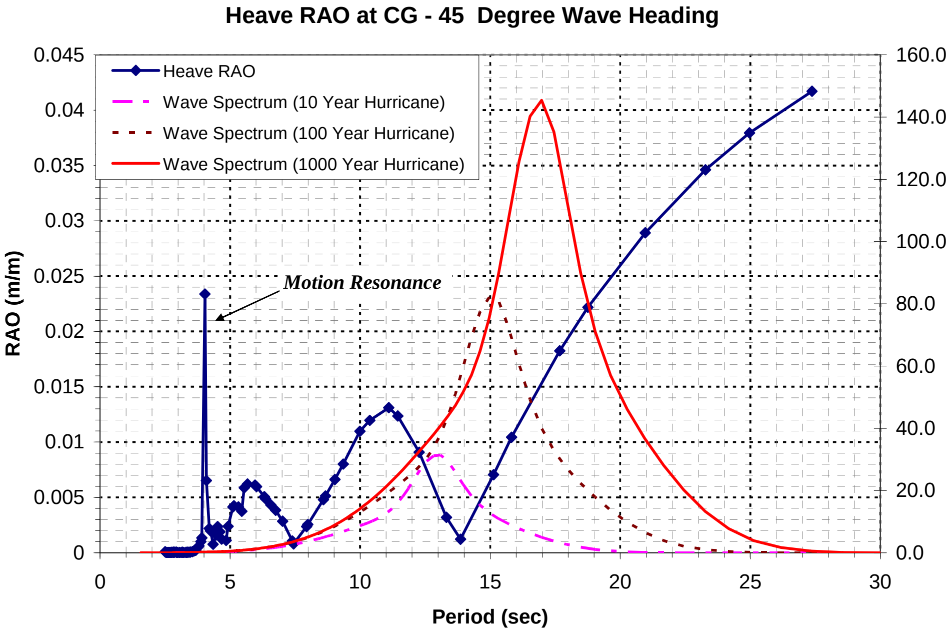

Figure 5.10 Heave RAO at Center of Gravity for 45 Degree Wave Heading – Intact Condition

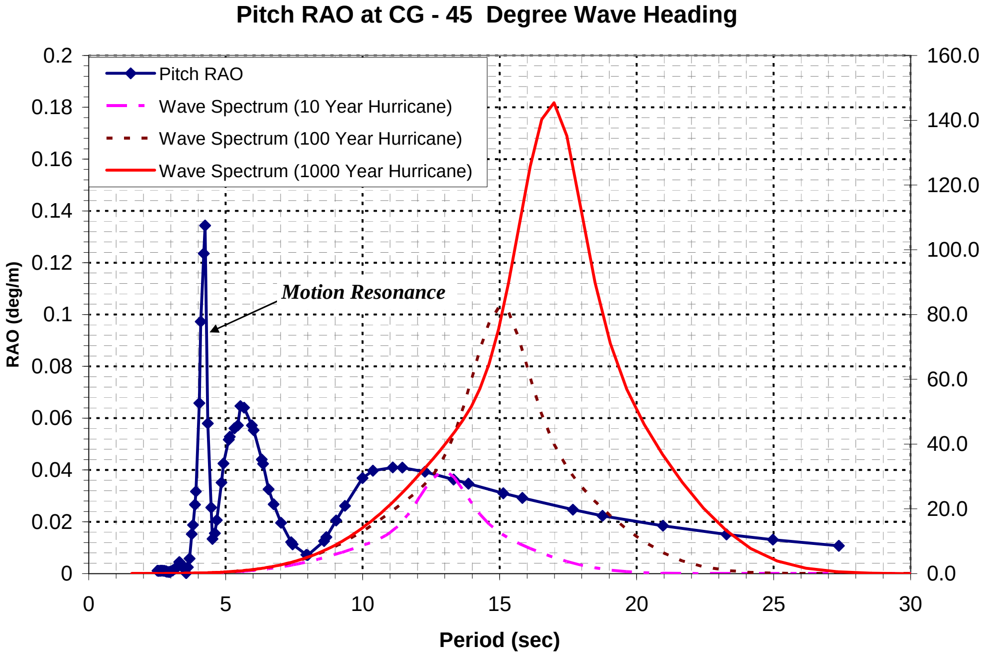

Figure 5.11 Pitch RAO for 45 Degree Wave Heading – Intact Condition

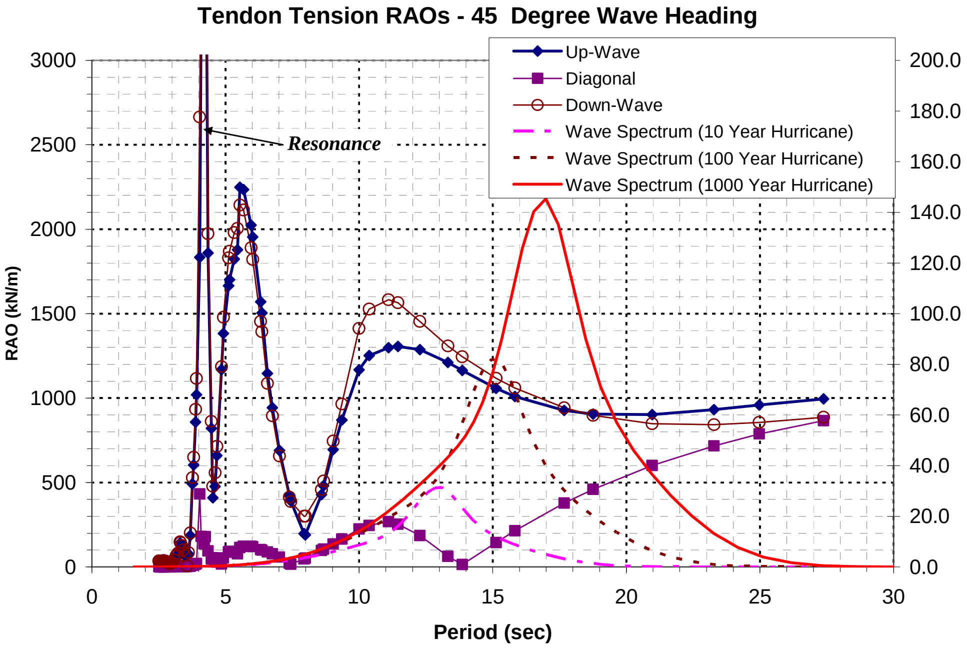

Figure 5.12 Up-wave, Down-wave and Diagonal Tendon Tension RAOs for 45 Degree Heading

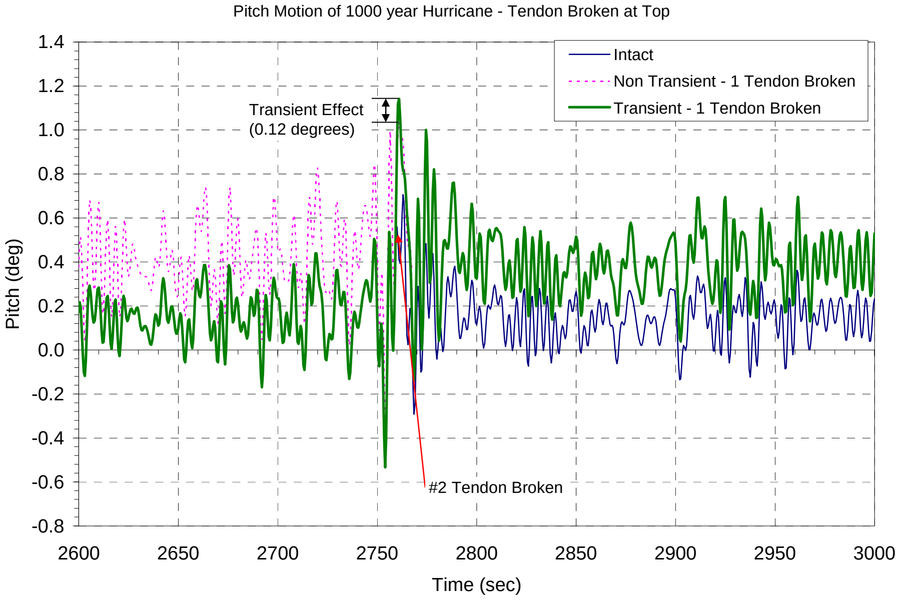

Figure 5.13 Time History of Pitch Motion for the One Tendon Breakage at the Top – 1000 Year

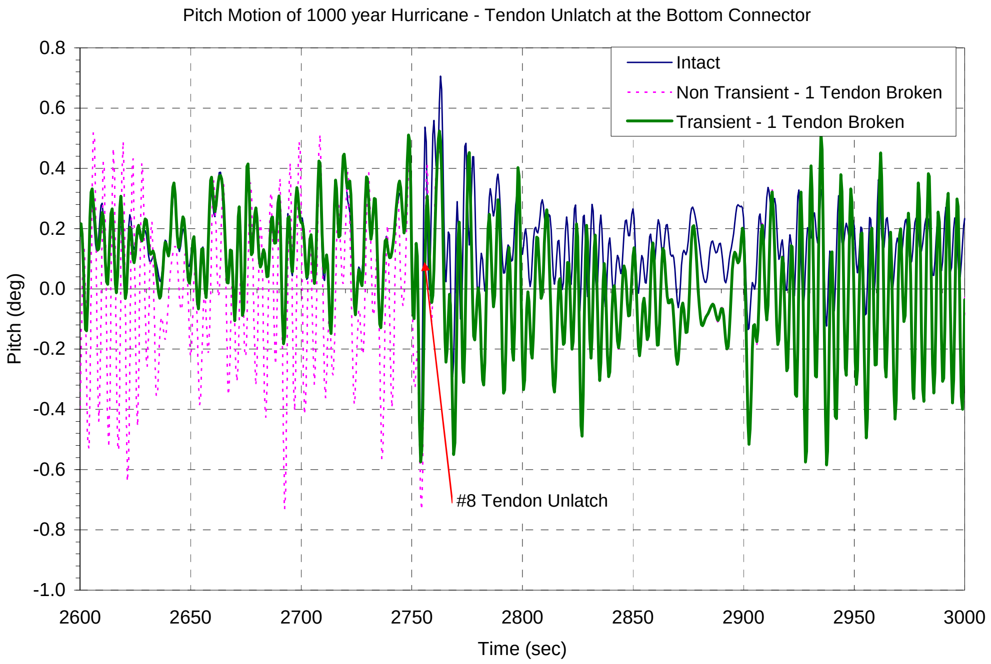

Figure 5.14 Time History of Pitch Motion for the One Tendon Unlatch at the Bottom – 1000 Year

Figure 5.15 and Figure 5.16 plot the RMS and the maxima of set-down and pitch for the three different environments. The current industry-standard practice when dealing with tendon breakage and unlatch does not include the transient effects. The cases that include the transient mode are specified as “transient” in the figures.

The mean heave is shifted upward in both breakage and unlatch cases since the system becomes softer after the loss of one tendon, which can be seen from the static offset and set-down curves. The difference between the breakage and the unlatched is due to the hanging tendon and its weight in the latter. However, the unlatched case has larger RMS than the intact as well as than the breakage at the top, and the maximum setdowns are larger than those cases, even though the mean has shifted upward. The pitch RMSs quantifies the time histories in Figure 5.13 and Figure 5.14. The unlatched case has larger RMS and the corresponding maximum pitch is larger than the intact, though the mean pitch shifted due to the unlatch at the down wave side. However, the transient effect of the unlatching on the motion is rarely shown for this cases considered in this study. The transient effect of the tendon breakage on the pitch motion is 11.3% for 1000 year, 16.5% for 100 year, but the milder condition, i.e. 10 year hurricane condition don't show any transient effect.

The horizontal offsets are not affected by either breakage or unlatch because the neighboring tendons take over the role of the damaged tendon and the total top tension remains the same. However, the loss of tendon affects the stiffness of the vertical-plane modes and the corresponding motions.

Figure 5.17 and Figure 5.18 plot the same cases as Figure 5.15 and Figure 5.16 for the scenario of two-tendon loss (#2-3 & #8-9). The tendon breakage shows very large effect of the transient mode on the pitch motion, while the unlatched at the bottom has a little difference between transient and the non-transient responses.

As a result of the comparison of the heave and pitch motions, the motions are more sensitive to the tendon breakage at the top than the unlatch at the bottom. The heel angle changes more sensitively due to the disconnection than the offset and the heave do.

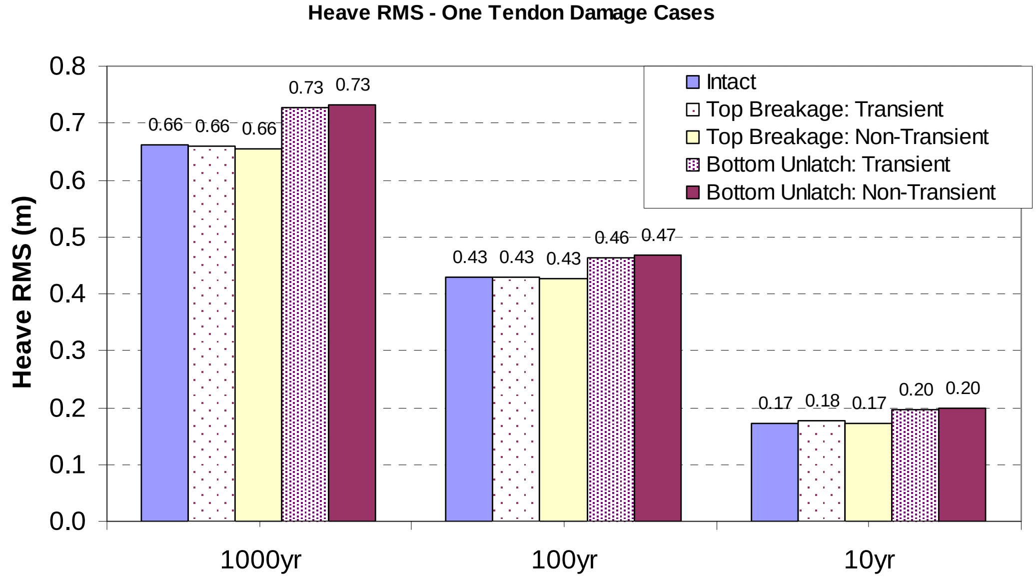

(a) Heave RMS

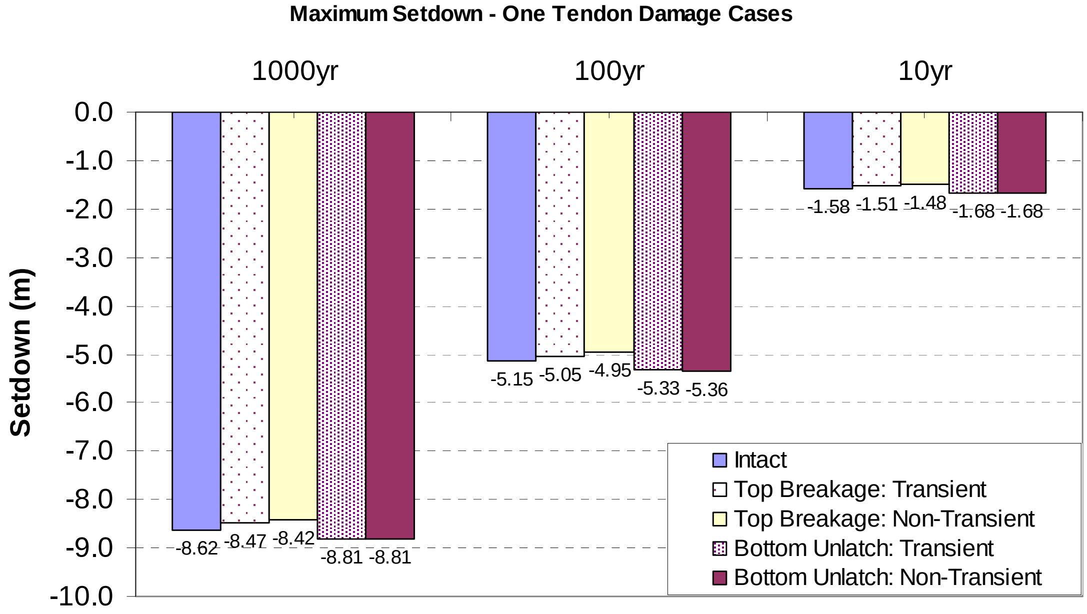

(b) Maximum Set-down

Figure 5.15 Heave RMS and Maximum Set-down for One Tendon Damage

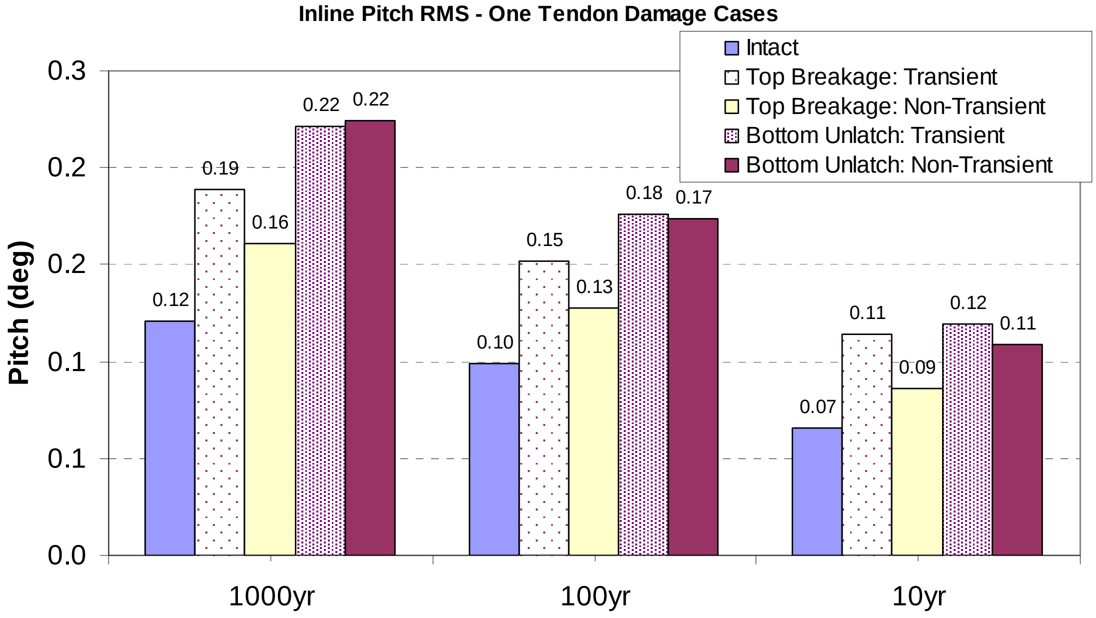

(a) Inline Pitch RMS

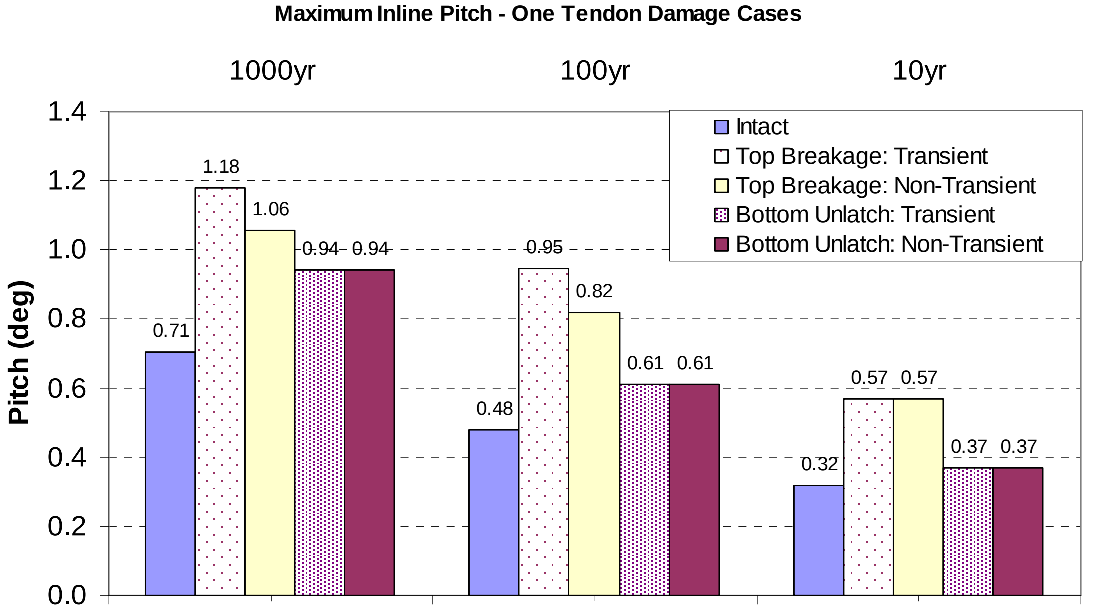

(b) Maximum Single Amplitude Inline Pitch

Figure 5.16 Inline Pitch RMS and Single Amplitude Maxima for One Tendon Damage

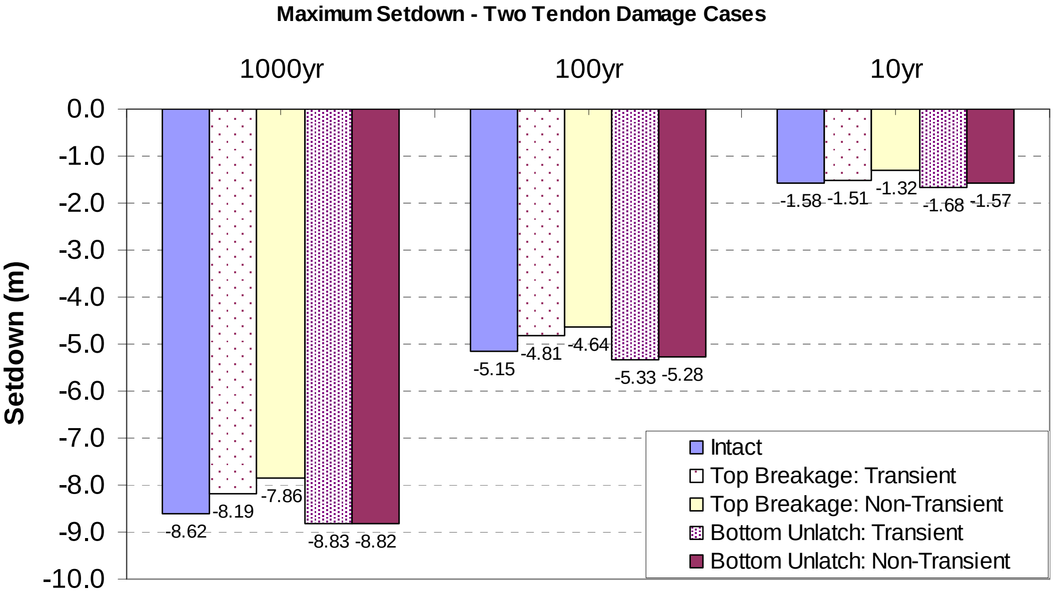

Figure 5.17 Maximum Set-down for Two Tendon Damage

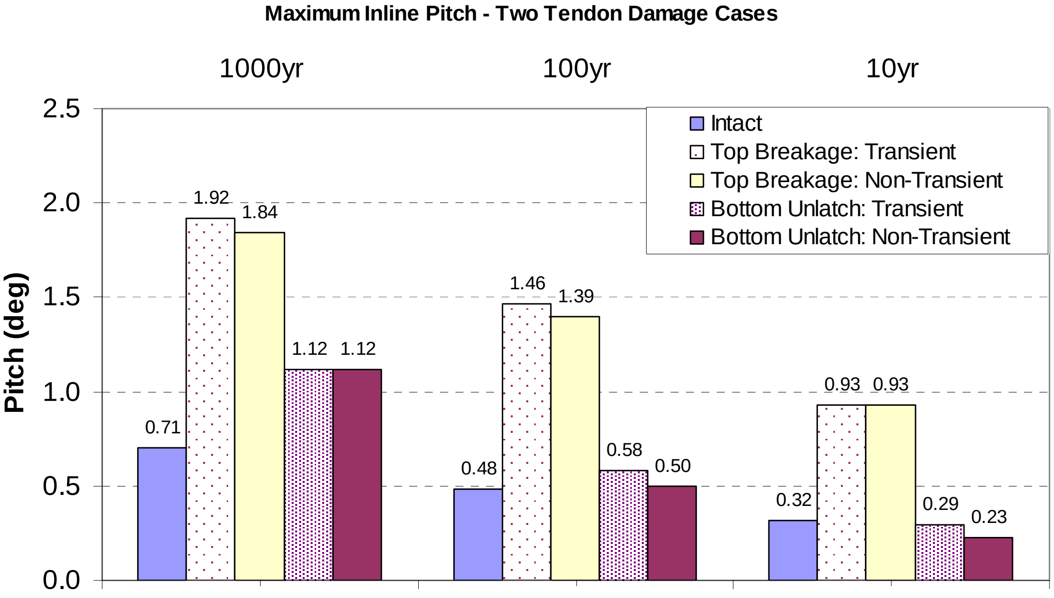

Figure 5.18 Maximum Pitch for Two Tendon Damage

Figure 5.19 shows the time history of the top tension of the nearest tendon when the #2 tendon breaks at the top. It compares the transient and non-transient results. It is seen that there exists non-trivial transient overshoot effects in the former. It also shows that the tension of the neighboring tendon is significantly increased by about 40.0 % compared to the intact case, which should be underscored in the tendon design.

Figure 5.20 shows the time history of top tension of the unlatched #8 and #9 tendons when they are unlatched successively. It shows that the top tension reaches its wet free-hanging weight after unlatch, while freely oscillating with the motion of the ETLP. It is noteworthy that the top tension right after the first unlatch of tendon #8 becomes negative with large magnitude and thus causes strong compression force on the top connector, which may cause significant damage at the connector. After the second unlatch of the tendon #9, smaller impact compression load is captured, but there is some sort of compression loads on the top connector after the unlatches. This important result can only be traceable by using the program including transient effects.

Figure 5.21 shows the time history of the top tension of the nearest tendon (#7) when the #8 tendon unlatches at the bottom. The overall trend is similar to that of Figure 5.14. However, the tension needs not be the maximum at the instant because the program forces the tendon unlatched at the instant of minimum bottom tension although the three hour simulation. The transient tension is less than the non-transient tension for this case. However, the transient tension exceeds the non-transient tension by about 20,000 kN after the second unlatch of tendon #9 as shown in Figure 5.20.

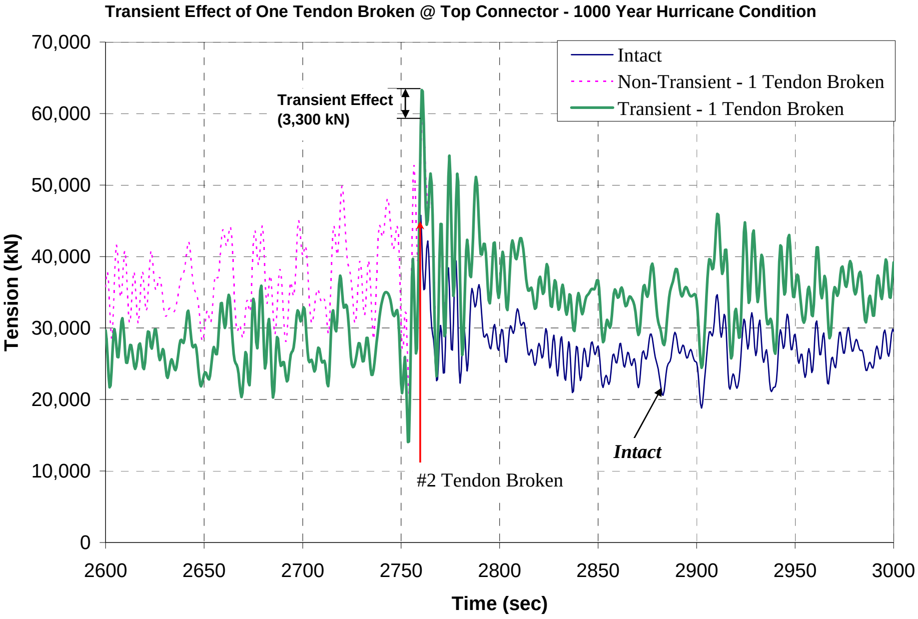

Figure 5.19 Comparison of Transient Effect after the Upwave Tendon Breakage at the Top – Top Tension of the Tendon #1

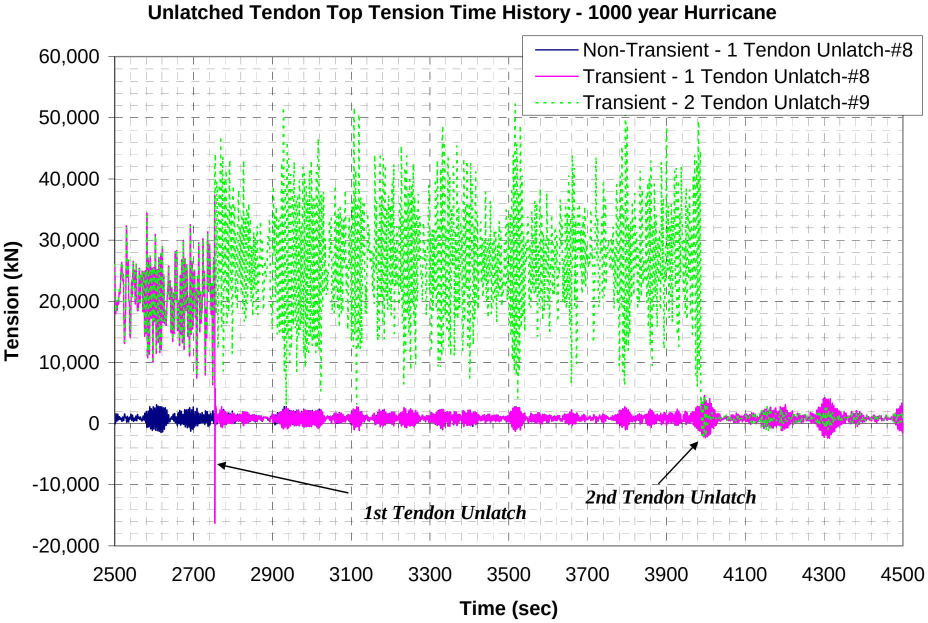

Figure 5.20 Comparison of Transient Effect after the Down-wave Tendon Unlatch at the Bottom – Top Tension of the Unlatched Tendons

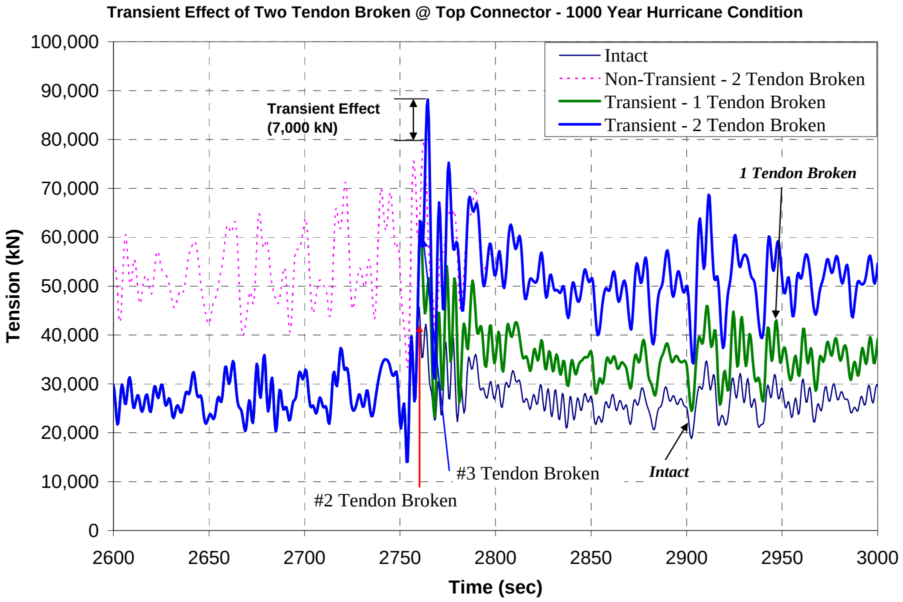

Figure 5.21 Comparison of Transient Effect after the Upwave Tendon Breakage at the Top – Top Tension of the Most Neighboring Tendon

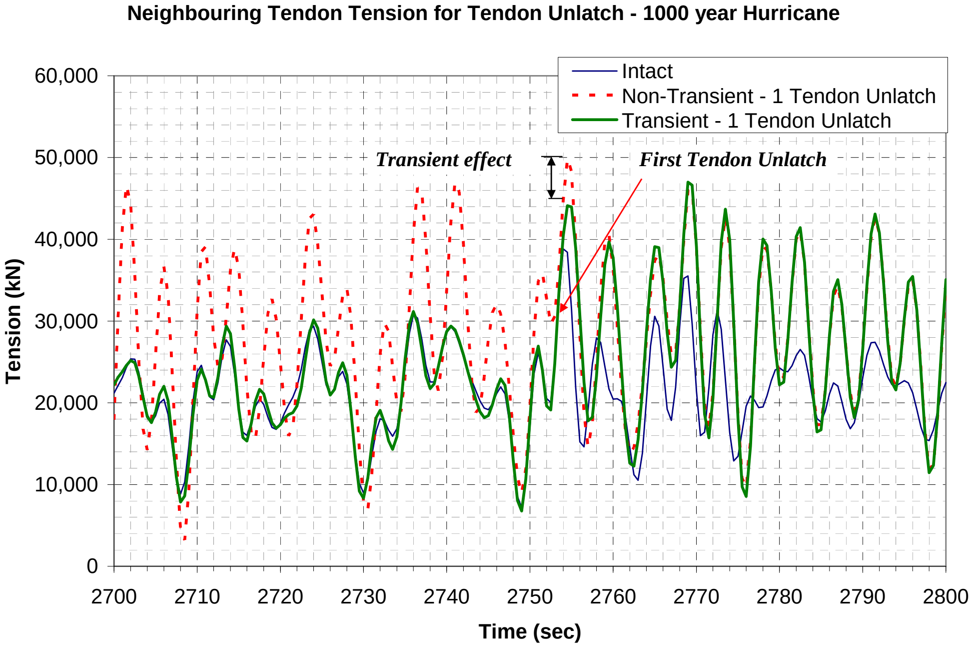

Figure 5.22 Top Tension Time History at the Neighboring Tendon after the 1st Down-wave Tendon Unlatch

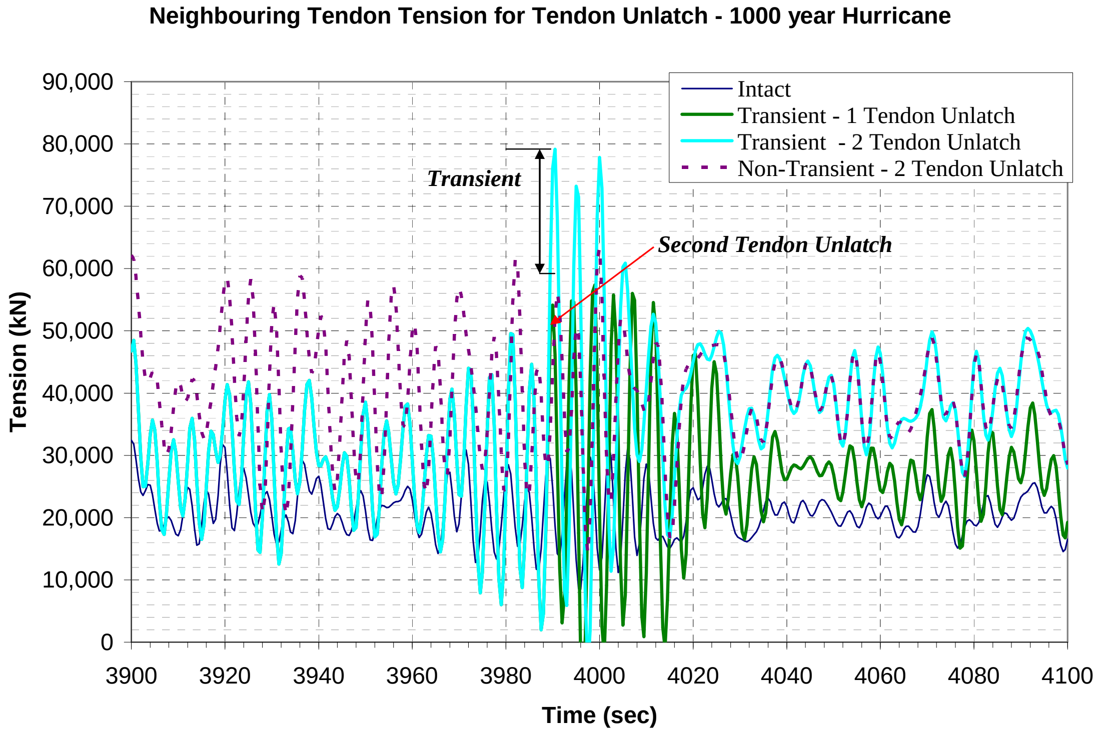

Figure 5.23 Top Tension Time History at the Neighboring Tendon after the 2nd Down-wave Tendon Unlatch

Figure 5.21 plots the top tension of the highest-tensioned tendon (#1) after losing #2 tendon for the three different environments. The maximum tensions at intact condition are 46,000 kN for 1000 year, and it is increased by 38% with the transient mode and by 30% without the transient effect. Thus, there is an over shooting by about 8% of the intact maximum tension for 1000 year hurricane condition. For 100 year, the over shooting is about 12% of the intact maximum and it is by 1% for 10 year hurricane condition.

Fig.28 plots the top tension of the highest-tensioned tendon (#7) after the unlatch of #8-tendon for the three different environments. There is no transient effect except for the 10 year hurricane condition, where the transient mode analysis gives less tension because the maximum tension is not necessarily at the instant of the unlatch.

Figs.29-30 plot the same cases as Figs.27-28 (top tension of #1 and #7 tendons) for the scenario of two-tendon loss (#2-3 & #8-9). The trends are the same as those for one line damage. For the two line breakage at the top, the increment ratio of the maximum tension for 1000 year hurricane is 93% with the transient mode analysis, while it gives 75% increase without the transient effect. Thus, the difference given by the transient mode is about 18% of the intact maximum tension. For 100 year hurricane and 10 year hurricane conditions, the differences are 14% and 0%, respectively. As a result, the difference due to the transient mode increases significantly as the number of the broken tendon increases for the tendon breakage cases.

Figure 5.28 and Figure 5.29 show the bottom tension and the stroke time histories when one up-wave tendon is broken for the 1000 year hurricane condition, and when two up-wave tendons broken for the 10 year hurricane condition. For 10 year hurricane condition, the negative bottom tension cannot be observed when one up-wave tendon is broken, so the successive one more tendon broken is considered after one most-loaded tendon is broken. Then, the instants of the negative tendon tension to give rise to the down stroke are captured. However, the simulations are based on the fixed bottom boundary condition, and only the negative tension is shown with no stroke. Figure 5.30 and Figure 5.31 shows the results of the down-stroke model for the same conditions. Figure 5.30 is for 1000 year hurricane condition when one up-wave tendon is broken and Figure 5.31 is for 10 year hurricane condition when two up-wave tendons are broken. There is high tensile load when the bottom connector is stroking up right after it down strokes. Small negative tensions are shown when the bottom connector is stroking down due to the friction force model.

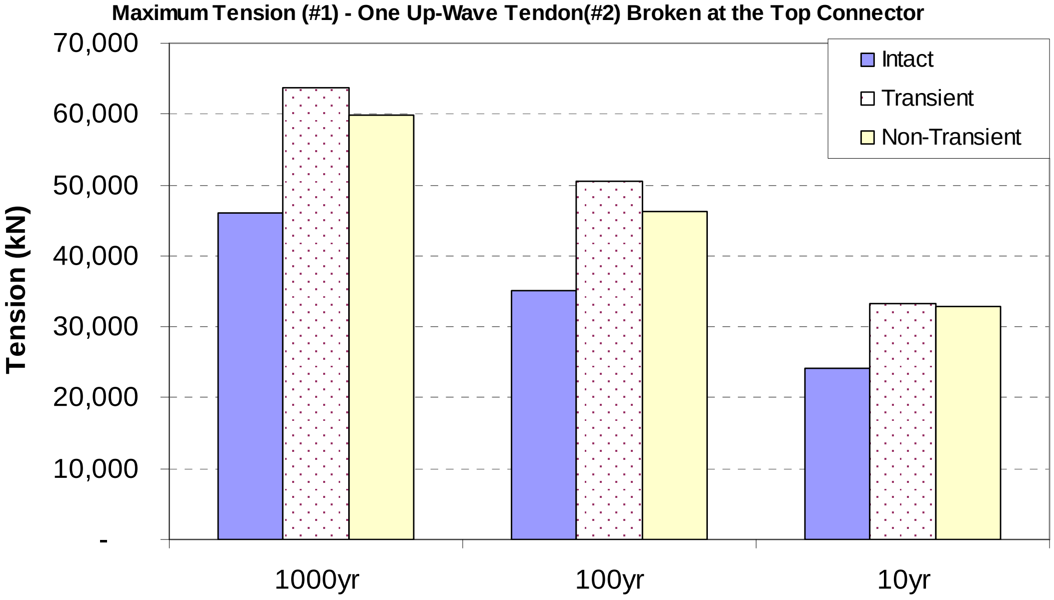

Figure 5.24 Maximum Top Tension of the Neighboring Tendon for Upwave Tendon Breakage at the Top for 1 Tendon Loss

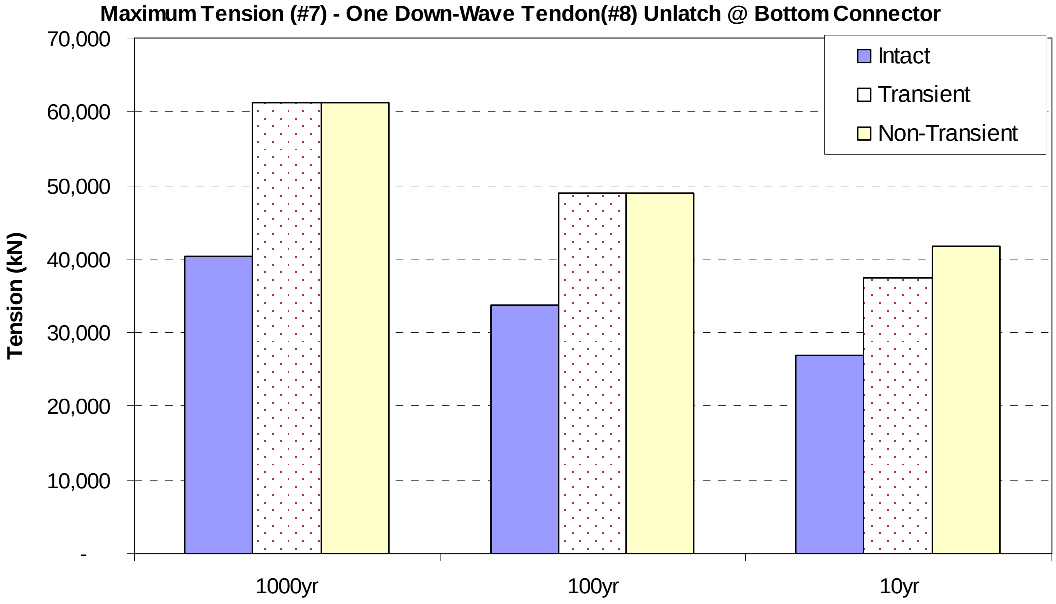

Figure 5.25 Maximum Top Tension of the Neighboring Tendon for Down-wave Tendon Unlatch at the Bottom for 1 Tendon Unlatch

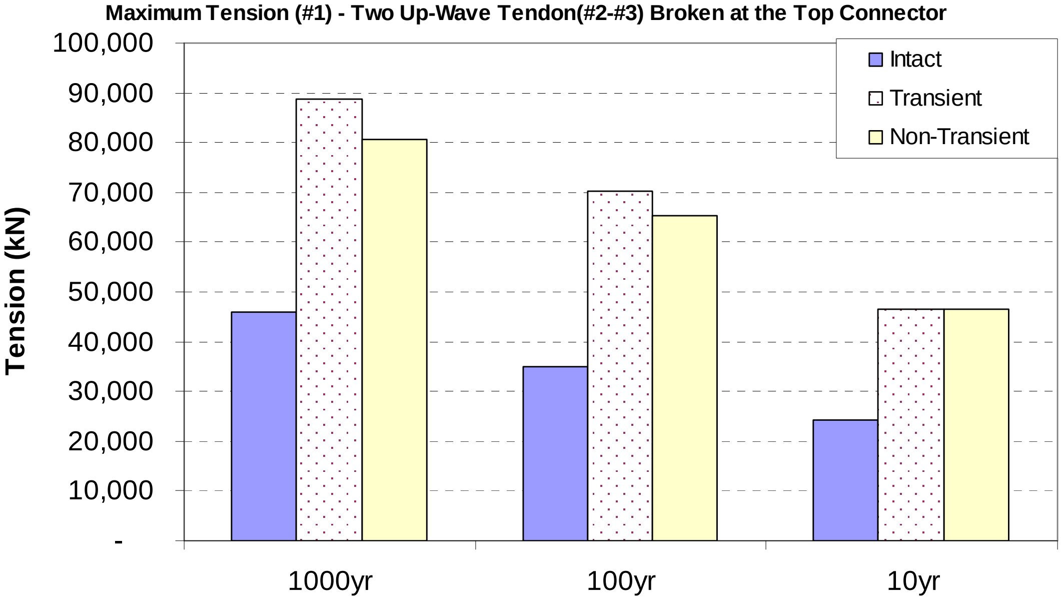

Figure 5.26 Maximum Top Tension of the Neighboring Tendons for Up-wave Tendon Breakage at the Top for 2 Tendon Loss

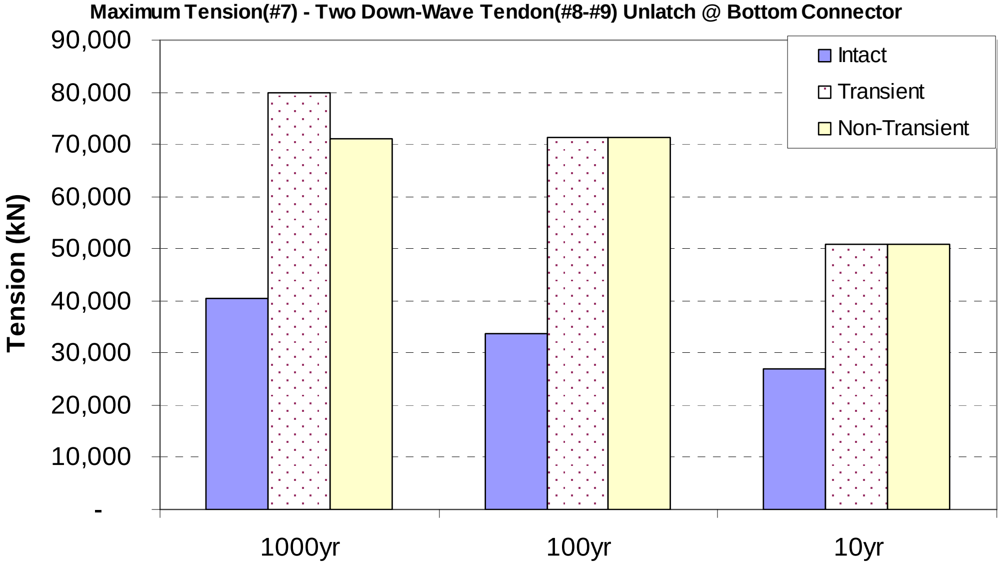

Figure 5.27 Maximum Top Tension of the Neighboring Tendons for Downwave Tendon Unlatch at the Bottom for 2 Tendon Unlatch

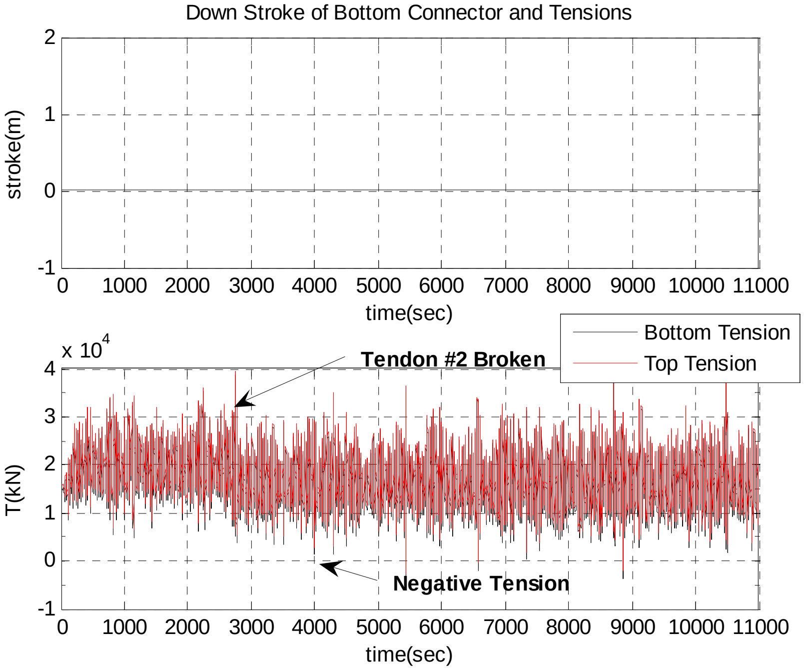

Figure 5.28 Down-wave Tendon Bottom Tension and Stroke after Up-wave Tendon Broken for 1000 Year Hurricane – Fixed Bottom Boundary Model

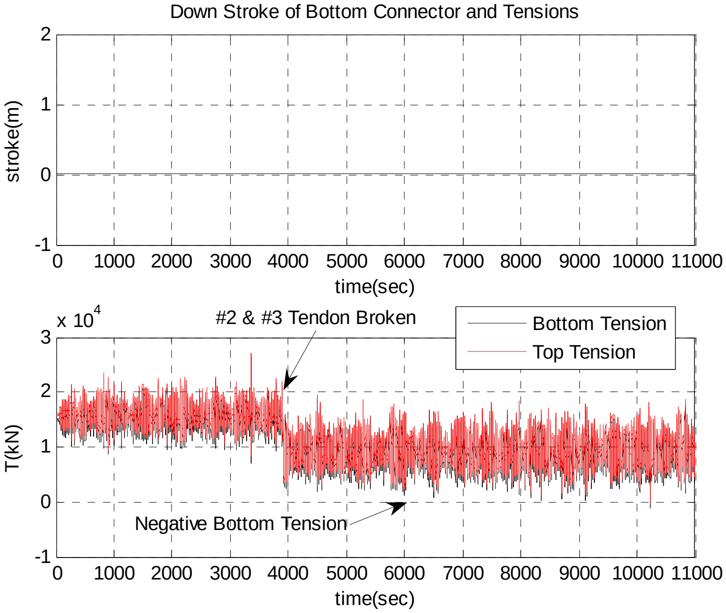

Figure 5.29 Down-wave Tendon Bottom Tension and Stroke after Up-wave Two Tendons Broken for 10 Year Hurricane – Fixed Bottom Boundary Model

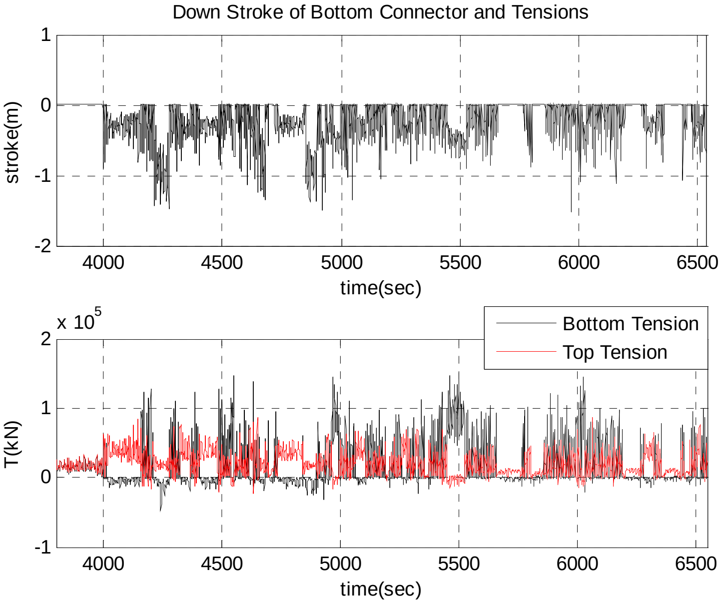

Figure 5.30 Down-wave Tendon Bottom Tension and Stroke after one Up-wave Tendon Broken for 1000 Year Hurricane – Down-stroke Bottom Boundary Model

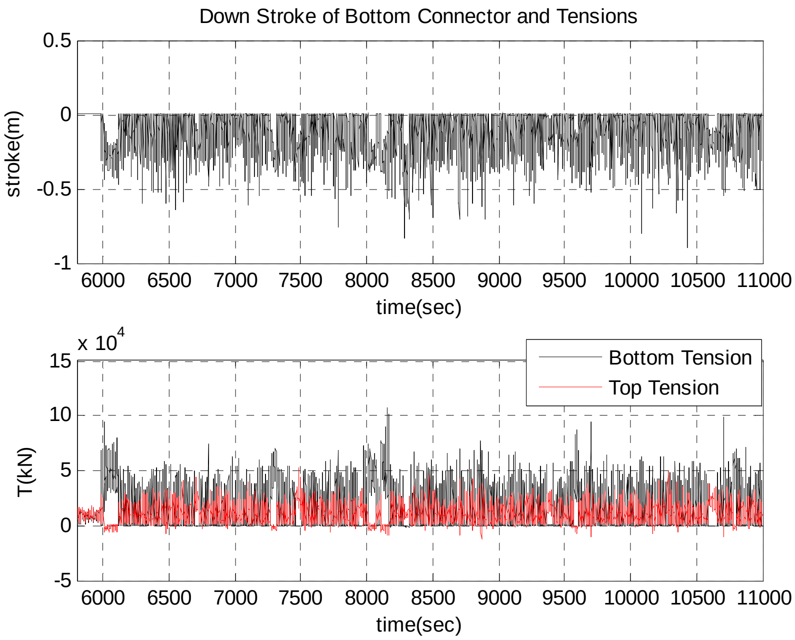

Figure 5.31 Down-wave Tendon Bottom Tension and Stroke after two Up-wave Tendons Broken for 10 Year Hurricane – Down-stroke Bottom Boundary Model

6. CASE STUDY 3: SAFETY ASSESSMENT OF THE DERRICK TIE-DOWN

6.1 Introduction

The performance of the clamps for a rig tie-down on a TLP (Tension Leg Platform) is investigated in 10 year, 100 year and 1000 year hurricane environments. The hurricane Ivan condition is selected as a 1000 year event. The inertia load on the derrick is obtained by the three hour time history of the platform motion, and the wind force as well as the gravitational force are also applied. Then, the connection loads between derrick and substructure and between the substructure and the deck are calculated to determine the safety of the connection during the hurricane environment. The coupled motion between the derrick and the platform is not solved simultaneously, but the linear and nonlinear inertia loads on the derrick are calculated based on the platform motion. The resultant forces are used to calculate the loads on the tie-down clamps at every time step by the quasi-static method.

The exact dynamic equations of derrick and the substructure are set up to include all the linear and the nonlinear force terms with the corresponding phase according to the time simulation which are ignored in the API-4F(API, 1995), where dynamic loads are obtained by linear motion assumption with the phase difference between the force components ignored. Three directional spring model is positioned at the connection point to calculate the shear and axial reaction forces. The calculation is to evaluate the maximum load on the tie-down equipment in the extreme survival condition, and to determine if it is safe from the slip, shear and tensile failure.

WAMIT(Lee et al., 1999) is used to calculate the hydrodynamic coefficients such as added mass and hydrodynamic damping and the first and second wave excitation forces. The external stiffness due to tendon and riser is calculated and included in addition to the hydrostatic stiffness due to hull geometry in WAMIT computation so that more accurate motions are obtained in frequency domain because the second order wave excitation force in frequency domain is motion-dependent. Due to the stiff tendon system of TLP, the heave, roll and pitch natural periods are around 3-4 seconds and the surge and sway natural periods are about 100-160 seconds, which are out of the wave frequency range. Thus, the second order wave loads of sum and difference frequencies are so important that they may not be ignored. The Charm3D is based on the hybrid model of Morison members and a panelized body. The potential forces on column and pontoon are obtained from WAMIT while the viscous effects are considered through the Morison equation.

It is assumed that the system to tie the derrick down to the deck structure is so stiff that the derrick motion relative to the TLP motion does not affect the TLP motion and that the derrick motion is identical to the TLP motion. The spring model is applied to calculate the reaction forces at the tie-down locations, which is necessary for the statically indeterminate problem with the insufficient number of equations compared with the unknowns to be solved. Assuiming there are four tie-down legs, we have 3x4=12 unknowns (3 directional reaction force per each leg), while there are only six

DOF (degrees of freedom) motion equations. To calculate the reaction shear and axial forces at a derrick base, equations of force and moment equilibrium of derrick are set up and solved combined with the spring restoring forces.

The connection may fail if the forces acting on the connector exceed the capacity of slip, shear and tensile failure modes. The capacities are predetermined by the pretension of the bolts, friction coefficient and the number of bolts at each footing (Salmon et al.,1995). The results are examined and discussed in the view point of the safety of a top side component in the severe hurricane condition.

6.2 TLP Specification

The principal dimensions of the platform are tabulated in Table 6.1 (Kim et al., 2001). The TLP consists of four circular columns of 16.46 m (54 ft) outer diameter which are connected at the keel by rectangular pontoons of 8.23 m (27 ft) width and 7.31 m (24 ft) height. The center to center distance is 60.96 m (200 ft). The hull is attached to eight tendons (two tendons at each column), and one drilling TTR and seven production TTRs are connected to the hull by hydraulic pneumatic tensioners at 36.60 m (120.08 ft) above the mean water level (MWL). The detailed configurations are shown in Figure 6.1 by the elevation and the plan views of it, which also shows the location of the TTR slots and the tendon porch.

The In-Place draft, 24.38 m (80 ft), is selected as a base case to estimate the hydrostatic and mass properties. The load condition and corresponding values are shown in Table 6.2. The total weight is 24,157 MT (53,256 kips), the total tendon pretension at the top(porch) is 7,031 MT (15,500 kips), and the riser total pretension at the top is 1,588 MT (3,500 kips). Vertical center of gravity (COG) is at 8.56 m (28.1 ft) above MWL and vertical center of buoyancy (COB) is at 15.18 m (49.8 ft) below MWL. The roll and pitch radii of gyration are 33.19 m (108.9 ft) and the yaw radius of gyration is 32.40 m (106.3 ft).

The wind load coefficient in x- and y- direction is $C_{eff\_X} = C_{eff\_Y} = F_w / V_{10}^2$ $=3.184$ kN/(m/sec)^2 $=0.0665$ kips/(ft/sec)^2 at the center of pressure 38.10 m (125 ft) from MWL, where F_w is total wind force on the hull above MWL and V_{10} is the 1 hour averaged wind speed at 10m level above MWL. For 135 degree heading, The wind load coefficient is obtained by $C_{eff\_135}=1.15\ C_{eff\_X}$ with the same center of pressure.

Eight tendons and 8 TTRs are modeled. The 8 TTRs are modeled as an equivalent one. The tensioner stiffness of a TTR is assumed to be 364.87 kN/m (25 kips/ft). The tendon and TTR configuration is shown in Table 6.3.

Table 6.1 Principal Dimensions of the TLP

Water Depth	(m)	914.36
Number of Column		4
Column Cross Section Diameter	(m)	16.46
Column Center to Center Distance	(m)	60.96
Column Freeboard	(m)	20.42
Pontoon Breadth	(m)	8.23
Pontoon Height	(m)	7.31
Height of Deck Bottom from MWL	(m)	22.86
Deck Height	(m)	12.19

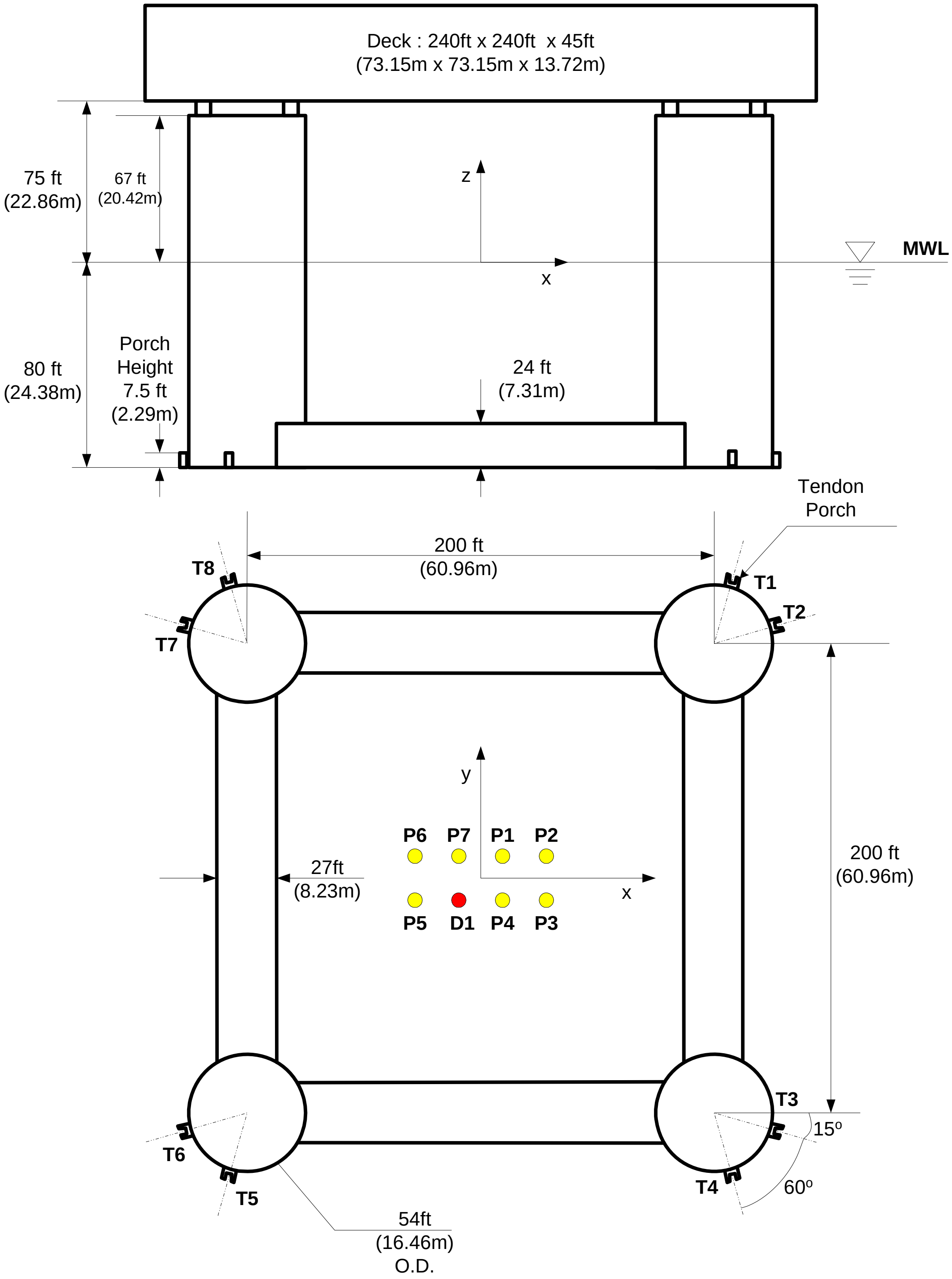

Figure 6.1 Configuration of the TLP Hull

Table 6.2 Hull Load Condition at In-Place Draft

Draft	(m)	24.38
Total weight	(MT)	24,157
Tendon Pretension at the top	(MT)	7,031
Riser Pretension at the top	(MT)	1,588
Displacements	(MT)	32,775
Vertical Center of Gravity from MWL	(m)	8.56
Vertical Center of Buoyancy from MWL	(m)	-15.18
Roll Radius of Gyration	(m)	33.19
Pitch Radius of Gyration	(m)	33.19
Yaw Radius of Gyration	(m)	32.40
Wind Load Coefficient*	(kN/(m/sec)^2)	3.18
Center of Pressure from MWL	(m)	38.10

* Wind load coefficient is for x- and y- direction, and 1.414 times of it is used for 135 degree heading.

Table 6.3 Configuration of the Tendons and TTRs

	#	X (m)	Y (m)	Z (m)	X (m)	Y (m)	Z (m)	To(MT)
Tendon	1	33.01	39.90	-22.10	33.01	39.90	-914.36	880.0
	2	39.90	33.01	-22.10	39.90	33.01	-914.36	880.0
	3	39.90	-33.01	-22.10	39.90	-33.01	-914.36	880.0
	4	33.01	-39.90	-22.10	33.01	-39.90	-914.36	880.0
	5	-33.01	-39.90	-22.10	-33.01	-39.90	-914.36	880.0
	6	-39.90	-33.01	-22.10	-39.90	-33.01	-914.36	880.0
	7	-39.90	33.01	-22.10	-39.90	33.01	-914.36	880.0
	8	-33.01	39.90	-22.10	-33.01	39.90	-914.36	880.0
Drilling Riser	1	-2.29	-2.29	36.60	-2.29	-2.29	-914.36	205.9
Production Riser	1	2.29	2.29	36.60	2.29	2.29	-914.36	104.3
	2	6.86	2.29	36.60	6.86	2.29	-914.36	104.3
	3	6.86	-2.29	36.60	6.86	-2.29	-914.36	104.3
	4	2.29	-2.29	36.60	2.29	-2.29	-914.36	104.3
	5	-6.86	-2.29	36.60	-6.86	-2.29	-914.36	104.3
	6	-6.86	2.29	36.60	-6.86	2.29	-914.36	104.3
	7	-2.29	2.29	36.60	-2.29	2.29	-914.36	104.3

6.3 Hydrodynamic Modeling

The added mass and radiation damping coefficients, first-order wave excitation forces, and second order sum and difference frequency forces are calculated by the second-order diffraction/radiation program, WAMIT[2]. The tendons and the TTRs are considered as an external stiffness in the frequency domain calculation. The stiffness is added to the hydrostatic stiffness due to the hull geometry, which increases the accuracy of the motion response and the second order forces as well. All the hydrodynamic coefficients are calculated in the frequency domain, and the corresponding forces are converted to the time domain using two-term Volterra series expansion. The frequency-dependent radiation damping was included in the form of convolution integral in the time domain simulation. In Figure 6.2, the panel configuration for the WAMIT is shown. The body fixed coordinate reference is on the free surface at the centroid of water plane area of the columns. The x-axis is parallel to the pontoon and the z-axis is upward positive. The TLP hull is discretized by 1420 panels and the free surface is discretized by 1070 panels inside a truncation radius.

The tendons and the risers are modeled by a FE method based on the slender rod theory (Garret., 1982). The tendons and the risers are all attached down to the sea bed with linear spring. The tendons are also coupled with the hull by the linear spring, while the TTRs are couple with it by numerical pneumatic tensioner model(Yang et al., 2006).

6.4 Environmental Criteria

10 year, 100 year and 1000 year return hurricane events are selected as environmental conditions. Table 6.4 shows the typical wave, wind and current

characteristics of each environmental condition. JONSWAP spectrum is used for the long crested irregular wave generation with the given peakedness parameter, Gamma. A time history of the wave signal and the power spectrum is exemplified for 1000 year hurricane condition in Figure 6.3. The Time varying wind speed is generated by using the API spectrum. Wave incident angle is assumed to be 135 degrees, and the wind and the current are associated with the wave in the direction. The current profiles which are varying in depth are applied on the submerged part of the platform.

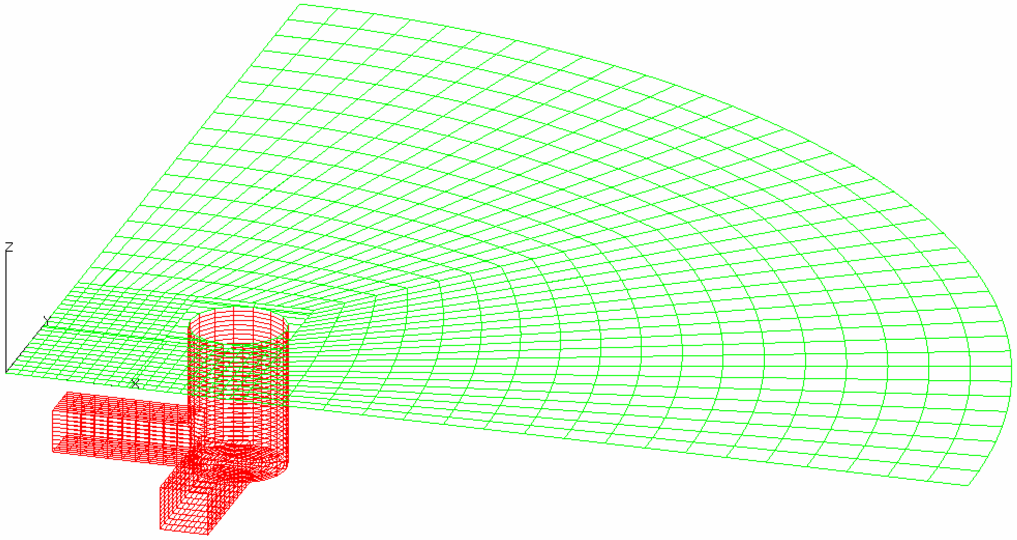

Figure 6.2 Panel for Hydrodynamic Computation by WAMIT and Body Fixed Coordinate System

Table 6.4 Environmental Criteria

Return Period	10 year		100 year		Ivan (1000 year)	
Hs (m)	7.59		12.19		15.57	
Tp (sec)	11.9		14		15.6	
Gamma *	2.4		2.4		3	
Wind Speed** (knot)	50.9		81.3		87.9	
Current Profile	Depth(m)	Speed(m/s)	Depth(m)	Speed(m/s)	Depth(m)	Speed(m/s)
	0.00	0.79	0.00	1.50	0.00	2.50
	29.99	0.60	29.99	1.15	5.00	2.50
	60.01	0.29	60.01	0.56	24.99	1.19
	90.00	0.10	90.00	0.10	50.02	1.12
	914.36	0.10	914.36	0.10	80.49	0.74
					100.00	0.31
					150.02	0.29
					300.00	0.27
					914.36	0.00

* JONSWAP spectrum is used for the irregular wave generation with the given peakedness parameter (Gamma)

** The wind speed is 1 hour averaged one at 10m above MWL, and API wind spectrum is used for the time varying wind speed generation.

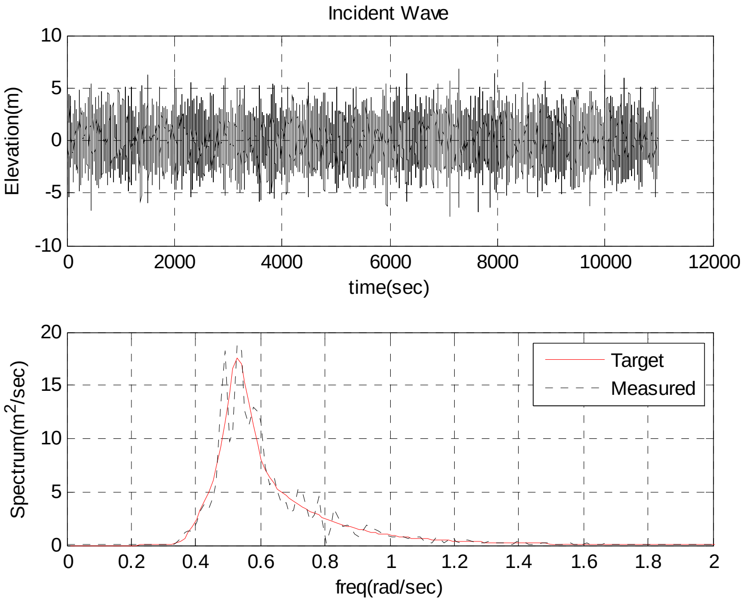

Figure 6.3 Incident Wave Time History and the Measured Power Spectrum Compared with the Target Spectrum (1000 Year Hurricane; Hs=15.82m, Tp=15.6, γ =3.0)

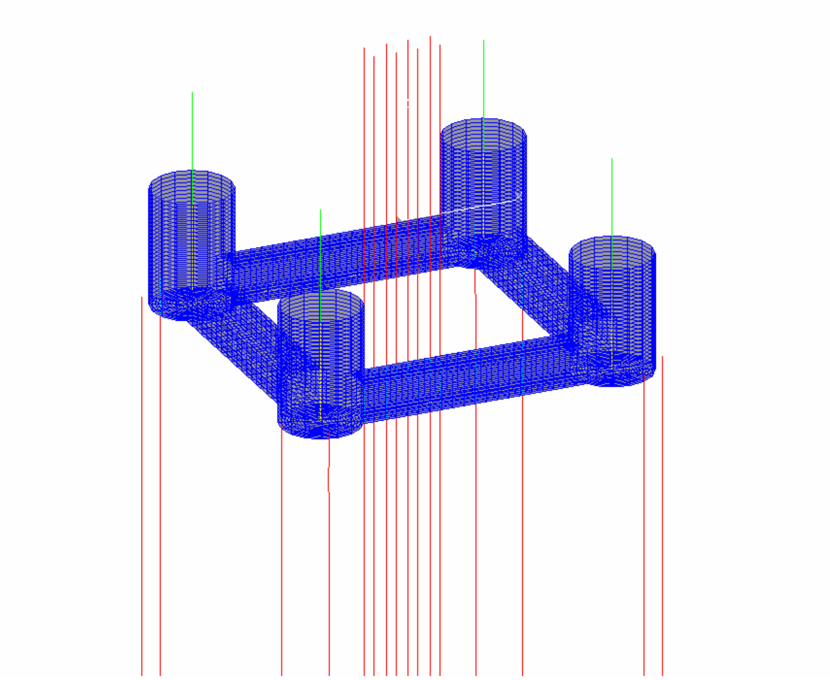

Figure 6.4 Zoom in of the Global Configuration of the System

6.5 Results

Figure 6.4 shows the global configuration of the platform and tendon/riser coupled system, where the TTRs are attached at the mean water level and the tendons are attached to the porch location. Y-axis is to the platform north and the x- axis is to the platform east, and the z-axis is pointing upward. The origin of the body coordinate is at the center of floatation on the mean water level. The water depth is 914 m (3000 ft).

The static offset, set-down curve in 135degree direction is shown in Figure 6.5. The free decay test to measure the natural period and the damping ratio is carried out for six modes and the results are shown in Table 6.5. The heave natural period is 3.35 seconds and the roll/pitch natural periods are 3.01/2.96 seconds. The surge and sway natural periods are around 170 seconds with the damping ratio of 11-12% of the critical damping.

A definition sketch of the free body diagram of the deck on the platform with the applied forces is shown in Figure 6.6. The gravity, inertia and wind loads as well as the connector reaction force on the derrick are taken in to account as was previously described.

Detailed configuration of the derrick and the substructure are introduced in Figure 6.7. The derrick is connected to the deck through the substructure. The footings of derrick connect the derrick and the substructure, and the substructure footings support the derrick and the substructure. The substructure footing is 33.36 m (116 ft) from the mean water level and the upper derrick footing is positioned 9.14 m (30 ft) above the substructure footing.

Table 6.5 Natural Period and Damping Factor

	Tn (sec)	X Critical Damping
Surge	169.98	11.15%
Sway	169.98	11.98%
Heave	3.38	4.77%
Roll	2.96	4.70%
Pitch	3.02	4.01%
Yaw	124.58	8.90%

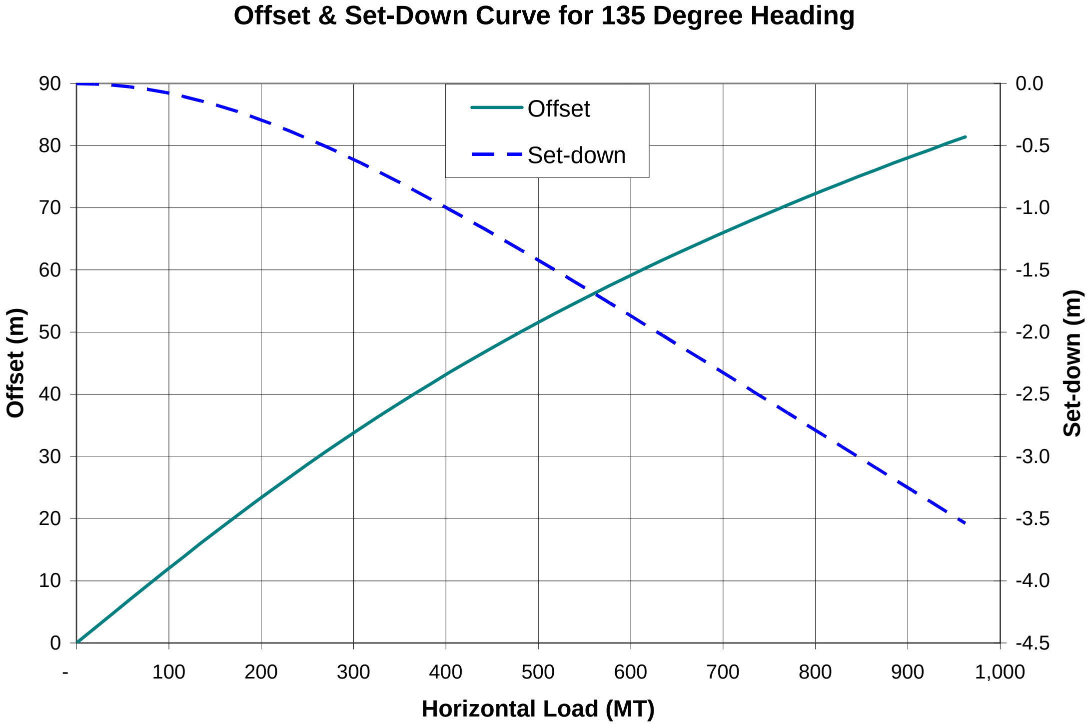

Figure 6.5 Static Offset and Set-down Curve in 135 Degree Heading

A plan view of the footing layout is in Figure 6.8. The upper derrick footings are on the rail which is parallel to the y-axis to allow the slip only in y-direction. The shear force in x-direction is transferred to the bolt directly and the bolts need to resist the shear force. On the contrary, the substructure footings are laid on the rail parallel to x-direction to allow the slip in x-direction. Thus, the y-directional shear forces are totally transferred to the bolts.

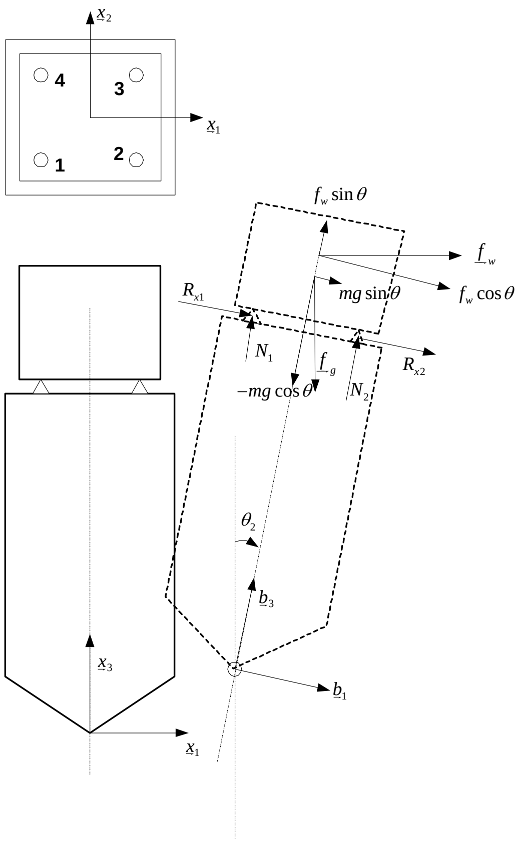

Figure 6.6 Definition Sketch of the Coordinate System and Free Body Diagram of the Derrick

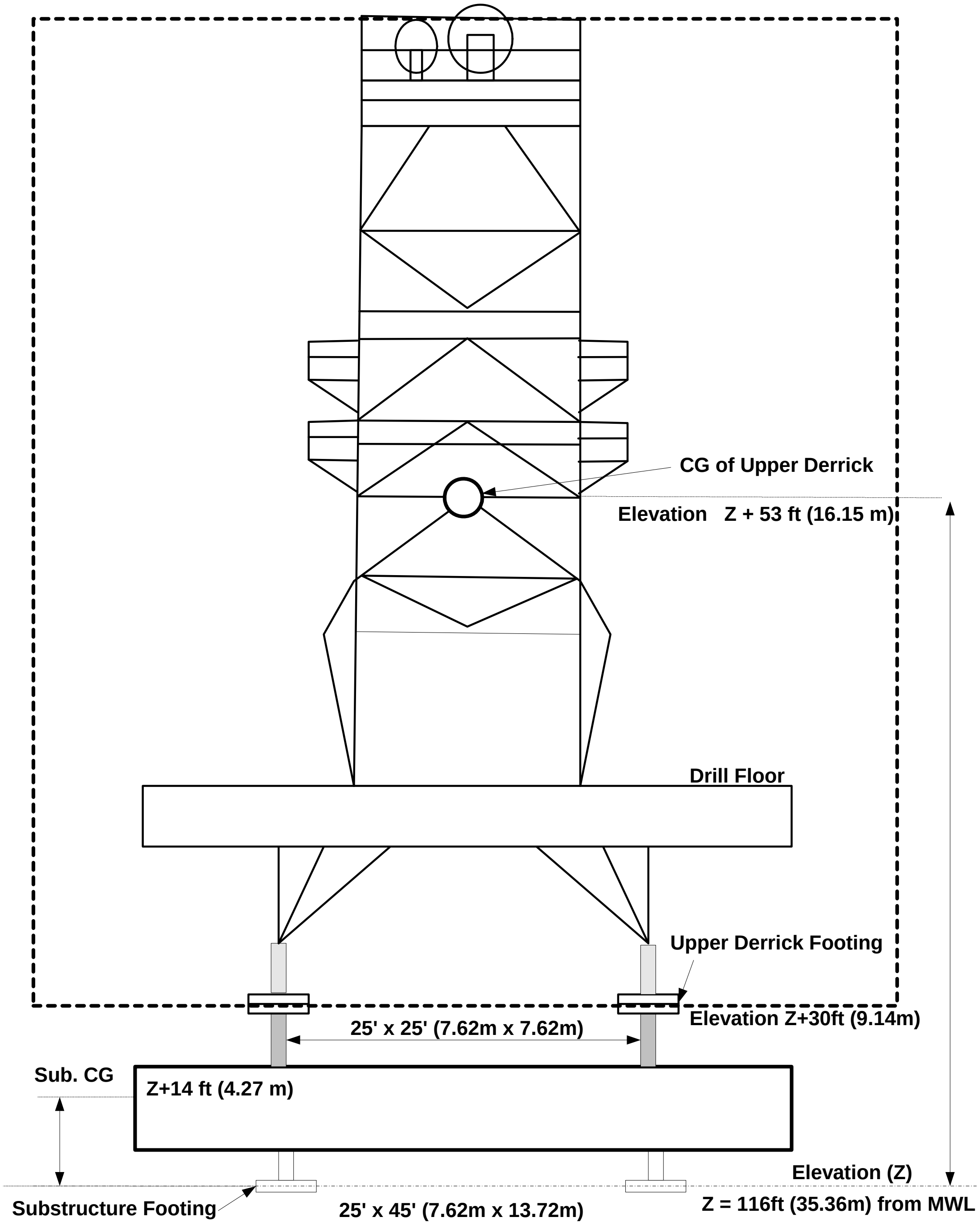

Figure 6.7 Configuration of the Derrick and the Substructure

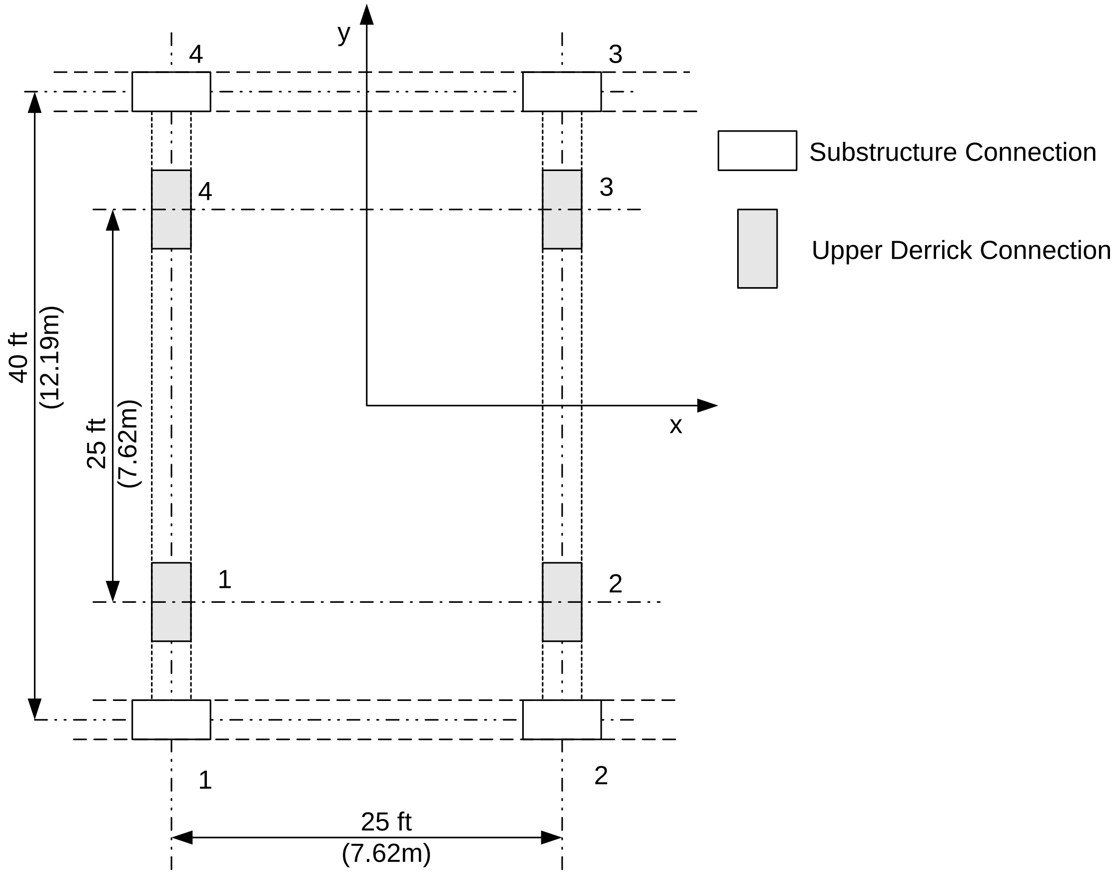

Figure 6.8 Configuration of the Upper Derrick and the Substructure Footings

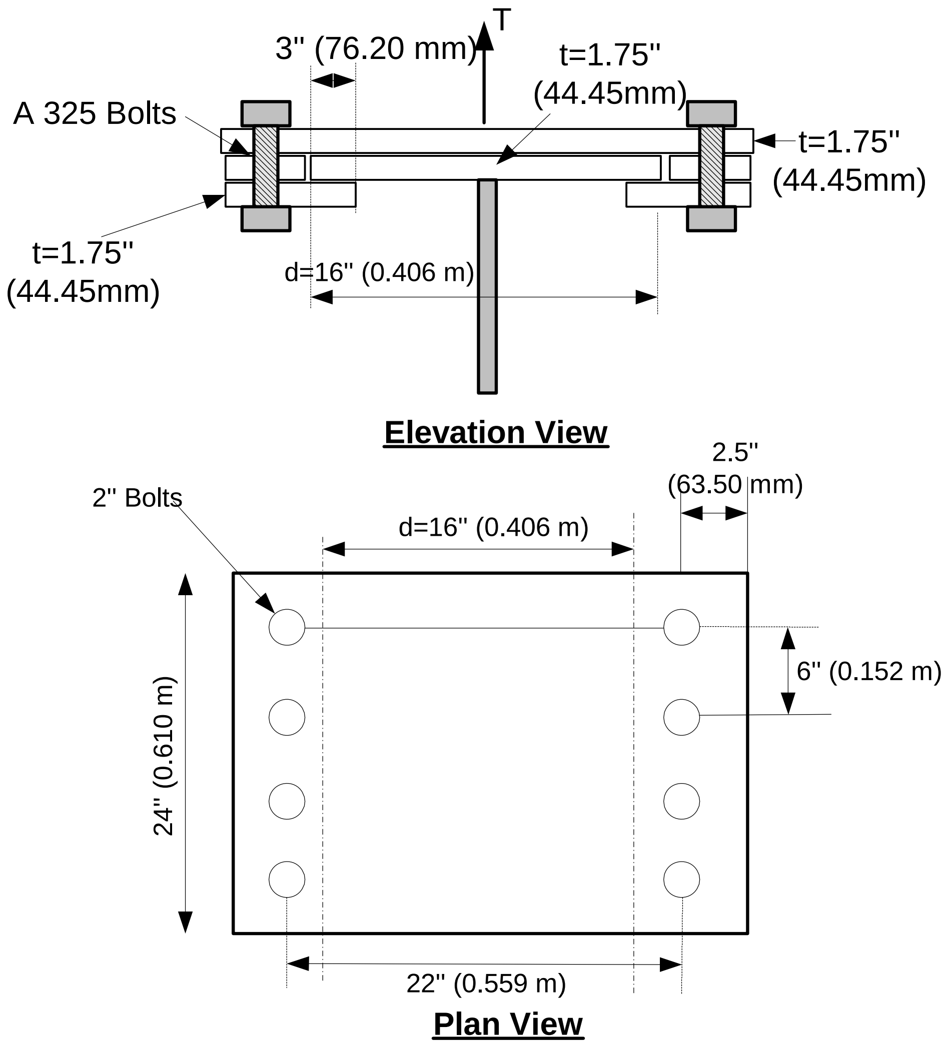

Figure 6.9 A Typical Connection at Derrick Base and Substructure Base

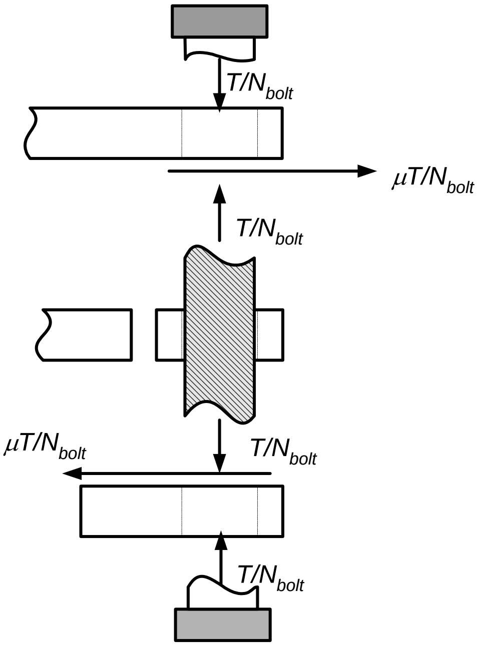

Figure 6.10 Transfer of Load in Pretensioned High Strength Bolted Connection

Each footing has the eight bolts to give the pretension for the slip, shear and tensile capacity as in Figure 6.9. Due to the layout of the bolts, the shear force is applied only to 4 bolts, while the tensile force is uniformly applied to 8 bolts. Therefore, the capacity of the shear force for a footing is determined by 4 bolts and the tensile capacity is by 8 bolts. 1-1/2 inch bolts are used to tie down the structure and the corresponding shear and the tensile capacities for each bolt are estimated through the material property. Figure 6.10 shows the mechanism how the pretensioned bolted connection transfer the load in the form of the friction force. The pre-tension generates the slip resistance by the friction force which is also dependent on the friction factor between two contacting materials.

Table 6.6 Friction Resistance Capacity (Slip Capacity)

Torq (N-m)	T0 (kN)	Friction Coeff	P0(kN)	Ptot (kN)	Pder	Pder_tot	Psub	Psub_tot
3,389	334	0.1	33	267	61	328	228	495
		0.3	100	801	183	984	684	1,485
		0.5	167	1,334	306	1,640	1,140	2,474
6,205	**611**	**0.1**	61	489	61	550	228	717
		0.3	183	1,466	183	1,649	684	2,150
		0.5	305	2,443	306	2,749	1,140	3,583
6,779	667	0.1	67	534	61	595	228	762
		0.3	200	1,601	183	1,785	684	2,285
		0.5	334	2,669	306	2,975	1,140	3,809
10,168	1,001	0.1	100	801	61	862	228	1,029
		0.3	300	2,402	183	2,586	684	3,086
		0.5	500	4,003	306	4,309	1,140	5,143

*P0 – Bolt Pretension Slip Capacity
*Ptot – Total Slip Capacity of a Flooting by the Bolt Pretension (=P0 × the Number of Bolts)
*Pder – Slip Capacity of the Upper Derrick Footing by the Derrick Weight
*Pder_tot – Total Slip Capacity of the Upper Derrick Footing by the Derrick Weight and the Pretension
*Psub – Slip Capacity of the Substructure Footing by the Weight
*Psub_tot Total Slip Capacity of the Substructure Footing by the Weight and the Pretension.

Table 6.7 Tensile Capacity with Pretension

Rn (kN)	Bolt Pretension (kN)	Ten. Cap. per Bolt (kN)	Total Capacity (kN)
1,100	334	767	6,135
1,100	611	490	3,918
1,100	667	433	3,466
1,100	1,001	100	797

Table 6.8 Shear Capacity of the Bolts

Shear Capacity per Bolt =	Rn =	909.7	kN
Total Connection Shear Capacity =	(N/2)*Rn=	3,639.0	kN

The slip, tensile and shear capacity of the footings and each bolt are summarized in Table 6.6, Table 6.7 and Table 6.8, respectively. Four pretensions are considered for the study, among which T0=611kN is AISC (American Institute of Steel Construction) recommended. The higher the pretension is, the higher the slip capacity with the same friction factor, but the lower the tensile capacity is. The slip capacity also varies depending on the friction factor (μ), and $\mu = 0.1$, 0.3 and 0.5 are considered in the study as introduced in Table 6.6.

The derrick and the substructure are assumed to be positioned at the center of the deck, i.e. at the CG of the TLP. The VCG of the derrick and the substructure are shown in Table 6.9. The center of pressure of the wind force and the wind area of derrick and the substructure are also shown in the table. For the derrick, the projected area in x-direction is 136.55 m^2 (1470 ft^2), but the front part does not shade the area at the down stream. Thus, the double of the projected area 273.11 m^2 (=2940 ft^2) is used. The wind areas are all for head and beam sea, and the wind area for oblique sea (135 degree) is approximated to be 1.414 times of that of head and beam sea.

The total wind forces are calculated based on the projected area, shape coefficient and height coefficient as follows.

$$F_{wind} = 1/2 \rho_{air} A_{project} C_h C_s V_{10m}^2 \left(t\right)$$

, where $V_{10m}(t)$ is the instantaneous wind velocity at 10m above mean water level and ρ_{air} is the air density. The resultant total wind area and the center of wind pressure at the last column are used to calculate the reaction forces on the substructure footings. C_h is the height coefficient to adjust the height of wind velocity from 10 m to the wind pressure center, and C_s is the shape coefficient to represent the drag coefficient. The radius of gyrations in roll, pitch and yaw directions are also given in the table.

6.6 Derrick Motion

Derrick motion statistics for 3 hour simulation are shown in Figure 6.11. The maximum offset at CG is 12.57% of WD for 100 year hurricane condition, and the maximum set down is -7.13 m under the condition. The maximum single amplitude heel angle which will give rise to the gravitational acceleration in the horizontal component of gravity on the derrick is 0.51 degrees for 100 year condition.

Table 6.9 Specifications of Upper Derrick

	Upper Derrick	Substructure	Total
Weight (MT)	249.48	680.40	929.87
Projected Area* (m^2)	273.11	46.45	319.56
Center of Pressure from MWL (m)	61.26	39.62	57.91
Center of Gravity from MWL (m)	51.51	39.62	42.82
Height Coefficient(Ch)	1.37	1.19	1.24
Shape Coefficient(Cs)	1.25	1.25	1.25
Radius of Gyration around CG (m)	4.57/4.57/3.05	4.57/4.57/3.05	6.10/6.10/3.05

* The projected area is for x- and y- direction, and 1.4142 times of it is used for 135 degree heading.

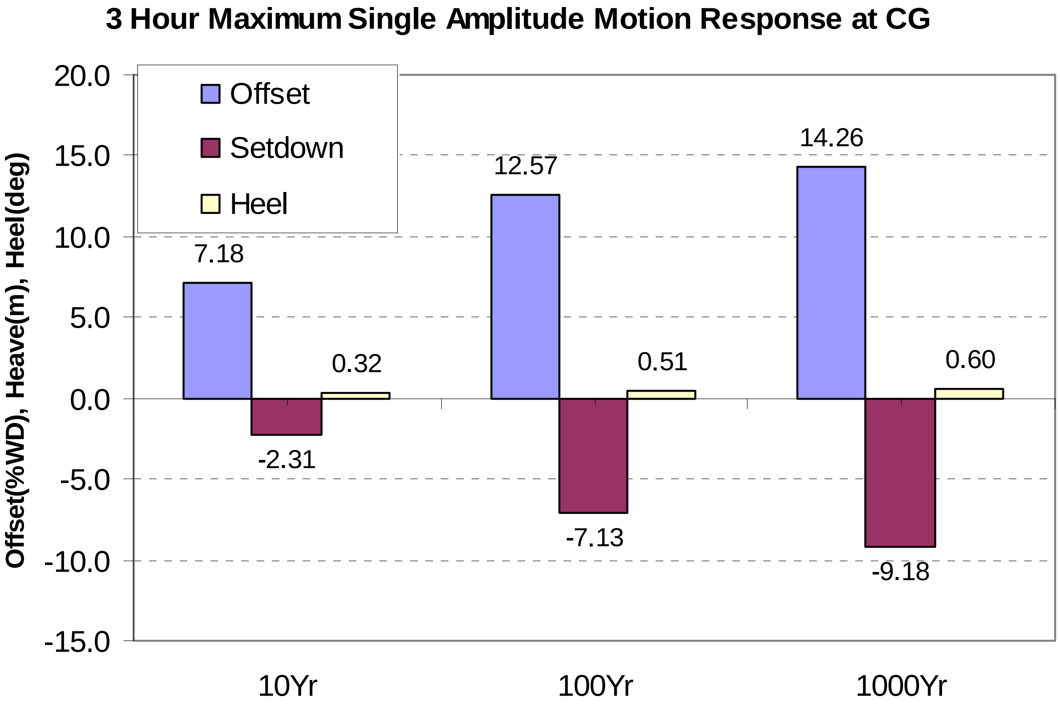

Figure 6.11 Statistics of System COG Motion

6.7 Derrick Acceleration

The API 4F recommend to calculate the maximum horizontal and vertical acceleration to design the structure by combining rotational motion as:

$$a_{x\max} = r\omega_P^2\theta_{\max} + g\sin\theta_{\max}$$
$$a_{z\max} = \omega_H^2 z_{\max}$$

, where

$\theta_{\max}$ = maximum pitch motion,

r = distance from CG to the point under consideration,

g = gravitational acceleration,

$z_{\max}$ = maximum heave,

ω_P , ω_H = pitch and heave periods.

Table 6.10 through Table 6.12 show the maximum x-acceleration and z-acceleration obtained in different 3 ways. The “API 4F” is obtained through the above equation, The “API Revised” is the method to calculate the low, wave and high frequency maximum acceleration separately, and to add all to get the total maximum acceleration. The “Measured” is the measured one through the time simulation. The “API Revised” gives closer values to the simulated one, and the current API method gives less magnitude of acceleration because the method only includes the wave frequency motion.

6.8 Dynamic Forces on Derrick and Substructure

Figure 6.12 exemplifies the resultant time history of inertia, gravity and wind force and moments acting on the upper derrick 1000 year hurricane condition, where the moment is with respect to the upper derrick footing level. The 3 hour maximum x-, and y- total force and each component are obtained and plotted in Figure 6.13 and Figure 6.14, respectively. The upper derrick horizontal force is more dominated by the wind force component. The substructure with derrick is dominated by inertia for 10 year hurricane condition, and the wind force component gets the more portion.as the environment become more severe. The gravity component on the horizontal force is very minor compared with the other components.

Table 6.10 Comparison of the Acceleration at the Center of the Derrick+Substructure (10 Year)

		Surge Acc. RMS			Pitch RMS / Max (deg)	Peak Period (sec)	3Hr Max Horz. Acc		Heave RMS (m)	Peak Period (sec)	Vert. Acc. Max (m/s^2)
		@ CG (m/s^2)	@ Sub-Foot (m/s^2)	@ Up-Foot (m/s^2)			@ Sub. CG (m/s^2)	@ Up.CG (m/s^2)			
Low Frequency		0.008	0.008	0.008	0.006	88.289	0.021	0.021	0.236	159.896	0.001
Wave Frequency		0.167	0.172	0.173	0.033	9.746	0.496	0.504	0.052	11.638	0.041
High Frequency		0.041	0.044	0.045	0.004	3.775	0.139	0.146	0.004	4.042	0.028
3Hr Max.	Coupled Analysis	0.607	0.623	0.628	0.170		0.625	0.632			0.078
	API 4F	0.167			0.033	9.746	0.496	0.504	0.052	11.638	0.041
	Revised						0.636	0.651			0.069

Table 6.11 Comparison of the Acceleration at the Center of the Derrick+Substructure (100 Year)

		Surge Acc. RMS			Pitch RMS / Max (deg)	Peak Period (sec)	3Hr Max Horz. Acc		Heave RMS (m)	Peak Period (sec)	Vert. Acc. Max (m/s^2)
		@ CG (m/s^2)	@ Sub-Foot (m/s^2)	@ Up-Foot (m/s^2)			@ Sub. CG (m/s^2)	@ Up.CG (m/s^2)			
Low Frequency		0.017	0.017	0.017	0.019	74.522	0.048	0.048	0.590	123.424	0.003
Wave Frequency		0.345	0.35	0.352	0.052	10.665	0.997	1.007	0.321	15.157	0.148
High Frequency		0.047	0.052	0.054	0.006	3.738	0.167	0.178	0.007	4.217	0.045
3Hr Max.	Coupled Analysis	1.189	1.196	1.199	0.358		1.197	1.201			0.251
	API 4F	0.345			0.052	10.665	0.997	1.007	0.321	15.157	0.148
	Revised						1.165	1.186			0.193

Table 6.12 Comparison of the Acceleration at the Center of the Derrick+Substructure (1000 Year)

		Surge Acc. RMS			Pitch RMS / Max (deg)	Peak Period (sec)	3Hr Max Horz. Acc		Heave RMS (m)	Peak Period (sec)	Vert. Acc. Max (m/s^2)
		@ CG (m/s^2)	@ Sub-Foot (m/s^2)	@ Up-Foot (m/s^2)			@ Sub. CG (m/s^2)	@ Up.CG (m/s^2)			
Low Frequency		0.015	0.015	0.015	0.016	78.013	0.042	0.042	0.521	130.162	0.003
Wave Frequency		0.277	0.282	0.284	0.046	10.229	0.809	0.819	0.187	13.775	0.105
High Frequency		0.047	0.052	0.053	0.005	3.755	0.162	0.171	0.007	4.234	0.045
3Hr Max.	Coupled Analysis	0.944	0.953	0.956	0.301		0.954	0.958			0.181
	API 4F	0.277			0.046	10.229	0.809	0.819	0.187	13.775	0.105
	Revised						0.972	0.990			0.150

The total horizontal force on the derrick and substructure is about 15% less than the summation of the maxima of each component, and the total force on the upper derrick is about 10% less than the summation of the maxima of each component. Thus, the phase between the force components should be taken into account to avoid too much conservatism (10-15%) on the top of the design margins when designing the topside structure.

Figure 6.15 shows the 3 hour maximum vertical force component and the total force, which is totally governed by the weight.

The 3 hour maximum roll and pitch moment on the (derrick+substructure) and the upper derrick are plotted in Figure 6.16 and Figure 6.17, respectively. The moments are dominated by the wind because the center of the pressure is much higher than the vertical center of gravity of the structures. For 1000 year condition, the total heeling moments on the (derrick+substructure) and upper derrick are $\sqrt{M_x^2 + M_y^2}$ = 42,420 kN-m and 24,040 kN-m(Figure 6.16 and Figure 6.17).

If the simple summation of the component maxima is used as a total moment, the total heeling moment on the (derrick+substructure) can be approximated to 47,406 kN-m (see Figure 6.16 and Figure 6.17), which is about 12% larger than that from the current method (42,420kN-m).

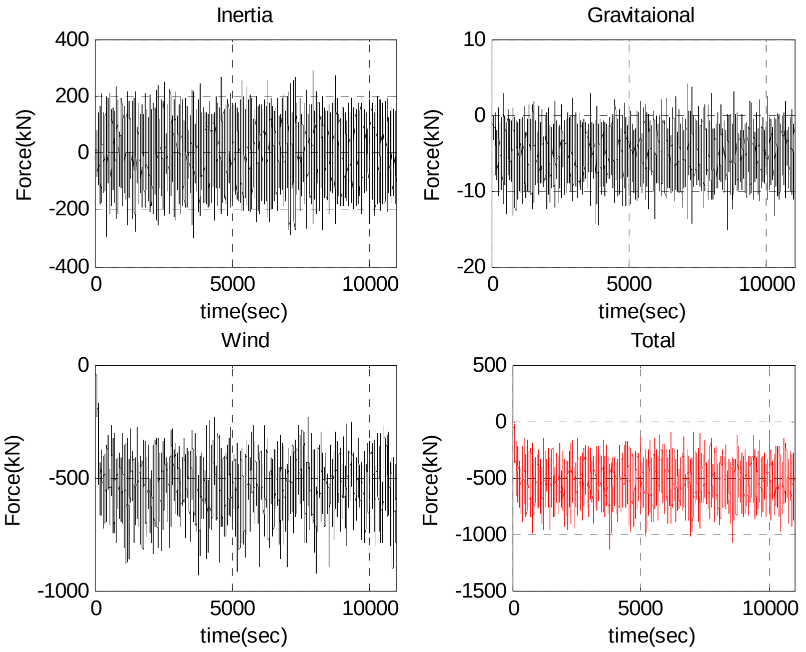

(a) Surge Direction

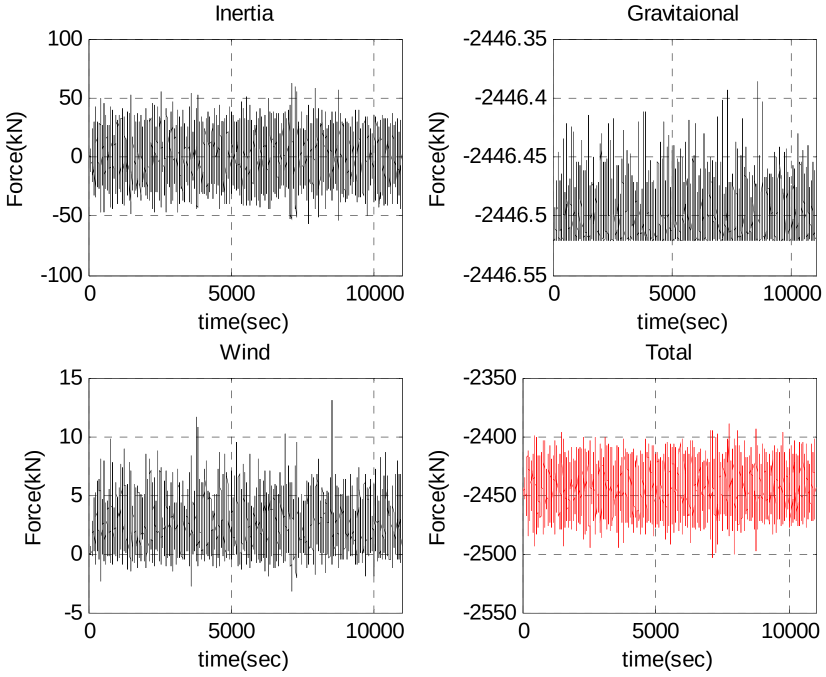

(b) Heave Direction

Figure 6.12 Resultant Inertia, Gravitational and Wind Forces and Moments Acting on the Upper Derrick for 1000 Year Hurricane Condition (Moment is with Respect to the Derrick Footing Level)

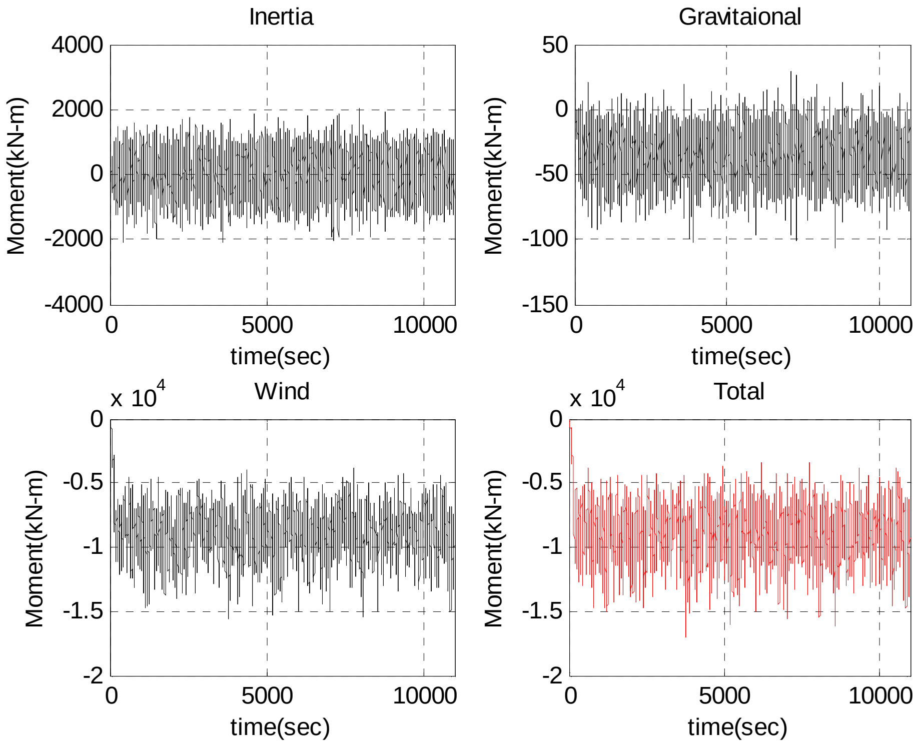

(c) Pitch Direction

Figure 6.12 Continued

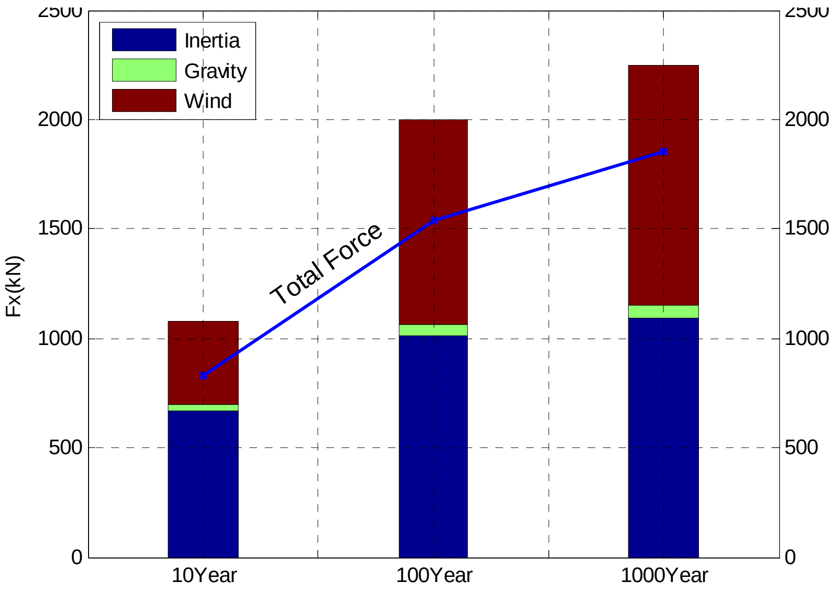

(a) Derrick and substructure

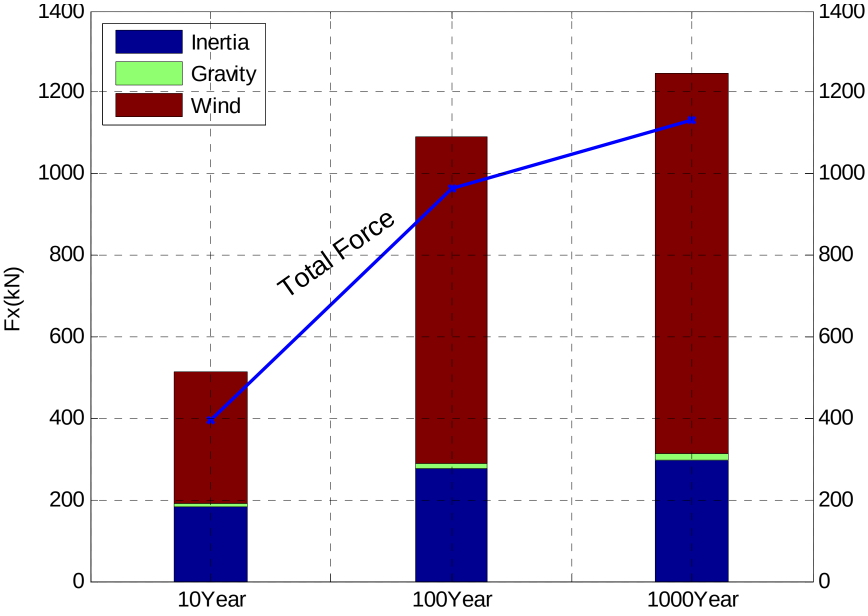

(b) Upper Derrick

Figure 6.13 Total x-Directional Force and the Force Breakdown Acting on the Derrick

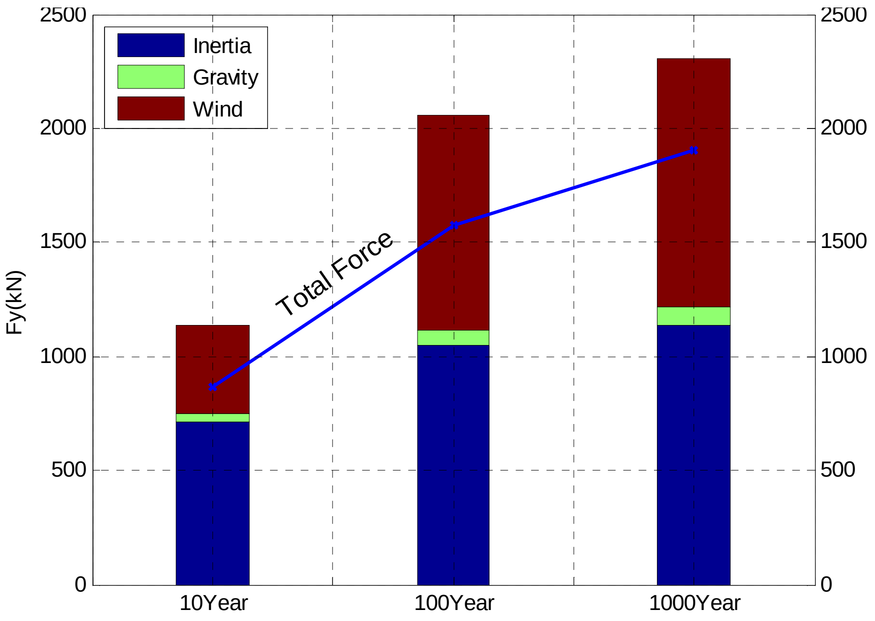

(a) Derrick and substructure

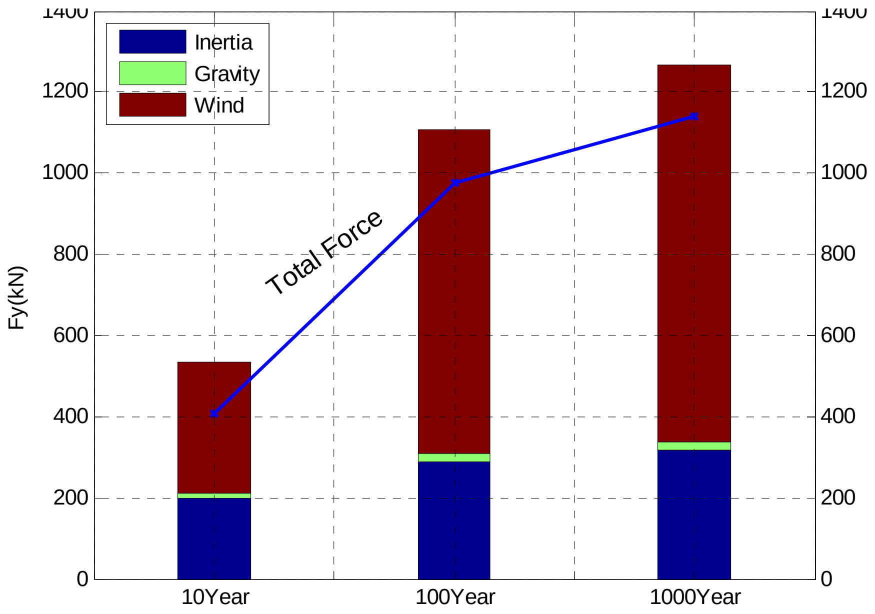

(b) Upper Derrick

Figure 6.14 Total y-Directional Force and the Force Breakdown Acting on the Derrick

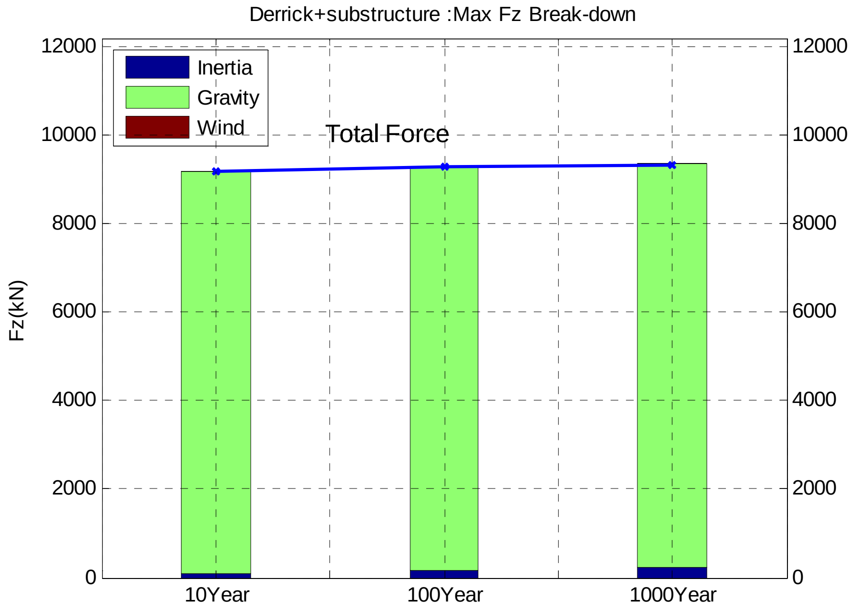

(a) Derrick and substructure

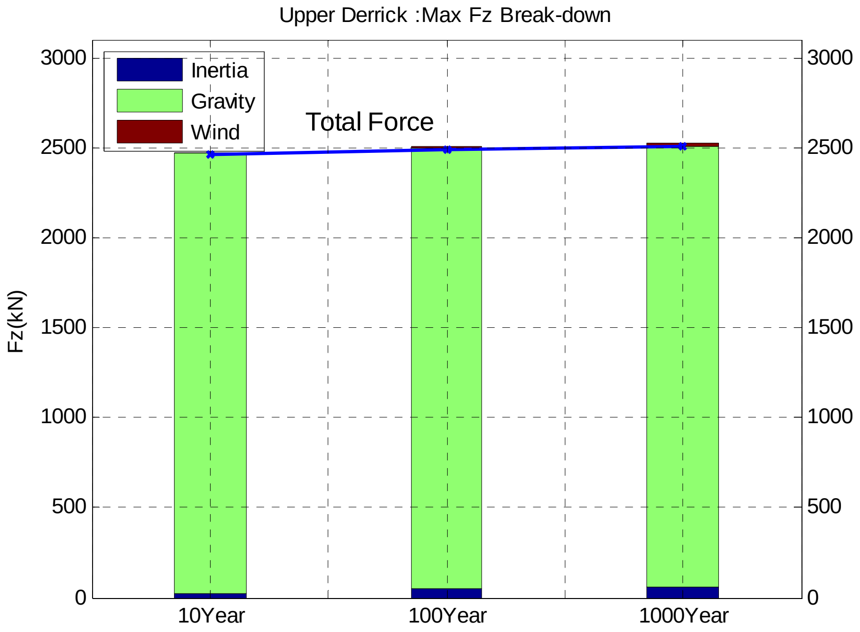

(b) Upper Derrick

Figure 6.15 Total Vertical Force and the Force Breakdown Acting on the Derrick

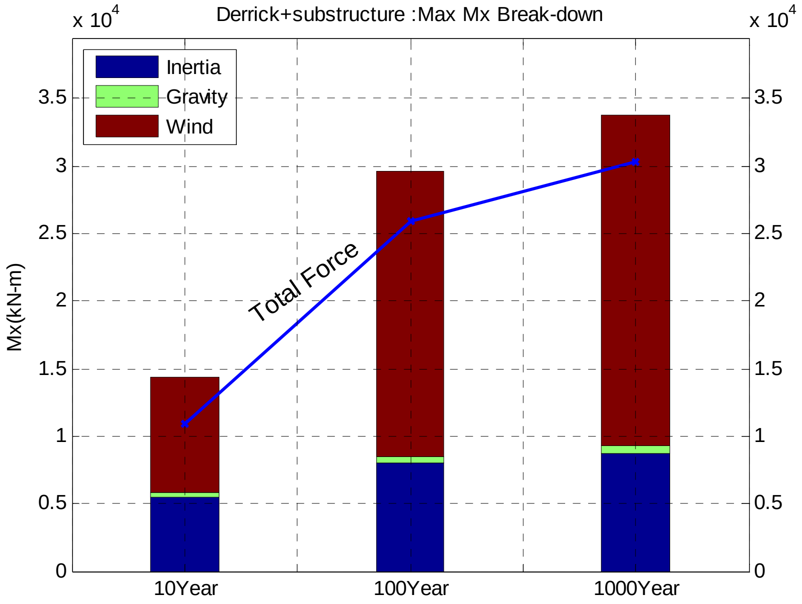

(a) Derrick and substructure

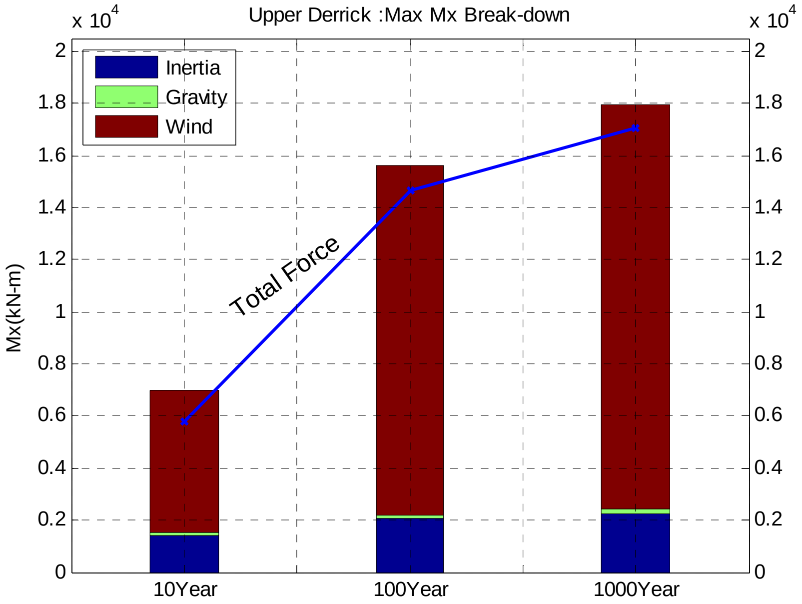

(b) Upper Derrick

Figure 6.16 Total x-Directional Moment and the Moment Breakdown Acting on the Derrick

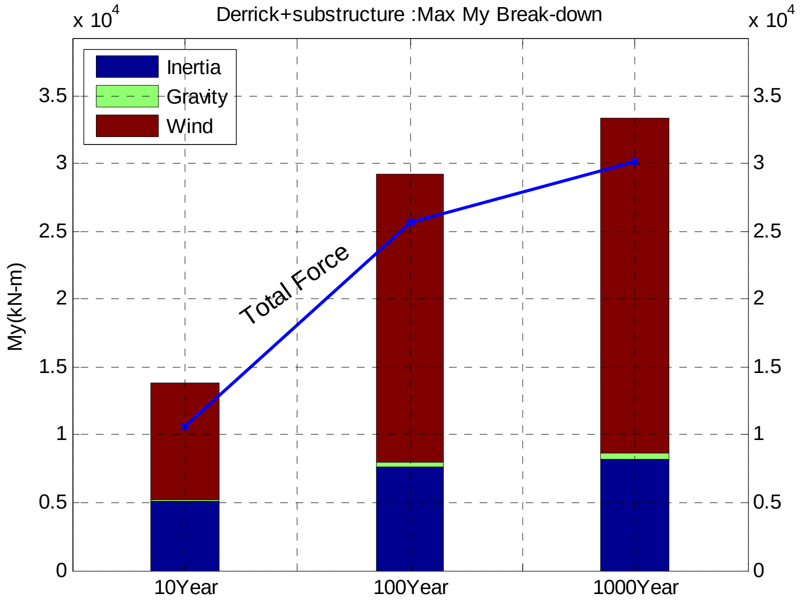

(a) Derrick and substructure

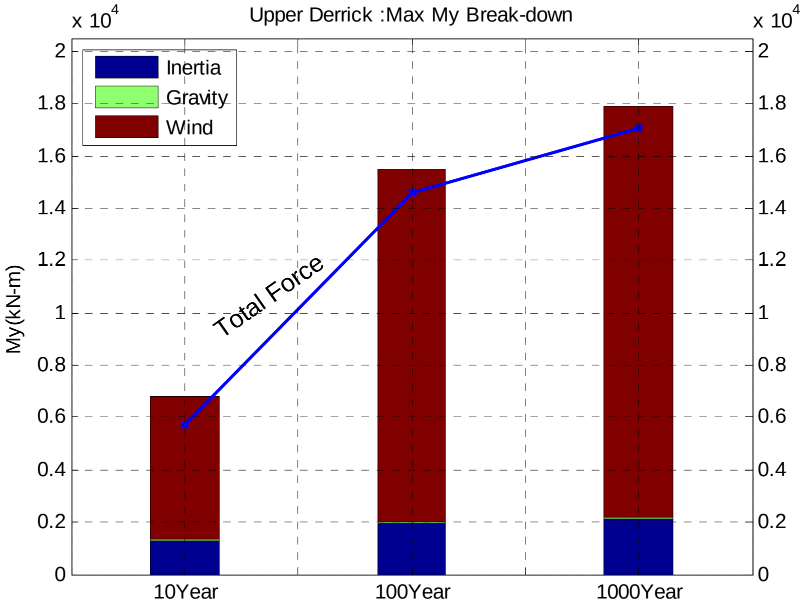

(b) Upper Derrick

Figure 6.17 Total y-Directional Moment and the Moment Breakdown Acting on the Derrick

6.9 Reaction Forces on the Footings and Safety Factor

The reaction forces are calculated by putting the spring at the footing location. The time history of the reaction forces in x-, y- and z- direction are plotted in Figure 6.18 1000 year hurricane condition. As the wave, wind and current are from foot #2 to foot #4 in 135 degree case, the foot #2, the up-wave footing is to have more tension, while foot #4, the down-wave footing has more compression force than the others. The slip and shear forces are similar in each footing. Thus, the up-wave footing which is most critical to the tensile safety is selected to show the time history. Horizontal forces start from 0 and the vertical force start from the structure weight divided by the number of the footings, and vary with time due to the environmental and the inertia loads. The negative vertical force is tensile and the positive is compression in the embedded spring reaction point of view.

The substructure and upper derrick footing spacings are 14.37 m and 10.776 m. If the maximum heeling moments for 1000 year hurricane obtained from the previous section are used, the maximum tensile forces at the substructure and upper derrick footings due to the heeling moments are 2952kN and 2230kN, respectively. If the structure weights per footing (2280kN and 611.8kN for derrick+substructure and upper derrick, respectively) are subtracted, the net maximum reaction tensile force on the up-wave footing is 672 kN and 1618 kN, respectively. The time history show good agreement in trend with the simple calculation.

If the heeling moments form the different methods are used, the simple summation of component maxima and the current API acceleration approximation would give the as much different tensile force as the heeling moment difference. The difference of the slip and shear reaction between the three different methods will have the similar trend to the tensile force.

The reaction forces and the minimum safety factors for each condition are tabulated in Table 6.13 through Table 6.18.

The current shear capacity is enough to resist the shear up to the 1000 year Hurricane environment. The safety factor of the substructure footing is smaller than the upper derrick one because of the higher horizontal forces due to the larger horizontal inertia load on the (derrick + substructure).

The slip safety factor is highly dependent on the pre-tension of the bolts (T_0) and the friction factor between the bolts and the plates (μ). The substructure slip safety factor is smaller than that of upper derrick footing because of the same reason for the shear safety factor. The safety factors are above one except for the case of substructure footing with low pre-tension (T_0 =333.6 kN) and μ = 0.1 in 100 year and 1000 year Hurricane condition.

For the 10 year hurricane environment, the loads cannot generate the tensile load on the bolts due to the weight of themselves, and only the results for 100year and 1000 year Hurricane are plotted. The safety factors of derrick footing are below one for both 100 year and 1000 year hurricane condition when T_0 =1000.8 kN. The substructure has safety factor below one only for 1000 year hurricane condition at the same pre-tension.

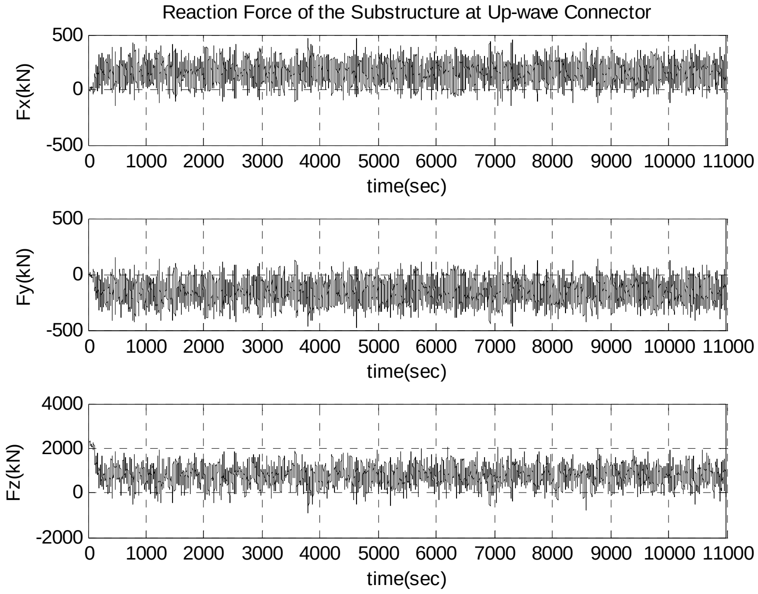

(a) Substructure Footing

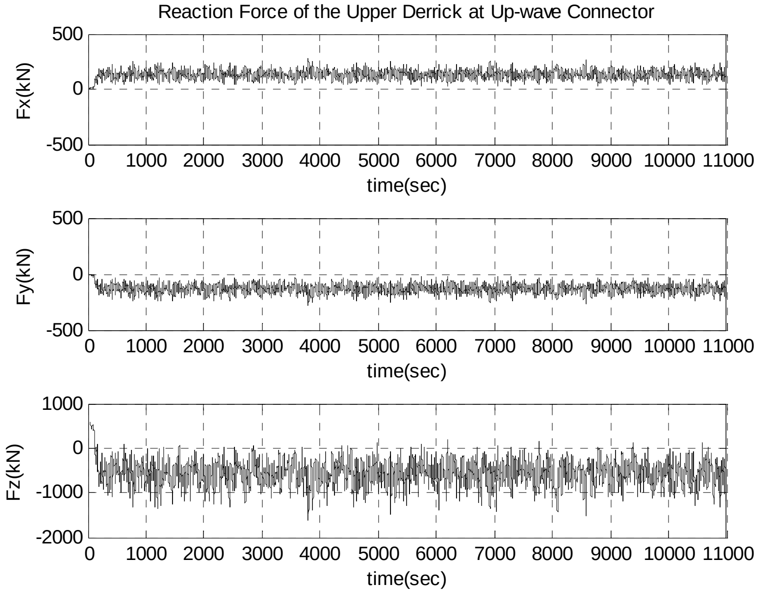

(b) Upper Derrick Footing

Figure 6.18 Reaction Forces at the Up-wave Footings (Positive Fz Means Upward and Negative Downward Direction in the Normal Reaction Force) for 1000 Year Hurricane Condition

Table 6.13 Minimum Safety Factor of the Upper Derrick Footing for 10 Year Hurricane Load Condition (Evaluated for 4 Different Pretension Conditions and 3 Friction Coefficients)

Pretension	Fx (kN)	Fy (kN)	Fz (kN)	Bolt Shear S.F.	Bolt Slip S.F.			T per Bolt	Tensile
(kN)	SHEAR	SLIP	TENSILE		0.1	0.3	0.5	(kN)	S.F.
333.6	99.2	101.6	139.2	36.7	3.2	9.7	16.2	17.4	44.1
610.7	99.2	101.6	139.2	36.7	5.4	16.2	27.1	17.4	28.1
667.2	99.2	101.6	139.2	36.7	5.9	17.6	29.3	17.4	24.9
1000.8	99.2	101.6	139.2	36.7	8.5	25.5	42.4	17.4	5.7

*Positive Fz is compression with the view point of the bolt, and does not add the tensile force to it. Only negative reaction force adds the tensile force to the bolt.

Table 6.14 Minimum Safety Factor of the Substructure Footing for 10 Year Hurricane Load Condition (Evaluated for 4 Different Pretension Conditions and 3 Friction Coefficients)

Pretension	Fx (kN)	Fy (kN)	Fz (kN)	Bolt Shear S.F.	Bolt Slip S.F.			T per Bolt	Tensile
(kN)	SLIP	SHEAR	TENSILE		0.1	0.3	0.5	(kN)	S.F.
333.6	208.6	216.1	0.0	16.8	1.6	4.7	7.9	0.0	Inf
610.7	208.6	216.1	0.0	16.8	2.6	7.9	13.2	0.0	Inf
667.2	208.6	216.1	0.0	16.8	2.9	8.6	14.3	0.0	Inf
1000.8	208.6	216.1	0.0	16.8	4.1	12.4	20.7	0.0	Inf

Table 6.15 Minimum Safety Factor of the Upper Derrick Footing for 100 Year Hurricane Load Condition (Evaluated for 4 Different Pretension Conditions and 3 Friction Coefficients)

Pretension	Fx (kN)	Fy (kN)	Fz (kN)	Bolt Shear S.F.	Bolt Slip S.F.			T per Bolt	Tensile S.F.
(kN)	SHEAR	SLIP	TENSILE		0.1	0.3	0.5	(kN)	S.F.
333.6	241.1	243.8	1302.3	15.1	1.3	4.0	6.7	162.8	4.7
610.7	241.1	243.8	1302.3	15.1	2.3	6.8	11.3	162.8	3.0
667.2	241.1	243.8	1302.3	15.1	2.4	7.3	12.2	162.8	2.7
1000.8	241.1	243.8	1302.3	15.1	3.5	10.6	17.7	162.8	0.6

Table 6.16 Minimum Safety Factor of the Substructure Footing for 100 Year Hurricane Load Condition (Evaluated for 4 Different Pretension Conditions and 3 Friction Coefficients)

Pretension	Fx (kN)	Fy (kN)	Fz (kN)	Bolt Shear	Bolt Slip S.F.			T per Bolt	Tensile
(kN)	SLIP	SHEAR	TENSILE	S.F.	0.1	0.3	0.5	(kN)	S.F.
333.6	385.0	394.2	446.2	9.2	0.9	2.6	4.3	55.8	13.7
610.7	385.0	394.2	446.2	9.2	1.4	4.3	7.1	55.8	8.8
667.2	385.0	394.2	446.2	9.2	1.5	4.6	7.7	55.8	7.8
1000.8	385.0	394.2	446.2	9.2	2.2	6.7	11.2	55.8	1.8

Table 6.17 Minimum Safety Factor of the Upper Derrick Footing for 1000 Year Hurricane Load Condition (Evaluated for 4 Different Pretension Conditions and 3 Friction Coefficients)

Pretension	Fx (kN)	Fy (kN)	Fz (kN)	Bolt Shear	Bolt Slip S.F.			T per Bolt	Tensile
(kN)	SHEAR	SLIP	TENSILE	S.F.	0.1	0.3	0.5	(kN)	S.F.
333.6	283.7	285.2	1618.5	12.8	1.2	3.5	5.8	202.3	3.8
610.7	283.7	285.2	1618.5	12.8	1.9	5.8	9.6	202.3	2.4
667.2	283.7	285.2	1618.5	12.8	2.1	6.3	10.4	202.3	2.1
1000.8	283.7	285.2	1618.5	12.8	3.0	9.1	15.1	202.3	0.5

Table 6.18 Minimum Safety Factor of the Substructure Footing for 1000 Year Hurricane Load Condition (Evaluated for 4 Different Pretension Conditions and 3 Friction Coefficients)

Pretension	Fx (kN)	Fy (kN)	Fz (kN)	Bolt Shear	Bolt Slip S.F.			T per Bolt	Tensile
(kN)	SLIP	SHEAR	TENSILE	S.F.	0.1	0.3	0.5	(kN)	S.F.
333.6	465.2	476.8	913.6	7.6	0.7	2.1	3.5	114.2	6.7
610.7	465.2	476.8	913.6	7.6	1.2	3.5	5.9	114.2	4.3
667.2	465.2	476.8	913.6	7.6	1.3	3.8	6.4	114.2	3.8
1000.8	465.2	476.8	913.6	7.6	1.9	5.6	9.3	114.2	0.9

7. CASE STUDY 4: CONTACT SPRING & FE MODEL APPLIED TO MULTIBODY COUPLING

7.1 Introduction

The economic advantage of having direct access to reservoirs in deep water through dry tree top tensioned risers (TTRs) is well known in the offshore oil and gas industry. At present, in water depths exceeding approximately 5,000 ft, the Spar is the sole option capable of supporting the TTR because of its small heave motions. The offshore floater industry is offering several new designs such as the dry tree semi submersible to compete with the Spar for deepwater and ultra deepwater developments. This design takes advantage of the attributes of the conventional semisubmersible, among which are dockside commissioning, which allows a minimum of at-sea hookup and commissioning (HUC) time, as well as a singe level deck area layout.

The dry tree semisubmersible designs emerging on the market are taking two approaches to supporting dry trees. One is to use existing designs of deep draft semisubmersibles with long stroke tensioners to compensate for the large heave motions. The other is to reduce the motions of the semisubmersible using stabilizing heave plates attached below the main semisubmersible hull. The TTR is typically supported by buoyancy cans or hydraulic/pneumatic tensioners. The latter type is best suited to the dry tree semi because buoyancy cans are exposed at the waterline inside the semisubmersible columns. Also, the cost of these tensioners can be reduced signinificantly if the over all stroke is kept below 30 ft since off-the-shelf proven designs are available for tensioners with strokes within this range.

The main components that comprise the total stroke of the tensioner include such parameters as tides, hull damage, and hull motions as the hull responds to environmental loading. Rotational motions of roll, pitch, and yaw contribute relatively small stroke components as compared to hull heave and horizontal offset, which cause riser pull-down. To a certain extent, horizontal offset can be controlled by the moorings and the restoring effects of the risers themselves, but the most effective way to minimize stroke is to minimize heave, which can be reduced by attaching heave plates to the semisubmersible hull.

This paper presents and discusses the mating of a truss supporting a number of heave plates to a semisubmersible. The objective of the analysis is to examine the behavior of the semisubmersible and the truss during the mating procedure and eventually identify the limiting sea states in which the operation can be carried out.

7.2 Truss to Semisubmersible Mating

The T-Semi considers two methods of truss installation: float mating and ground mating. In the float mating method, the truss is transported to the mating site by a barge vessel, and launched. The truss stays afloat while its ballast is adjusted prior to mating. The truss is positioned under the semisubmersible hull, lifted by on-board lines and winches, then connected to the hull. In the ground mating method, the truss is transported to a shallow water location near shore, launched, and lowered to the seabed. The semisubmersible hull is moved over the truss, which is subsequently lifted into position and connected in a similar manner to that used in the float mating method. In either case, the dynamics of the final stages of lifting the truss from the initial position beneath the floating semisubmersible are similar. The primary objective is to lift the truss using onboard equipment in a controlled manner and avoid damage to either the hull or truss as it is being positioned and connected. In a particular environment de_ned by waves and currents, certain parameters of the installation can be controlled, such as the ballasting of the truss and the semisubmersible vessel, the rate at which the truss is lifted, and the mechanical properties of fenders used to absorb contact forces between the hull and the truss as it is maneuvered into position. The motions of the semisubmersible and truss have limited control in response to the environments to which they are exposed. The responses are limited for the most part by identifying the maxima sea states in which the operation can be carried out. The lifting speed of the truss is about 1.0 ft/min. The operation of lifting the truss once it is position under the semisubmersible can be completed in a matter of hours.

7.3 Installation Procedure

The lifting installation setup for the truss is illustrated in Figure 7.1. This setup represents the condition after the truss is either floated under the semisubmersible hull or lifted from a position on the sea floor. The semisubmersible is equipped with a number of fenders to absorb interactive loads between the truss and the semisubmersible hull during the installation.

The semisubmersible is assumed to have a constant draft of 40.0 ft, with a 2.0-ft freeboard to the top of the pontoon. The operating draft of the semisubmersible is 72 ft.

During the installation, the fenders of linear stiffness Kc are installed on the semisubmersible hull on the locations shown on Figure 7.1.

The modeled deflection/force characteristics of the fenders are shown in Figure 7.2. The model assumes a gap of 1.0 ft between the fender and the truss at the initial condition of the procedure. When contact is made, there is a linear force/deflection interaction. The lifting lines are assumed to have a modulus EA of 2,700 kips. The initial freeboard of the top of the truss is set as the initial condition for the truss.

Three truss drafts are considered in the analysis. These drafts, together with the other condition for the tree initial positions, are provided in Table 7.1. Lifting lines connect the top of the truss and the main hull. Line properties are also provided in Table 7.1. The EA value is assumed constant. The lifting line length varies depending on the truss freeboard. The EA is chosen such that the lifting line makes a very soft connection.

Figure 7.3 shows an illustration of the two-body model of truss mating. The model assumes the semisubmersible hull is one body and the truss is the other body. The equations of motion of the semisubmersible hull and truss are solved with multibody-WAMIT. The truss section members supporting the heave plates are modeled as Morison members for the time domain analysis. The top portions of the truss are modeled with FE frame model to incorporate the stiffness of the truss while it is contacting the fender by the horizontal relative motion of semi hull and the truss during the installation. The fenders are modeled with the gap-contact model.

Waves were simulated using a JONSWAP spectrum with an enhancement factor of 2.0 and a peak period of 6.0 sec for each significant wave heights of 4.0 ft, 5.0 ft and 6.0 ft.

A constant uniform current of 1.0 kts is used in conjunction with all wave conditions. The setup is analyzed for truss draft values of 390.8 ft, 375.0 ft and 342.5 ft. In each position the motions of the semisubmersible and truss were simulated in a time domain solution along with the lifting line tensions.

7.4 Simulation and Mating Analysis

Figure 7.4 and Figure 7.5 show the heave response amplitude operator (RAO) of the semisubmersible and truss, respectively. These RAOs are generated from the coupled model, which considers the interaction effects between the semisubmersible hull and the truss. The semisubmersible is held at a constant draft of 40.0 ft, while the truss is connected at three drafts. Results show that the semisubmersible heave is not sensitive to the truss drafts. The truss RAO changes at the higher periods above approximately 10 seconds. Since the wave spectrum peak period is 6.0 sec, relative motions are unaffected by the truss position for the wave and current conditions used in the present analysis.

It is important to avoid a resonant condition as the truss is being lifted. The natural periods of the coupled truss and semisubmersible system can be determined by modeling the setup as a two-degree-of-freedom mass spring system. The well-known general solution provides two periods that represent the natural periods of the coupled system. These periods were checked for three truss draft positions because the periods change as the lifting line length changes.

Since the draft of the semisubmersible remains constant and the heave plates remain submerged, the added mass of each body is assumed to be constant throughout the operation.

Figure 7.6 shows time history of the reaction force at the fender. There are gaps in the time trace where the force is zero due to the non-contact condition. The maximum load of 600 kips is a manageable force between the hull and truss. The elastic effect of the truss also reduced the impact load on the fender when truss hits the fender. The truss leg diameter is 7 ft and the thickness is 1.25 inches. The corresponding EI of the truss main leg is 5.50E+7 kips-ft^2 and the length of the leg above the bracing is 80 ft long. Thus, the effective spring stiffness of each leg is 322 kips/ft, which is smaller than the fender stiffness assumed. The effect is numerically considered by the FE model of the main leg above the bracings with 10 linear finite elements per each leg. The axial stiffness of the leg is also modeled, but it is much larger than the lifting line stiffness.

Figure 7.7 shows the time trace of a lifting line tension. It is critical to set the ballast condition on the truss such that all lines remain in tension during the procedure. To a certain extent, this can be controlled by the stiffness of the lifting lines.

The water plane stiffness term increases linearly as the truss is lifted into position. The non-linearity in the curves shown in the Figure is due to the axial stiffness term, which is inversely proportional to the length of the lifting line. The increase in tension for line lengths longer than approximately 30.0 ft is due to the increase in truss weight as it is lifted.

As the lines become shorter, in the range of 10 ft or less, the tension is very sensitive to the line length. The practical solution is to position the lifting winches such that a minimum of 20.0 ft to 30.0 ft of lifting line is paid out when the truss is in its final position.

Figure 7.8, Figure 7.9 and Figure 7.10 show the relative heave motions between the semisubmersible hull and the truss for 0-deg, 45-deg and 90-deg headings, respectively, as a function of significant wave height. The response appears to be relatively insensitive to the draft of the truss at the 0-deg and 45-deg headings. There is a significant decrease in the relative motion at the 90-deg heading for the truss draft of 342.5 ft. As expected, the response at all headings increases with significant wave height.

In general, the relative motion increases as the truss is lifted in the 0-deg and 45-deg headings. The opposite trend is shown, however, at the 90-deg heading. This is due to the asymmetric shape of the semisubmersible hull and its sensitivity to wave forces from each direction. The simulation results are summarized in Table 7.2.

7.5 Simulations Compared with Model Tests

The results of the simulations are compared to some limited model test results in Figure 7.11 and Figure 7.12. These compare the RMS heave for the semisubmersible at wave incident angles of 45-deg and 90-deg, respectively. The model test and the simulation show only qualitative agreement. The heave RMS for the model test is consistently larger than that of the simulation.

One explanation for these discrepancies in that the model tests had a still water level at the top of pontoon (draft = 42.0 ft), and the nonlinear change of the water plane area due to the motion and incident wave made the motion larger for the model test. The simulations assume a constant waterplane area. These results suggest that the top of the semisubmersible pontoon should remain out of the water during the mating process to improve motions. This effect will require further investigation in future tests.

Table 7.1 Condition for the Positions of Truss

	d_{top} (ft)	Draft$_{Truss}$ (ft)	Kc (kips/ft)	δ (ft)	EA (kips)
Pos 1	19.20	390.80	1000.00	1.00	2,700
Pos 2	35.00	375.00	1000.00	1.00	2,700
Pos 3	67.50	342.50	1000.00	1.00	2,700

Table 7.2 Summary of Motion, Rope Tension and Fender Reaction Force

Position	Heading		Semi Hull		Truss		*Relative Motion	Pulling Rope	Fender	
	Angle (Deg)	Hs (ft)	Max Heave Range (ft)	Max Heel (Deg)	Max Heave Range (ft)	Max Heel (Deg)	Max Heave Range (ft)	Tmax (kips)	Fmax (Kips)	Frms (Kips)
1	0	4	1.25	0.28	0.32	0.45	1.30	138.92	678.02	78.73
		5	1.51	0.32	0.42	0.76	1.60	138.83	780.14	87.35
		6	1.83	0.40	0.41	0.90	1.97	147.46	806.08	91.92
	45	4	0.62	0.19	0.21	0.78	0.64	135.61	575.47	54.03
		5	0.77	0.20	0.25	0.95	0.85	136.29	663.26	66.82
		6	0.90	0.23	0.27	1.00	0.94	136.34	643.33	70.05
	90	4	0.93	0.38	0.22	0.70	1.01	143.94	661.68	64.90
		5	1.18	0.47	0.21	0.68	1.21	146.76	701.91	76.55
		6	1.42	0.58	0.24	0.94	1.47	158.82	745.64	83.67
2	0	4	1.31	0.45	0.33	0.61	1.40	154.05	740.87	90.87
		5	1.65	0.51	0.45	0.76	1.76	157.54	861.38	102.57
		6	1.97	0.59	0.41	0.88	2.08	173.46	1067.08	108.31
	45	4	0.66	0.19	0.24	0.58	0.70	133.48	625.75	48.45
		5	0.77	0.23	0.25	0.65	0.85	139.44	734.20	69.41
		6	0.93	0.28	0.25	0.77	0.97	151.36	702.84	71.94
	90	4	0.90	0.42	0.18	0.54	0.95	137.79	672.22	63.41
		5	1.10	0.54	0.17	0.55	1.14	157.57	695.67	68.89
		6	1.28	0.64	0.31	0.75	1.39	159.57	806.42	79.33
3	0	4	1.27	0.32	0.45	0.56	1.41	147.13	750.90	90.21
		5	1.63	0.33	0.45	0.74	1.72	162.83	830.05	105.93
		6	1.94	0.38	0.42	0.67	2.06	164.23	967.34	115.84
	45	4	0.63	0.24	0.17	0.51	0.69	170.30	564.78	54.20
		5	0.79	0.30	0.24	0.70	0.87	196.25	644.93	64.19
		6	0.94	0.29	0.30	0.64	1.00	197.04	777.78	72.19
	90	4	0.58	0.55	0.12	0.20	0.62	168.31	635.51	50.06
		5	0.75	0.66	0.24	0.67	0.77	207.40	751.28	68.86
		6	0.87	0.80	0.25	0.79	0.92	222.54	811.42	80.38

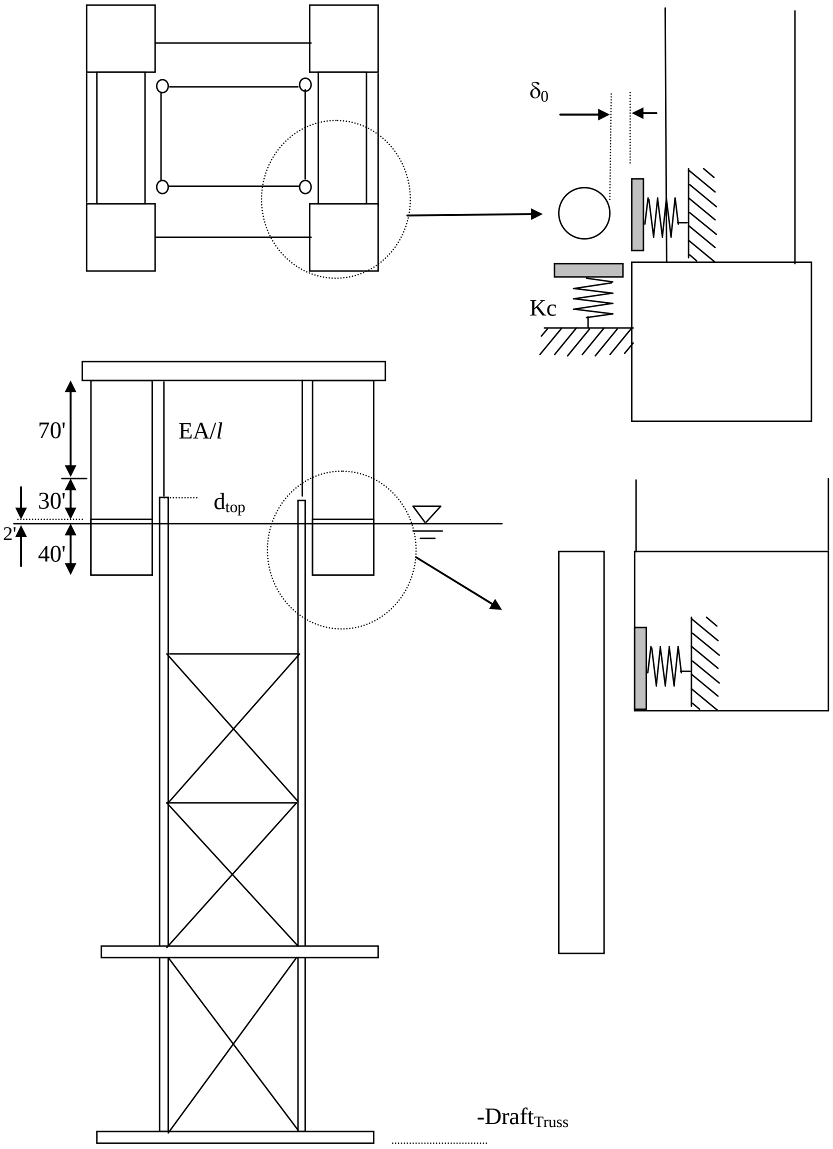

Figure 7.1 Definition Sketch of the Truss Mating Analysis and the Parameters

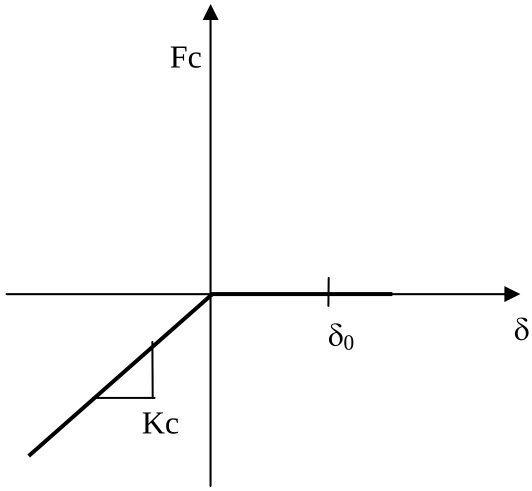

Figure 7.2 Characteristics of the Fender Spring and Reaction Force Dependent on the Gap

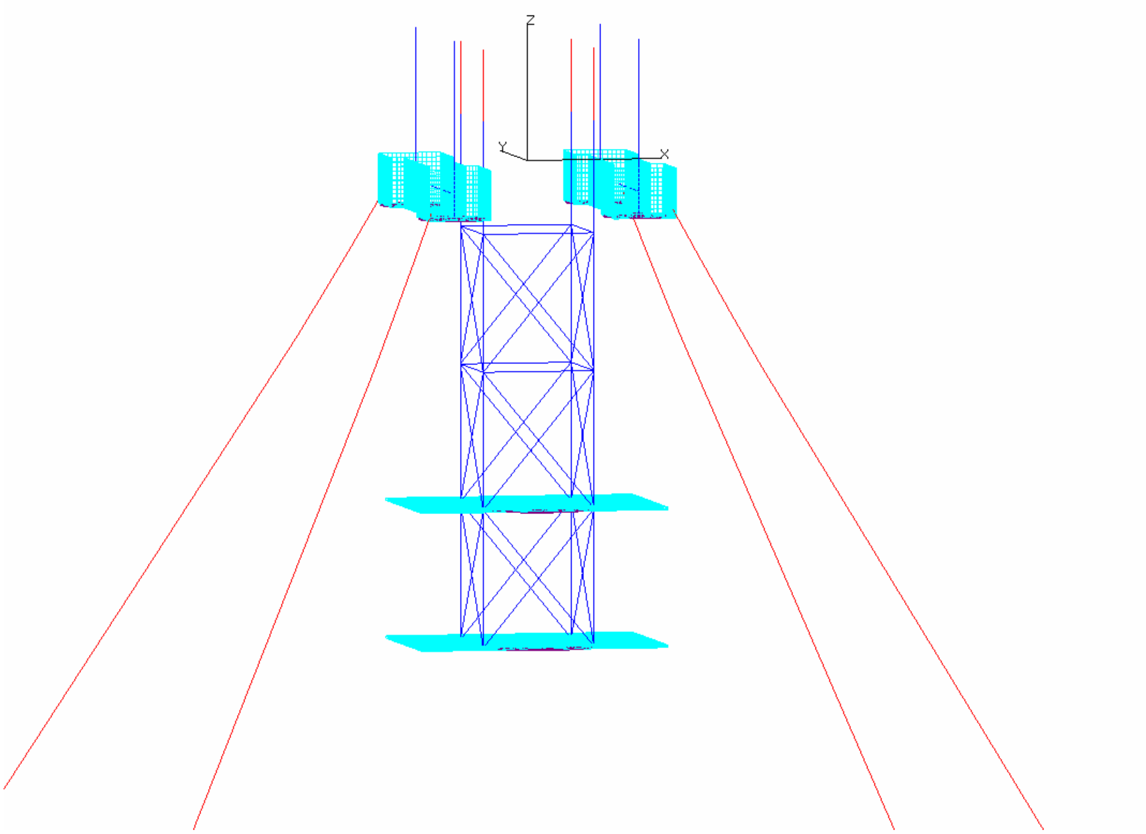

Figure 7.3 Configuration of Semisubmersible and Truss Mating

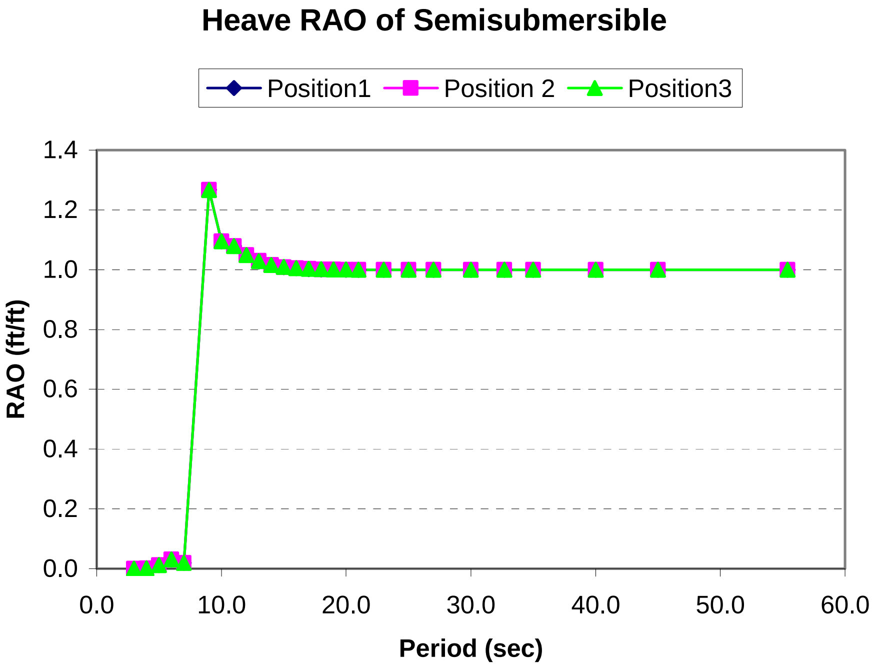

Figure 7.4 Heave RAO of Semisubmersible for Two Body Coupled Motion

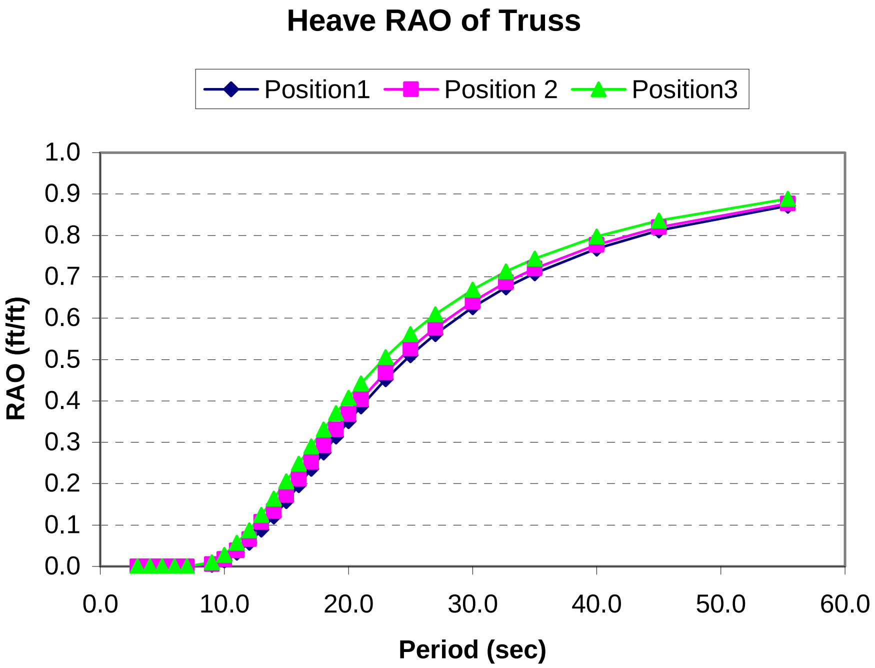

Figure 7.5 Heave RAO of Truss for Two Body Coupled Motion

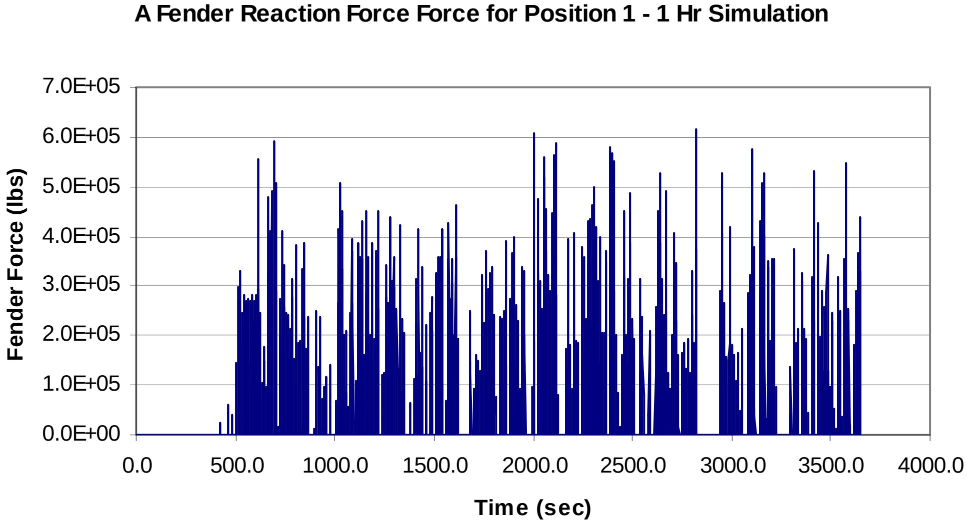

Figure 7.6 An Exemplified Reaction Force Time History at the Fender for Position 1 with Hs=4 ft

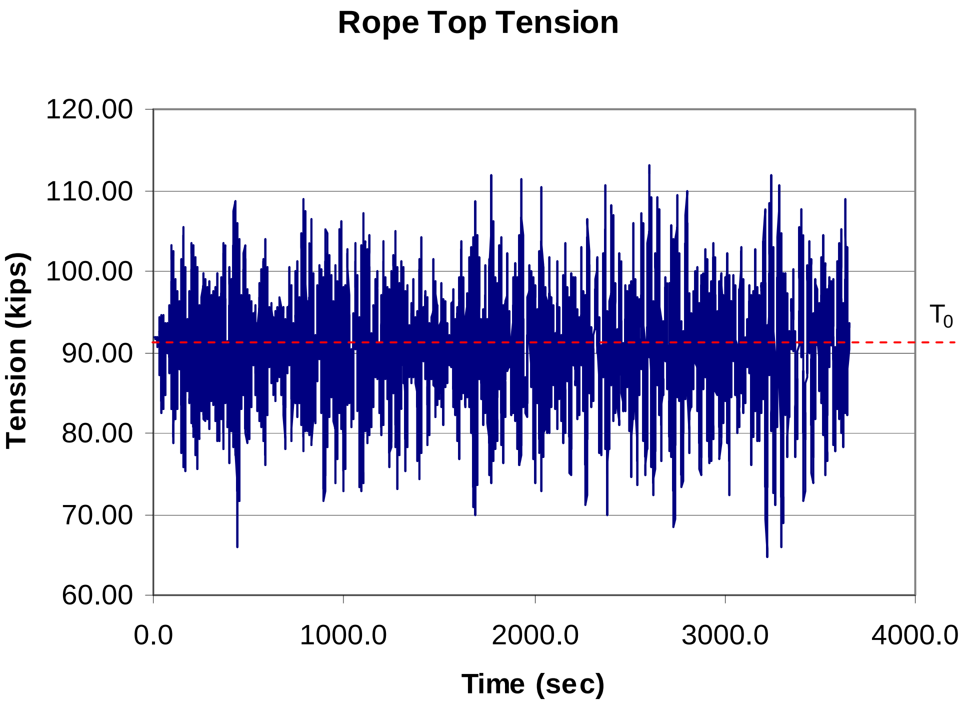

Figure 7.7 An Exemplified Top Tension Time History of Pulling Rope (With Pretension T_0)

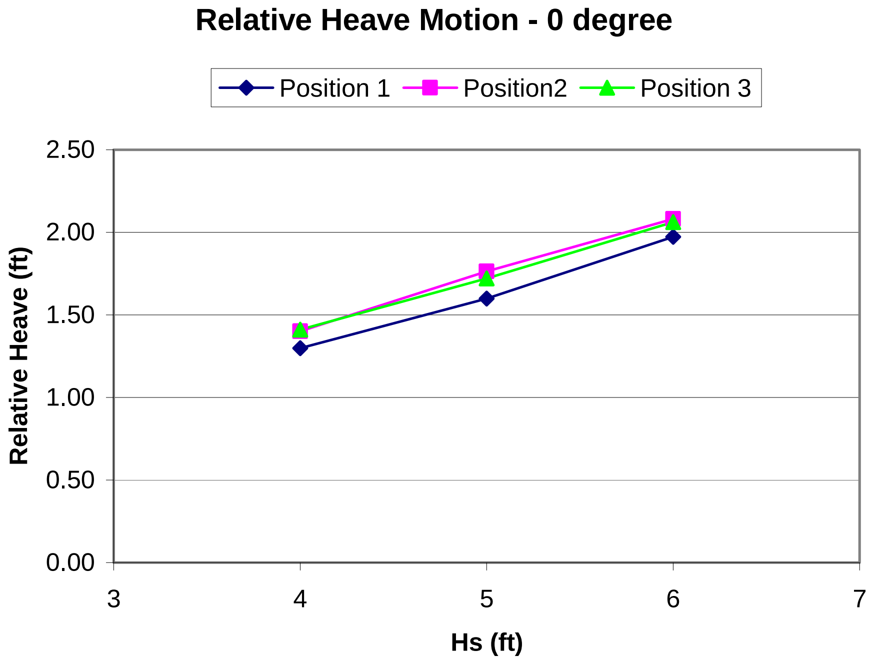

Figure 7.8 Relative Heave Motion for 0 Degree Incident Angle

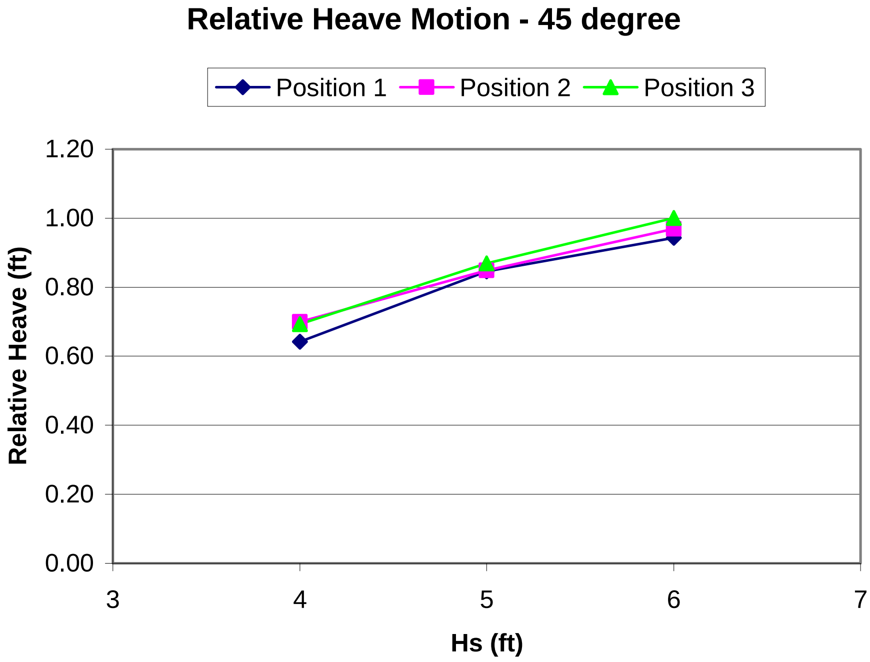

Figure 7.9 Relative Heave Motion for 45 Degree Incident Angle

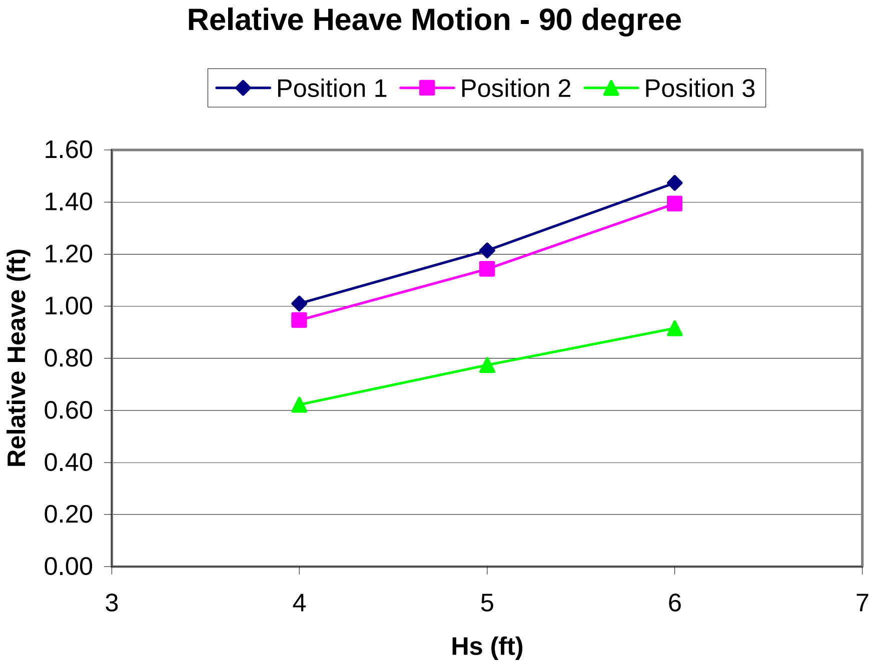

Figure 7.10 Relative Heave Motion for 90 Degree Incident Angle

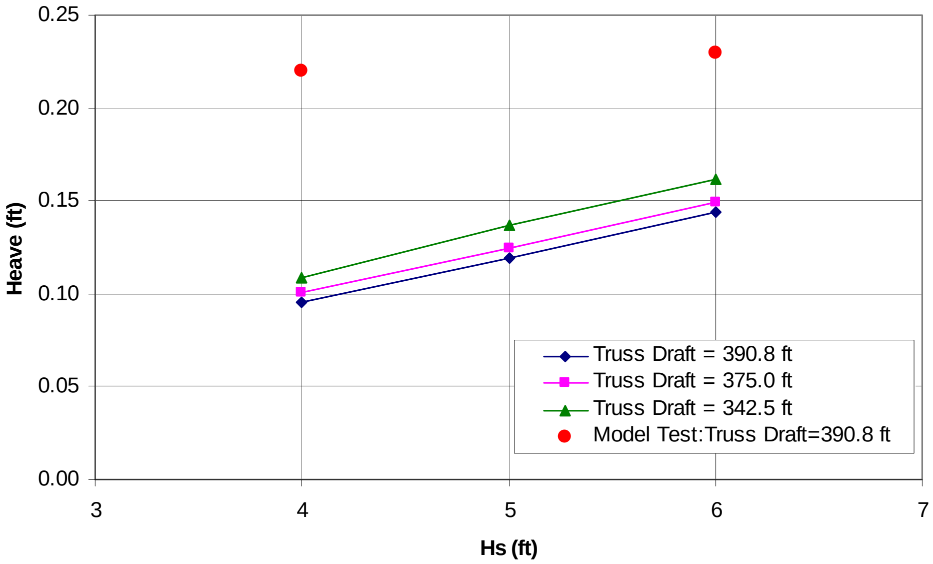

Figure 7.11 Semisubmersible Heave RMS – 45 Degree Wave Incident Angle

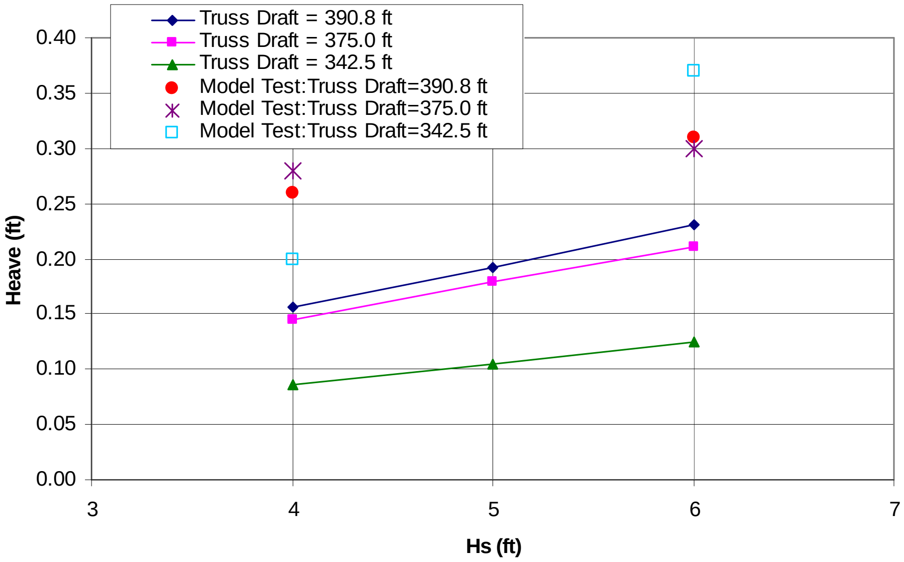

Figure 7.12 Semisubmersible Heave RMS – 90 Degree Wave Incident Angle

8. CONCLUSIONS

8.1 Pneumatic Tensioner

The nonlinear characteristics of hydro-pneumatic tensioner is investigated by a nonlinear numerical model and is compared with the conventional linear spring-dashpot model for the extreme environmental conditions. The numerical models are validated through static and dynamic tests. Two models show considerable discrepancy even though the linear model is carefully tuned by preliminary free decay test. As a result of the simulation, some significant conclusions can be drawn as follows.

1) The difference between the linear and nonlinear model becomes larger as the environmental condition gets more severe.
2) The surge/sway and pitch/roll motions are not sensitive to the tensioner model, but the heave motion which is highly related with the tensioner stroke is affected by the nonlinearity of the tensioner. For the 1000 year hurricane condition, the average and standard deviation of heave motion can be different by 18% and 30%, respectively, between the linear and nonlinear model.
3) The stroke limits restrict the stroke in a range by using the stiff spring in the nonlinear model, while the linear model does not. As a result, the stroke may exceed the stroke limit for the harsh environmental condition if the linear model is used. On the other hand, the high tension is loaded on the riser in the instant when the stroke exceeds its limit for the nonlinear model.

4) The maximum riser tension can be underestimated by 10% for the 100 year hurricane condition if linear tensioner model is used. The difference is even larger for the 1000 year hurricane condition, when the nonlinear model has the piston stopped as the stroke meets its down-stroke limit.

Conclusively, the nonlinear model is strongly recommended to capture the nonlinear characteristics of the pneumatic tensioner, especially for the harsh environmental condition.

8.2 Tendon Broken/Unlatch

The effects of tendon disconnection due to the breakage at the top and the unlatch at the bottom are investigated with the effect of the transient mode. An ETLP designed under the GoM environment condition is selected, which has twelve tendons, three at each corner, and twelve production TTRs. The post-Katrina API 10 year, 100 year and 1000 year hurricane conditions are applied, and the significant conclusions are drawn as follows:

1) The vertical motions, especially the pitch motion, is more sensitively affected by the tendon breakage and unlatch.
2) The tendon breakage affects the motion more significantly than the unlatch does because it removes the weight of the tendon once it is disconnected while unlatching keeps minimum static vertical balance even after it unlatches.
3) The case of the tendon unlatched has more RMS in pitch due to the excitation of the freely hanging tendon after it is unlatched and the increased mass effect.

4) The transient effect, especially for the breakage at the top, on the pitch motion is caught and the corresponding top tension change at the neighboring tendon is pronounced.
5) The unlatched tendon may have the negative top tension which may result in a compressive force applied at the top connector.
6) The transient effect increases as the number of the broken line at the top increases, which goes up to 18% of the intact maximum tension for 1000 year hurricane condition for this case. However, the maximum tension is not much affected by the transient mode of the tendon tension because the unlatched instant is when the tension is minimum and it is not necessary to have the maximum tension during the transient.

8.3 Derrick Tie Down

A method to assess global performance of the tie-back clamp of the derrick on a floating production platform was developed and was applied to Deepstar TLP (3000ft) with the collinear wind, wave, and current with 135 degree heading angle. Three different environmental conditions, 10yr, 1000yr, 1000yr (IVAN), are considered. The possibility of slip and tensile failure at upper-derrick and substructure footings are checked by using the quasi-static method with the full dynamic equation of the derrick and substructure itself.

The global motion of the TLP was first simulated by using hull-mooring-riser coupled dynamic time-domain analysis program, Charm3D. Then, the platform motion and acceleration time series are input to the exact dynamic equations for a derrick to obtain the maximum shear force causing slip and maximum separation force causing additional tensile loading on bolts.

The exact results are compared with the current industry methodology based on API-4F. API-4F recommendation for the dynamic loading estimation is based on a simple formula neglecting phase differences between accelerations and forces hoping that it will lead to conservative results. Furthermore, API formula neglects the effects of rotational inertia and centrifugal forces, which turned out to be insignificant in the present example.

1) One of the drawbacks of the current API-4F recommendation is the calculation methodology of the maximum acceleration, which is to be calculated by maximum motion amplitude multiplied by peak frequency (of input spectrum) squared. In the case of TLP, the actual peak frequency of pitch acceleration is quite different from the input-spectrum peak frequency. Therefore, in this kind of case, the maximum acceleration values read directly from the acceleration time series had better to be used.
2) If bolt pretension is too small, slip failure is likely to occur. In case bolt pretension is too large, the system is vulnerable to tensile failure. Therefore, maintaining proper middle-range tension especially during the hurricane is important. The pretension recommended by AISC keeps the structure within the slip and tensile capacity for all the cases.

3) It is important to check how much slip capacity can be reduced during the wet weather condition. If the friction fact reduced to 0.1, the safety of the derrick system under this condition should be checked.
4) Another uncertainty associated with slip failure is to find the actual grip force by bolts to prevent slip. It needs to be checked how much the slip capacity can be reduced by the present bolt-based connection method.
5) Substructure connection is more vulnerable to the slip failure compared to upper-derrick connection, so stronger tightening method needs to be used.
6) In case of TLP, API4F dynamic loading based on motion amplitude is larger than that with acceleration time series if the wave peak period is used for the pitch motion period. Simple formulas with acceleration. time series but without considering phase differences between constituent forces tend to be conservative in the case of present example.
7) A new method using the platform global-motion time series and exact derrick dynamic equations is recommended as a new methodology to check the slip and tensile failure of derrick connection.

8.4 Truss/Heave Plate Mating

The mating of a truss to a semisubmersible at three angles for environmental incidence, each at three significant wave heights and at three truss drafts for a total of 27 conditions is investigated. The analysis identifies trends based on the heading, truss draft, and significant wave height.

The following conclusions are based on the calculations in the analysis:

1) The coupled response is sensitive to the angle of incidence. The highest response is found at a 0-deg heading, and the lowest response is found at the 45-deg heading. Orienting the installation setup to a 45-degree heading reduces the relative motions. Similar trends were found in the lifting line tensions and fender forces.
2) As the truss nears the final position relative to the semisubmersible hull, the draft of the truss decreases, and its response increases in terms of relative motion. Similar trends are found in the lifting line tensions and fender forces.
3) Since the stiffness of the lifting line increases with decreased length, the tension increases for approximately the same relative motion between the hull and the truss. The increase in lifting line tension as the truss is lifted is proportional to the waterplane stiffness of the truss legs. Large increases and decreases in tension occur as the lifting line length becomes shorter. These can be controlled by having about 30.0 ft of line paid out when the truss is in its final position.
4) Because the relative heave motion is approximately 1.0 ft at the 45-deg heading, it is practical to arrest the truss relative to the semisubmersible using a jacking system for the final connection in sea states up to 6.0-ft significant wave height.

REFERENCES

AISC Manual Committee, Manual of Steel Construction, Allowable Stress Design, Ninth Edition, American Institute of Steel Construction, Chicago, USA.

Andrighetto, P.L., Valdiero, A.C. and Carlotto, L., 2005. Study of the Friction Behavior in Industrial Pneumatic Actuators, Proceedings of 18th International Congress of Mechanical Engineering, Ouro Preto, MG.

API, 1993. Recommended Practice for Planning, Designing and Constructing Fixed Offshore Platforms – Load and Resistance Factor Design, American Petroleum Institute, Washington DC, USA.

API, 1995. Specification for Drilling and Well Servicing Structures – API Spec. 4F Second Edition, American Petroleum Institute, Washington DC, USA.

API, 2005. Design and Analysis of Stationkeeping Systems for Floating Structures, API Recommended Practice 2SK 3rd Edition, American Petroleum Institute, Washington DC, USA.

API, 2007a. Planning, Designing, and Constructing Tension Leg Platforms, Draft RP2T Rev.3, American Petroleum Institute, Washington DC, USA.

API, 2007b. Interim Guidance on Hurricane Conditions in the Gulf of Mexico, Bulletin, 2INT-MET, American Petroleum Institute, Washington DC, USA.

Bas Buchner, Adri van Dijk and Jaap de Wilde, 2001, Numerical Multiple-Body Simulations of Side-by-Side Mooring to an FPSO, Proc. of 11th ISOPE Conference, June 17-21, Stavanger.

Breedveld, Peter C., 2000. An Alternative Model for Static and Dynamic Friction in Dynamic System Simulation. Preprints, 1st IFAC-Conference on Mechatronic Systems, Sep. 18-20, Darmstadt, Germany, Vol.2, pp.717-722.

Chakrabarti, P., Chandwani, R., Larsen, I., 1996. Analyzing the Effect of Integrating Riser/Mooring Line Design, Proceedings of OMAE'96, Florence, Italy.

Colby, C., Sodahl, N., Katala, E., Okkenhaug, S., 2000, Coupling Effects for a Deepwater Spar, OTC 12083.

Correa, F.N., Senra, S.F., Jacob, B.P., Masetti, I.Q., Mourelle, M.M., 2002, Towards the Integration of Analysis and Design of Mooring Systems and Risers, Part II: Studies on a DICAS System. OMAE 2002-28151, Oslo.

Cummins, W.E., 1962. The impulse response function and ship motions, Schiffstechnik, 9, 101-109.

Garrett, D.L. 1982. Dynamic Analysis of Slender Rods. Journal of Energy Resources Technology, 104, 302-307.

Garret D.L., Chappell J.F., Gordon R.B., 2002. Global Performance of Floating Production Systems, OTC 14230.

Gupta, A., Yang, C.K., Murray, J., Shen G. and Nah, E., 2007. Riser Analysis for a Dry Tree Semi-Submersible, Proceedings of Semi Submersible Asian Conference'07, Singapore.

Gupta, A., Yang, C.K., Murray, J., Shen, G., Hussain, A. and Nah, E., 2008. Riser Analysis for a Dry Tree Semi-Submersible, Proceedings of 27th Conference of OMAE, June 15-20, Portugal.

Heurtier, J.M., le Buhan, P., Fontaine, E., le Cunff, C., Biolley, F., Berhault, C., 2001. Coupled Dynamic Response of Moored FPSO with Risers, Proceedings of the ISOPE’01, June 17-21, Stavanger, Norway.

Huijsmans, RHM, Pinkster, JA and Wilde, JJ de, 2001. Diffraction and Radiation of Waves around Side-by-Side Moored Vessels, Proc. of 11th ISOPE Conference, June 17-21, Stavanger, Norway, ISOPE01-JSC-291.

Kim, C.H. and Chou, F., 1972. Motions of a Semi-submersible Drilling Platform in Head Seas, SNAME News, April 3, pp.112-123.

Kim, M.H, Tahar, Arcandra, & Kim, Y.B., 2001. Variability of TLP Motion Analysis against Various Design Methodologies/Parameters. Proc. Int. Offshore and Polar Eng. Conference, ISOPE 3, Stavanger, Norway, vol.3, pp.467-473.

Kim, M.H. AND Yue, D.K.P., 1988. The nonlinear sum-frequency wave excitation and response of a TLP, Proc. 5th Conf. Behavior of Offshore Structures (BOSS”88), Norway, 687-703.

Kim, M.H. & Yue, D.K.P., 1991. Sum- and difference-frequency wave loads on a body in uni-directional Gaussian seas, Journal of Ship Research, 35, 127-140

Kirk, C.L., 1985. Technical note – Resonant Heave Motion of Semisubmersible Vessels, Ocean Engineering, 12, 2, pp.177-184.

Koo, B.J., Kim, M.H., and Randall, R.E., 2004. The effect of Nonlinear Multi-contact Coupling with Gap between Risers and Guide Frames on Global Spar Motion Analysis. Ocean Engineering, 31, 11-12, pp.1469-1502.

Lee, C.H., Newman, J.N., Kim, M.H.. & Yue, D.K.P. 1991. The Computation of Second-order Wave Loads. Proc. 10th Offshore Mechanics and Artic Eng. Conference, Stavanger, Norway.

Lee, C.H. and Korsmeyer, F.T., 1999. WAMIT User Manual. Dept. of Ocean Engineering, MIT, MA, USA.

Ma W., Lee M.-Y., Zou J., Huang E.W, 2000, Deepwater Nonlinear Coupled Analysis Tool. OTC 12085.

Mansour, Alaa M., Huang, Edward W., Phadke, Amal C. and Zhang, Shaosong S., 2006. Tension Leg Platform Survivability Analysis, Proceedings of OMAE 2006 in Hamburg, Germany, June 4-9.

Murray, J., Sidarta, D. E., Lu, X., Gupta, H. and Beynet, P., 2002. Effects of Slip-Stick on Top Tensioned Riser Fatigue. Proceedings of OMAE, Oslo, Norway, June 23-29.

Murray, J., Tahar, A., Eilertsen, T., 2006. A Comparative Assessment of Spar, Tension Leg Platform and Semisubmersible Floaters for Deepwater Application. Proc. Of DOT International Conference and Exhibition, Houston.

Murray, J., Tahar, A., Yang, C.K., 2007a. Hydrodynamics of Dry Tree Semisubmersible. Proceedings of ISOPE’07, Lisbon, July 1-6.

Murray, J. and Yang, C.K., 2007c, Moored Floater Responses to Arctic and Sub-Arctic Ice Conditions, Proceedings of Deep Offshore Technology’07, Norway, October 10-12.

Murray, J., Yang, C.K., Yang W., Krishnaswamy P. and Zou J., 2008a. An Extended Tension Leg Platform for Post-Katrina Gulf of Mexico, Proceedings of ISOPE, Vancouver, Canada, July 6-11 .

Murray, J., Yang, C.K., Chen, C., and Nah, E., 2008b. Two Dry Tree Semisubmersible Designs for Ultra Deep Water Post-Katrina Gulf of Mexico, Proceedings of 27th Conference of OMAE, Estoril, Portugal, June 15-20.

Murray, J., Chen, C.Y. and Yang, C.K., 2008c. Mating Analysis of the Truss and Hull Sections on the Truss Semisubmersible in Open Water, Proceedings of the MOSS, Singapore, March 5-7.

Murray, J., Yang, C.K., Lee, H., Yang, W. and Gupta, A., 2008d. Sensitivity Analysis of Deepwater Floaters to New Gulf of Mexico Metocean Criteria, Proceedings of DOT Conference, Houston, February 12-14.

Ohkusu, M., 1969. On the heaving motion of two circular cylinders on the surface of a fluid, Reports of Research Institute for Applied Mechanics, 17, 58, pp.167-185.

Oran, C., 1983, Overall Dynamic Characteristics of Tension Leg Platforms, Proceedings of OTC’83, OTC4640, pp.507-516.

Ormberg, H., Larsen, K., 1998, Coupled analysis of floater motion and mooring dynamics for a turret-moored ship, Applied Ocean Research 20, 55-67.

Paulling, J.R., 1977, Analysis of Semi-submersible catamaran-type platforms, OTC paper 2975, Houston.

Ran, Z., & Kim, M.H., 1997. Nonlinear coupled analysis of a tethered Spar in waves, Journal of Offshore & Polar Engineering, 7, 2, 111-118.

Ran, Z., Kim, M.H., & Zheng, W. 1999. Coupled Dynamic Analysis of a Moored Spar in Random Waves and Currents (Time-Domain Versus Frequency-Domain). Transaction of the ASME, 121, 194-200.

Salmon, C.G. and Johnson, J.E., 1995. Steel Structures Design and Behavior, Fourth Edition, HarperCollins College Publishers, NY.

Senra S.F., Correa F.N., Jacob B.P., Mourelle M.M., Masetti I.Q., 2002, Towards the Integration of Analysis and Design of Mooring Systems and Risers, Part I: Studies on a Semisubmersible Platform. OMAE 2002-28046, Oslo, June 23-27.

Sgouros, G.E., Pritchett, W.M., Schafer, D.R. and Jones, D.L., 2005. Shell’s Experience with Hurricane Ivan, Proceedings of Offshore Technology Conference, OTC17733.

Ursell, F., 1949. On the heaving motions of a circular cylinder on the surface of a fluid, Quarterly Journal of Mechanics and Applied Mathematics, 2, pp. 218-231.

Ward, E.G. and Gebara, J.M., 2006. Assessment of Storm Sea Fastenings for Drilling and Workover Rigs on Floating Production Systems during Hurricane Ivan: Phase 1, Proceedings of Offshore Technology Conference, OTC 18324.

Wichers, J. and Devlin, P.V., 2004. Benchmark Model Tests on the Deepstar Theme Structures FPSO, Spar, and TLP OTC #16582.

Yang, C.K., Lee, D.H., Kim, M.H., Park, B.N., Yang, Y.T., 2005, Load-out, Towing, and Float-off Operation of a Land-built COT on Dual Transportation Barges, Proceedings of OMAE, Greece, June 12-17, OMAE2005-67553.

Yang, C.K. and Murray, J., 2007a, Characteristics of Global Performance of Floating Platforms in Offshore Oil Field, Proceedings of UKC’07, Washington D.C.

Yang, C.K., Arcandra, T. and Kim, M.H., 2007b. Linear and Nonlinear Approach of Hydro-Pneumatic Tensioner Modeling for Spar Global Performance, Proceedings of 26th OMAE Conference, San Diego, USA, OMAE2007-29209.

Yang, C.K., Padmanabhan, B., Murray, J. and Kim, M.H., 2008a. The Transient Effect of Tendon Disconnection on the Global Motion of ETLP, Proceedings of 27th Conference of OMAE in Portugal, OMAE2008-57521.

Yang, C.K., Murray, J., Nah, Nah, E. and Hussain, A., 2008b. An Investigation of Stability and Workability of ESEMI under the Pre-service Condition in Gulf of Mexico, 27th Conference of OMAE in Portugal, OMAE2008-57879.

Yang, C.K., Gupta, A., Murray, J., Shen, G., Lee, H. and Nah, E., 2008c, A Global Performance Assessment of an ESEMI II in Gulf of Mexico Environment, Proceedings of DOT Conference, Houston.

Yang, C.K., Murray, J., Lee, H., Choi, M., Chen, C.Y., Ding, Y., 2009. A Truss Semisubmersible Optimized for the Post Katrina Environment in Gulf of Mexico Correlated with the Model Test, Proceedings of ASME 28th International Conference on OOAE in Hawaii, USA, OMAE 2009-79717.

Zardecki, D., 2002. Simulation Studies of Stick-Slip Process in Car Steering System. Proceedings of III Conference of Problems of Safety in Road Vehicles, 305-312.

Zhang, J., Lecture Notes on Nonlinear Wave-Wave Interaction in Ocean Waves & Its Implication to Ocean Engineering, (2005), Texas A&M University.

VITA

Chan Kyu Yang received his Bachelor of Science degree in naval architect and ocean engineering from Seoul National University in 1992. After having served in the Korean Army for 2 years, he entered the graduate school of Seoul National University. He majored in naval architect and ocean engineering, and he received his Master of Science degree after two years. After the graduation, he was employed by Korea Research Institute of Ships and Ocean Engineering (current MOERI) and worked for 8 years. He worked as a senior research engineer to carry out R&D projects in the field of offshore and coastal engineering. He was also involved in the projects to set up the model test procedure at the ocean engineering wave basin and in the model test of floating structure. Thereafter, he entered the Ocean Engineering program at Texas A&M University in September 2003 and received his Doctor of Philosophy in May 2009. He also worked for offshore engineering companies (American Bureau of Shipping, J. Ray McDermott Engineering) in 2005 and has been working for FloaTEC, LLC as a lead hydrodynamics since 2006.

He is married to Jeonghyun Oh, and has two lovely daughters Kelly and Chloe and a precious son Andrew.

His permanent address is 14701 St. Mary’s Lane, Suite 250, Houston, TX 77079 and his email is ckyang@FloaTEC.com.